Department of Exploration Geophysics

Effect of scale and saturation on effective properties of porous rocks for seismic monitoring of CO_2 sequestration

Eva Caspari

This thesis is presented for the Degree of
Doctor of Philosophy
of
Curtin University

August 2013

To the best of my knowledge and belief this thesis contains no material previously published by any other person except where due acknowledgment has been made. This thesis contains no material which has been accepted for the award of any other degree or diploma in any university.

Abstract

Prediction of the time-lapse seismic signal caused by CO_2 saturation effects requires knowledge about the geospatial distribution of fluids and the elastic properties of the storage formation. The distribution of fluids in the subsurface can be obtained from multi-phase flow simulations and information about elastic subsurface properties can be obtained from several different sources such as core, well log and seismic measurements. These data sets provide effective properties of the rock and describe the average physical behaviour of the generally heterogeneous rock on a certain scale. The variability of physical properties, the measurement scale and the resolution of the simulation grid have to be taken into account to obtain consistent relations between the various properties on the same scale. This is crucial for meaningful predictions of the time-lapse seismic response.

The thesis focus is the effect of scale and CO_2 saturation on effective properties of the porous rocks in a time-lapse seismic study. First, the time-lapse seismic response is predicted from reservoir simulations for two different reservoir types a saline aquifer and a depleted gas reservoir. The modelling results show that the challenge for the detection of a time-lapse signal in the depleted gas reservoir is the small contrast in fluid properties and the challenge for the saline aquifer is a thin gas plume that is below the resolution of the seismic data.

Next different methods to parameterise the elastic model of the subsurface are analysed. To build an elastic model of the subsurface consistent and calibrated elastic property - porosity relations are crucial. Though, the different approaches reproduced the data trends of the log data quite well, they differed regarding their predictions of the TL seismic signal. These differences are mainly caused by different estimations of the dry rock compressibility. The dry compressibility is difficult to estimate. Laboratory measurements on rock samples are the only way to measure this property directly. Another pathway to improve the estimation of this parameter might be rock physics modelling constrained by geological information.

The case studies illustrate that the magnitude of changes in elastic properties is strongly controlled by the properties of the reservoir, resulting in very different velocity-saturation relations. However, if the pore space of a rock is saturated with two immiscible fluids, such as brine and CO_2, the velocity- saturation relation also depends on the distribution of the fluids in the pore space and the frequency of the measurement. A velocity-saturation relation at reservoir depth is retrieved from time-lapse sonic and neutron porosity logs from the Nagaoka CO_2 sequestration experiment. It is shown that the mechanism of wave-induced

fluid flow can explain this velocity-saturation relation. At seismic frequencies, different fluid distributions (obtained from reservoir simulation) lead to different magnitudes of the predicted time-lapse seismic signal. However, wave-induced fluid flow has only minor effects. These differences can be explained by multiple scattering.

The frequency regime in which wave-induced fluid flow occurs depends not only on the length scales, but also on the hydraulic conductivity of the medium. The hydraulic conductivity can vary significantly and dependence on the frequency of the measurement itself. Finally, a model for a frequency-dependent effective hydraulic conductivity is proposed, that takes strong fluctuations in conductivity into account. Furthermore, it is shown that these fluctuations in hydraulic conductivity influence the velocity-saturation relation.

Acknowledgments

Firstly I would like to thank sincerely my supervisors Boris Gurevich and Tobias M. Müller for their outstanding supervision. Without their invaluable input and support my time as a PhD student would not have been the same. I have greatly benefited from their knowledge, ideas and physical insights through plentiful discussions.

I would like to thank Roman Pevzner for his assistance with seismic modelling, for providing me with matlab codes and improving the performance of my codes. I have enjoyed our discussions and collaborations. I am grateful to Maxim Lebedev and Milovan Urosevic for their support. And I would like to thank Maxim for his insights into experimental measurements.

I am grateful to German Rubino for providing us with numerical simulations of the slow P-wave for a 2D water saturated rock sample with hydraulic conductivity fluctuations.

I wish to acknowledge the funding provided by the Australian government through the CRC Program to support CO2CRC research and Curtin University for financial support through a CIPRS scholarship, CSIRO for a top-up scholarship and the Curtin Reservoir Geophysics Consortium (CRGC).

My PhD was done in collaboration with other researchers from the CO2CRC Otway project. This gave me the great opportunity to work on a field scale project and I greatly benefited from the insights and input of other researchers in various fields. A special thanks goes to Tess Dance, Jonathan Ennis-King and Yildiray Cinar for providing me with their modelling results and for their patience explaining me the basics of geological and dynamic modelling. Further, I would like to thank CO2CRC for giving me the opportunity to attend several conferences and workshops.

I am greatful to Olivia Collet, Robert Galvin and Elmar Strobach for proofreading my thesis.

My final thanks goes to all of my colleagues and friends.

Contents

Nomenclature

Abbreviations

CCT	Contact cement model
DEM	differential effective medium (DEM)
GH	Gassmann-Hill
GW	Gassmann-Wood
HS	Hashin-Shtrikman
VSR	velocity-saturation relationship

Greek

α	Biot-Willis coefficient
Δ_1, Δ_2	dimensionless coefficients
η	fluid shear viscosity
λ	wavelength
λ_d	diffusion length
ν	Poissons's ratio
ν	pore-space tortuosity
ω_B	Biot's characteristic frequency
ω_D	characteristic frequency of the diffusion process
ϕ	porosity
ϕ	volume fraction
ϕ_c	critical porosity
ϕ_{clay}	porosity within the clay
ϕ_e	effective porosity
ρ	density
$\boldsymbol{\sigma}$	total stress tensor

σ^2_{MM} normalized variance of the fluid storage modulus

τ_n normal stiffness

τ_t tangential stiffness

Indices, Sub- and Superscripts

d drained or dry

f pore fluid

s solid phase (grain material)

u undrained

Roman

a pore size parameter

a radius of contact area

AI acoustic impedance

C coordination number

D diffusivity

d characteristic length scale (correlation length)

F source term

f volume fraction

G shear modulus

G shear modulus

H P-wave modulus

H_0 background P-wave modulus

K bulk modulus

K bulk modulus

k hydraulic permeability

k_D slow P-wave number

L dry P-wave modulus

M fluid storage coefficient

N poroelastic parameter

P applied hydrostatic confining pressure

p	pore fluid pressure
P, Q	geometrical factors
R	radius of the sphere
R	reflectivity
S	cement saturation of the pore space
s	degree of inhomogeneity of the medium
u	total displacement field
v_p	P-wave velocity
W	wavelet
$\mathbf{w}$	relative fluid-solid displacement

Chapter 1

Introduction

Carbon Dioxide Capture and Storage (CCS) has the potential as a greenhouse gas reduction technology to capture and store CO_2 from industrial facilities in suitable rock formations such as depleted hydrocarbon reservoirs, deep saline formations and unmineable coal seams. CCS research, pilot and demonstration projects have been undertaken (Table 1.1), e.g., in Norway at the Sleipner Field an offshore saline aquifer (*Chadwick et al.*, 2010), in Japan at Nagaoka an onshore saline aquifer (*Xue and Ohsumi*, 2004; *Xue et al.*, 2006), at the Otway Basin, Australia an onshore depleted gas field (*Underschultz et al.*, 2011; *Jenkins et al.*, 2011) and the Canadian Weyburn-Midale CO_2 Project for enhanced oil recovery (*White et al.*, 2004) to understand the processes and develop effective monitoring networks. The first worldwide CCS project at the Sleipner Field has shown that time-lapse 3-D seismic can provide valuable information about reservoir characteristics and CO_2 migration pathways in the reservoir (*Arts et al.*, 2004). In principle, an understanding of the detected changes in geophysical measurements due to CO_2 injection is necessary to facilitate safe storage and reliable monitoring.

Seismic surveys are routinely used in the petroleum industry to obtain information about the subsurface. The primary aim of seismic data interpretation is to image the subsurface to infer structural features of the geology and detect potential reservoirs. In recent years time-lapse seismic methods have been developed to monitor and to better plan hydrocarbon production from such reservoirs. The goal of these techniques is to infer information about the migration path-

Table 1.1: Geological storage projects

Project	Country	Type	Injection start	Storage type
Sleipner	Norway	Commercial	1996	Saline formation
Weyburn Midale Project	Canada	Commercial	2000	CO_2-EOR*
Minami-Nagoaka	Japan	Demo	2002	Saline formation
Qinshui Basin	China	Pilot	2003	CO_2-ECBM*
In Salah	Algeria	Commercial	2004	Saline formation
K12B	Netherlands	Demo	2004	CO2-EGR***
Frio	USA	Pilot	2004	Saline formation
Ketzin	Germany	Demo	2006	Saline formation
Snohvit	Norway	Commercial	2008	Saline formation
Otway Stage 1	Australia	Pilot	2008	Depleted gas reservoir

* EOR: Enhanced Oil Recovery; ** ECBM: Enhanced Coal Bed Methane; *** EGR: Enhanced Gas Recovery

ways and distribution of fluids (hydrocarbon) from changes between subsequent 3D seismic surveys. In order to achieve this, relationships between the in-situ rock properties of the reservoir and the seismic response have to be established, this is the field of seismic rock physics.

The same technique can be applied to monitor the distribution of CO_2 in storage formations. Successful time-lapse seismic monitoring has been reported at various measurement scales including sonic well logs, crosswell seismic and surface seismic surveys (*Xue et al.*, 2006; *Ajo-Franklin et al.*, 2013; *Chadwick et al.*, 2010). The ability to monitor CO_2 in the subsurface with seismic methods depends on several factors, i.a. the geometrical size of the gas plume, rock and fluid properties at in-situ conditions as well as data resolution, quality and repeatability of measurements. Therefore, before a CO_2 project is undertaken, site-specific seismic modelling is important to assess the feasibility of a seismic monitoring program. Further predictive modelling helps to understand measured time-lapse effects and improves the interpretation of time-lapse data.

1.1 Prediction of the time-lapse seismic response

Prediction of the time-lapse seismic response of CO_2 injection requires an elastic model of the subsurface as well as the geospatial distribution of CO_2 in the storage formation (Figure 1.1). Information regarding elastic subsurface properties can be obtained from several different sources such as core, well log and seismic

measurements. The distribution of fluids in the subsurface, dissolution of CO_2 in formation fluids and changes of in-situ conditions e.g. pressure and temperature can be modelled using multi-phase flow simulations. Reservoir simulations predict the migration pathways of injected CO_2 based on a reservoir flow model, which in turn utilizes the static geological model of the storage formation. In order to employ reservoir simulation results for predictions of the time-lapse seismic response, we have to link the reservoir flow model and the elastic model of the subsurface. This requires on one hand that all parameters are on the same scale and integrated on one modelling grid and on the other hand that the petrophysical properties are consistent with each other. A consistent integration of the two domains, the seismic and reservoir engineering domain (Figure 1.1), is an on-going research topic to improve 4D time-lapse seismic studies. One integrated approach is geostatistical inversion (*Dubrule*, 2003) of seismic data, which provides elastic and petrophysical reservoir properties on a vertical scale suitable for reservoir simulations, constrained by seismic data and geological information (*Sams et al.*, 2011). Another possibility is the transformation of porosity information in the static geological model into elastic properties using rock physics relations. This step is sometimes called the petro-elastic model. *Amini et al.* (2012) stressed the importance of a proper parameterisation of the model with a special focus on porosity and scaling effects. In both workflows it is crucial to have calibrated relationships between the elastic properties and the petrophysical properties of the reservoir to obtain meaningful modelling results.

Changes in elastic properties of the rock due to the presence of CO_2 in the pore-space can be caused by various physical mechanisms depending on the in-situ conditions. These mechanisms include saturation and pressure effects as well as geochemical reactions between the rock and CO_2. *Vanorio et al.* (2010) demonstrated in laboratory experiments that geochemical reactions between the rock and fluids such as precipitation and dissolution affect the rock microstructure, which in turn changes the transport and elastic properties of the rocks. Injection of CO_2 into brine-saturated sandstone caused precipitation of salt, which stiffened the rock matrix, while dissolution was observed in carbonates which

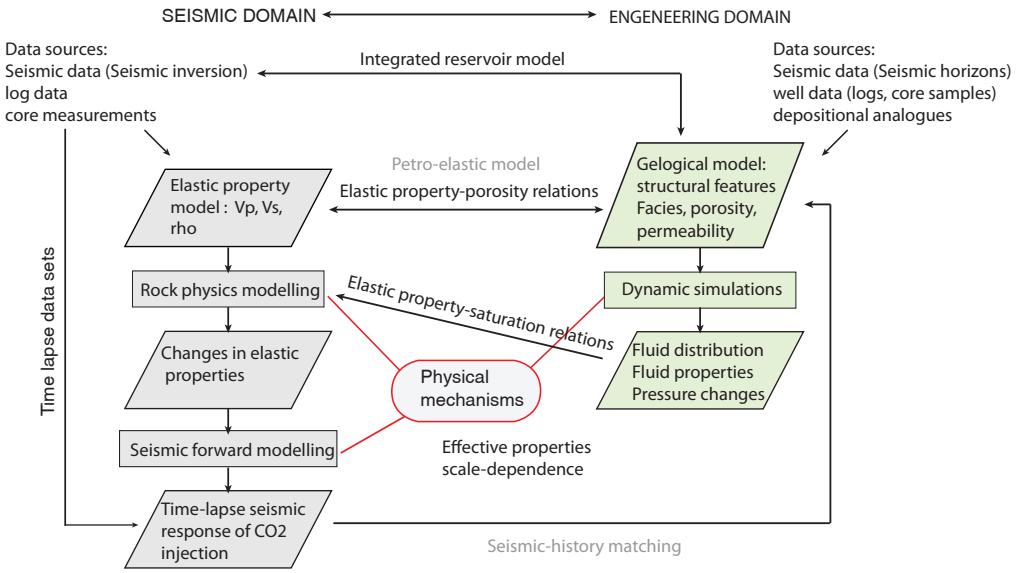

Figure 1.1: Steps to predict the time-lapse seismic response

increased the compressibility of the rock. In large scale projects such as the In Salah CO_2 project a significant increase in pore pressure due to the injection of CO_2 has been observed. *Wang et al.* (1998) report that velocity changes in a CO2-EOR (McElroy field, West Texas) project could not be explained by saturation effects alone. They conclude that the additional decrease in P-wave velocity is caused by pore pressure build up in the reservoir during CO_2 flooding. Saturation effects, where in-situ fluids are replaced by CO_2, are probably the primary effect on the elastic properties in most storage formations. While velocities as a function of CO_2 saturation have been directly measured at a laboratory scale (*Lei and Xue*, 2009; *Lebedev et al.*, 2013), petrophysical relationships between the seismic properties and the saturation of the rock at the reservoir scale are more difficult to obtain. These velocity-saturation relations depend on the frequency of the measurement as well as on the distribution of the fluids in the pore-space. It is still a matter of debate what are adequate velocity-saturation relations at seismic frequencies. The main focus of this thesis will be on saturation effects in time-lapse seismic modelling.

Once an elastic model of the subsurface and changes in elastic properties due to CO_2 injection are computed, one can calculate synthetic seismic data sets.

Various workflows exist to calculate synthetic seismograms which take in to account different aspects of seismic wave propagation. In general, seismic wave propagation in the first 2 km of the subsurface is a complex physical process. Depending on structural features of geological formations and heterogeneities of the rock, different physical aspects will control the propagation of seismic waves and the measured seismic signatures.

The various data sources, interpretation tools and modelling approaches utilized in a 4D seismic study describe the average physical behaviour of the generally heterogeneous rock on a certain scale. Thus, the success of modelling the time-lapse seismic signal depends on a sound understanding of the physical processes on various scales and their scaling effects.

1.2 Scales and measurements of porous media

Heterogeneities of the subsurface on various scales will influence the seismic signature. Though natural porous media are heterogeneous on many length scales, it is common to classify spatial variability at three different scales, pore-scale (microstructure of the rock), formation scale and regional scale (*Dagan*, 1986; *Gelhar*, 1986). As the formation scale heterogeneity is intermediate between pore-scale heterogeneities and regional scale heterogeneities it is sometimes referred to as mesoscopic heterogeneity. This means that the characteristic length scale ℓ_{meso} of these heterogeneities obeys the relation

$$\ell_{\text{pore}} \ll \ell_{\text{meso}} \ll \ell_{\text{regional}} \,, \tag{1.1}$$

where ℓ_{pore} represents pore scale heterogeneity such as grain size or pore throat diameter and ℓ_{regional} is a proxy for the volume of investigation (support volume) such as the sample size or the seismic wavelength. Mesoscopic heterogeneities include e.g. thin layering of the formation, clay inclusion embedded in a sand matrix or two or more fluids occupying the same rock.

Physical properties of porous rocks are defined by the properties of its com-

ponents, the solid grain material and fluids, and the microstructure of the rock. The microstructure of the rock is determined by the structure of the pore-space and grain matrix. If all micro-structural information and the grain and fluid properties are known the overall elastic and transport properties of the porous rock can be calculated (*Guéguen and Palciauskas*, 1994). Obviously, this is impractical and impossible to achieve at a reservoir scale. Commonly porous rocks are described by measurable quantities such as velocity, density, porosity (volume of the pore-space) and hydraulic conductivity (ability of the pore-space to transmit a fluid). These measured quantities are effective properties of the rock and describe the average physical behaviour of the rock at a certain measurement scale. Effective properties of a porous rock can be obtained e.g. from laboratory measurements on core samples, well log data and seismic data. These data sets are measured at different frequencies and hence provide a different level of detail of the subsurface properties. Information from surface seismic measurements at frequencies up to $100\,Hz$ resolve structural features and geological layers of the reservoir in the order of tens of meters, crosswell seismic tomography can resolve thin reservoir layers of 1-10 m, whereas sonic well log data at around $10\,kHz$ can provide a high resolution of several centimetres and ultrasonic-measurements at $100\,Mhz$ might be sensitive to pore-scale structures.

The complexity of heterogeneous porous media and the spatial variability of physical properties as well as the resolution of the measurement have to be taken into account in a seismic time-lapse study. For example micro structural features of the rock, such as cementation of grain contacts determine the compressibility of the rock. This in turn affects the sensitivity of the rock to changes in pore fluid and thus the magnitude of the time-lapse seismic response. On the other hand the proper choice of a velocity saturation relationship depends on the length scale of saturation heterogeneities compared to the measurement frequency. The frequency range at which a velocity-saturation relation is applicable also depends on the hydraulic conductivity of the medium. Hydraulic conductivity of natural porous rocks is, in earth science, one of the parameters with the highest variability. Its values vary over several orders of magnitude. In general, the choice of

an appropriate up-scaling method to obtain effective rock properties for a reservoir model depends on the contrast of the material properties, the size of the heterogeneities as well as the time-dependence of the physical mechanism.

1.3 Objectives and thesis outline

The objective of this thesis is to analyse which scales, properties and physical processes have to be considered in a time-lapse seismic study to predict the seismic response caused by saturations effects. The thesis is structured as follows

Chapter 2: This chapter contains a summary of theoretical models which will be used throughout the thesis. It includes mathematical models of seismic wave propagation, effective medium models to calculate effective elastic properties of the rock and velocity-saturation relations to predict changes in elastic properties caused by fluid injection. The aim is to provide an overview of the basic concepts and physical mechanisms. Since these models are well-established and their derivations are published, they will not be repeated.

Chapter 3: In chapter 3 two case studies are presented with different workflows to predict the time-lapse seismic signal based on reservoir simulator results. These approaches consider different aspects that can influence the magnitude of the time-lapse seismic signal. The aim is to assess the ability to detect injected gas with the time-lapse seismic reflection imaging method for two different reservoir types, a depleted gas reservoir and a saline aquifer. The two examples are investigated on the data sets acquired within the CO2CRC Otway project.

Chapter 4: The elastic models of the subsurface for the previous case studies are analysed in more detail. The first part of this chapter is concerned with practical problems arising from scale differences of various input data sets utilized to build an elastic model of the subsurface. The second part of the chapter focuses on consistent relationships between elastic and petrophysical properties of the reservoir and the importance of the dry rock

compressibility for predictions of the time-lapse seismic response.

Chapter 5: Velocity-saturation relations are investigated at different measurement frequencies. First time-lapse logs of the Nagaoka CO_2 project are analysed. This provides insight into the characteristic length scales of saturation heterogeneities at sonic frequencies. Then a sensitivity study is performed for the data of the CO2CRC Otway project to study the influence of fluid distribution at seismic frequencies.

Chapter 6: The frequency range at which velocity-saturation relations are valid is not only determined by the length scales of saturation heterogeneities but also by the hydraulic conductivity of the medium. In this chapter a model for a frequency-dependent effective hydraulic conductivity with strong fluctuations in this material property is derived. This model can be utilized in the velocity-saturation relations of the previous chapter to investigate the effect of variations in hydraulic conductivity.

Chapter 2

Theoretical background

This chapter contains a summary of the theoretical concepts that will be used throughout the thesis. The chapter is structured as follows. First mathematical models that describe seismic wave propagation through the subsurface and the basic mechanisms of wave attenuation are summarized. In the following, models are introduced to estimate the parameters of these wave equations (the elastic properties of the subsurface). These rock physics models can be divided into groups. The first group so-called effective medium models, link the effective elastic behaviour of a rock to its micro-structure. The second group provides effective elastic properties of the rock as a function of fluid saturation, so-called velocity-saturation relations.

In the following, the basic concepts, the physical mechanisms and associated model parameters are summarized as well as the conditions at which these models are applicable. Since these models are well-established and their derivations are published in reviews and text books, they will not be repeated here. Multiple rock physics model equations used in this chapter are conveniently summarized in the "Rock Physics hand book" of *Mavko et al.* (1995).

2.1 Mathematical models of seismic wave propagation

Seismic wave propagation through the first kilometers of the subsurface is a complex physical process. Depending on the structural features of the geological

formation and heterogeneities of the rock on various scales, different physical phenomena control the propagation of seismic waves and the recorded seismic signatures. Several physical models exist to predict the seismic response of the subsurface. In this thesis, acoustic, elastic and poro-elastic models are utilized. The fundamental difference between them is the response of the material to an external force (constitutive relations). The acoustic approximation of a rock assumes that the coupling between compressional and shear waves can be neglected and the dominant wave type is the compressional wave. The elastic model on the other hand takes shear waves into account. For a poro-elastic material, the interaction between the porous rock and the fluid in the pore space are considered. The wave equations for these three material types can be solved analytically in some simple cases. For instance the response of an infinite homogeneous medium to an impulse is known exactly. This impulse response is the solution of the wave equation for a point source, the so called Green's function solution. However to solve the wave equations for complex geological structures, numerical methods are necessary, which can be computationally expensive.

Due to their genesis, physical properties of sedimentary rocks often vary strongly with depth, while they are laterally more or less homogeneous. Therefore, a common idealization of sedimentary rocks is a stacked sequence of homogeneous layers. This simplification allows to use computationally fast algorithms to generate synthetic seismograms. In the following the basic concepts, the required parameters and the considered wave types and physical phenomena are briefly discussed.

2.1.1 Convolutional model

The seismic response can be interpreted as a convolution of the impulse response of the subsurface with the wavelet of the seismic source. Convolution is the process of applying a stationary linear filter to an input signal. For the seismic response, stationarity means that the source wavelet does not change with time as it travels through the subsurface. Since the filter is assumed to be linear, the final synthetic seismogram is a superposition of the individual responses of

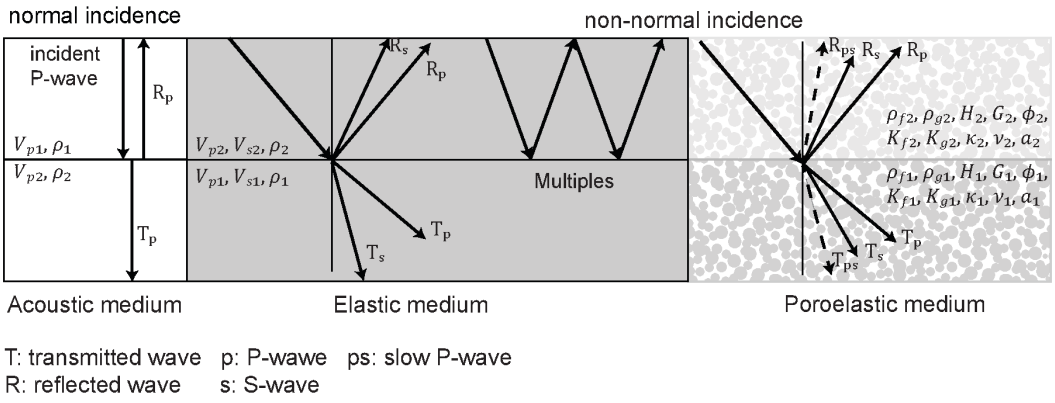

Figure 2.1: Wave types in an acoustic, elastic and poroelastic medium and their respective material properties

different interfaces in the subsurface.

1D convolution model

The simplest synthetic seismogram can be obtained from the impulse response of a 1D layered acoustic medium. The acoustic wave equation in a 1D medium is given by

$$\rho\, \partial_t^2 u_z = v_p^2 \partial_z^2 u_z \,, \tag{2.1}$$

where u_z, v_p, ρ denote the vertical displacement field, P-wave velocity and density. The solution of the acoustic wave equation with appropriate boundary conditions is characterized by reflection and transmission coefficients of the interfaces in the subsurface. These coefficients specify the amount of reflected and transmitted energy (*Aki and Richards*, 1980). The reflectivity series of the layered medium is given by

$$R_{n+1} = \frac{AI_{n+1} - AI_n}{AI_{n+1} + AI_n}, \quad \text{with} \quad AI_n = V_{pn}\rho_n \,, \tag{2.2}$$

where AI_n, v_{pn} and ρ_n are the acoustic impedance, P-wave velocity and density of the n^{th}-layer, respectively. Such a reflectivity series $R(z)$ in depth can be easily obtained from sonic and density well log data. With the velocity information of the sonic log and check shots, $R(z)$ can be converted into a time series $R(t)$ of two-way travel time (TWT). Then $R(t)$ is convolved with the seismic wavelet W

to simulate the bandlimiting (limited frequency content) imposed by the seismic source. Thus a single seismic trace $S(TWT)$ is calculated by

$$S(TWT) = R(t) * W\,. \tag{2.3}$$

This seismogram takes the primary P-wave reflections of each layer at normal incident into account. The 1D convolution model can be a reasonable approximation of the reflection amplitude of post-stack seismic data. This is the case for an approximately layered subsurface with a small contrast between layers, so that multiples are negligible, or if they have been eliminated in the processing. To obtain a realistic seismogram a representative wavelet of the processed seismic data has to be chosen for convolution. This model will be referred to as convolutional model.

2.1.2 Elastic wave equation

For a non-normal incident P-wave at an interface in an elastic medium, mode conversion occurs, which means that reflected and transmitted shear-waves are coupled. To account for coupling between these wave types the elastic wave equation has to be solved. The equation of motion for an elastic medium can be written as

$$\rho\,\partial_t^2\mathbf{u} + \nabla\cdot\boldsymbol{\sigma} = -F\,, \tag{2.4}$$

where $\mathbf{u}$ is the total displacement field, $\boldsymbol{\sigma}$ is the total stress tensor and F is a source term. The constitutive equation for an isotropic linear elastic medium is given by Hooke's law, which relates the total stress tensor to the deformation of the medium. Then the stress tensor can be expressed in terms of the total displacement as follows

$$\boldsymbol{\sigma} = [(H-2G)\nabla\cdot\mathbf{u}]\mathbf{I} + G[\nabla\mathbf{u} + (\nabla\mathbf{u})^T]\,, \tag{2.5}$$

where H is the P-wave modulus defined as $H = K + 4/3G$ with K and G being the bulk and shear modulus of the medium, respectively, and $\mathbf{I}$ denotes the unit

tensor. Combined, these two equations describe elastic wave-propagation. To solve the elastic-wave equation for a 3D model with complex geometry, numerical methods such as finite difference modelling are required.

For a horizontally stratified elastic earth model and plane waves, the equations governing reflection and transmission at an interface are known exactly (*Aki and Richards*, 1980). These Zoeppritz equations (*Zöppritz*, 1919) give the complete solution of the amplitudes for transmitted, reflected and converted waves. The approximations of these equations and the estimation of the approximate parameters from field data provide insight into the amplitude variation with offset (AVO). AVO analysis is important for lithology and fluid interpretation.

Full waveform synthetic seismogram

To obtain a full waveform synthetic seismogram, the effect of all multiples has to be included. To model full waveform synthetics we use the OASES software (*Schmidt and Tango*, 1986). The program provides numerical solutions for elastic wave propagation in a horizontally stratified medium for homogeneous and isotropic layers. The numerical solution for the full elastic wave-field is based on a Green's function approach, where the depth-dependent Green's function for the layered subsurface is determined by a direct global matrix method (*Schmidt and Tango*, 1986). This depth-dependent Green's function depends on the boundary conditions between the layers. The Green's function solution in the Laplace domain, so called transfer functions are calculated for each receiver by wavenumber integration.

For an appropriate choice of parameters the numerical solution includes all arrivals, direct, reflected, refracted, converted waves and multiples as well as surface seismic waves and trapped modes. The 1.5D modelling code also accounts properly for 3D wave propagation effects, such as geometrical spreading. However, all propagation effects caused by structurally complex features such as steep dipping horizons and faults, which can lead to diffractions and side reflections, are not considered due to the simplified layered earth model.

2.1.3 Poroelastic wave equation

Biot's theory of dynamic poroelasticity (*Biot*, 1956a,b, 1962) describes wave propagation in a porous rock saturated with a single pore fluid by a system of two coupled wave equations. The theory predicts one S-wave and fast and slow P-waves. The fast P-wave behaves similar to the compressional wave in an elastic medium. The characteristics of the slow P-wave differ at low and high frequencies. At high frequencies the slow wave behaves like an acoustic wave propagating in fluid, while at low frequencies this wave becomes a diffusion wave and is strongly attenuated.

Biot's theory is valid if (a) the pore-space of the rock is fully connected, (b) the porous medium is statistically isotropic, (c) the wavelength is much larger than the microstructure of the medium and (d) deformations are small to ensure linear elastic material behaviour of the rock matrix. Then, the constitutive relations for a porous medium can be obtained by extending the elastic expression as follows

$$\boldsymbol{\sigma} = [(H - 2G)\nabla \cdot \mathbf{u} + \alpha M \nabla \cdot \mathbf{w}]\mathbf{I} + G[\nabla \mathbf{u} + (\nabla \mathbf{u})^T] \tag{2.6}$$

$$-p = \alpha M \nabla \cdot \mathbf{u} + M \nabla \cdot \mathbf{w}\,, \tag{2.7}$$

where $\mathbf{w}$ is the relative fluid-solid displacement given by $\mathbf{w} = \phi(\mathbf{U} - \mathbf{u})$ with ϕ, $\mathbf{U}$, $\mathbf{u}$ denoting the porosity and the macroscopic fluid and solid displacements, respectively. The parameter p is the pore fluid pressure. In a poroelastic medium, the moduli G and H represent the shear wave modulus of the porous material and the undrained, low-frequency P-wave modulus. The undrained P-wave modulus is defined as $H = L + \alpha^2 M$ with the dry P-wave modulus L, the Biot-Willis coefficient α and the fluid storage coefficient M. The parameters α and M can be related to the bulk moduli of the drained frame K_d, the solid phase K_s and the fluid phase K_f. These moduli are described in more detail in section 2.4.1

Biot's equations of motion for a fluid saturated porous medium can be written

as

$$\begin{aligned}\nabla \cdot \boldsymbol{\sigma} =& \rho\, \partial_t^2 \mathbf{u} + \rho_f\, \partial_t^2 \mathbf{w} \\ \nabla p =& \rho_f\, \partial_t^2 \mathbf{u} + \frac{\rho_f \nu}{\phi}\, \partial_t^2 \mathbf{w} + Y \frac{\eta}{k} \partial_t \mathbf{w}\,,\end{aligned} \tag{2.8}$$

where k is the hydraulic permeability, η is the fluid shear viscosity and ν is the pore-space tortuosity. The parameter ρ is the bulk density given by

$$\rho = \phi\rho_f + (1-\phi)\rho_s\,, \tag{2.9}$$

where ρ_s and ρ_f denote the density of the solid grains and the density of the pore fluid, respectively. The viscodynamic operator Y describes the frequency-dependence of viscous drag between the fluid and rock (*Mavko et al.*, 1998) and is given by

$$F(\xi) = \frac{1}{4}\left(\frac{\xi T(\xi)}{1 + 2iT(\xi)/\xi}\right) \quad \xi = a\sqrt{\frac{\omega\rho_f}{\eta}} \tag{2.10}$$

$$T(\xi) = \frac{e^{i3\pi/4} J_1(\xi e^{i\pi/4})}{J_0(\xi e^{i\pi/4}} \tag{2.11}$$

where $J_n()$ are Bessel functions of nth order and a denotes the pore-size parameter. The pore-size parameter depends on the shape of the pore-space.

The frequency dependence of the viscodynamic parameter can be divided into a high and low frequency regime. In the high-frequency regime inertial forces acting on the fluid are dominant and the slow P-wave is a propagating wave, while in the low-frequency regime viscous forces are dominant and the slow P-wave becomes a diffusion type wave (*Biot*, 1956b). The transition between these two regimes is determined by Biot's characteristic frequency

$$\omega_B = \frac{\eta\phi}{k\nu\rho_f}\,. \tag{2.12}$$

Attenuation of the fast P-wave in a homogeneous porous medium has a maximum at this frequency. The propagating compressional wave causes pressure gradients between the troughs and peaks of a wave, which result in relative fluid and solid

movement accompanied by internal friction (*Biot*, 1956a). The relaxation process, that is the equalization of these pressure gradients, is called Biot's global flow mechanism. The mechanism is termed global flow since it occurs at the scale of the wavelength λ. Biot's characteristic frequency is typically on the order of 100 kHz to a couple of MHz. Thus, Biot attenuation is negligible at seismic frequencies.

2.2 Attenuation and heterogeneity

Attenuation describes an exponential decay of wave amplitude with distance and can be caused by a variety of physical phenomena. The principal of causality requires that attenuation is always accompanied with dispersion (Figure 2.2). Dispersion is the variation of propagation velocity with frequency.

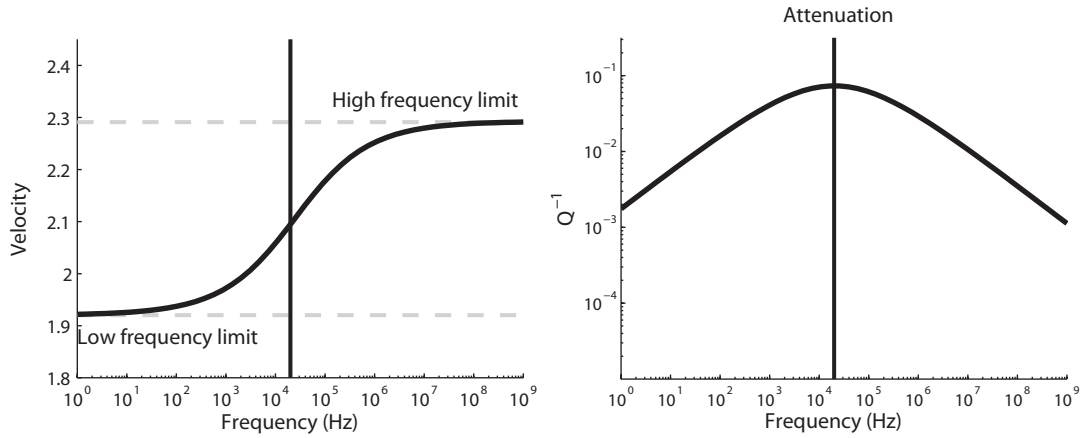

Figure 2.2: Velocity and attenuation as function of frequency

Wave attenuation can be divided in two classes, apparent and intrinsic attenuation. Apparent attenuation refers to elastic processes, in which energy is redistributed from the primary wavefield while the total energy of the wavefield is conserved (e.g. elastic scattering). This kind of seismic wave amplitude loss can be caused by layer-related phenomena such as transmission, multiples and converted waves and is described by elastic wave propagation.

In contrast, intrinsic attenuation is caused by non-elastic energy losses, where

wave energy is converted into heat. This kind of attenuation is a property of the material itself. For instance, dissipation of energy can occur due to thermoelastic effects, solid friction and fluid effects.

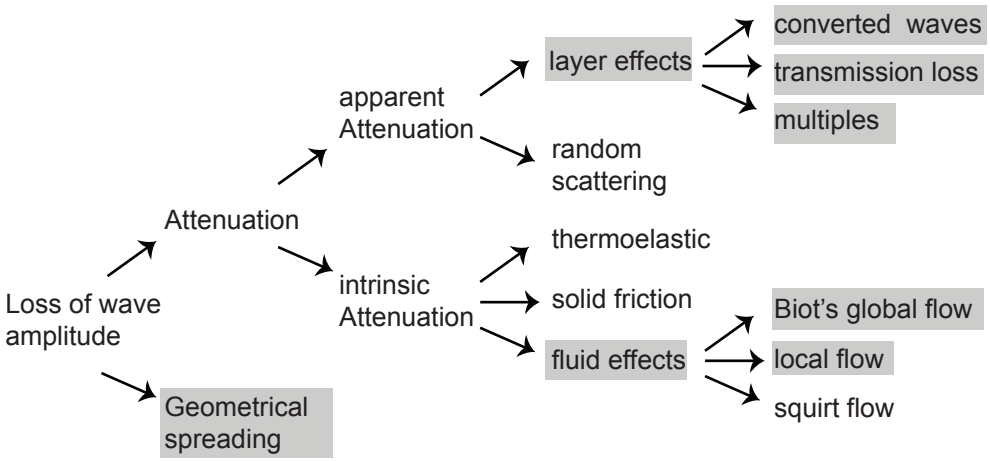

Figure 2.3: Classification of mechanisms that cause a loss in seismic wave amplitude. The grey boxes mark the mechanisms which are considered in the modelling approaches for the following data examples.

One way to account for energy dissipation, which results in decay of the wave amplitude, is the phenomenological concept of linear viscoelastic material behaviour (*Aki and Richards*, 1980). In contrast to elastic material behaviour, a viscoelastic material has a time-dependent strain rate associated with a relaxation process. A measure for energy dissipation associated with viscoelasticity is the so called quality factor Q. The inverse quality factor (attenuation factor) describes the relative dissipated energy per one cycle of oscillation (*Mavko et al.*, 1998). In time-lapse seismic studies, where one fluid is replaced by another fluid, the interest is in attenuation related to the presence of fluids in the pore-space. Though, this can be modelled with the theory of linear viscoelasticity, the phenomenological character of this theory is not suitable for the interpretation of measurements in terms of rock properties (*Müller et al.*, 2010). A theory which relates this kind of attenuation directly to the physical properties of the rock and pore fluid is Biot's theory of dynamic poroelasticity (*Biot*, 1962).

Heterogeneity

The elastic and poroelastic models are continuum mechanic models that describe a homogeneous or a piecewise homogeneous medium, such as a layered earth model. However, natural porous rocks are inhomogeneous on many length scales. To properly predict the seismic response, representative values for the layer properties are required, which describe an average physical behaviour at the length-scale of the layer thickness. Such properties can for example be directly obtained from log measurements. However, the sampling of log data is quite fine and would result in models that are computationally expensive. A proper method to upscale sonic log data is Backus averaging (*Backus*, 1962).

In order to predict changes in elastic properties caused by CO_2 injection, yet another parameter, the compressibility of the dry solid rock frame, is required. This parameter cannot be measured directly in-situ and depends i.a. on the microstructure of the medium. One way to estimate such properties are effective medium theories, which make certain assumptions about the micro-structure of the rock. The use of effective medium models is valid as long as the volume of investigation (measurement scale) is much larger than the micro-structure. These models are static approximations and described in the next section. If the time-dependence (frequency of the measurement) of the physical mechanism becomes important, effective properties of the medium become a frequency-dependent quantity and attenuation has to be taken into account.

This kind of attenuation may occur in a poroelastic medium in the presence of (mesoscopic) heterogeneities due to mode conversion between fast and slow P-waves. The phenomenon is different to ordinary elastic scattering, since the slow P-wave is a diffusive wave and strongly attenuated in the vicinity of its origin (*Gurevich and Lopatnikov*, 1995). Thus, it causes dissipation of the wavefield energy. This loss-mechanism can be interpreted in a layered porous medium, as equilibration process of pore pressure gradients that occur across each interface, resulting in fluid flow between layers until pressure gradients are equilibrated. The slow diffusive P-wave is a proxy for the relaxation process of these local pore

pressure gradients. The characteristic frequency of the process depends on the length-scale of the heterogeneities ℓ_{meso} and is given by

$$\omega_D = \frac{D}{\ell_{meso}^2} \tag{2.13}$$

where D is the pressure diffusivity. This attenuation mechanism takes place on the so-called mesoscale and does not account for pore-scale heterogeneities. To cause significant attenuation the degree of heterogeneity, or equivalently, the contrast between two porous layers has to be large. An example are water and gas saturated porous layers. The attenuation mechanism might play a role in time-lapse seismic studies, since it can cause attenuation in a broad frequency-range (*Pride et al.*, 2004; *Müller et al.*, 2010). To model poroelastic effects in a layered medium the Biot module of the OASES software code is employed. A theoretical model to estimate the effect of random saturation heterogeneities in a 3D porous medium is described in section 2.4.2.

2.3 Effective elastic properties

A crucial parameter for time-lapse seismic studies is the compressibility of the dry rock, which itself depends on the porosity, the compressibility of the solid grain material and the micro-structure of the rock. The compressibility of the dry rock can not be measured directly in-situ. Laboratory measurements on rock samples are the only way to measure the dry rock compressibility directly, thus available information on that property is typically limited to few samples.

However, models exist to estimate the dry rock compressibility. These models provide relations between the effective elastic behaviour of a heterogeneous rock and its micro-structure. Although, these models are idealized approximations, they capture certain aspects of the micro-structure and may provide some insight in the elastic behaviour of the porous medium.

2.3.1 Bounds

The effective elastic properties of a rock depend on all geometrical details of the micro-structure. If only the volume fractions of the different components and their elastic moduli are known, the best prediction are upper and lower bounds (*Mavko et al.*, 1998). For an isotropic elastic medium these limits are given by the upper and lower Hashin-Shtrikman (HS^+ and HS^-) bounds (*Hashin and Shtrikman*, 1963), which correspond to the stiffest and softest arrangement of the medium components, respectively. The effective moduli for N components (*Berryman*, 1995) can be written as follows

$$K^* = \left(\sum_{i=1}^{N} \frac{\phi_i}{K_i + G_m} \right)^{-1} - \frac{4}{3} G_m$$

$$G^* = \left(\sum_{i=1}^{N} \frac{\phi_i}{G_i + z} \right)^{-1} - z \quad \text{with} \quad z = \frac{G}{6} \frac{9K_m + 8G_m}{K_m + 2G_m}$$

$$\text{HS}^+ : \quad K_m = max(K_i) \quad \& \quad G_m = max(G_i) \tag{2.14}$$

$$\text{HS}^- : \quad K_m = min(K_i) \quad \& \quad G_m = min(G_i) \tag{2.15}$$

where K denotes the bulk modulus, G the shear modulus and ϕ_i the volume fraction of the ith component. In case that one component is a fluid with zero shear modulus, the lower Hashin-Shtrikman bound of the bulk modulus becomes identical to the Reuss bound (*Reuss*, 1929) given by,

$$K^* = \left(\sum_{i=1}^{N} \frac{\phi_i}{K_i} \right)^{-1} . \tag{2.16}$$

The Reuss average, describes the effective elastic properties of a suspension of grains in a fluid. If only the bulk modulus is different and both components have the same shear modulus, the upper and lower HS-bound coincide and the effective bulk modulus yields

$$K^* = \left(\sum_{i=1}^{N} \frac{\phi_i}{K_i + (4/3)G} \right)^{-1} - \frac{4}{3} G \,, \tag{2.17}$$

which is the so-called Hill average (*Hill*, 1963).

To improve the predictions, one can include assumptions on the geometry and arrangements of the components into the model. In the following, three different models are presented, representing a rock with isolated pores, an unconsolidated sand and a cemented sandstone (Figure 2.4). The first model belongs to the group of inclusion models, while the other two are granular medium models. Inclusion models are characterized by a solid matrix containing isolated pores and cracks, whereas a granular medium is composed of individual solid grains in contact (*Berryman*, 1995). To obtain the effective properties, so-called mean field or effective medium theories are applied. The fundamental assumption of effective medium theory is that the volume of investigation, that is the sample size or seismic wavelength, is much larger than the scale of the heterogeneities.

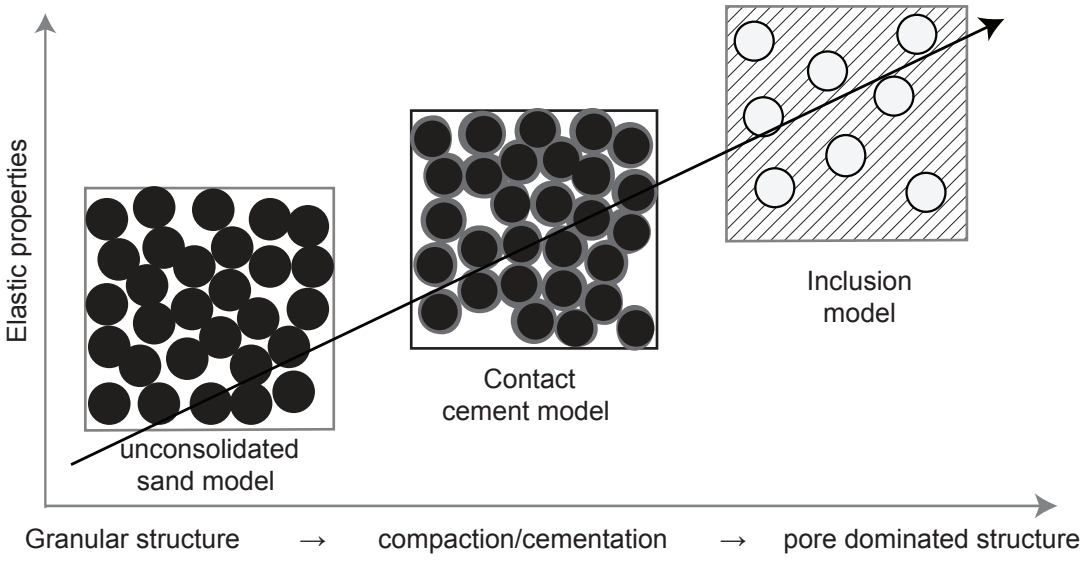

Figure 2.4: Increase of elastic moduli due to diagenetic effects and schematic of rock physics models, which describe different states of compaction and cementation.

2.3.2 Inclusion model

The basic idea of the derivation of effective elastic properties of an inclusion model is to treat the isolated pores as scatterers of elastic wave-energy. If a plane P-wave encounters a pore, scattered waves are created, since the strain of the

pore differs from the solid matrix which in turn generates local stress gradients (*Avseth and Johansen*, 2012). These gradients are sources of scattered elastic waves. If the wavelength is much larger than the single pore (long-wavelength approximation), the scattered waves have the same wavelength as the incident wave. In the far field of the scatterer, the resulting wavefield can be described as a superposition of the incident and scattered wavefields. In this framework, it is assumed that a scattered wave created by a single inclusion does not interact with other inclusions. This is the so-called first order scattering approximation, which holds true for a sparse distribution of inclusions.

Kuster and Toksöz (1974) derived an effective medium model for a sparse distribution of inclusions based on first order scattering. The starting point is a large sphere with a small amount of embedded inclusions. The wavefield outside of the sphere is evaluated in two ways, 1) for a homogeneous large sphere with effective elastic properties and 2) as a superposition of scattered waves from the embedded inclusions. Equating these two solutions leads to the final expressions for the effective elastic properties. *Berryman* (1980) provide a collection of expressions for a variety of inclusions geometries.

To overcome the limitation of a small amount of inclusions, multiple scattering has to be considered. Another way to incorporate higher volume fractions of inclusions is the differential effective medium (DEM) scheme (*Norris*, 1985). The basic idea is that a small amount of inclusion is embedded incrementally into the homogeneous matrix. The procedure is as follows (*Avseth and Johansen*, 2012):

a: A small concentration of pores is added to the matrix and the effective properties are calculated by the Kuster-Toksöz model.

b: These effective properties ($K^*(y)$, $G^*(y)$) build the new homogeneous matrix in which a new concentration of pores is embedded.

c: The procedures is repeated until the desired amount of pores is reached

The differential equations for this process are given by (*Berryman*, 1992)

$$\begin{aligned}(1-y)\frac{d}{dy}[K^*(y)] &= (K_2 - K^*)P^{2*}(y) \\ (1-y)\frac{d}{dy}[G^*(y)] &= (G_2 - G^*)Q^{2*}(y)\,,\end{aligned} \tag{2.18}$$

where K_2 and G_2 are the moduli of the inclusion and $P^{2*}(y)$ and $Q^{2*}(y)$ are geometrical factors depending on the shape of the inclusions. The parameter y gives the probability of replacing inclusion material by embedding a new inclusion, whereas $1-y$ is the probability to replace matrix material.

2.3.3 Granular medium model

To obtain effective elastic properties of a granular medium, so-called contact models can be employed. Contact models start with an aggregate composed of individual solid grains in contact with each other. The idea behind these models is that the elastic properties of a granular medium, are determined by the stiffness of the grain to grain contact. *Digby* (1981) derived effective elastic properties for a random pack of identical solid spheres as a function of average number of grain contacts (coordination number C), porosity ϕ of the rock and normal τ_n and tangential τ_t stiffness of the contacts. The effective elastic properties of a random sphere pack are given by

$$\begin{aligned}K^*_{CM} &= \frac{C(1-\phi)}{12\pi R}\tau_n \\ G^*_{CM} &= \frac{C(1-\phi)}{\tau_n + 1.5\tau_t}\,,\end{aligned} \tag{2.19}$$

where R is the radius of the sphere. The stiffnesses of the grain to grain contacts are estimated by micro-mechanical contact models of two spherical spheres.

Several different schemes exist. The Hertz-Mindlin theory (*Winkler*, 1983) assumes that the tangential force is much smaller than the normal force, which yields the following stiffnesses

$$\tau_n = \frac{4aG}{2-\nu} \quad \tau_t = \frac{8aG}{2-\nu}, \tag{2.20}$$

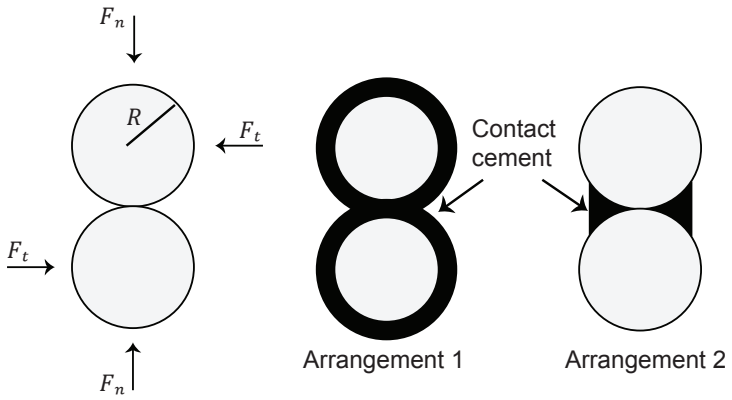

Figure 2.5: Schematic representation of micromechanical models (reproduced after *Mavko et al.* (1998))

where ν is Poissons's ratio an a denotes the radius of the contact area between two spheres. The contact area is derived to be

$$a = R\left(\frac{3\pi(1-\nu)}{2C(1-\phi)G}P\right) \tag{2.21}$$

where P is the applied hydrostatic confining pressure. The predicted pressure dependence works quite well for the bulk modulus at low pressures (less than 10 MPa), however it cannot explain the behaviour of the shear modulus satisfactorily (*Makse et al.*, 2004). *Makse et al.* (2004) lists possible reasons why the shear modulus might be different as predicted from the Hertz-Mindlin theory. Nevertheless, in the remainder of the thesis it is assumed that the theory still provides a reasonable approximation for the effective elastic properties of the rock.

The theory describes a precompacted rock and can be used in combination with the lower Hashin-Shtrikman bound to model porosity reduction in an uncemented sandstone (*Dvorkin and Nur*, 1996). The uncemented sand model heuristically interpolates between the mineral point, the solid matrix of the rock without porosity and the high-porosity end-member given by the Hertz-Mindlin theory at critical porosity ϕ_c. The critical porosity is the porosity at which the transition from grains in a fluid suspension to grains in a loadbearing matrix occurs (*Avseth et al.*, 2005).

Another scheme is the contact cement model (*Dvorkin et al.*, 1994), in which

the micromechanical model of two spheres is extended by a thin cement layer at the contact area. Hence, the stiffnesses of the contact area depend on the elastic properties of the cement and grain material as well as on the amount of cement. The expressions for these stiffnesses become quite complicated and have to be solved numerically (*Dvorkin et al.*, 1994). A statistical approximation of the cementation theory suggested by *Dvorkin and Nur* (1996) leads to closed-form expressions. The effective elastic moduli of the contact cement model can be written as

$$\begin{aligned} K^*_{CCT} &= \frac{1}{6}C(1-\phi_c)H_c\hat{\tau}_n \\ G^*_{CCT} &= \frac{3}{5}K^*_{CCT} + \frac{3}{20}C(1-\phi_c)G_c\hat{\tau}_t\,, \end{aligned} \tag{2.22}$$

where H_c and G_c are the P-wave and shear wave modulus of the cement, respectively. The parameters $\hat{\tau_n}$ and $\hat{\tau_t}$ are proportional to the stiffnesses of a cemented grain contact and given by the following expressions (*Dvorkin and Nur*, 1996):

$$\begin{aligned} \hat{\tau_n} &= a_n\alpha^2 + b_n\alpha + c_n \\ a_n &= -0.024153\lambda_n^{-1.3646} \\ b_n &= 0.20405\lambda_n^{-0.89008} \\ c_n &= 0.00024649\lambda_n^{-1.9864} \\ \lambda_n &= \frac{2G_c}{\pi G_g}\frac{(1.0-\nu_g)(1-\nu_{clay})}{1-2\nu_{clay}} \end{aligned} \tag{2.23}$$

$$\begin{aligned} \hat{\tau}_t &= a_t\alpha^2 + b_t\alpha + c_t \\ a_t &= -0.01(2.26\nu_g^2 + 2.07\nu_g + 2.3)\lambda_t^{0.079\nu_g^2+0.1754\nu_g-1.342} \\ b_t &= (0.0573\nu_g^2 + 0.0937\nu_g + 0.202)\lambda_t^{0.0274\nu_g^2+0.0529\nu_g-0.8765} \\ c_t &= 0.0001(9.654\nu_g^2 + 4.945\nu_g + 3.1)\lambda_t^{0.01867\nu_g^2+0.4011\nu_g-1.8186} \\ \lambda_t &= \frac{G_c}{\pi G_g} \end{aligned} \tag{2.24}$$

where ν_g and ν_c are Poisson's ratio of the cement and grain mineral, respectively and G_g denotes the shear modulus of the grain mineral. These relations depend

on the amount of contact cement α as well as the arrangement of the cement. By assuming that porosity reduction occurs due to cementation, the amount of cement is linked to the porosity of the granular medium. Two different schemes for the arrangement of the cement (deposition) have been suggested (see Figure 2.5) by *Dvorkin and Nur* (1996). In the first scheme all cement is deposited at the grain contacts, while in the second scheme the cement forms a shell around the quartz grains and the contact point of two cement layers builds the contact cement. The formula for the second scheme is given by

$$\alpha = \sqrt{\frac{2S_c\phi_c}{3(1-\phi_c)}} \tag{2.25}$$

where S is the cement saturation of the pore space. The model describes how the effective elastic properties of the porous rock change due to porosity reduction by precipitation of cement at grain contacts. *Dvorkin et al.* (1994) found that to first order the amount and arrangement of cement determines the stiffness. The effect of the cement moduli itself is much smaller.

2.4 Velocity-Saturation relations

To predict saturation effects on seismic velocities, we have to understand the dependence of seismic velocities (elastic properties) on pore fluids. If a mixture of two or more immiscible fluids occupies the same pore space, one speaks about partial saturation. This is the case when CO_2 is injected into a reservoir and replaces the in-situ fluids. Since the in-situ fluid will not be completely replaced by CO_2, patches of the two fluids can occur on several length-scales. If a seismic wave passes through such a medium, pore pressure gradients are created between the regions of different fluids, which in turn result in wave-induced fluid flow until the pressure gradients are equilibrated (*Johnson*, 2001; *Tserkovnyak and Johnson*, 2002; *Müller et al.*, 2010). The slow P-wave in the low-frequency regime of Biot's theory of dynamic poroelasticity is a proxy for this pore pressure diffusion process. Note, that this does not include squirt flow (*Mavko and Jizba*, 1991), which occurs due to grain-scale inhomogeneities (e.g. microcracks and loose grain

contacts) and is therefore a microscopic effect. In the following squirt flow effects will not be considered and the focus is on partial saturation on the mesoscale (i.e. heterogeneities larger than the pore-scale).

If the porous rock itself is homogeneous and the only heterogeneities are caused by the spatial variability of saturation, exact theoretical limits are available for the effective elastic properties of the fluid saturated rock. These limits are given by the well-known velocity-saturation relationships (VSRs), the uniform and patchy saturation models (*Mavko and Mukerji*, 1998). These two relationships give the low (uniform) and high (patchy) frequency limits of VSRs, respectively, and represent lower and upper bounds such that the velocity lies within these bounds for any given measurement frequency. Both of the limiting cases can be modelled by the Biot-Gassmann theory and their effective elastic properties are frequency-independent (real valued).

2.4.1 Biot-Gassmann theory

The Biot-Gassmann relation (*Gassmann*, 1951) is contained in Biot's dynamic theory of poroelasticity in the static limit. The theory describes the relationship between the elastic properties of a saturated rock with a single pore fluid and the elastic properties of the dry rock frame K_d, the solid grain material K_s and the porosity ϕ. The dry rock frame is assumed to be statistically isotropic and microscopically homogeneous with a fully connected pore space. In this context microscopically homogeneous means that the solid grain material is characterized by a single bulk (K_s) and shear modulus (G_s).

Then, in a quasi-static deformation experiment a small increment of compression of the rock causes an incremental change in pore pressure which in turn resists the compression and stiffens the rock (*Gassmann*, 1951). This deformation experiment can be performed under drained and undrained conditions (Figure 2.6), which results in two limiting cases of material behaviour. The undrained condition correspond to the state where the fluid is trapped in the porous medium, while under drained condition the fluid can flow freely and the pore pressure is

zero (or equivalently equilibrated). The relationship between theses undrained (saturated) and drained (dry) elastic moduli is described by Gassmann's equations as follows

$$K_u = K_d + \alpha^2 M$$
$$G_u = G_d \,. \tag{2.26}$$

The shear modulus is not affected by the pore fluid and the saturated bulk modulus K_u can be obtained from the dry properties of the rock. The Biot-Willis coefficient $\alpha = 1 - K_d/K_s$ is a measure of the ratio of pore volume to bulk volume change at a constant pressure (*Mavko et al.*, 1998). The fluid storage coefficient M is given by $M = [(\alpha - \phi)/K_s + \phi/K_f]^{-1}$ and the parameters K_d, K_s, K_f denote the drained frame, the solid phase and the fluid phase bulk moduli, respectively.

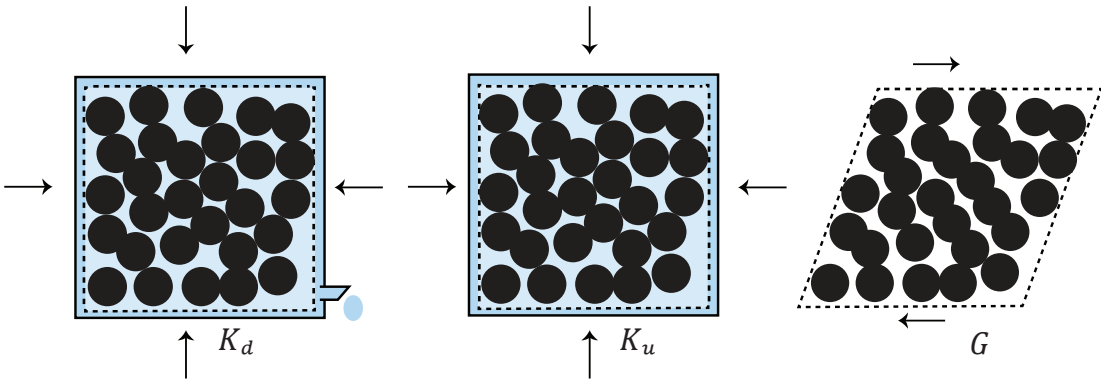

Figure 2.6: Schematic of drained K_d and undrained K_u deformation experiment and shear G deformation reproduced after *Wang* (2000)

Gassmann's equations are valid if fluid pressure induced by a passing wave has time to equilibrate throughout the pore space during the time-scale of wave-propagation. Therefore they are applicable at low frequencies. These equations are widely used in petroleum industry to estimate how the elastic properties of a rock change with a change in fluid properties - the so-called fluid substitution problem (*Smith et al.*, 2003). The sensitivity of the rock to changes in fluid properties is to first order determined by the dry bulk modulus and porosity.

2.4.2 Partially saturated rocks

In a rock with partial saturation, different fluid pressures are induced within fluids with different compressibilities upon compression of the rock. *Chandler and Johnson* (1981) have shown that the fluid pressure equilibration process is governed by a diffusion equation contained in Biot's equation of poroelasticity. The diffusion length λ_d of this process is given by

$$\lambda_d = \sqrt{\frac{D}{\omega}} \quad \text{with} \quad D = \frac{kN}{\eta}, \tag{2.27}$$

where N is a poroelastic parameter defined as $N = ML/H$. If the characteristic length scale d of the saturation heterogeneities is much smaller than the diffusion length $d \ll \lambda_d$ pore-pressure differences between adjacent fluid regions can equilibrate within the half-period of the wave and an isostress situation is reached (*Mavko and Mukerji*, 1998). In this case, Wood's mixing rule (*Wood*, 1955) can be applied to calculate an effective fluid bulk modulus

$$K_W = \left(\sum_{i=1}^{N} \frac{S_i}{K_f^i} \right)^{-1}, \tag{2.28}$$

where S_i denotes the saturation of the ith fluid. Then, the effective elastic properties of the rock can be obtained from the Gassmann-Wood (GW) relation given by

$$K_{GW}^* = K_d + \alpha^2 M(K_W)\,. \tag{2.29}$$

Contrary, if the characteristic length scale of the heterogeneities is much larger than the diffusion length $d \gg \lambda_d$ there is no-communication between the regions with different fluids, and fluid effects can be ignored. Then, Gassmann's equation can be applied to each fluid region separately. Since the shear modulus remains the same, the effective bulk modulus of the rock is given by Hill's average (*Johnson*, 2001)

$$K_{GH}^* = \left(\sum_{i=1}^{N} \frac{S_i}{K_u^i + 4/3G} \right)^{-1} - \frac{4}{3}G\,, \tag{2.30}$$

where K_u is the saturated bulk modulus calculated for a single fluid region. The Gassmann-Wood and Gassmann-Hill (GH) relations are the so-called uniform and patchy saturation models, respectively. At all intermediate frequencies, attenuation and dispersion occurs due to wave-induced fluid flow and the effective moduli of the saturated rock become frequency dependent. *White* (1975) first analysed these effects for a medium with periodic layering of gas- and liquid saturated layers in a homogeneous rock matrix. *Dutta and Odé* (1979) derived a more general solution based on Biot's equation of poroelasticity. A more general model for 3D regular patch distributions for arbitrary shapes of fluid patches has been proposed by *Johnson* (2001). This model is based on a branching function approach. *Gurevich and Lopatnikov* (1985) noted the importance of random saturation heterogeneities, in particular random layering of a porous medium. To calculate frequency-dependent effective moduli in a medium with random inhomogeneities, the continuous random media models of *Müller and Gurevich* (2004) and *Toms et al.* (2007) can be used. These models, will be utilised in the case studies of chapter 5 and are described in the following.

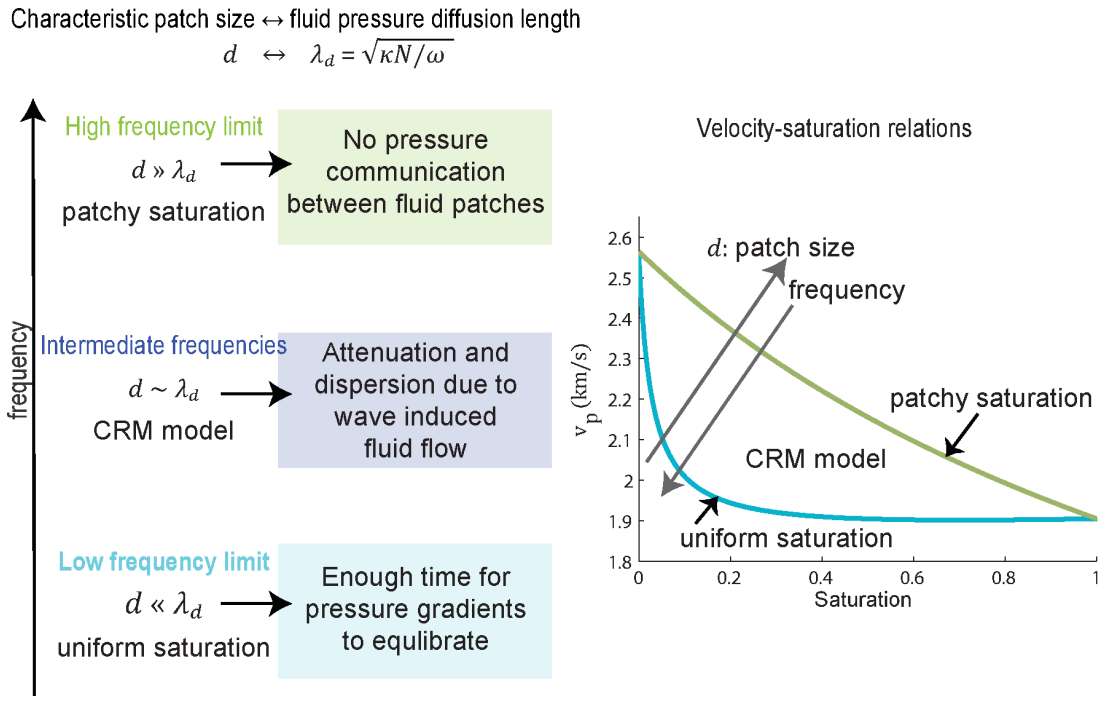

Figure 2.7: Classification of velocity-saturation relations

Continuous random media model

The continuous random media (CRM) models are based on the idea that attenuation is caused by conversion scattering from fast P-waves into slow P-waves, which in Biot's low frequency regime leads to dissipation of wavefield energy. *Gurevich and Lopatnikov* (1995) derived closed-form dispersion relations for the fast P-wavenumber in a porous medium with random layering. These expressions yield effective frequency-dependent moduli for the fast P-wave and the corresponding attenuation. The theory has since been extended to 3D CRM by *Müller and Gurevich* (2005).

The starting point of the CRM models are Biot's equations (low-frequency approximation) with spatially varying poroelastic coefficients $c(\mathbf{r})$. These coefficients can be seen as random parameters describing the inhomogeneities of the medium and can be expressed as follows

$$c(\mathbf{r}) = \langle c(\mathbf{r}) \rangle + \tilde{c}\,, \tag{2.31}$$

where $\langle c(\mathbf{r}) \rangle$ is a constant background value and $\tilde{c}$ denotes the fluctuations of the material properties around the background value. The spatial variations of the physical properties are described statistically. In principle, all statistical moments of the medium properties are needed to characterize the random medium completely. However, approximations based on lower order truncated statistical moments can provide good estimates of the effective properties. The CRM models take into account the volume concentration of the properties and the autocorrelation function B_{cc} of the material inhomogeneities. This function reflects the extent to which properties at two points are correlated in the system and defines the characteristic length scale of fluid patches. *Toms-Stewart et al.* (2009) showed how this characteristics length scale can be obtained from CT images of partially saturated pore samples.

A solution of Biot's equation with variable coefficients is obtained by the method of statistical smoothing, the so-called Bourret approximation (*Karal Jr*

and Keller, 1964). Contrary to the Kuster-Toksöz model in section 2.3.2, the volume fractions of the material components are not limited. However, only small variations of material properties from the background value are allowed. Hence, the resulting dispersion relations for the fast P-wave number are valid for weak contrasts between material properties.

For the case that inhomogeneities within the medium are only caused by partial saturation of the rock, the effective frequency-dependent P-wave modulus for a system of alternating layers with different fluid saturations and random thicknesses (*Müller and Gurevich*, 2004) can be expressed as

$$H_{1D}^{*}(\omega) = H_0 \left(1 - isk_D \int_0^{\infty} B_{MM}(r) e^{ik_D r} dr\right). \tag{2.32}$$

The effective slow P-wave number k_D is given by

$$k_D = \sqrt{\frac{i\omega}{k}} \frac{\sum_{i=1}^{2} \sqrt{\eta_i N_i} S_i}{\sum_{i=1}^{2} N_i S_i}, \tag{2.33}$$

where N_i and S_i are the poroelastic coefficient and saturation of the ith fluid phase, respectively. The function $B_{MM}(r)$ is the normalized autocorrelation function of the fluctuating fluid storage modulus M and s characterizes the degree of inhomogeneity of the medium

$$s = H_{GH}/H_{GW} - 1. \tag{2.34}$$

H_{GW} and H_{GH} denote the P-wave modulus defined by the Gassmann-Wood and Gassmann-Hill theory, respectively.

The effective frequency-dependent P-wave modulus for random saturation heterogeneities (*Toms et al.*, 2007) in a 3D porous medium can be written as

$$H_{3D}^{*}(\omega) = H_0 \left(1 - \Delta_2 - \Delta_1 k_D^2 \int_0^{\infty} \mathbf{r} B_{MM}(\mathbf{r}) e^{ik_D \mathbf{r}} d\mathbf{r}\right)^2. \tag{2.35}$$

The dimensionless coefficients Δ_1 and Δ_2 are given by

$$\Delta_1 = \frac{L}{H}\Delta_2 \quad \text{with} \quad \Delta_2 = \frac{\alpha^2 M \sigma_{MM}^2}{2H}\,, \tag{2.36}$$

where σ_{MM}^2 is the normalized variance of the fluid storage modulus. The effective P-wave modulus in Eq. (2.35) is only valid for weak contrast in fluid moduli. However, since the exact limits for a partially saturated rock are known, *Toms et al.* (2007) derived an effective P-wave modulus based on Eq. (2.35) by introducing the following scaling function

$$H_{SC}^{*} = H_{GW}\left[1 + \frac{H_{GH} - H_{GW}}{H_h - H_l}\frac{H_{eff} - H_l}{H_{GW}}\right], \tag{2.37}$$

where H_l and H_h are the low and high frequency limits derived from H_{eff}. They are given by the expressions

$$H_l = H_0(\Delta_2 - 1)^2, \quad H_h = H_0(1 - \Delta_2 + \Delta_1)^2\,. \tag{2.38}$$

This scaled P-wave modulus is now consistent with the exact bounds for large contrast in fluid moduli.

Permeability

The frequency range, in which dispersion and attenuation of the fast P-wave occurs, is not only determined by the length-scale of saturation heterogeneities but also by the diffusivity D of the medium. Pressure diffusion in a porous medium will be dominated by the permeability of the medium. *Müller et al.* (2007) have shown that in the presence of random fluctuations of permeabilities, a frequency shift of the attenuation and dispersion curves occurs. Permeability or hydraulic conductivity of natural porous rocks is one of the parameters with the highest variability in earth science. In chapter 6 a model for a two-component medium with strong fluctuations of hydraulic conductivity (mesoscopic heterogeneities) based on Biot's equations is derived. This random two-component medium can be thought of as a 'double conductivity structure'.

2.4.3 Fluid substitution in shaly sediments

The fluid substitution models of the previous section are only valid for a rock consisting of one mineral type. For a clean sandstone the elastic properties of quartz are a good approximation for the moduli of the solid grain material. However, in clay rich sandstone, the basic assumption of Gassmann's equation, namely, that the pore pressure is equilibrated within the pore-space, may be violated due to immobile bound water in clay minerals, which is not in hydraulic equilibrium with the rest of the pore fluids (*Carcione et al.*, 2000).

Dvorkin et al. (2007) suggested a fluid substitution scheme for shaly sediments to overcome this problem. In their model, the wet porous clay forms a part of the solid rock matrix. Hence, the porosity within the clay ϕ_{clay} is excluded from the total porosity ϕ, so that the porosity accessible to the injected fluid is an effective porosity ϕ_e. This effective porosity can be written as

$$\phi_e = \phi - f_{clay}\phi_{clay}\frac{1-\phi}{1-\phi_{clay}}\,, \tag{2.39}$$

where f_{clay} is the volume fraction of the clay mineral in the solid matrix. The volume fraction of the porous clay in the solid matrix is given by

$$f_{Pclay} = \frac{f_{clay}}{1-\phi_{clay}+\phi_{clay}f_{clay}}\,. \tag{2.40}$$

The effective modulus of the solid material K_{se}, consisting of quartz and porous clay, can for example be obtained by one of the bounds described in section 2.3.1. Then, Gassmann's equation for the saturated bulk modulus is given by

$$K^*_{\phi_e} = K_d(K_{se},\phi_e) + \alpha(K_{se})^2 M \quad \text{with} \quad M = \left(\frac{\alpha(K_{se})-\phi_e}{K_{se}} + \frac{\phi_e}{K_{fe}}\right)^{-1}\,, \tag{2.41}$$

where K_{fe} is the effective fluid bulk modulus. The saturation of the injected fluid S_2 in the effective pore-space is

$$S_e = \frac{\phi(1-S_2)}{\phi_e}. \tag{2.42}$$

Note, that the largest difference between the standard Gassmann and the modified version occurs at small porosities and high clay content. This is due to the fact that in the latter method, the volume fraction, for the same amount of injected fluid in the accessible pore-space ϕ_e, is much higher than in the pore-space of the standard scheme (*Dvorkin et al.*, 2007).

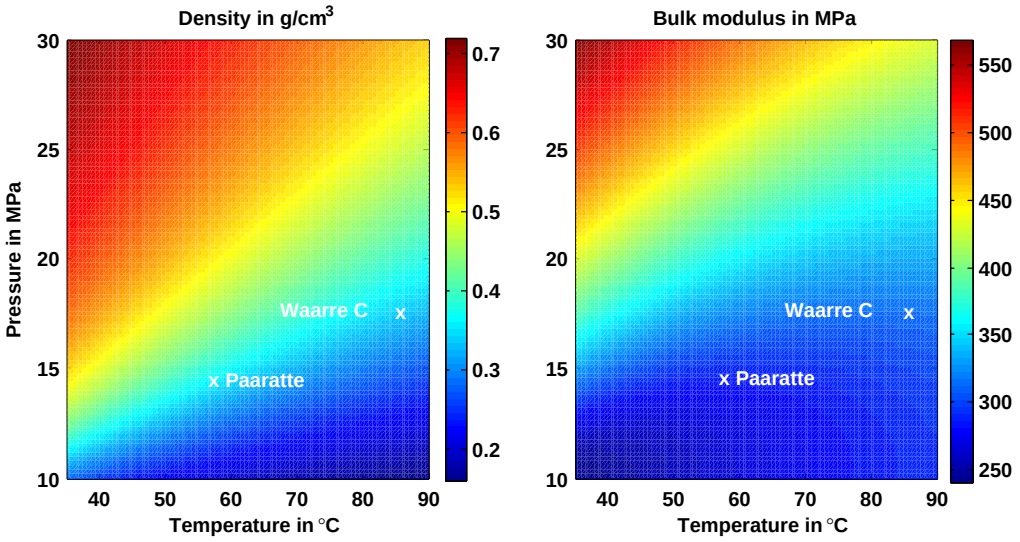

Figure 2.8: Bulk modulus and density of a gas mixture with 80% CO_2 and 20% CH_4. The white crosses indicate the in-situ temperature and pressure conditions of two reservoir zones which will be analysed in depth later in the thesis.

2.5 Fluid properties

For many storage reservoirs, CO_2 will be in supercritical state having a complex and highly variable physical and chemical behavior. The critical pressure of CO_2 is 7.38 MPa and the critical temperature is 31.1°C (*Span and Wagner*, 1996). At the transition from a gaseous state to a supercritical state, a significant change in density and compressibility occurs. The properties of CO_2 can be even more complicated, if the gas contains impurities like methane. To calculate these properties we use the equation of state of the GERG 2004 model (*Kunz et al.*, 2006). In the following case studies a gas mixture of 80% CO_2 and 20% CH_4 is considered. Figure 4.28 shows the density and bulk modulus for a range of temperatures and pressures for this gas mixture.

The properties of in-situ brine are calculated by the formula of *Batzle and Wang* (1992). These formulas predict the bulk modulus and density of brine as function of pressure, temperature and salinity. In principle, these relations also account for the effect of dissolved gas into brine. However, they predict a decrease in the bulk modulus when gas dissolves in brine, which is the case for most natural gases. But it is contrary to experimental results for brine saturated with CO_2, which indicate an increase in the bulk modulus (*Liu*, 1998). Therefore, we calculate the brine bulk modulus in the following for gas free brine. The density of brine is taken from the output of reservoir simulations.

2.5.1 Reservoir simulation

Reservoir simulations predict the distribution of fluids in the subsurface, dissolution of CO_2 in formation fluids and changes of in-situ conditions e.g. pressure and temperature. These simulations are based on the multiphase flow extension of Darcy's law, describing the displacement of the in-situ fluid by the injected fluid (*Donaldson and Alam*, 2008). Further, capillary effects determine the motion of the injected fluid as it flows through a medium initially occupied by the in-situ fluid. These effects are taken into account by relative permeability and capillary pressure functions (J-functions). Relative permeability describes the reduction of the effective permeability due to the presence of the second fluid (*Donaldson and Alam*, 2008). The capillary pressure describes the difference in pressure in the two fluids as a result of surface tension (*Bear*, 2013).

In the next chapter, predictions of reservoir simulations, fluid distributions and saturation, are utilized to estimate the time-lapse seismic response of CO_2 injection. The predictions utilized in the following case studies are compositional simulations. In these simulations the phase behaviour of the fluid is computed either by the GERG 2004 model (*Kunz et al.*, 2006) or the Peng and Robinson equation of state (*Peng and Robinson*, 1976).

Chapter 3

Forward modelling of the seismic response of CO_2 injection

The applicability of seismic monitoring depends on the effect of CO_2 injection on the seismic response. Time-lapse (TL) seismic signals are influenced by several factors, including the geological setting, the geospatial distribution of the CO_2 plume, the formation properties and their changes due to gas injection as well as the seismic acquisition parameters (e.g. distribution of offsets) and the repeatability of the measurement.

The geometrical size of the plume, thickness and lateral extent, depends on the structure, heterogeneity and permeability of the reservoir. For instance, in a small closed system we can expect a more compact and thicker gas plume than in an open system. High formation permeability results in strong buoyancy effects and the injected gas migrates upwards to the top seal. In an open-system this may lead to a thin gas layer below the seal.

The ability to resolve the gas plume (top and bottom) with surface seismic data, depends on the impedance contrast of the gas plume to the surrounding formations and the vertical resolution of seismic data. The vertical resolution of seismic data can be defined as the ability to distinguish between the top and bottom of a thin bed (*Yilmaz*, 2001). The vertical resolution depends on the dominant frequency of the measurement, or equivalently, the seismic wavelength.

If the thickness of the layer is larger than the seismic wavelength, the top and bottom are resolved by two events. For a thickness of less than one-quarter of the wavelength, reflections interfere constructively and produce a single event of high amplitude. This is the so-called tuning thickness (*Widess*, 1973). Below this thickness two events become indistinguishable in time. However, the amplitude of the monitoring seismic signal will still change due to a change in the impedance contrast between the seal and reservoir layer containing CO_2, resulting in a TL signal. Further, the change in velocity caused by CO_2 injection leads to misalignment of reflections between TL surveys, so called velocity push down phenomena, which are a part of the TL signal.

The detection of the gas plume in the subsurface depends on the strength of the TL seismic signal compared to the noise level of the seismic data. Therefore, to simulate a field experiment adequately, the noise level of the data has to be estimated and compared to the TL signal with noise. Hence, accurate "noise polluted" synthetic datasets are required to identify whether modelled changes caused by the injected CO_2 can be detected with the data quality that can reasonably be expected in a field experiment.

3.1 CO2CRC Otway project

In the following, the ability to detect injected CO_2 with the TL seismic reflection imaging method is assessed for two different reservoir types, a depleted gas reservoir and a saline aquifer. These two examples are investigated on data sets acquired within the CO2CRC Otway project. The CO2CRC Otway project is located on-shore in Victoria (Figure 3.1).

Stage 1 of the Otway project consisted of injection of a CO_2/CH_4 mixture into the depleted Naylor gas field. The gas reservoir was produced in 2002 - 2003. A free gas cap at the top of the reservoir and immobile residual gas saturation remained in the formation. This Waarre-C formation is fault-bounded on three sides and the overlaying low permeability Flaxmans formation builds the seal

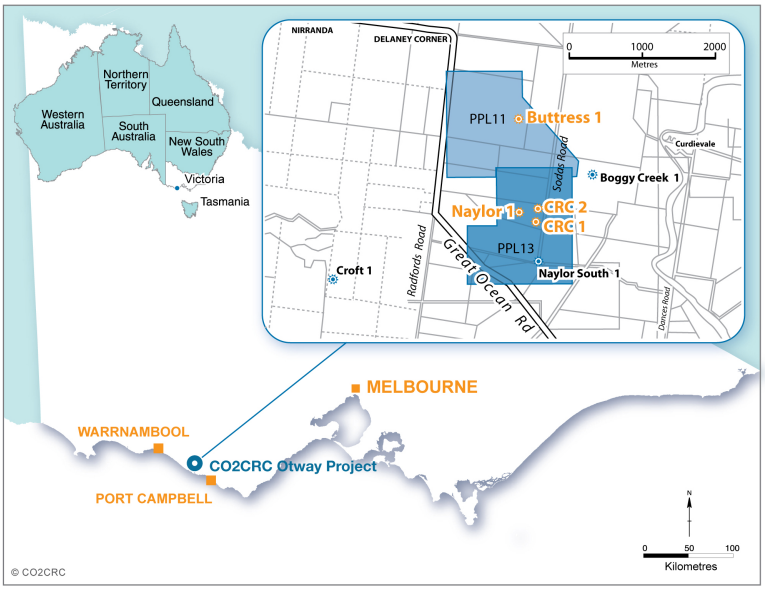

Figure 3.1: Location map of the CO2CRC Otway Project, showing the injection wells CRC-1 (Stage 1), CRC-2 (Stage 2) and the production well Naylor-1 (Copyright by CO2CRC).

(*Dance et al.*, 2009). The complex faulting forms a structural trap for injected gas (closed system). For Stage 1 the injected gas mixture was produced from the nearby CO_2 rich Buttress gas field (Figure 3.2). The gas consists of approximately 80% CO_2 and 20% CH_4. Injection of the Buttress gas into the Waarre-C formation started in 2008 and finished in 2009. Three surface seismic surveys and two 3D VSP surveys were acquired with similar acquisition parameters and an additional seismic data set from a large scale seismic survey in 2000 is available.

In Stage 2 of the Otway project, injection of a small amount of Buttress gas in an open saline aquifer with no local structural closure is planned. The selected Paaratte formation comprises heterogeneous reservoir sections that vary from clean, high porosity sandstone to shaly sandstone; the clean intervals often contain stiff rocks strongly cemented by diagenesis. These reservoir sections are interspersed with shale layers, which act as possible flow barriers for the injected CO_2/CH_4 (*Dance et al.*, 2012).

In both case studies, we estimate the TL seismic signal from results of reservoir simulations, which in turn are based on the static geological model. The petrophysical properties in the static geological models are stochastically distributed

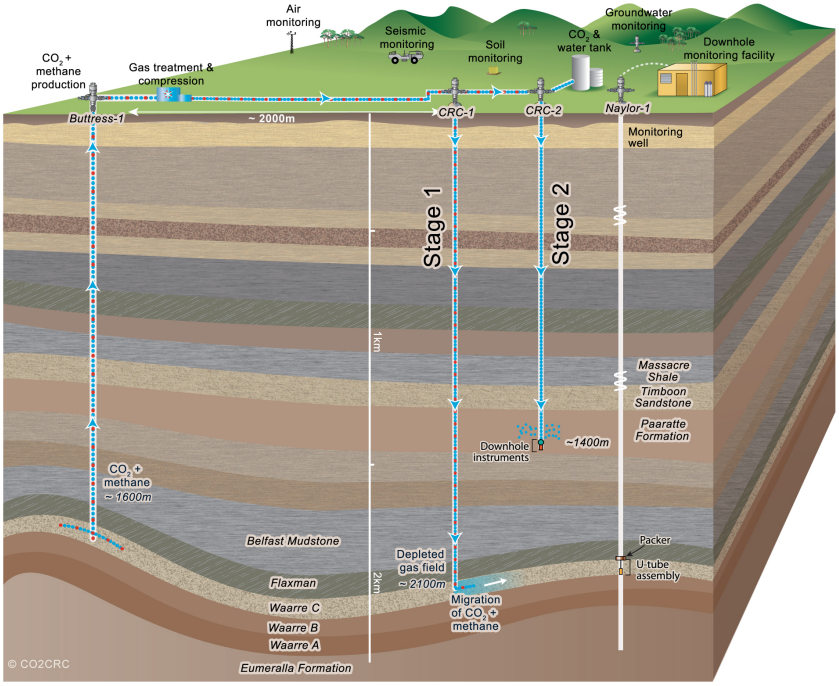

Figure 3.2: Concept of the Otway project (Copyright by CO2CRC).

Table 3.1: Data sets

	Pre-production 2000	Pre-Injection 2007/2008	during injection 2009	Post-injection 2010
Surface seismic	x	x	x	x
3D VSP	-	x	-	x
Naylor-1	x	-	-	-
CRC-1	-	x	-	-
CRC-2	-	-	-	x
Reservoir simulations	-	x	x	x

based on the interpreted depositional environments, core and log analysis, and various other parameters and algorithms. A detailed description of the models can be found in *Dance et al.* (2012) and *Dance et al.* (2009). The reservoir simulations are described in detail in (*Ennis-King et al.*, 2011) and (*Watson et al.*, 2012). The times to which different measurements and modelling results correspond are listed in Table 3.1.

The case studies described in this chapter, were conducted together with other researchers from the CO2CRC Otway project and are not solely my own work. My contribution to these case studies mainly involves the rock physics modelling and some of the seismic forward modelling. Most of the presented results are published

in CO2CRC reports (*Watson et al.*, 2012; *Pevzner et al.*, 2011a) and conference papers (*Caspari et al.*, 2012; *Pevzner et al.*, 2012, 2013). These references are not cited in the following.

3.2 CO_2 injection into a depleted gas reservoir

In the first case study, we investigate and model the seismic TL signal from CO_2/CH_4 injection into the depleted Naylor gas field. Stage I of the Otway project consisted of the injection of 66,000 t of a CO_2/CH_4 mixture into a depleted gas reservoir located at a depth of ∼2 km. It is a relatively small, heterogeneous, dipping formation surrounded by complex faulting (Figure 3.3). Two wells, 300 m apart, intersect the reservoir (Waarre-C formation), the injection well CRC-1 and the production/monitoring well Naylor-1. After gas production, a gas cap at the top of the formation around the Naylor-1 well was formed, and approx. 20% residual gas saturation remained in the rest of the reservoir.

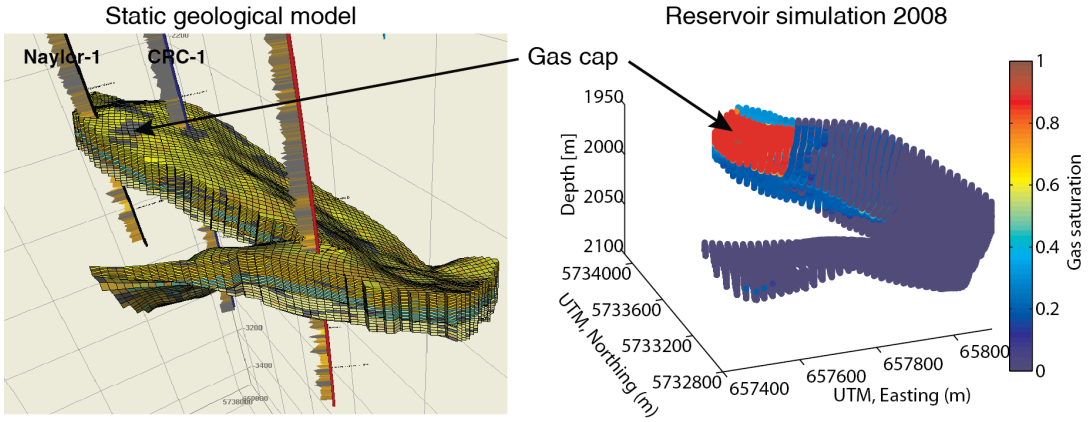

Figure 3.3: Static geological model of the Waarre C reservoir and the result of reservoir simulation for the condition pre-injection.

3.2.1 Saturation and pressure effects

Depending on the in-situ conditions and elastic properties of the geological site, different mechanism can alter the elastic properties of the reservoir in a CO_2 sequestration project. These mechanisms include saturation effects, pressure effects and geochemical reactions of the rock with CO_2. In this study, geochemical

reactions of the rock are not taken into account since the produced gas of the Naylor field contained small amounts of CO_2, so that it is assumed that possible geochemical reactions already took place. As a first step, we estimate the effects of pressure and saturation changes using core measurements and well log information.

To estimate the effect of gas saturation on the elastic properties of the Waarre-C formation, we compare elastic property - saturation curves for the fluid mixtures of CH_4/brine and CO_2/CH_4/brine. These relationships are calculated using Gassmann's fluid substitution workflow (*Smith et al.*, 2003). This workflow requires knowledge of the dry compressibility of the rock frame, the solid grain material and fluid mixtures as well as the porosity of the reservoir. Characteristic formation properties of the Waarre-C reservoir are inferred from well data. All values are summarized in Table 3.2. In-situ gas properties are calculated from the equation of state of the GERG 2004 model (*Kunz et al.*, 2006) and in-situ brine properties are computed from the empirical formula of *Batzle and Wang* (1992). This formula predicts a decrease in the bulk modulus when gas dissolves in brine, which is the case for most natural gases. However, this is contrary to experimental results for brine saturated with CO_2, which indicate an increase in the bulk modulus (*Liu*, 1998). Therefore, the brine bulk modulus is calculated for gas free brine. To estimate the fluid bulk modulus of the gas/brine mixtures, we apply Wood's mixing rule (Eq. (2.28)), given by

$$K_{fluid} = \left(\frac{S_{brine}}{K_{brine}} + \frac{S_{gas}}{K_{gas}} \right)^{-1} . \tag{3.1}$$

The use of Wood's equation assumes a uniform saturation of the rock (*Mavko and Mukerji*, 1998). This assumption is valid if the two immiscible fluids (brine and free gas) are mixed on the finest scale so that during the time scale of seismic wave propagation, wave-induced pressure gradients between the two fluids have time to equilibrate. Consequently, the choice of a mixing rule depends on the scale of saturation heterogeneities and the seismic measurement frequency. For the remainder of the chapter, Gassmann's fluid substitution with Wood's mixing rule (Eq. (2.29)) is applied and it is assumed that its conditions are fulfilled. The

effect of scale-dependence will be analysed in Chapter 5.

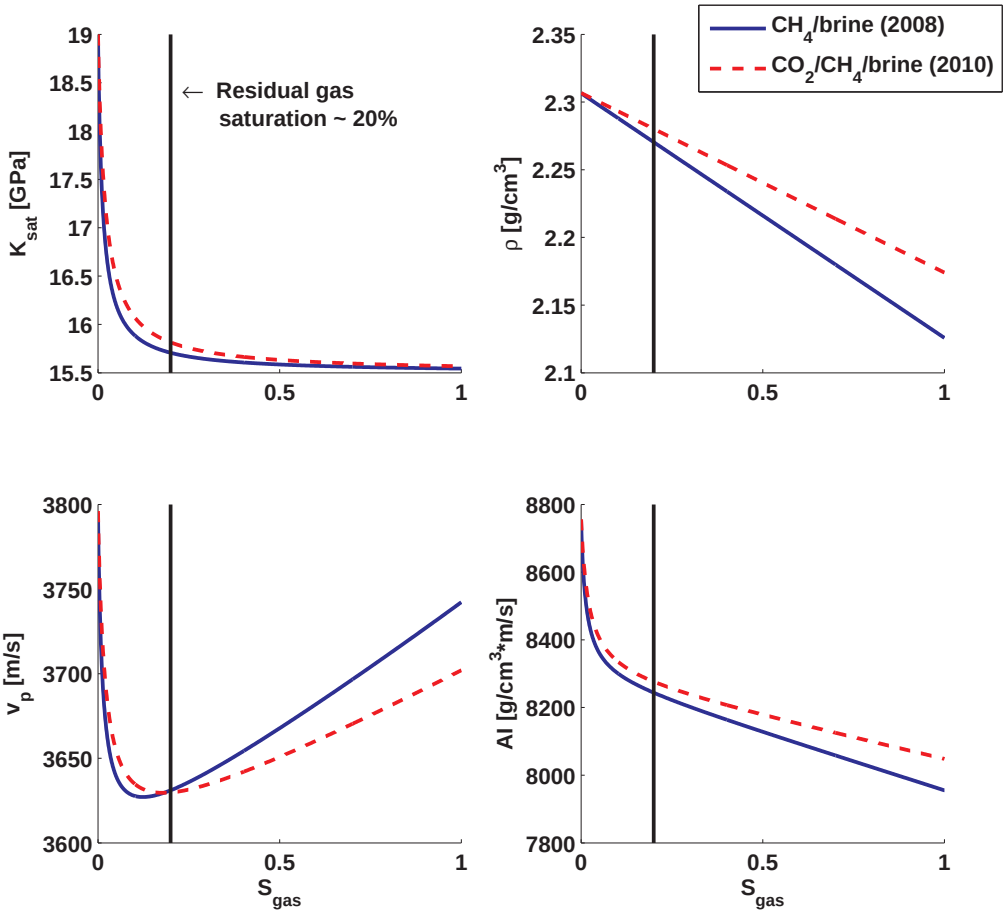

Figure 3.4: Bulk modulus, density, P-wave velocity and acoustic impedance as function of gas saturation. The used rock properties are listed in Table 3.2.

Figure 3.4 displays the behaviour of the bulk modulus, density and acoustic impedance (AI) as functions of gas saturation. The elastic property - saturation relations are quite similar for the two gas types. It can be observed that the change of the bulk modulus for any gas saturation larger than 20% (residual gas saturation) is negligible. On the other hand, the density exhibits some sensitivity to the different gas types. Consequently, the differences in P-wave velocity and acoustic impedance are caused by a density effect. This indicates that due to the residual gas in the reservoir, changes in elastic properties caused by saturation effects and in turn, the TL seismic response will be small.

Table 3.2: Petrophysical properties Waarre-C formation

Rock properties	Kg (GPa)	K_d (GPa)	μ (GPa)	ρ_g (g/cm^3)	ϕ
	35	15.5	10.7	2.64	0.20

In-situ conditions	T (°C)	P (MPa)
	85	17.6 (2008) / 20 (2010)

Fluid properties	K (GPa)	ρ (g/cm^3)	Salinity (ppm)
Brine (2008/2010)	2.557 / 2.575	0.992 / 0.993	21000
CH_4	0.0283	0.102	
CO_2(80%)/CH_4(20%)	0.0442	0.339	

Changes in pore pressure due to gas injection will also affect the TL seismic signal. Reservoir simulations predict a pore pressure increase in the reservoir of around 2 - 3 MPa between 2008 (pre-injection) and 2010 (post-injection). *Siggins et al.* (2010) measured ultrasonic velocities as a function of pressure on core samples for different saturation conditions in the laboratory. The measurement results for a core sample from the target zone are summarized in Figure 3.5. The results indicate that an increase in pore pressure (decrease in effective pressure) might additionally lower the seismic velocities in the reservoir. This effect on the velocities is less than half the effect of saturation on velocity. For simplicity, pressure effects are not considered in the following modelling. However, they may lead to a stronger TL signal as predicted.

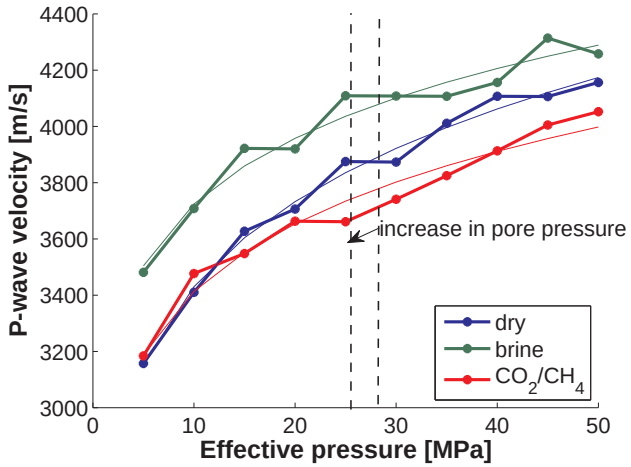

Figure 3.5: P-wave velocity as a function of effective pressure measured on a core sample from the target formation with different fluid saturations. The two dashed lines indicate the in-situ conditions pre-injection and post injection.

3.2.2 Time-lapse seismic response from reservoir simulations

The purpose of this modelling study is to evaluate whether the injection of CO_2/CH_4 into the depleted Waarre-C gas reservoir produced a TL signal that can be detected with the acquired seismic data. Therefor, the TL seismic response is modelled based on predictions of reservoir simulations. These results are then compared to the achieved level of repeatability of the field data.

Elastic model of the subsurface

The first step in a 4D seismic modelling study is to build an elastic model of the subsurface. In this study, the elastic model is based on the porosity of the static geological model and log data. To assign elastic properties to each cell of the static geological model (Figure 3.3), log data from the wells CRC-1 and Naylor-1 are interpolated and extrapolated by collocated cokriging, using the ChronoSeis© software package (Ikon Science). This geostatistical interpolation technique utilizes spatial information from an auxiliary property to guide the interpolation process. Since we are interested in an elastic model that is consistent with the porosity of the static geologic model, porosity is used as a guide for the interpolation. The underlying assumption is that porosity and elastic properties are correlated with each other. A problem arises for low porosities in the geological model. The interpolated elastic values and low porosity values are not consistent in some cells of the reservoir model since low porosity values are not represented in the log data, which are used for the correlation process. This causes the breakdown of Gassmann's fluid substitution workflow. Therefore, porosities below 6% are not considered in fluid substitution modelling. However, the reservoir simulations predict that only a very small amount of the injected gas enters these rock types and hence, the effect on the seismic modelling results should be small.

The seismic response is calculated by simple convolutional modelling, which only requires an acoustic impedance model of the reservoir. Therefore, the reservoir model is subsequently populated with acoustic impedance values and P-wave moduli of the grain material from the well data. The P-wave modulus of the solid

grain material is assumed to be a mixture of clay and quartz and its effective properties are computed by averaging of the upper (Eq. (2.14)) and lower (Eq. (2.15)) Hashin-Shtrikman bounds. Since the logs in CRC-1 and Naylor-1 are measured at different times post- and pre-production, respectively, we perform fluid substitution so that the AI values correspond to the same gas saturation (20% residual gas saturation) in both wells. After interpolating the log data, fluid substitution is applied to the 3D reservoir model to match the gas saturation pre-injection (2008) using the prediction of the reservoir simulations. Outside of the reservoir the acoustic impedance model consists of the acoustic impedance inversion volume of the seismic baseline data (*Asgharzadeh et al.*, 2010). A cross section of the model at reservoir depth is shown in Figure 3.6 A.

Changes in elastic properties

The effect of CO_2/CH_4 injection on the 3D acoustic impedance model, is calculated using an approximate method for solving Gassmann's equation suggested by *Mavko et al.* (1995) which is based on the P-wave modulus without the use of shear-wave velocity. The reason for using an approximate method is twofold. First the measured shear wave velocities in the wells CRC-1 and Naylor-1 differ quite significantly. Further, even though the values in CRC-1 seemed to be more reliable they lead to negative Poisson ratios for a few data points. A second reason is that we want to compare this elastic model in the next chapter to a model based on AI inversion results.

In the utilized fluid substitution workflow the P-wave modulus of a rock saturated with a fluid 2 is computed from the P-wave modulus of a rock saturated with fluid 1, the P-wave moduli of the fluid mixtures and the solid grain material as well as porosity. In the Waarre-C reservoir, fluid 1 is a mixture of formation brine and residual gas (mainly CH_4), and fluid 2 is a mixture of brine, CO_2 and CH_4. The in-situ brine properties are computed from the empirical formula of *Batzle and Wang* (1992). The gas saturations (Figure 3.6) and gas properties are obtained from the reservoir simulation results (GERG 2004 model).

We perform fluid substitution modelling for the following conditions: pre-injection (2008), injection of 35 kt (2009) and 65 kt (2010) of the CO_2/CH_4 mixture. Figures 3.6 (B) and(C) display the difference in AI between the years 2009 - 2008 and 2010 - 2008, respectively. It can be observed that the AI in the reservoir decreases since brine is replaced by CO_2/CH_4. In both cases, the absolute values in AI differences are of the same order. However, the thickness of the gas plume increases as the injected gas fills up the reservoir below the gas cap. The reservoir simulations do not predict any migration of the injected gas into the gas cap, located at the top of the reservoir near the Naylor-1 well. Therefore, the largest changes in the seismic response are expected to occur approximately half-way between the wells Naylor-1 and CRC-1, where the gas cap does not mask the effect of CO_2/CH_4 injection.

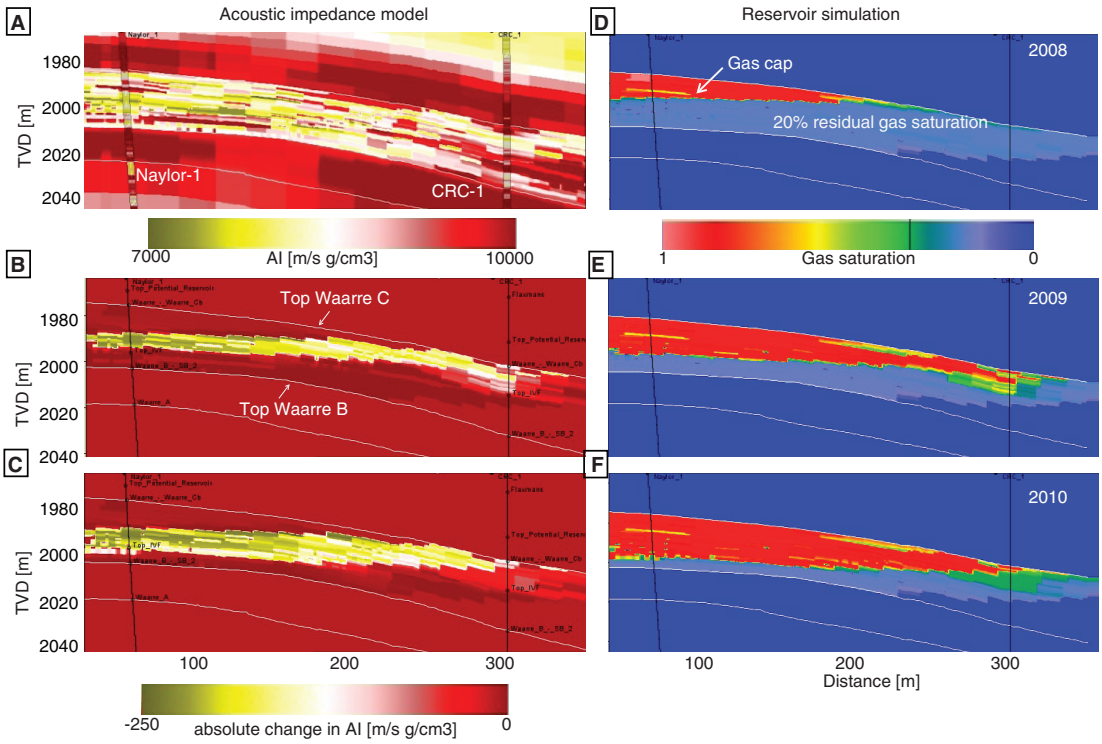

Figure 3.6: Cross section through the reservoir on an line along Naylor-1 and CRC-1: (A) acoustic impedance model of the reservoir; (B,C) absolute difference in acoustic impedance for 2009 - 2008 and 2010 - 2008, respectively; (D,E,F) Predictions of gas saturation (reservoir simulations)

3.2.3 Comparison of synthetic and time-lapse field data

The modelled scenarios correspond to the monitoring surface seismic data in 2009, 2010 and to the 3D VSP data in 2010. To compare the modelling results to the seismic data, zero offset synthetics are computed by convolving the obtained AI volumes with a statistical wavelet, extracted from the surface seismic data (2008). Figure 3.7 presents a comparison between the synthetic and surface seismic data in 2008 and the TL signal 2008 - 2010. For comparison, the amplitudes of the field and synthetic data are calibrated. The left column shows a synthetic seismic section (A) compared to the field data (C) in 2008. The differences in the amplitude distribution along the Waarre-C horizon are discussed in detail in Section 4.1. However, these differences do not affect the principal outcome of the study. The right column shows the predicted TL response (B) and a slice through the TL difference volume obtained from the seismic data (D). The modelled signal level is significantly smaller than the TL noise in the surface seismic data.

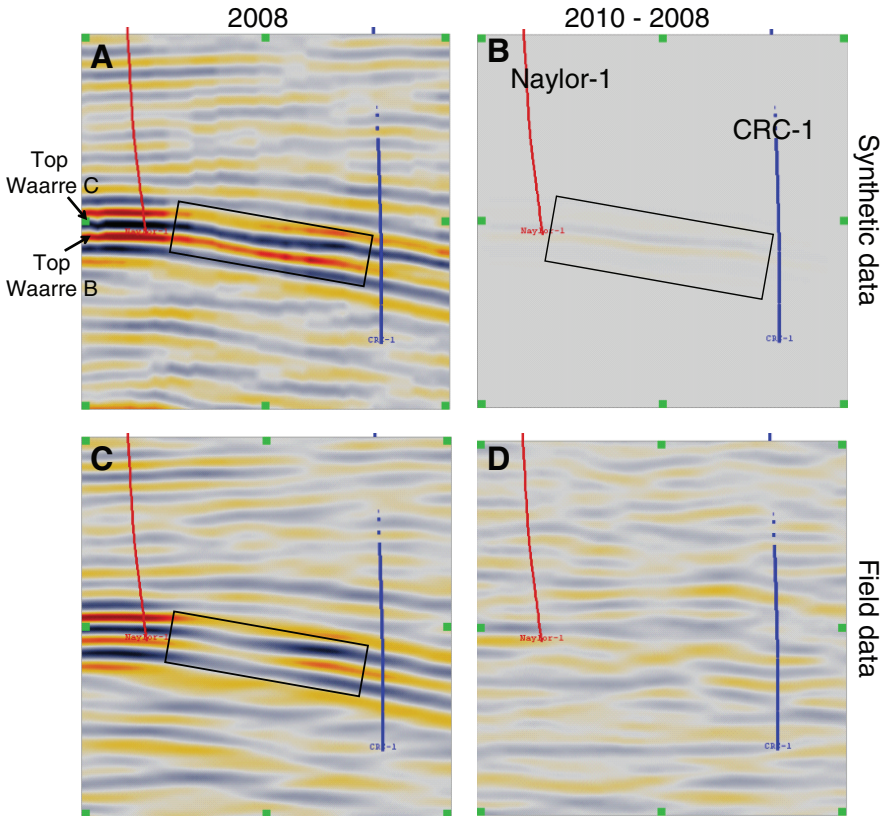

Figure 3.7: Synthetic data (A,B) and field data sections (C,D) on an inline along the wells CRC-1 and Naylor-1; A and C show the data in 2008 and B and D are the TL signals for 2010-2008. The black box indicates the reservoir between the two wells.

For further comparison, the NRMS (normalized root mean square) difference (*Kragh and Christie*, 2002) of the data set 2010 - 2008 is computed over all differences related to changes in the reservoir level (60 ms window). The NRMS difference is a measure of the relative strength of the signal (noise). The resulting maps are displayed in Figure 3.8. Comparing the predicted signal strength to the NRMS map of the surface seismic data shows that the repeatability of the surface seismic data is too low to detect the signal (Figure 3.8). For the time-lapse 3D VSP data, the achieved NRMS difference is also below the level required to detect the signal robustly. However, in this case the predicted signal has at least a similar order of magnitude as the TL noise.

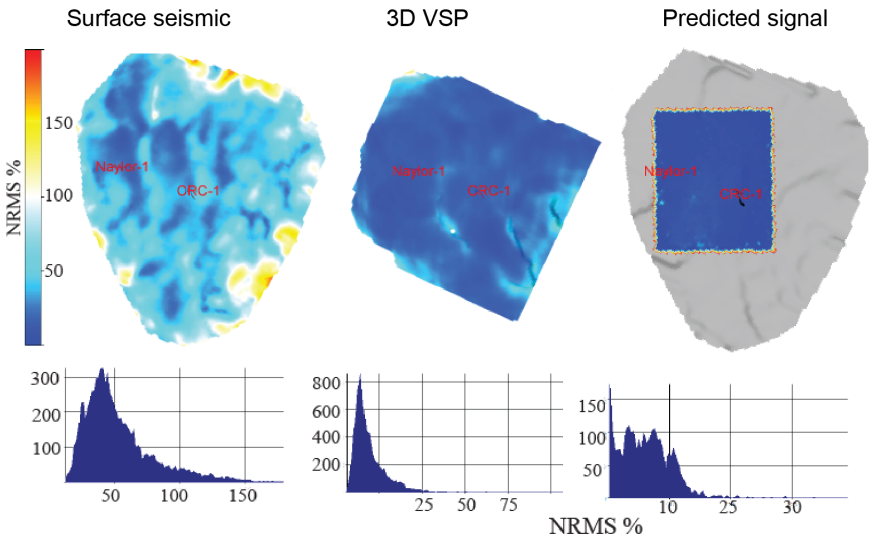

Figure 3.8: NRMS difference (2010-2008) computed over the Waarre C horizon in a 60 ms window for surface seismic (left), 3D VSP (middle) surveys and synthetic data; Histograms of NRMS values are shown below the maps.

Gas injection into a depleted gas reservoir does not provide favourable conditions for seismic monitoring since changes in elastic properties caused by saturation effects are small. In general, the seismic modelling study confirms that the TL signal is too small or the TL noise too high to detect a signal robustly with the acquired surface seismic data. However, the predicted signal has the same order of magnitude as the repeatability of the 3D VSP datasets. Further, a previous repeatability study of the surface seismic data showed a significant increase in repeatability between the first (2009/2008) and the last (2009/2010) pair of surveys due to an increase in the CMP fold and a more powerful seismic

source (*Pevzner et al.*, 2011b). Hence, we can speculate that if a similar improvement in the repeatability of the 3D VSP data could be achieved, the 4D VSP method would probably be applicable to monitor the injection of CO_2/CH_4 in the depleted Waarre-C gas reservoir. Further, the modelled signal might slightly underestimate the TL response since pressure effects are not considered.

3.3 CO_2 injection into a saline aquifer

A key objective of Stage 2 of the CO2CRC Otway Project is to explore the ability of geophysical methods to detect and monitor injection of greenhouse gas into a saline formation. For this purpose, injection of some 10,000 - 30,000 t of gas mixture (80% CO_2 / 20 %CH_4 in supercritical state) into the Paaratte formation, a saline aquifer located at a depth of about 1400 m is planned. Before such an injection experiment is undertaken, a seismic modelling study was performed to investigate whether the TL seismic reflection imaging methods can detect changes of the seismic response caused by injection of a small amount (10,000 - 30,000 t) of CO_2/CH_4 gas into the Paaratte Formation.

Two possible perforation intervals in the Paaratte formation are investigated. Zone-1 is a thin 7 m high porosity clean sandstone interval and Zone-2 is more heterogeneous with a thickness of approx. 15 - 20 m (Figure 3.9). The results of reservoir simulations reveal that the gas plume in both zones will have a relatively small thickness with 2 - 4 m and up to 15 m, respectively. Thus, the main challenge of the seismic program is the detection of a very thin plume. Therefore, the modelling of the seismic response is based on well log data, which have the highest vertical resolution. Further, we assess if different injection volumes and realisations of the geological model and the corresponding varying geospatial distribution of fluids will have a significant effect on the detectability of the gas plume.

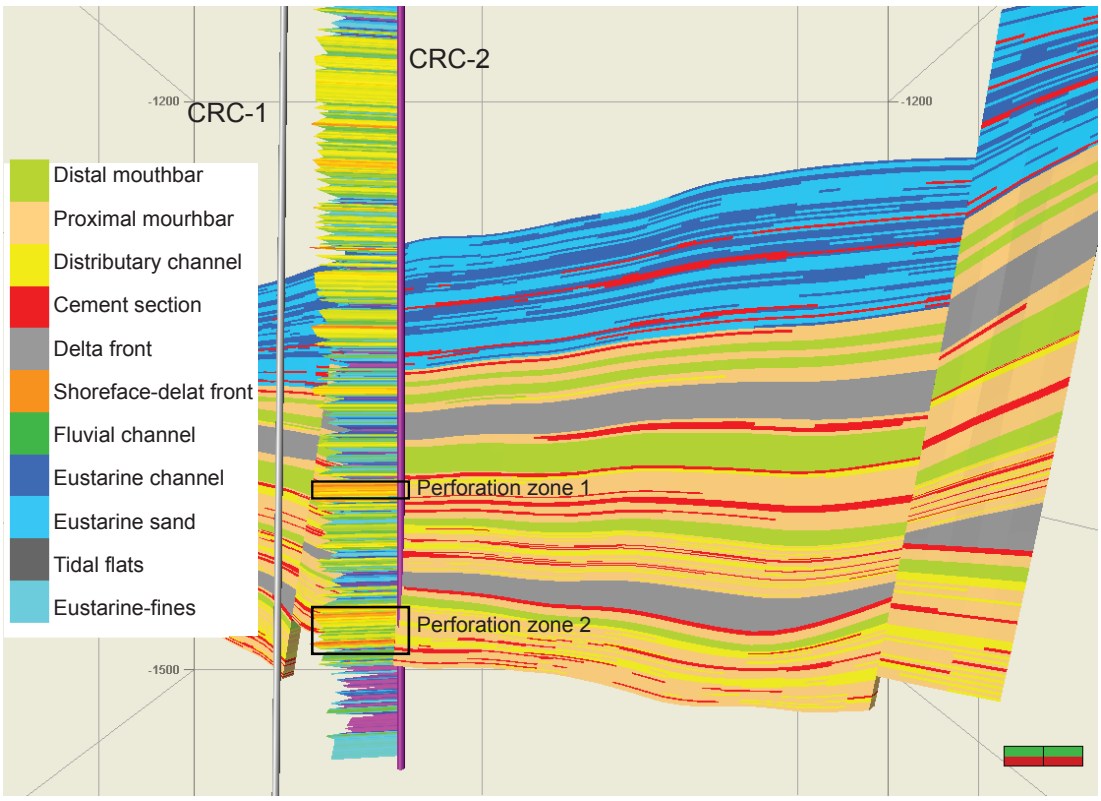

Figure 3.9: North-south cross section through the static geological model of the lower Paaratte formation. Facies are shown for the base realisation R1.

3.3.1 Detectability of a thin gas plume

To assess the detectability of a thin gas plume for the two injection zones, we take into account three main aspects which influence the magnitude of the TL seismic signal: the thickness of the gas plume, changes in elastic properties caused by saturation effects and a realistic acquisition geometry for a surface seismic survey.

Since the predicted gas plume is very thin, numerical modelling requires very small grid sizes, thus making full 3D seismic simulations unfeasible in terms of modelling cost and duration. To overcome this problem a fast 1.5D full waveform modelling workflow is applied, which still accounts for a variable plume thickness (obtained from reservoir simulations) as well as a realistic acquisition geometry. This modelling workflow is summarized in Figure 3.10. First, a 1 dimensional model of the subsurface based on well logs is created and the changes in elastic properties for different plume thicknesses are estimated. For these models accurate and efficient 1.5D full-waveform modelling is performed to predict the seismic signal. Then, for each lateral location of the reservoir simulation grid, an effec-

tive thickness of the plume is calculated as the sum of the thicknesses of those cells which reach a certain threshold in changes in elastic properties ("seismic thickness"). Afterwards, the 1.5D full-waveform modelling results for different plume thicknesses, the effective thickness maps and the offset distribution of the actual 3D seismic data set are merged to generate synthetic seismic volumes that reflect the offset distribution of the 3D seismic field data. This, in turn, makes it possible to facilitate actual TL seismic noise, inferred from the TL 3D field data of Stage 1 of the Otway project, to produce realistic "noise polluted" data sets.

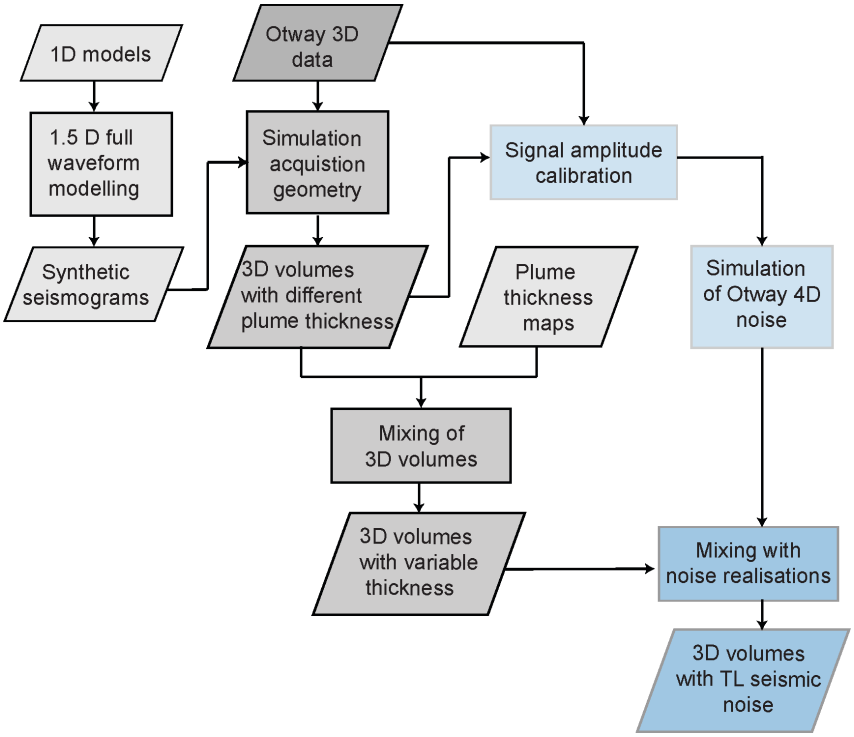

Figure 3.10: Workflow: Modelling of the TL seismic signal using 1.5D full waveform modelling (grey charts) and comparison to TL noise realisations based on TL seismic data (blue charts).

Elastic properties of the subsurface

Since the calculation of the seismic signal is based on the log data, a 1D model of the subsurface is built at the CRC-2 well location. The CRC-2 well logs start at a depth of 500 m. Hence, for the shallow part of the model, we complement the model with data from the CRC-1 well. A problem is that in several cases the P-wave velocities derived from the sonic log of the CRC-2 well have very low

Table 3.3: Petrophysical properties Paaratte formation

Rock properties	K_g (GPa)	G_g (GPa)		ρ (g/cm^3)
Quartz*	37	44	mineral	2.72
Clay*	11.3	3	brine	0.9876

* literature value *Mavko et al.* (1998)

velocity readings, leading to negative Poisson's ratios, instead of the expected very high velocities for thin cemented layers. This is corrected by calculating the P-wave velocities at these points from S-wave velocities using a representative Poisson's ratio of 0.2.

The estimation of saturation effects using Gassmann's fluid substitution workflow requires additional parameters. The dry compressibility of the rock frame is obtained from the sonic velocities in the CRC-2 well (fully brine-saturated conditions) by solving the inverse Gassmann equation. This involves knowledge of the grain material. Given that the considered perforation intervals vary from clean high porosity sandstone to shaly sandstone, we assume that the rock matrix is a composite of clay and quartz (Table 4.1). The effective properties of the composite material are calculated from an average of upper and lower Hashin-Shtrikman bounds (Eqs. (2.14) and (2.15)).

To obtain the thickness of the gas plume for each location in the actual 3D seismic data, we utilize reservoir simulation results. As in the previous example (depleted gas reservoir), P-wave and S-wave velocities are assigned to each cell of the static geological model by collocated co-kriging. Figures 3.11 and 3.12 display the log data (P-wave velocity, S-wave velocity, density and porosity) from the wells CRC-1 and CRC-2, on which the elastic models for the two injection zones are based. To estimate the post injection velocities using Gassmann's fluid substitution workflow, the additional parameters are obtained in the same way as for the log data. Further, the calculation of the effective properties of the grain material requires information of the clay content for each cell in the simulation grid. Therefore, we obtain empirical porosity - clay relations from the log data for

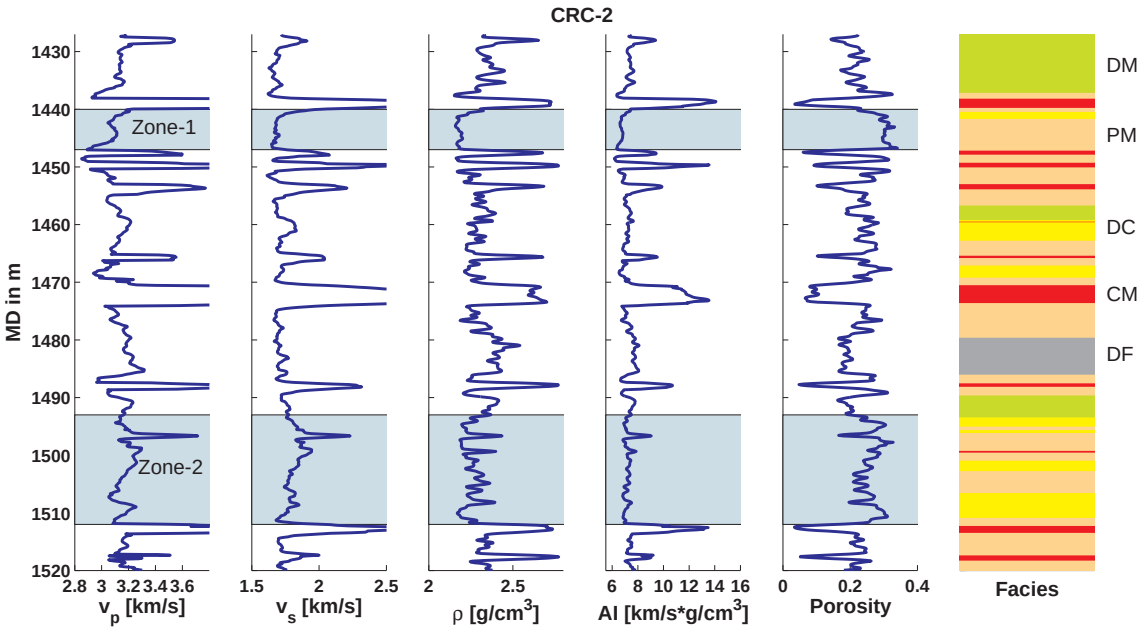

Figure 3.11: CRC-1 log data: P-wave velocity, S-wave velocity, density, AI, porosity and geological facies. Blue marked areas are the perforation intervals.

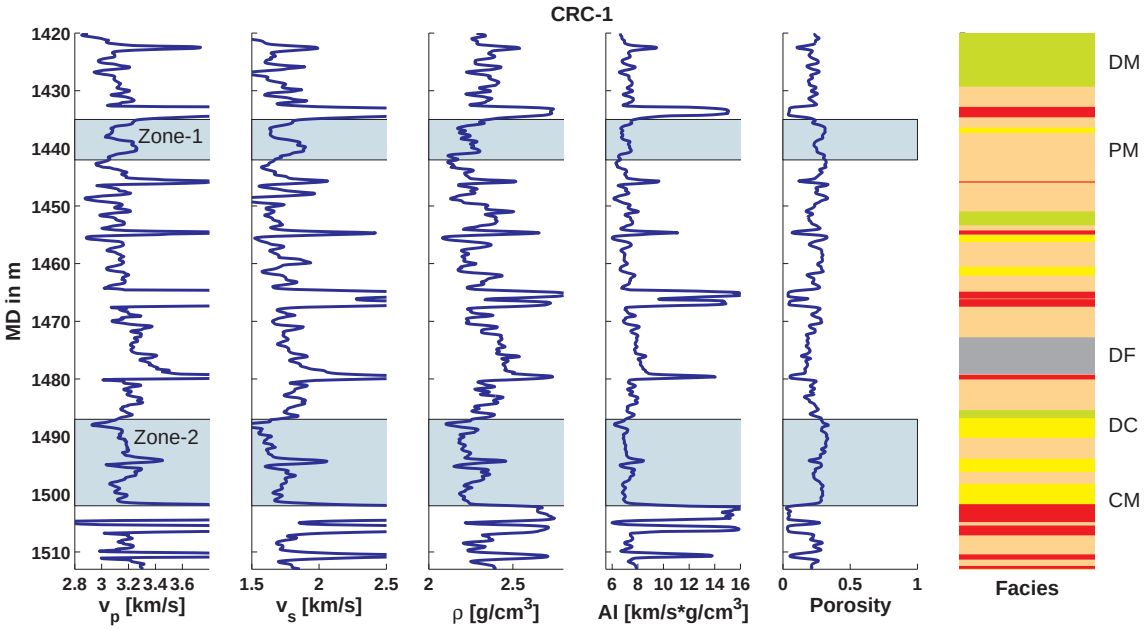

Figure 3.12: CRC-2 log data: P-wave velocity, S-wave velocity, density, AI, porosity and geological facies. Blue marked areas are the perforation intervals.

each zone. Then, the clay content is given by

$$V_{clay} = -2.36\phi + 0.84 \quad (\text{Zone } 1)\,, \tag{3.2}$$
$$V_{clay} = -1.44\phi + 0.57 \quad (\text{Zone } 2)\,.$$

The density is directly calculated from porosity values using (Table 4.1)

$$\rho = (1 - \phi)\rho_g + \phi\rho_{brine}\,, \tag{3.3}$$

where ρ_g and ρ_{brine} denote the density of the grain material and brine, respectively.

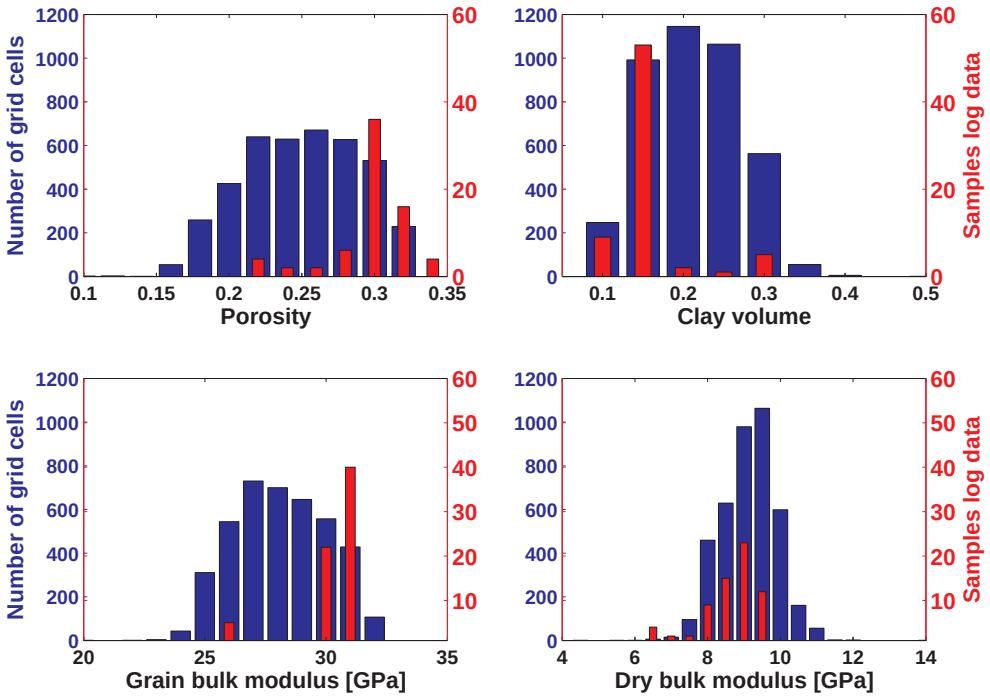

Figure 3.13: Histograms of formation properties of the perforation Zone-1 for the log data of the CRC-2 well (red) and the 3D reservoir model (blue).

Figures 3.13 and 3.14 display histograms of the formation properties, namely porosity, clay volume, grain and dry bulk moduli, for the log data and the 3D reservoir models of both perforation intervals. For the reservoir models, only grid cells with gas saturation are displayed. The perforation Zone-1 in the CRC-2 well is a very high porosity clean sandstone interval. However, the formation properties of this reservoir zone encountered in other wells show more variability. Therefore, the formation properties of the 3D model exhibit a greater variability than the properties of the log data (Figure 3.13). In particular, the high porosity values and low clay content associated with a higher grain bulk modulus lead on average to lower dry bulk moduli for the log data. Perforation Zone-2 is a more heterogeneous section at the CRC-2 well location than zone 1. Yet, the histograms of the log data are shifted to higher porosities, lower clay content and

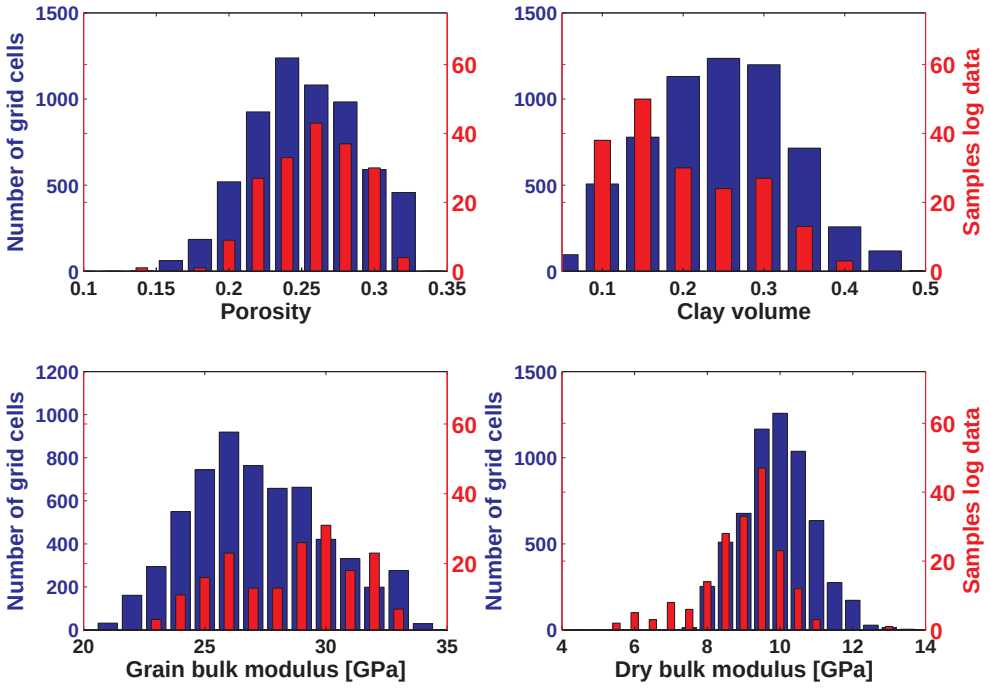

Figure 3.14: Histograms of formation properties of the perforation Zone-2 for the log data of the CRC-2 well (red) and the 3D reservoir model (blue).

consequently, to lower dry bulk moduli compared to the histograms of the 3D model. This is due to the fact that the 3D geological model incorporates facies in this zone which are not present in the CRC-2 well. However, the discrepancies are compensated for by choosing appropriate cut-offs for the seismic plume thickness maps in the next section.

Changes in elastic properties

Pressure changes in the reservoir during injection might play a role in TL seismic studies. However, pore pressure changes in the Paaratte formation predicted by reservoir simulations are only around 0.2 MPa. Such small pressure changes will have a negligible effect on the elastic properties. This is supported by effective pressure vs. ultrasonic velocity measurements on dry core samples, shown in Figure 3.15 (*Lebedev et al.*, 2013).

Hence, the chosen modelling approach considers only changes in elastic properties caused by variations in fluid saturation. In order to perform Gassmann

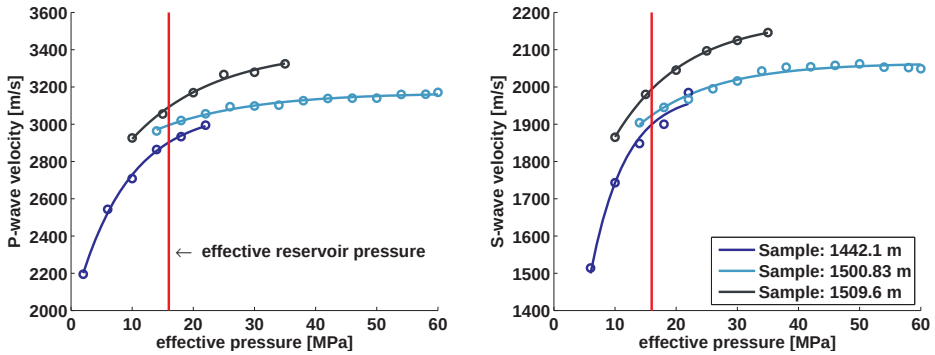

Figure 3.15: Dry core measurements: ultrasonic P- and S-wave velocities at different effective pressures; the red line indicates approx. the effective reservoir pressure before injection.

fluid substitution modelling, information regarding the fluid properties at in-situ conditions is necessary. The fluid properties are inferred from the reservoir simulation results. The simulations provide predictions of gas distribution, gas saturation, gas dissolution into brine and gas composition in the free gas as well as predictions of pore pressure. From the predicted gas composition and pressure values, we compute the elastic properties of the free gas for each cell of the flow simulation grid using the GERG 2004 model (*Kunz et al.*, 2006). The temperature is assumed to be constant. The brine density is obtained from the flow simulation results, which employ the *Peng and Robinson* (1976) equation of state and the in-situ brine bulk modulus is calculated from the empirical formula of *Batzle and Wang* (1992).

Fluid substitution modelling is performed for the reservoir simulation results of 30.000 t of injected CO_2/CH_4 at the end of injection. For each grid cell of the reservoir zones, we compute the relative changes in acoustic impedance. The resulting histograms are shown in Figure 3.16. Since modelling of the seismic response is based on the log data, the effect of CO_2/CH_4 injection on the sonic and density logs in CRC-2 is estimated for both injection intervals. This requires saturation values for the log data. To represent the relative changes in acoustic impedance of the 3D models as adequately as possible a saturation value that recreates a similar distribution of the relative changes in AI is chosen instead of an average gas saturation for the reservoir simulations. The chosen gas saturations are 15% and 5% for the injection intervals 1 and 2, respectively. The

resulting histograms are shown in Figure 3.16. Note that for Zone-2 30% gas saturation leads to a better representation of the 3D model. However, large values in relative changes in AI are slightly over represented.

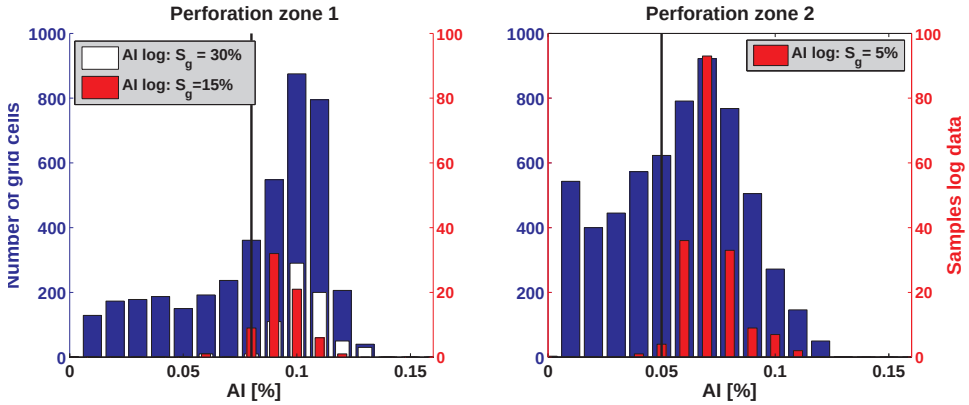

Figure 3.16: Histograms of relative changes in acoustic impedance for 30,000 t of injected CO_2/CH_4 for the 3D reservoir model and for gas saturations of 30%, 15% and 5% for the log data.

In the next step, plume thickness maps are calculated. Since changes in AI below 5% and 8% are not represented by the histograms of the log data, they are not taken into account for the calculation of the plume thickness. Subsequently, for each lateral location of the reservoir simulation grid, the effective thickness of the gas plume is calculated as the sum of the thicknesses of those cells that have more than 8% change in AI for Zone-1 and more than 5% change in AI for Zone-2. Figure 3.17 shows the "effective seismic thicknesses" in map view. The perforation Zone-2 provides a thicker gas plume, but the average relative changes of AI are smaller with 6% compared to 10% in injection interval 1. Figure 3.18 displays the distribution of the original gas saturation in the 3D model compared to the distribution with the AI cut-off. These histograms illustrate that quite a substantial part of the gas plume with low gas saturation values is not considered in the estimation of the "seismic plume thickness". Most of the low gas saturations accumulate at the bottom of the gas plume, the so called "diffuse gas" (*Chadwick et al.*, 2005).

Then, we perform 1D modelling for different plume thicknesses, 1 - 7 m and 1 - 17 m for Zone-1 and 2, respectively (Figures 3.19 and 3.20). These 1D-velocity

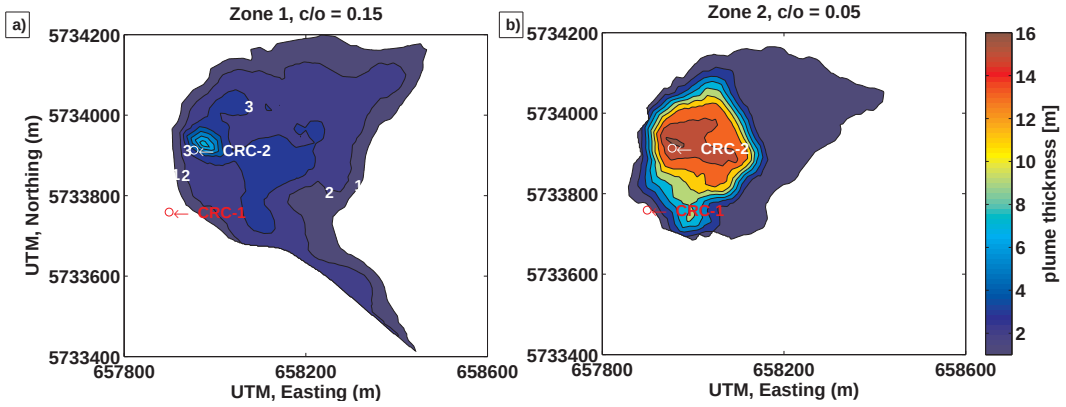

Figure 3.17: Seismic thickness of the plume for 30.000 t of injected CO_2/CH_4 injection interval 1 (a) and injection interval 2 (b), calculated for relative changes in AI that are greater than 8% and 5%, respectively (reproduced after (*Pevzner et al.*, 2013)).

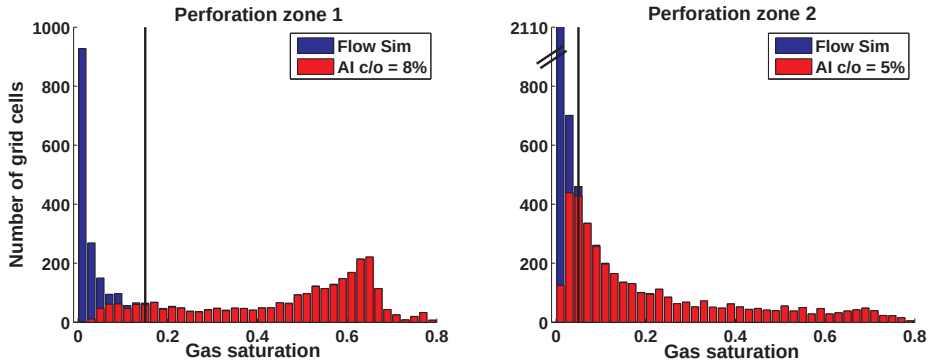

Figure 3.18: Histograms of gas saturation from reservoir simulations and after the acoustic impedance cutoff.

models are the input for the 1.5D seismic modelling.

Seismic signal

A 1.5D full wave-form modelling workflow was developed to generate synthetic seismic volumes that mimic the offset/angle distribution of the Otway field data (*Pevzner et al.*, 2011a). This method considers the full wavefield (reflected, refracted and converted waves as well as multiples) and takes AVO effects properly into account. These effects can play an important role in the case of gas injection. The workflow is illustrated in Figure 3.10 and includes three main steps:

- Generation of synthetic seismograms for the 1D velocity models with different plume thicknesses

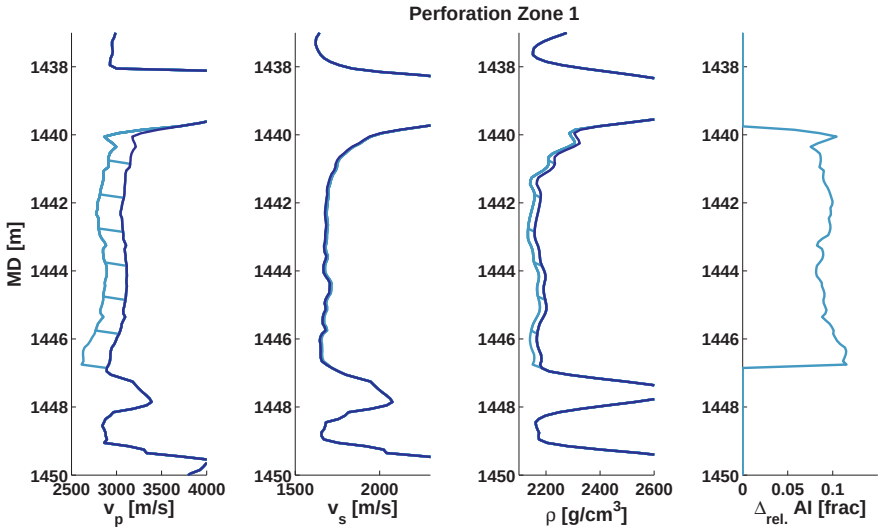

Figure 3.19: 1D elastic models (column 1-3) for the perforation interval 1 for different plume thicknesses and a gas saturation of 15%. The last column shows the relative changes in AI.

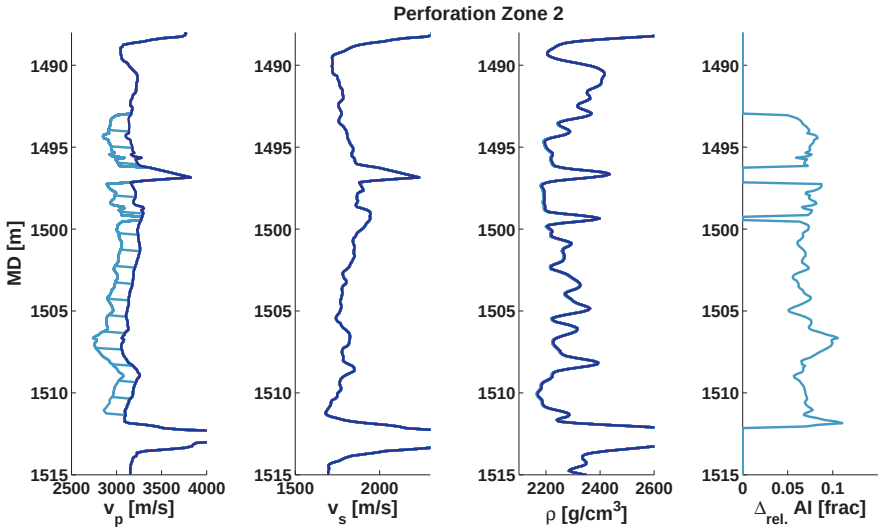

Figure 3.20: 1D elastic models (column 1-3) for the perforation interval 2 for different plume thicknesses and a gas saturation of 5%. The last column shows the relative changes in AI.

- Simulation of the Otway 3D seismic acquisition geometry by computing a 3D volume for each synthetic seismogram of the previous step that corresponds to a gas plume with infinite lateral extent and a constant thickness

- Generation of synthetic seismic volumes, that correspond to a plume with finite lateral extent and variable thicknesses, by combining the synthetic volumes of the previous step so that the plume geometry (plume thickness maps) for different injection volumes is matched

1.5D full waveform forward modelling is performed using the OASES© software package (*Schmidt and Tango*, 1986). Parameters of the forward modelling are designed to produce seismograms similar to the actual field data. The synthetic seismograms are generated with a central frequency of 45 Hz and an offset range of 0 - 3000 m with 5 m receiver spacing. The source is located 1 m below the surface to suppress surface waves. The results are convolved with a Ricker wavelet with a central frequency of 45 Hz to mimic the vertical resolution of the Otway 3D surface seismic data.

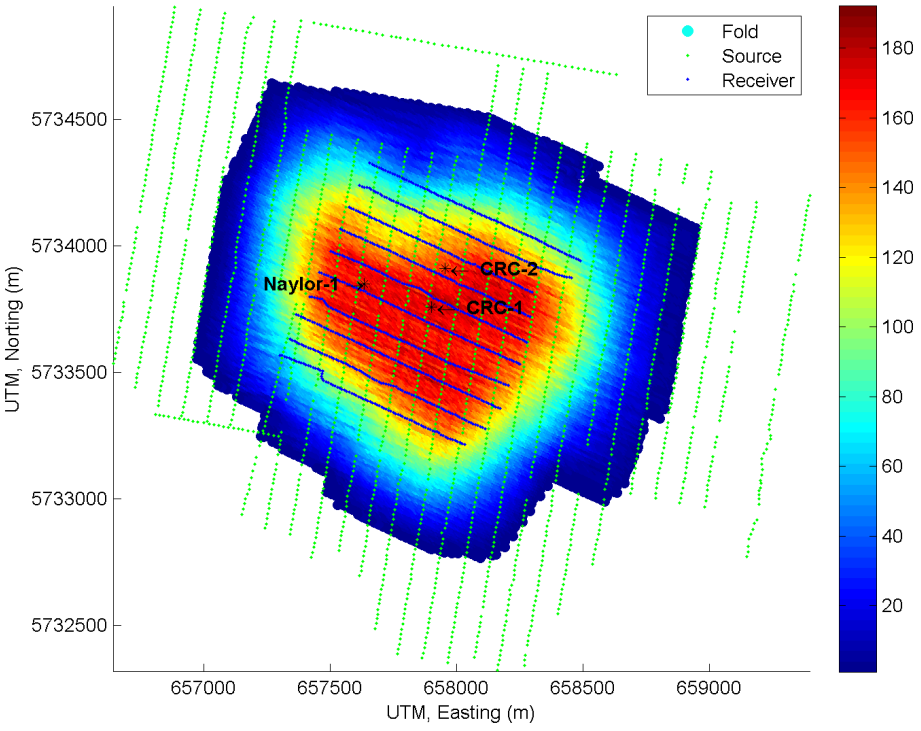

Figure 3.21: Otway 3D seismic acquisition geometry and total fold map (*Watson et al.*, 2012). The colour scheme corresponds to the total fold.

To simulate a reasonable acquisition geometry, the 2010 3D seismic data set of the Otway project is utilized. Figure 3.21 shows the acquisition geometry and the corresponding fold map. For each synthetic seismogram, a synthetic volume, which simulates the acquisition geometry of the field data, is produced. This is done by substituting every trace of the 3D field survey by a trace with the same absolute offset from the 1.5D reflectivity modelling. The procedure is performed pre-stack for all different plume thickness scenarios. Then, stacked

volumes corresponding to different plume thicknesses and the baseline data are obtained from the generated synthetic 3D volumes. The following processing steps are applied:

- F-K filter in a cone window to suppress strong P-S reflected waves with $T_0 > 700$ ms
- Amplitude correction
- Normal moveout correction (stretch mute 30%)
- Mean CMP ensemble stack

Vertical sections of the stacked volumes for the two perforation intervals and different plume thicknesses are presented in Figure 3.22. The TL signal produced by a gas layer of 2 - 4 m, is already quite significant. Gas layers with larger thicknesses produce one of the strongest reflected events in the sections. However, this analysis does not address two important issues: the finite lateral size of the plume and the presence of non-repeatable noise in the data.

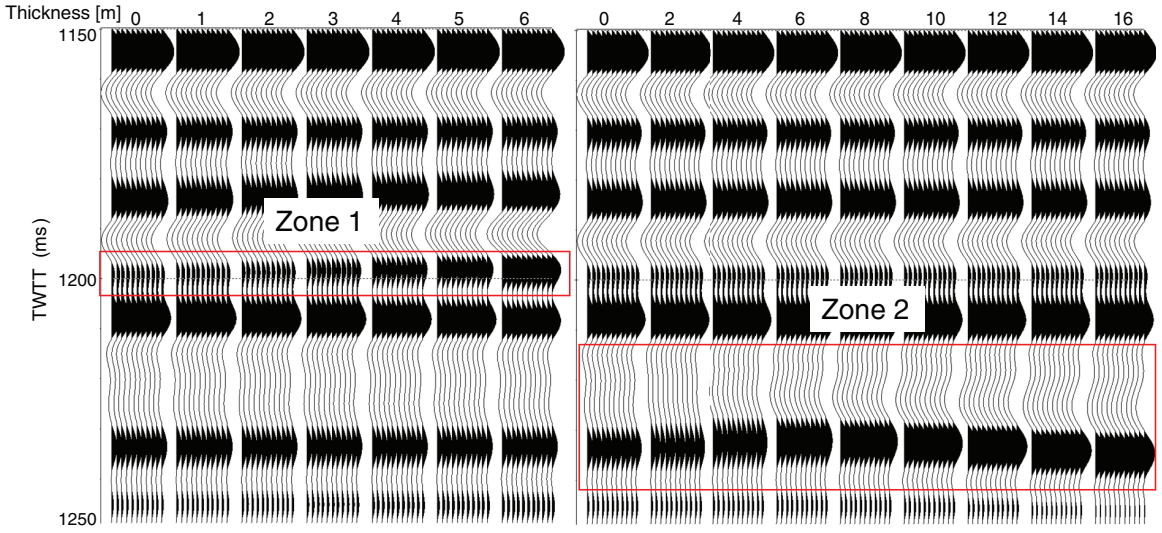

Figure 3.22: Stacked volumes for Zone-1 and 2 for varying plume thicknesses (0 - 6 m and 0 - 16 m) with gas saturations of 15 % and 5 %, respectively.

In the final step, synthetic seismic volumes are generated which correspond to a CO_2/CH_4 plume with finite lateral extent and variable thickness. These seismic volumes are computed by combining different volumes with a constant

plume thickness according to the plume thickness maps shown in Figure 3.17. In order to achieve this, each CMP stacked trace of the resulting synthetic volume is calculated by linear interpolation between traces with the same CMP number but a different plume thickness to match the plume thickness map. Vertical sections of the results along an inline direction near the CRC-2 well are shown in Figures 3.23 and 3.24. Both injection scenarios produce a TL signal comparable to other visible reflections in the section.

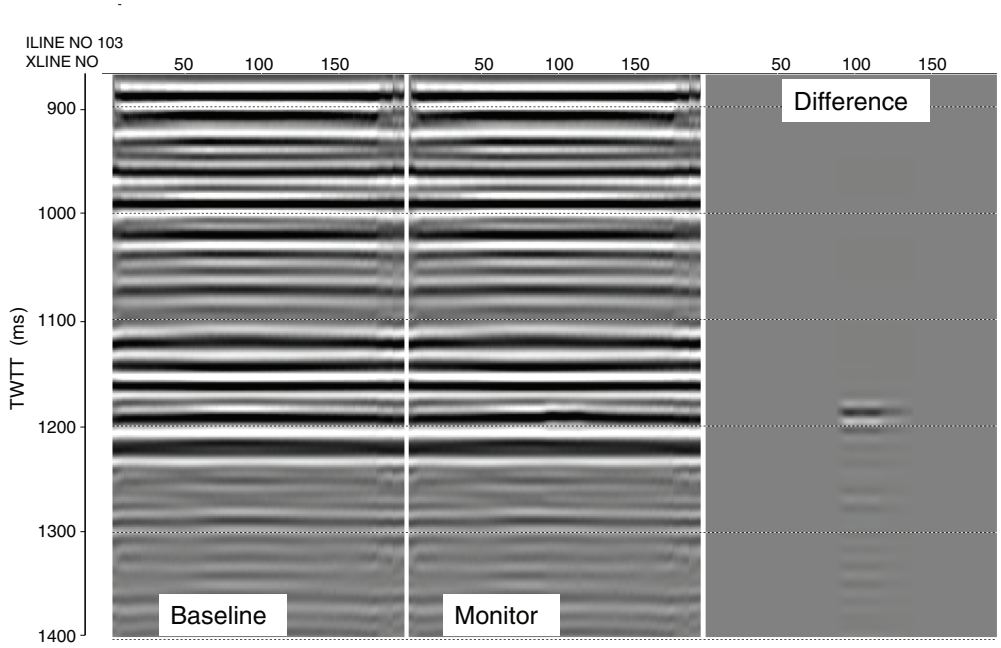

Figure 3.23: Perforation Zone-1: Stacked synthetic baseline and monitor data along an inline direction near the CRC-2 well and the difference volume for the gas plume with finite lateral extent.

Time-lapse seismic noise

The ability to detect and analyse the TL signal is always limited by the noise level of the data. For TL seismic monitoring this noise level is determined by the data repeatability of subsequent surveys. The 3D seismic surveys acquired in Stage 1 of the Otway project provide the opportunity to account for actual data repeatability (TL noise) since no signal-related changes are expected in the part of the record that corresponds to the potential injection intervals. Hence, TL noise, obtained from the field data, can be added to the modelled TL signal. The resulting "noise polluted" data sets for both injection intervals are shown in Figure 3.25. For the shallower injection interval the signal slightly exceeds the

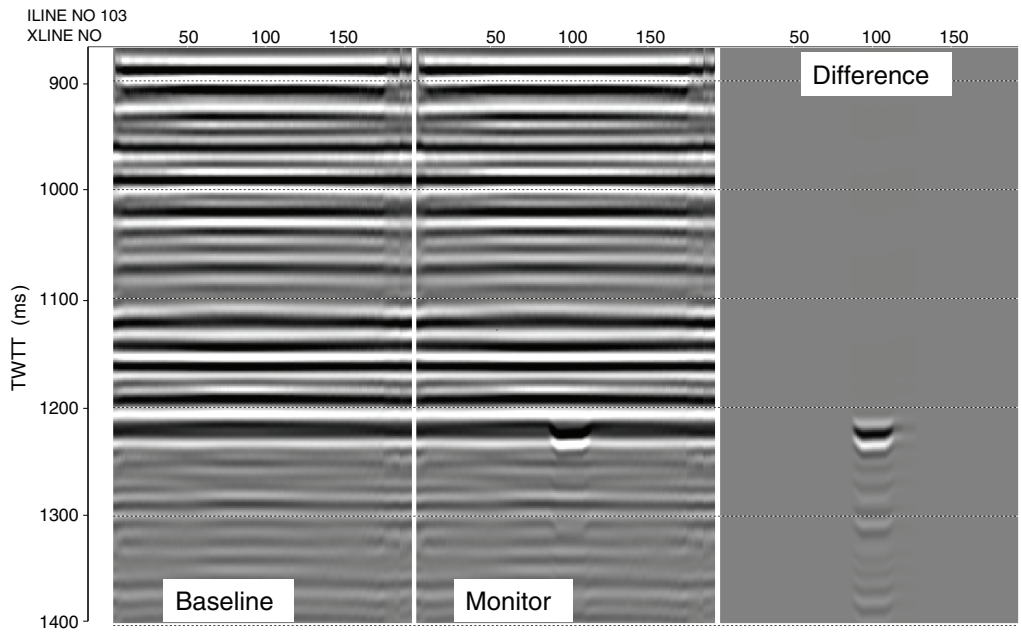

Figure 3.24: Perforation zone 2: Stacked synthetic baseline and monitor data along an inline direction near the CRC-2 well and the difference volume for the gas plume with finite lateral extent (reproduced after *Pevzner et al.* (2013)).

noise level, whereas the deeper zone creates a much stronger and clearly visible signal.

A workflow to quantify the uncertainty of plume detection related to TL noise was developed for the feasibility study. The basic concept is summarized in the following. First a large number of noise realisations with the same spatial and temporal characteristics and amplitudes as the field TL noise are created. For each noise realisation, the traces that exceed a certain signal to noise ratio N

$$\frac{RMS(signal + noise)}{RMS(noise)} > N\,, \tag{3.4}$$

and possess an amplitude that is 10% greater than the global maximum amplitude of the target reflection are counted. From these traces an effective plume diameter for each noise relation is estimated. Then a mean plume diameter and its standard deviation is computed for a couple of signal to noise ratios. Figure 3.26 displays the effective plume diameter for both injection zones as a function of the signal to noise ratio defined in Eq. (3.4). For a ratio of 1 the effective plume diameter is slightly larger for Zone-1 than for Zone-2. This is not surprising since

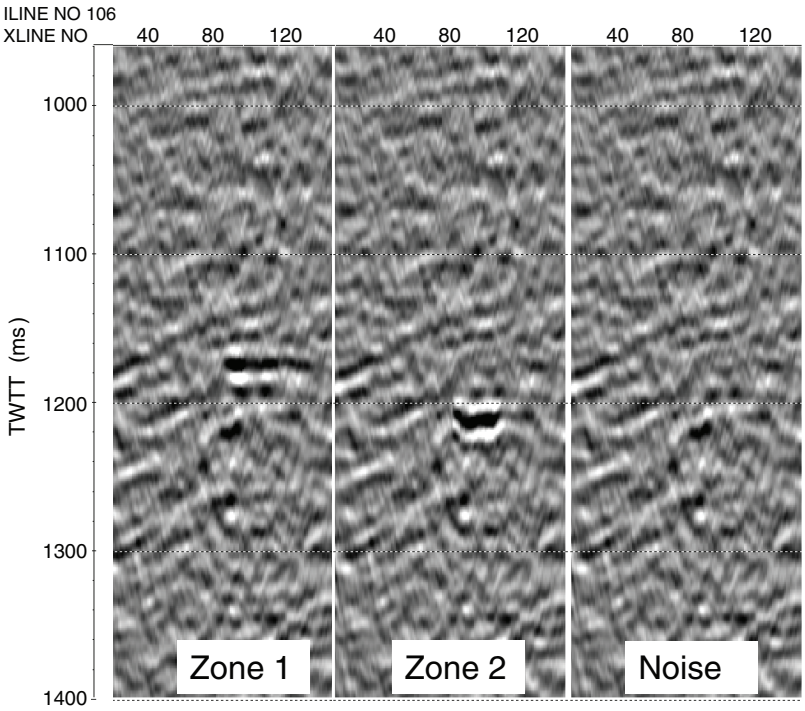

Figure 3.25: Synthetic difference volumes contaminated with the actual TL noise of the field. The last column shows the TL noise of the field data (reproduced after *Pevzner et al.* (2013)).

the lateral extent of the plume is larger. However, with increasing ratios corresponding to TL seismic signals that can be detected more robustly, the effective diameter of the plume in the second perforation zone becomes larger. The reason is that the gas plume in the first zone is thinner than for the second zone.

In summary, the deeper perforation interval provides a thicker plume, but the average relative changes of AI are smaller with 6% compared to 10% in the shallower injection interval. Combining actual TL noise from the field data and the TL signal of the synthetic data, suggests that the injection of 30 kt into the perforation Zone-2 is likely to be detected by the surface seismic reflection method using the Otway 3D acquisition geometry. The detectability of the gas plume in Zone-1 seems to be a bit more challenging. Although the changes in elastic properties are on average higher for Zone-1, the crucial factor for the detectability of the gas plume in the two perforation intervals is the thickness of the plume.

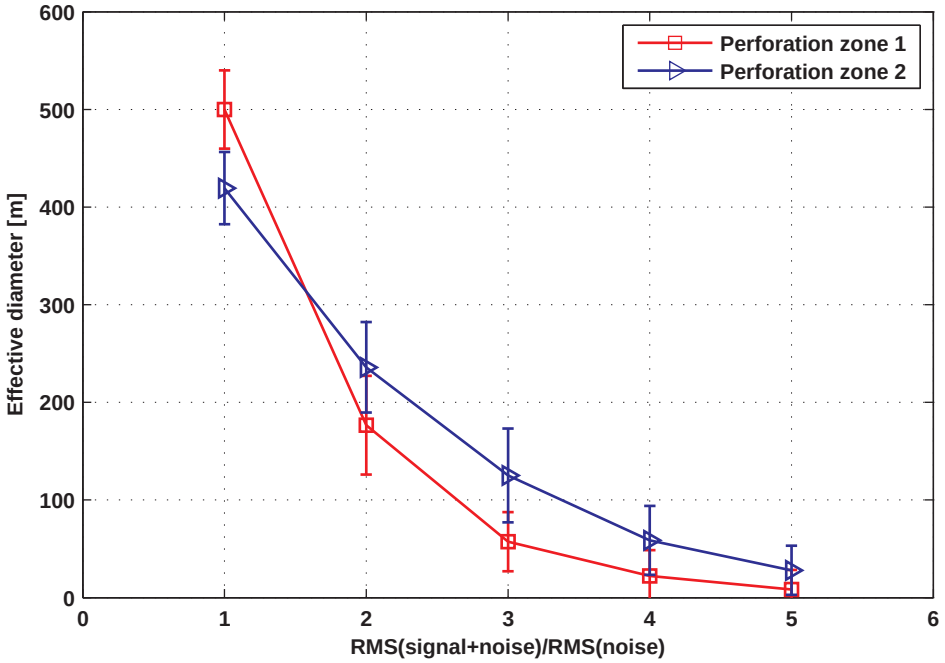

Figure 3.26: Comparison of the effective plume diameter for the first and second perforation zone as function of the signal to noise ratio.

3.3.2 Injection volumes and geological realisations

This section focuses on the effect of different injection volumes and geological realisations, which in turn result in different geospatial distributions of the gas plume, on the seismic response. A similar workflow as in the case of the depleted gas reservoir is utilized. The main difference is that calibrated rock physics models are employed to assign elastic properties to the reservoir simulation grid since this allows a faster evaluation of several scenarios. The rock physics models are described in detail in Section 4.2.2. The elastic model outside of the flow simulation grid is based on log data from the CRC-1 and CRC-2 wells. For the resulting elastic models, we perform computational fast convolutional modelling with a statistical wavelet estimated from the seismic field data to generate zero-offset (simulating a migrated stack) synthetic volumes. Finally, the detectability of the TL seismic signal is evaluated using the noise model described in the previous section. This workflow accounts for all changes related to gas saturation on the elastic properties and takes into account the spatial fluid distribution as predicted by reservoir simulations. The analysis is done for the perforation Zone-2 and the modelled scenarios are summarized in Table 3.4.

Table 3.4: Scenarios perforation zone-2

Geological realization	R1	R1-R5	R1
Injection volume	10 000 t	15.000 t	30.000 t
Time step	90 days, 1 yr, 2 yrs	135 days, 1 yr, 2 yrs	270 days , 1 yr, 2 yrs

Injection volume

For the base realization (R1) of the geological model, we investigate if different injection volumes (10 kt, 15 kt and 30 kt) have an influence on the prediction of the magnitude and effective diameter of the TL seismic signal. Three time steps are selected the end of injection, 1 year and 2 years after the injection started. Figures 3.27 and 3.28 display the results of the reservoir simulations as gas column heights and plume thickness maps, respectively. Note, that gas saturations below 1% are not considered in the calculation of the maps.

The reservoir simulations predict that the gas plume spreads out in the reservoir with time, predominantly in a thin layer below the reservoir seal (Figure 3.28). The plume thickness in the immediate area around the injection well CRC-2 changes only slightly with time, while the gas content in this region decreases between the end of injection and 1 year after the injection started. Only minor changes can be observed for the following year. For an injection volume of 30 kt, the gas plume reaches the greatest lateral extent, but the area around the CRC-2 well with a considerable thickness of 10 - 20 m is similar to the case of 15 kt gas injection.

Changes in elastic properties For each grid cell of the reservoir zone relative changes in AI are calculated and the resulting histograms are shown in Figure 3.29. These histograms indicate that the plume spreads out (more grid cells contain gas) in the reservoir section with time without affecting the obtained values of relative changes in AI. The reason is that for the assumption of uniform saturation, the acoustic impedance saturation curve decreases steeply at small gas saturations, whereas changes with higher gas saturations are small (Figure 3.30). The peak around 10% at the time steps 1 year and 2 years for the 30 kt scenario is caused by the thin layer of CO_2 that spreads out below the seal of the per-

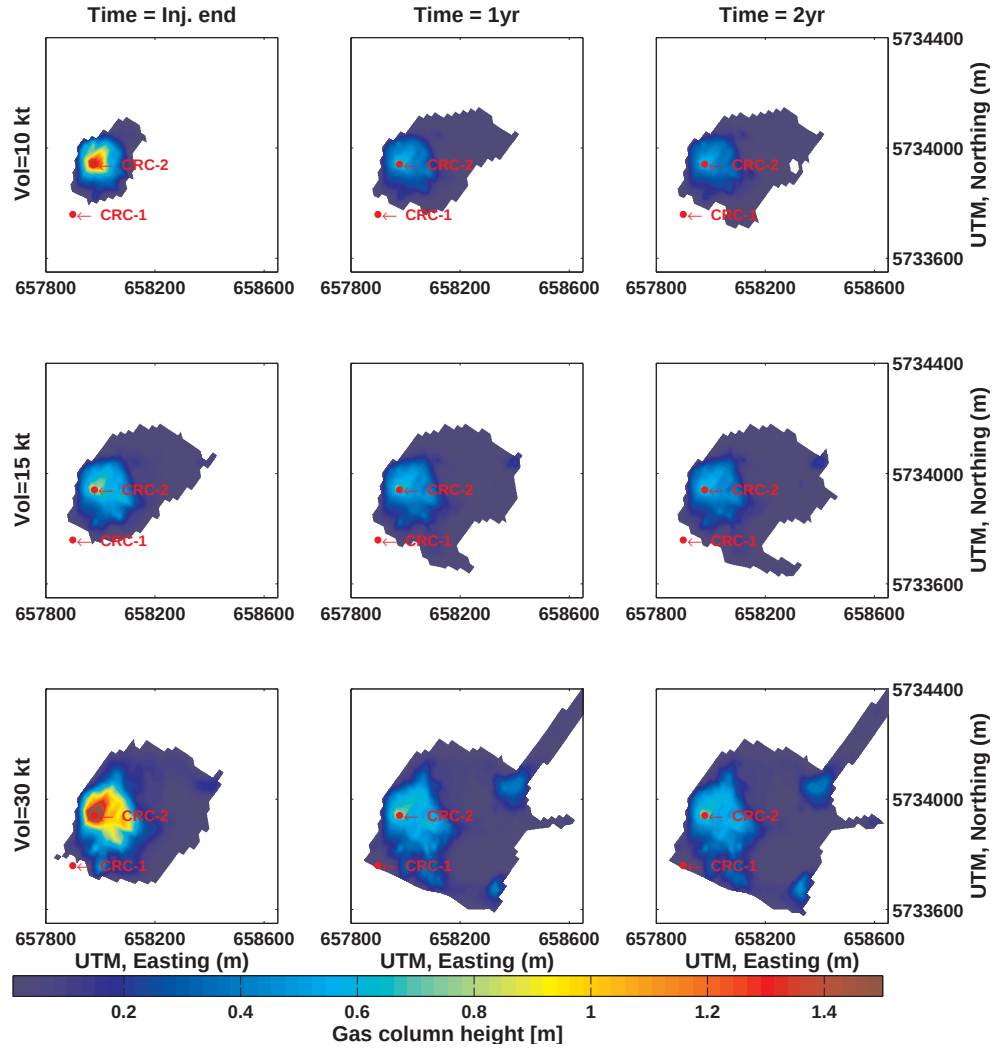

Figure 3.27: Gas column height for the injection volumes 10 kt, 15 kt and 30 kt at the time steps end of injection, 1 year and 2 years.

foration interval (Figure 3.27). Even though, this high porosity layer with high gas saturations produces large changes in AI, the layer is not expected to contribute significantly to the TL signal since the layer thickness is too small to be detectable. Note that the thickness of the plume is considerably larger than for the previous modelling workflow, since small gas saturations above 1% (diffusive gas) are taken into account and no cut-offs are set for relative changes in AI.

Comparison of the time-lapse seismic signal with noise The seismic response for the different scenarios is computed by simple convolutional modelling. Gas injection into a saline aquifer substantially reduces the compressional wave velocity. This, in turn, causes a time-shift between the baseline and monitor

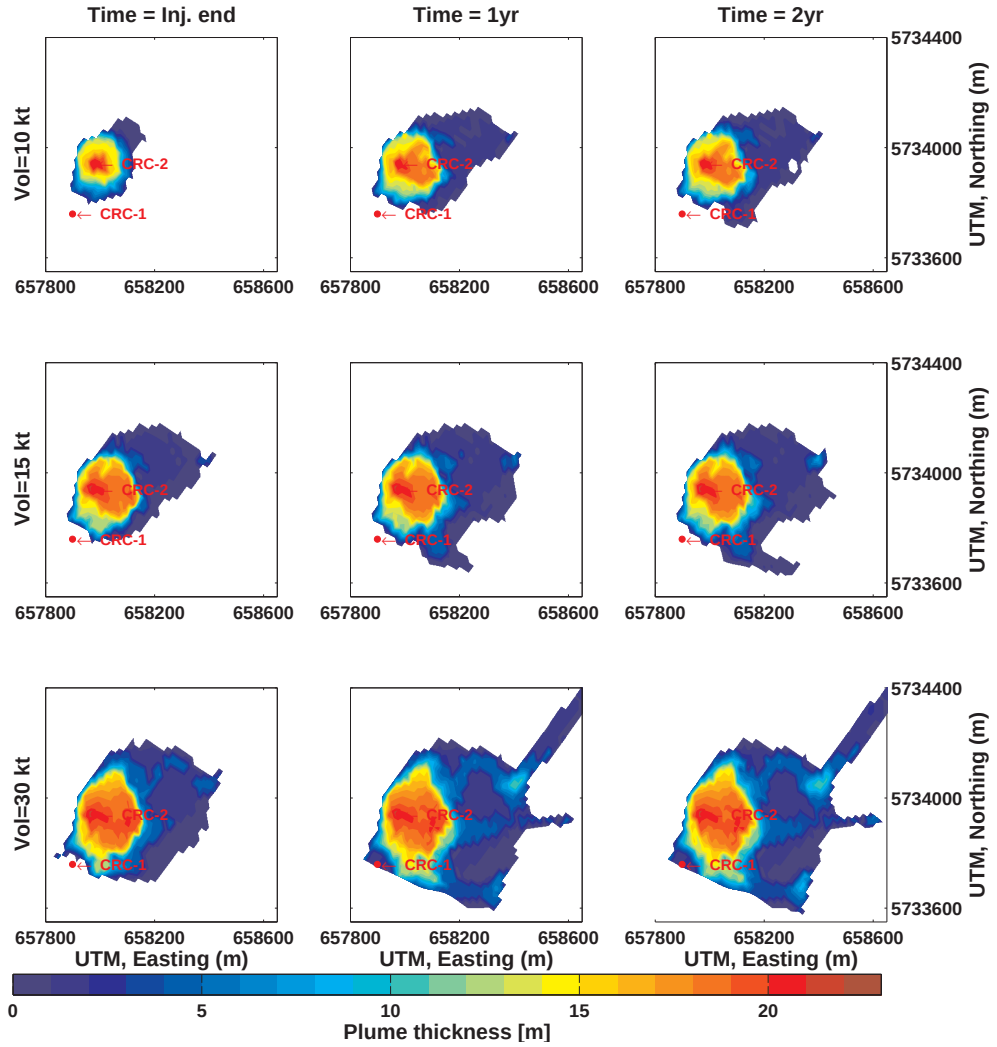

Figure 3.28: Plume thickness for the injection volumes 10 kt, 15 kt and 30 kt at the time steps end of injection, 1 year and 2 years.

surveys for seismic events below the reservoir top. Misalignments of reflections between TL surveys, so called velocity push down phenomena, are an essential part of the TL signal and taken into account in the modelling. Figure 3.31 shows cumulative push-down maps, which account for all time-shifts from the bottom of the reservoir. For all three cases an area of approx. 200 m in diameter underneath the gas plume will be affected by a pull down exceeding 1 ms. This should be visible in the field data.

To quantify the amplitude of the TL seismic signal RMS amplitude difference volumes with a sliding window of 30 ms are computed. In order to compare the predicted TL signal to the measured TL field data of Stage 1, the amplitudes

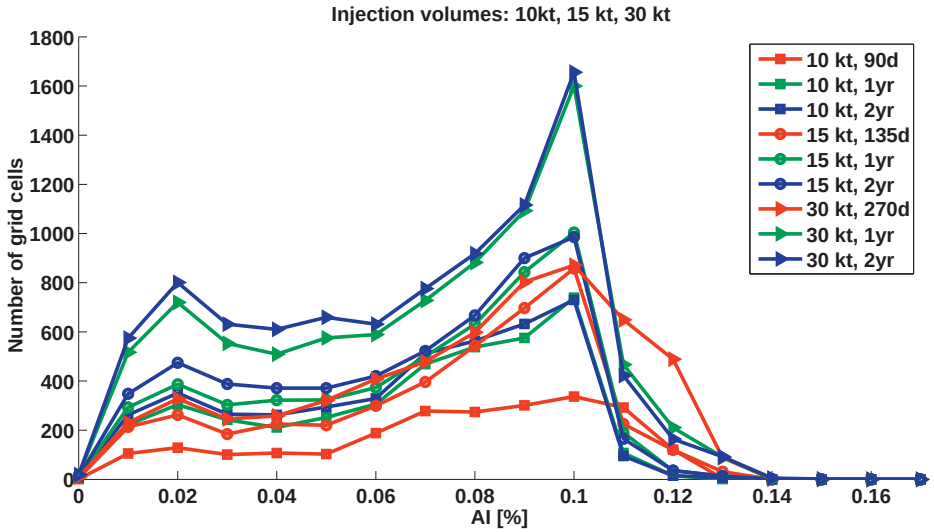

Figure 3.29: Histograms of relative changes in AI for the injection volumes 10 kt, 15 kt and 30 kt at the time steps end of injection, 1 year and 2 years.

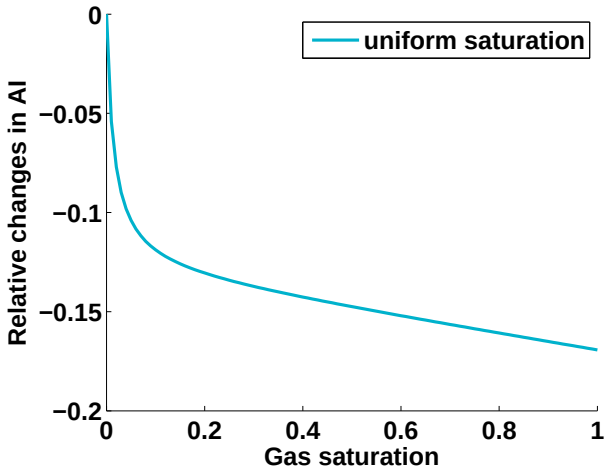

Figure 3.30: Relative changes in AI as function of gas saturation for a core sample of the CRC-2 well.

are calibrated with each other. For the central part of the gas plume, the RMS amplitudes of the signal are on average larger than the recorded TL noise of the target horizon (Figure 3.32). The portion of the plume which exceeds the TL noise is slightly larger for 30 kt gas injection.

The detectability of the gas plume is evaluated by calculating the effective diameter of the plume for different signal to noise ratios based on the workflow described in Section 3.3.1 (Figure 3.33). Injection of 15 kt creates a sufficiently larger plume straight after the injection compared to 10 kt, however, the difference in the effective diameter decreases with time. It is also apparent that a further increase of the injection volume to 30 kt will not improve the detectability of the

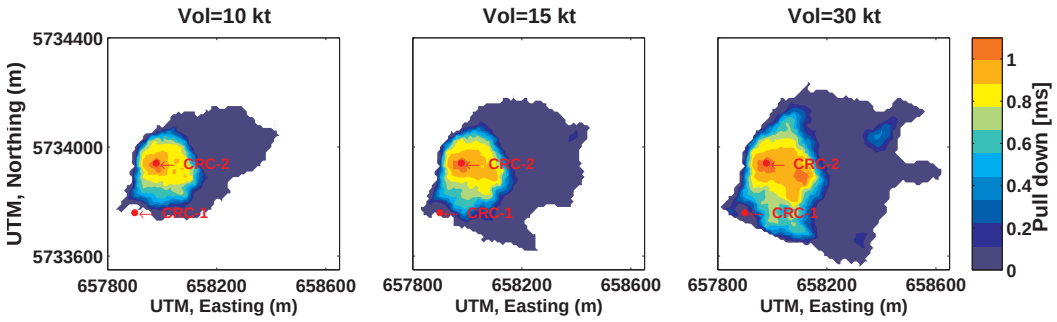

Figure 3.31: Push down maps for the injection volumes 10 kt, 15 kt and 30 kt at the time step of 1 year.

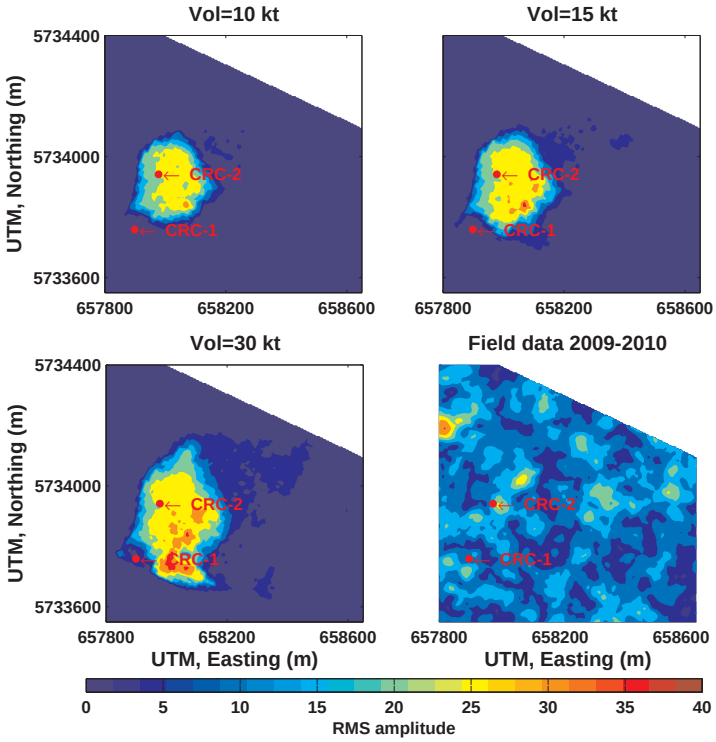

Figure 3.32: RMS amplitudes of the predicted seismic signal for the injection volumes 10 kt, 15 kt and 30 kt at the time step of 1 year and the TL difference of the field data.

gas plume significantly since most of the gas spreads out in a thin layer. Moreover, the strength of the signal is not decaying substantially in the first two years.

Geological Realizations

The main uncertainty in the static geological model associated with geological heterogeneity is the distribution and the lateral extent of the cement baffles. These thin cement layers, interbedded in the reservoir formations, have potentially the greatest impact on the spatial distribution of the injected gas because

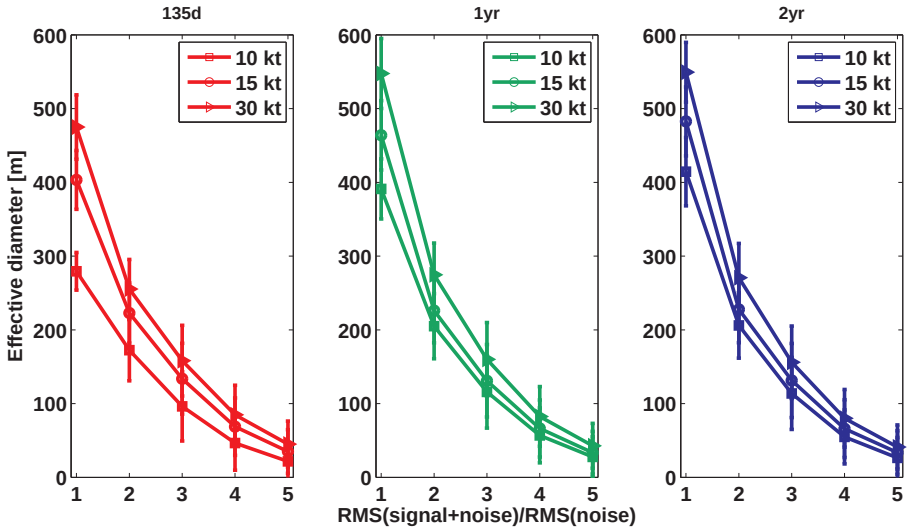

Figure 3.33: Effective diameter for the injection volumes 10 kt, 15 kt and 30 kt as a function of the signal to noise ratio at different time steps.

of a strong contrast in porosity and permeability. Five equi-probable geological realisations are considered with cement layers that have a lateral extent over 300 m. To evaluate the influence of the gas distribution on the seismic response the scenario of 15 kt gas injection is investigated at the end of injection as well as 1 year and 2 years after the injection started.

Figures 3.27 and 3.28 display the results of the reservoir simulations as gas column heights and plume thickness maps, respectively. These predictions show different spatial distributions of the gas in the reservoir, which are reflected in the shape of the gas plume in the maps. However, the obtained plume thicknesses are comparable for all five realisations. Furthermore, in all cases a thin layer of gas spreads out at the top of the reservoir as predicted for the base realisation (R1).

Changes in elastic properties The different geological realisations produce similar results in terms of relative changes in AI (Figure 3.36). Nevertheless, the distribution of the data in the AI histograms varies slightly, especially for scenario R1 at the end of injection. For R1, the gas plume reaches the largest lateral extent, which causes a higher peak around 10% in the AI histogram. This difference is more pronounced at the end of injection and reduces to some extent

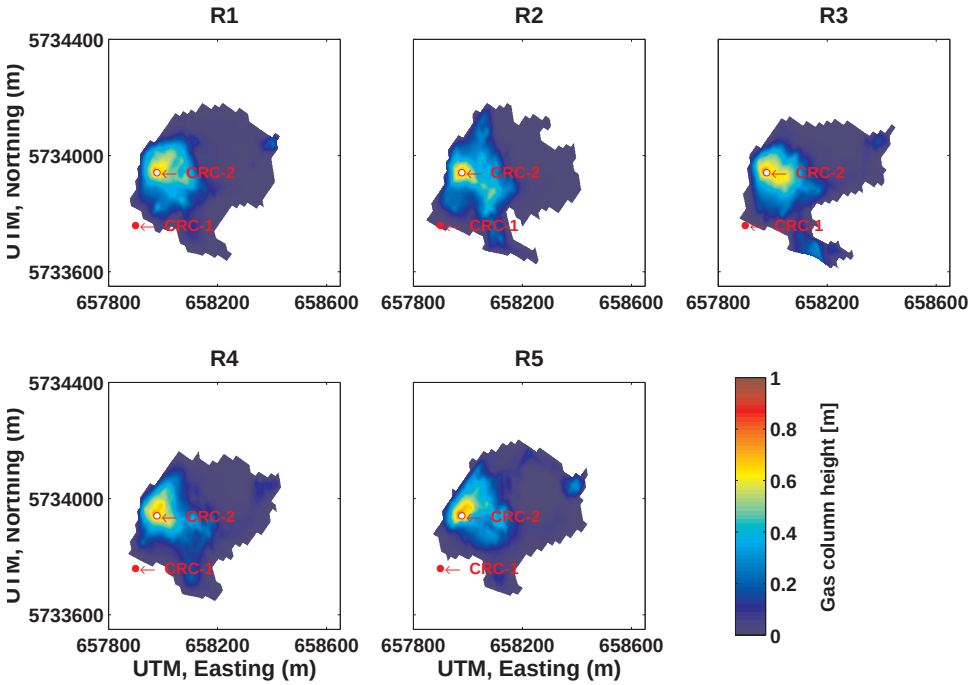

Figure 3.34: Gas column height for 5 geological realisations with an injection volume of 15 kt at the time step of 1 year.

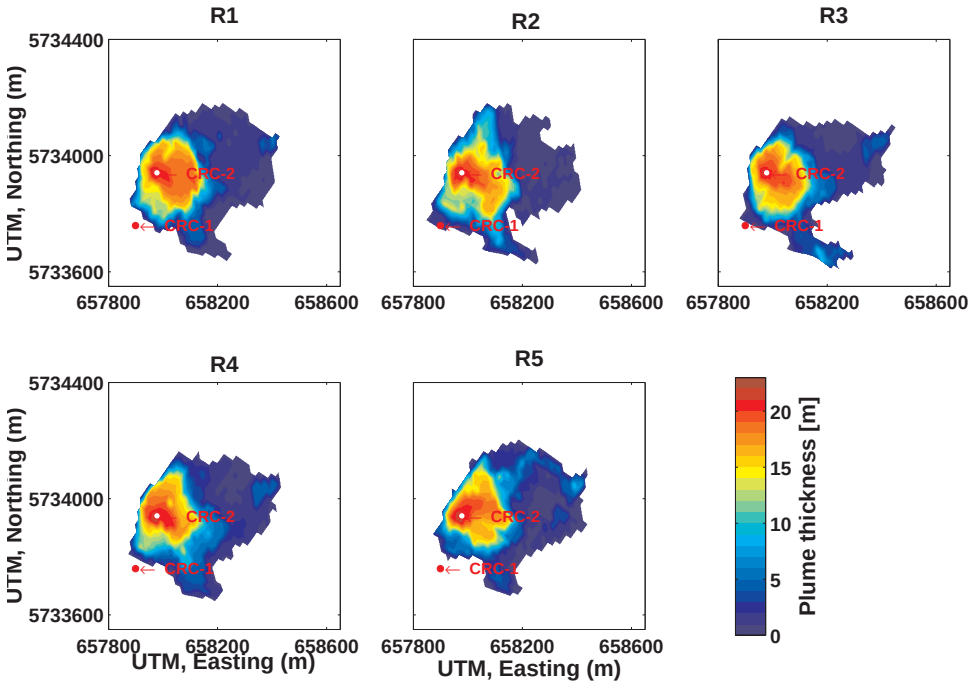

Figure 3.35: Plume thickness for 5 geological realisations with an injection volume of 15 kt at the time step of 1 year.

with time since for all cases, the gas spreads out below the seal of the reservoir in a thin layer of 1 - 2 m thickness. This part of the gas plume will be very difficult

to detect with the surface seismic reflection method.

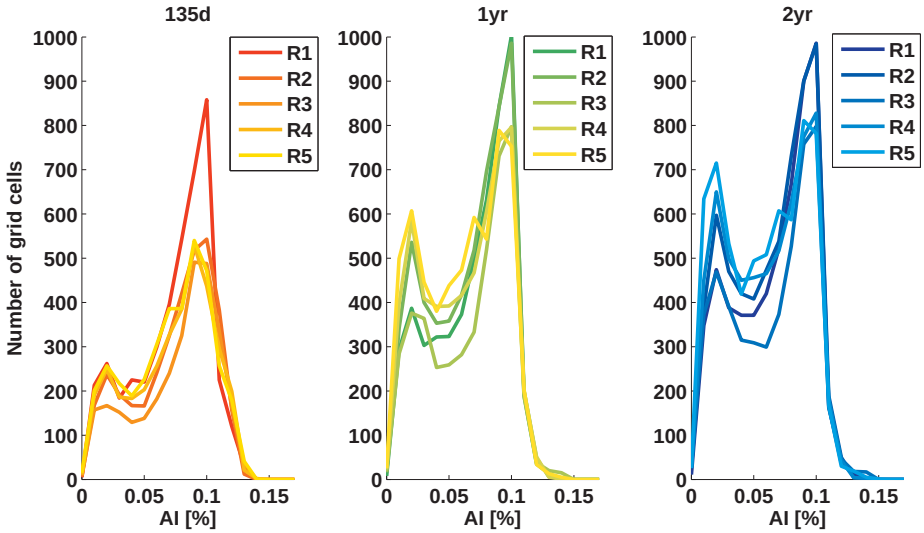

Figure 3.36: Histograms of relative changes in AI for 5 geological realisations at the time steps end of injection, 1 year and 2 years.

Comparison of the time-lapse seismic signal and noise Figures 3.37 and 3.38 display cumulative push-down maps and the RMS amplitudes of the TL signal. The plume area with a pull down around 1 ms is larger for R1 than for the other realisations as well as the region which exceeds the amplitude of the noise significantly. To assess the uncertainty of detection related to uncertainties of the geological models, we apply the same signal/noise analysis as in Section 3.3.1. The largest difference in the effective plume diameter occurs at the end of injection for a S/N threshold of 1. The effective diameter of the plume for the S/N threshold of 2 varies between 180 to 210 m and for the threshold of 3 between 87 to 136 m. All these values indicate a high likelihood of successful plume detection even with the current surface 4D seismic acquisition geometry. However, this does not necessarily mean that the TL amplitude response does not vary with time.

In summary, the analysis of different injection volumes shows that there is an increase in the signal level due to an increase of the injection volume. However, after 1 year and for S/N ratios over 1, a higher injection volume of 30 kt does not provide a significant improvement for the seismic detectability of the gas

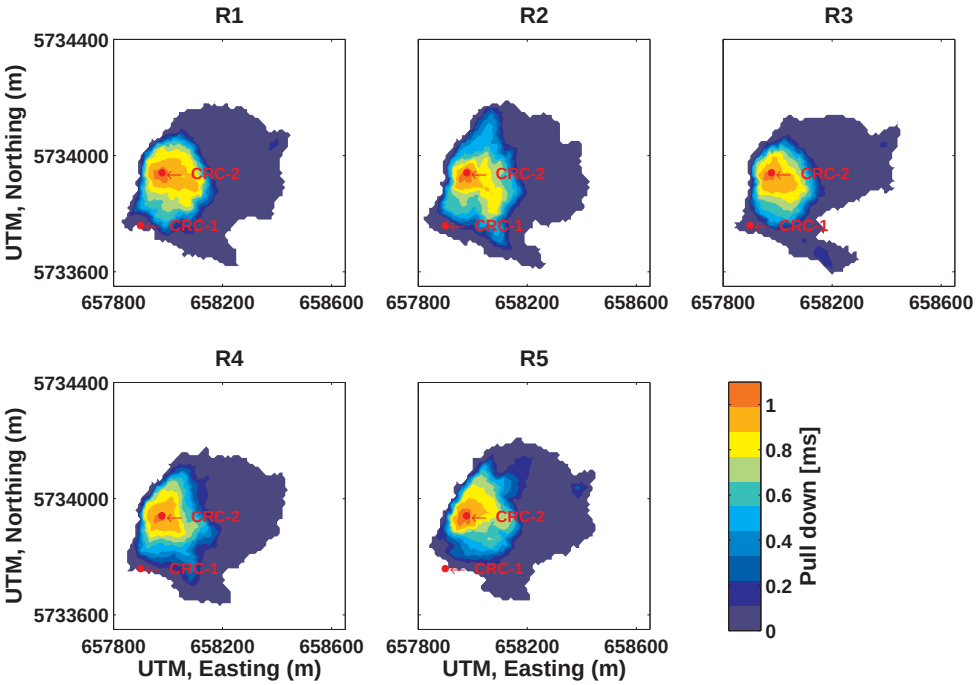

Figure 3.37: Push down maps for 5 geological realisations with an injection volume of 15 kt at the time step of 1 year.

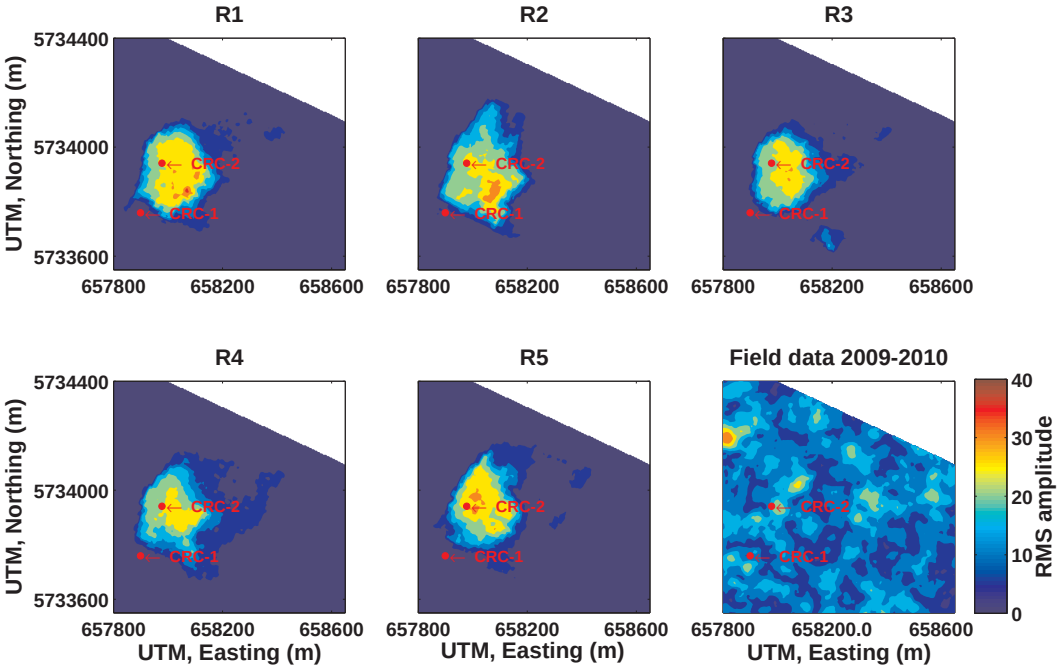

Figure 3.38: RMS amplitudes of the predicted seismic signal for 5 geological realisations with an injection volume of 15 kt at the time step of 1 year and the TL difference of the field data.

plume. Using 15 kt as the injection scenario, we computed TL seismic signals for five different realisations of the geological model and three time steps, namely,

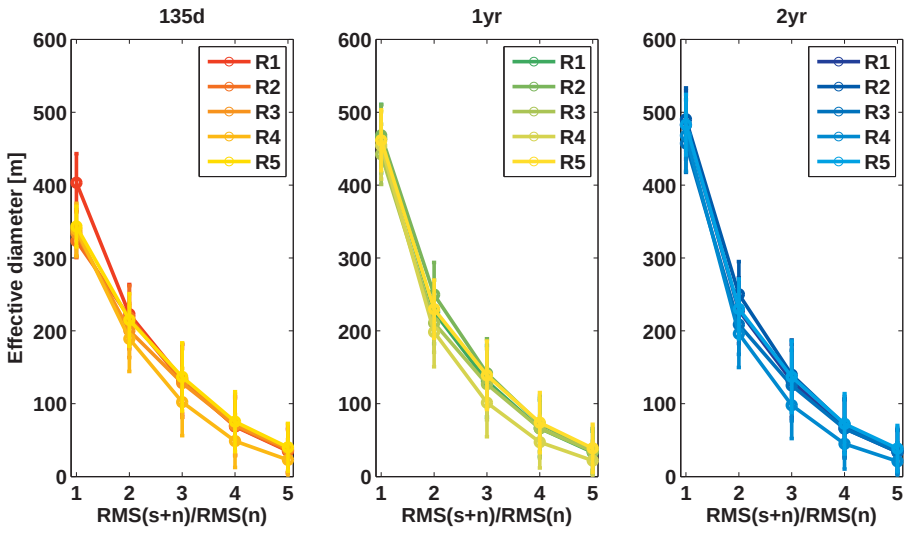

Figure 3.39: Effective diameter of the predicted seismic signal for 5 geological realisations as a function of the signal to noise ratio.

end of injection, one and two years after the injection started. For all scenarios, the injection will cause a substantial change in the shape and amplitude of the reservoir reflection leading to an area of approx. 200 m in diameter, for which the signal exceeds the noise of the field data.

3.4 Conclusions

The ability of the seismic reflection imaging method to detect a CO_2/CH_4 gas plume was assessed for two different reservoir types, a depleted gas reservoir and a saline aquifer. The modelling studies emphasise the importance of site-specific modelling before an injection experiment is undertaken since every storage site has unique challenges. The challenge for seismic monitoring in the depleted gas reservoir is the small change in elastic properties due to a low contrast in fluid properties. This case study confirmed that the TL signal is too small or the TL noise too high to detect a signal robustly with the acquired surface seismic data. On the other hand the feasibility study for the saline aquifer indicates that the main challenge will be a thin gas plume. The analysis of two different zones in the Paaratte formation showed that a thicker and more heterogeneous formation might be more favourable for seismic monitoring than a thin very permeable clean sandstone interval. In the latter case, strong buoyancy effects may lead to a thin

gas layer at the top of the formation which is more difficult to detect.

Furthermore, the influence of different injection volumes and geological realisations were investigated. Though an increase in the injection volume resulted in a spatially larger signal, after one year of injection and S/N ratios larger than 1, the modelling results do not predict a significant improvement for the seismic detectability of the gas plume. The reason is that most of the additional gas volume is predicted to spread out below the reservoir seal in a thin layer. The layer thickness is close to the detection limit of the seismic method. Different realisations of the static geological model resulted in different geospatial distributions of the fluids. Though, this caused spatial variations in the predicted TL signals, in all cases a substantial signal, which exceeded the TL seismic noise of the field data was obtained.

For the modelling of CO_2/CH_4 injection into the saline aquifer, two workflows were utilized. The first workflow considers the full wavefield and represents the offset/angle distribution of the field seismic data. The second workflow is based on the reflectivity series of the subsurface and considers only vertical wave propagation (zero offset). However, in contrast to workflow-1 which relies basically on a 1D saturation profile, workflow-2 takes the spatial distribution of fluids into account as predicted by reservoir simulations. A comparison of the two approaches shows that the predicted effective plume diameter for 30 kt gas injection at the end of injection matches for both approaches quite well. The effective plume diameter is ∼255 m for workflow-1 compared to ∼240 m for workflow-2. It is likely that the convolutional modelling (workflow-2) approach gives a slightly larger signal as we use the gas saturation as predicted by reservoir simulations and not its lower limit as in workflow-1. However, in the convolutional modelling (workflow-2) we are probably still underestimating the signal strength by ignoring the AVO effect.

Chapter 4

Parameterisation of the elastic model of the subsurface

A key part of a 4D seismic feasibility study described in Chapter 3 is to build an elastic model of the subsurface. To calculate changes in elastic properties caused by CO_2 saturation effects, it is necessary to populate the elastic model with a consistent data set including velocities of the saturated rock, porosity and dry rock and grain material compressibilities.

Information on elastic properties of the subsurface comes from core samples, well log and seismic data (VSP and surface seismic). These data sets possess different vertical resolution, spatial coverage and information about the physical properties of the rock. Though the spatial coverage of surface seismic data is quite dense compared to well log data, the vertical resolution is much lower. Well log data is at best available at a couple of locations in the area of interest and core samples are only available from some points in the well. On the other hand, post-stack inversion results of seismic data will at most provide acoustic and elastic impedance properties. Contrary, well log data might provide P- and S-wave velocities and density data of the saturated rock at in-situ conditions as well as information about porosity, saturation, lithology and mineral composition. However, the dry compressibility of the rock, a crucial parameter to estimate the effect of CO_2 saturation on the elastic properties, can only be measured directly on core samples in the laboratory.

An additional scale comes into play if the modelling of the time lapse signal is based on the results of reservoir simulations. The grid of the reservoir simulator has in most cases/our examples a finer vertical scale than the resolution of the seismic data, but a coarser scale compared to the log data. This causes some practical issues since the reservoir simulation results, which are based on the static geological model, have to be linked to the elastic model of the subsurface.

The first part of this chapter illustrates practical problems arising from these scale differences. The second part of the chapter focuses on consistent relations between the different parameters and the estimation of the dry rock compressibility for fluid substitution modelling. The chapter is based on an expanded abstract "Caspari, E., J. Ennis-King, R. Pevzner, and B. Gurevich (2012), Prediction of the seismic time-lapse signal of CO_2/CH_4 injection into a depleted gas reservoir - Otway project, *in ASEG Extended Abstracts*, (1), 1-4" and a report for the CO2CRC Otway project "Watson, M., Y. Cinar, T. Dance, R. Pevzner, E. Tenthorey, E. Caspari, J. Ennis-King, V. Shulakova, M. Bunch, M. Urosevic, R. Singh, B. Gurevich, L. Paterson, C. Jenkins, and M. Raab (2012), Otway Stage 2C Science Report - Verification of CO_2 Storage in a Saline Formation (Paaratte) Using Time Lapse Seismic., (Publication Number RPT12-4109)", which will not be cited again in the following text.

4.1 Scale differences between the seismic and engineering domain

This section illustrates scale differences between data domains using the data example of CO_2/CH_4 injection in the depleted Naylor gas reservoir. The following data sets were available to build a 3D elastic model of the reservoir: the acoustic impedance inversion result of the seismic baseline data acquired in 2008 (*Asgharzadeh et al.*, 2010), the static geological model (*Dance et al.*, 2009) on which the reservoir simulations (*Ennis-King et al.*, 2011) are based, and log data. These data sets are in different domains, e.g. the acoustic impedance inversion is in time

and the geological model in depth, and on different scales. To combine the data sets, the RokDoc Chronoseis© package (Ikon Science) is utilized. The software package provides a platform to integrate seismic data, log data and reservoir simulation results and facilitates rock physics modelling to estimate CO_2 saturation effects on the seismic response.

The workflow is as follows: first, a model framework in time is built from seismic time-horizons of the 2008 data set which were used in the acoustic impedance inversion. To convert the time framework into a depth model, a simple layer-cake method is applied. In this approach, the depth surfaces are computed from pseudo interval velocities based on well tops and time horizons. The created depth surfaces are fixed to the well tops in the CRC-1 and Naylor-1 well. To fit the flow simulation grid, which is in depth, into the RokDoc depth model, the top and bottom horizons of the Waarre-C reservoir are replaced by the corresponding depth surfaces of the reservoir simulation grid (geological grid). The software package matches the two property sets in a grid less approach.

In principle, all data sets can be loaded into the model framework once this first step is achieved: acoustic impedance from the seismic inversion, porosity from the geological model, saturation predictions from the reservoir simulations and well log data. However, the static geological model, which provides porosity estimates, has a much finer vertical scale than the vertical resolution of the acoustic impedance inversion result (Figure 4.1). To compare these scales, two models with different levels of detail in the reservoir properties are built, a fine scale and a coarse scale model.

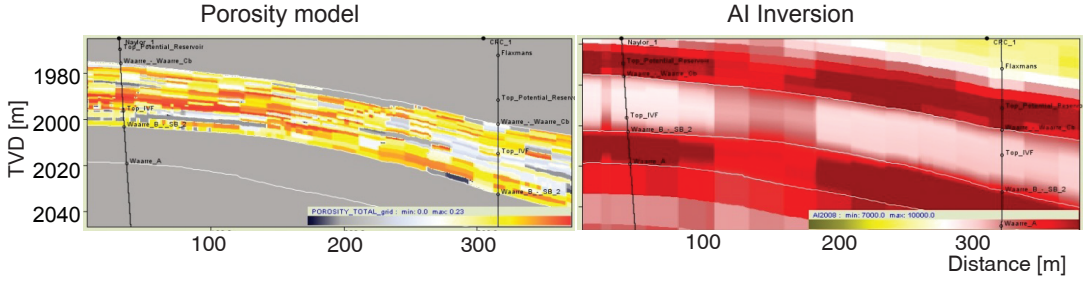

Figure 4.1: Slice through the porosity model and acoustic impedance inversion result.

4.1.1 Elastic models at different scales

The fine scale model (Model 1) is based on the porosity of the static geological model and is already described in Section 3.2. In this case, the reservoir model was subsequently populated with calculated AI values and P-wave moduli of the grain material from the well data by applying collocated kriging with the porosity model as a guide for the interpolation. The P-wave modulus of the solid grain material was computed by averaging the upper and lower Hashin-Shtrikman bounds of the clay and quartz volume fractions obtained from the well logs. Since the logs in CRC-1 and Naylor-1 are measured at different times post- and pre-production, respectively, for the interpolation process fluid substitution is performed so that the AI values correspond to the same saturation (20% residual gas saturation). Afterwards, fluid substitution is applied to the 3D reservoir model to match the pre-injection (2008) gas saturation using the prediction of the reservoir simulations. Outside the reservoir, the AI model is built from the AI inversion volume of the seismic baseline data (2008).

In the coarse scale model (Model 2), the AI volume from the inversion of the seismic baseline data (2008) is utilized. The seismic baseline data was inverted using a model based inversion algorithm based on the convolutional model (*Russell and Toksöz*, 1991). In this case, we smooth the static porosity model, which shows structures on a much smaller scale by applying a simple low-pass filter. The porosity model is smoothed to obtain a model with data sets on the same scale. The P-wave modulus of the grain material is set to the value for quartz.

Figure 4.2 presents a comparison between the AI and porosity values of Model 1 and Model 2. It is apparent that Model 1 is much more detailed than Model 2, but the average values of AI and porosity in both models are of the same order of magnitude. In summary, Model 1 honours the static geological model and Model 2 honours the inversion result of the seismic data.

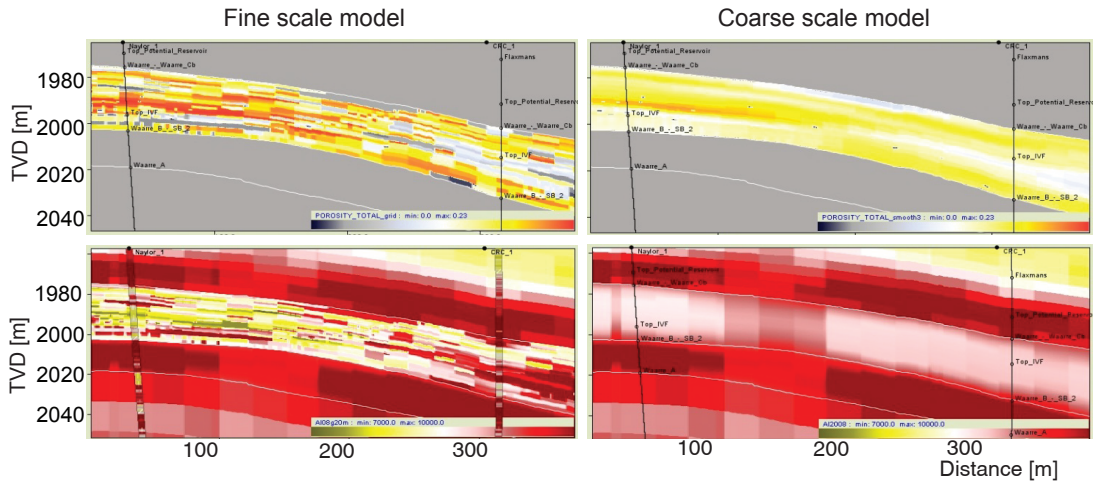

Figure 4.2: The top figures show a slice through the porosity model and the bottom figures show the acoustic impedance inversion result.

Change in elastic properties

To estimate changes in elastic properties, reservoir simulation results for the injection of 65 kt of CO_2/CH_4 (2010) are utilized. Then, fluid substitution modelling is performed for both models by employing an approximate method to solve Gassmann's equation (*Mavko et al.*, 1995). The method is based on the P-wave modulus without the use of shear-wave velocity. For the remaining parameters, the same methods/values as in section 3.2 are used. The results of the modelling are shown in Figure 4.3. The absolute difference in AI between the baseline and monitor models are of the same order of magnitude for the fine and coarse scale model. However, the values for the fine scale model show more variability.

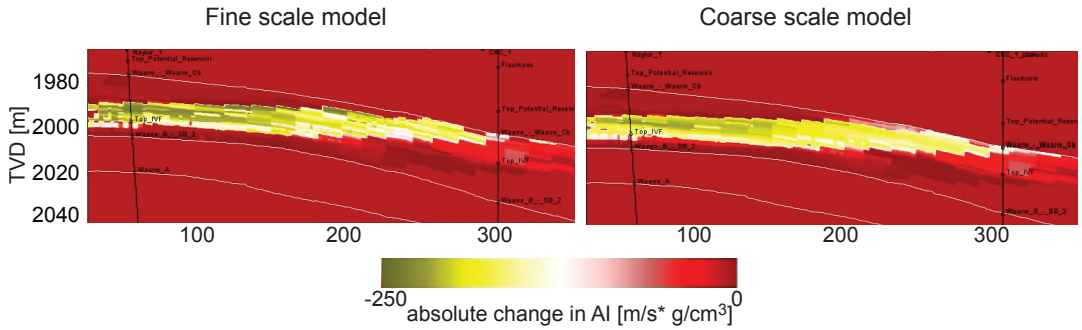

Figure 4.3: Absolute difference in AI for the fine and coarse scale model

4.1.2 Influence on the seismic response

In a next step, zero incident synthetics are computed by convolving the obtained AI volumes with a statistical wavelet, extracted from the 2008 surface seismic data.

As expected, the coarse scale model represents the amplitude distribution of the field data better since it is directly based on the inversion of the field data. The fine-scale model does not reproduce the amplitude distribution between the wells: the amplitudes in this area are higher than in the field data (Figure 4.4). The mismatch is not surprising since the geological model is a statistical model based on spatially sparse well and core data. The only information from seismic data incorporated in the model stems from structural interpretation, such as seismic horizons and faults, and hence the geological model is not conform with seismic amplitude information.

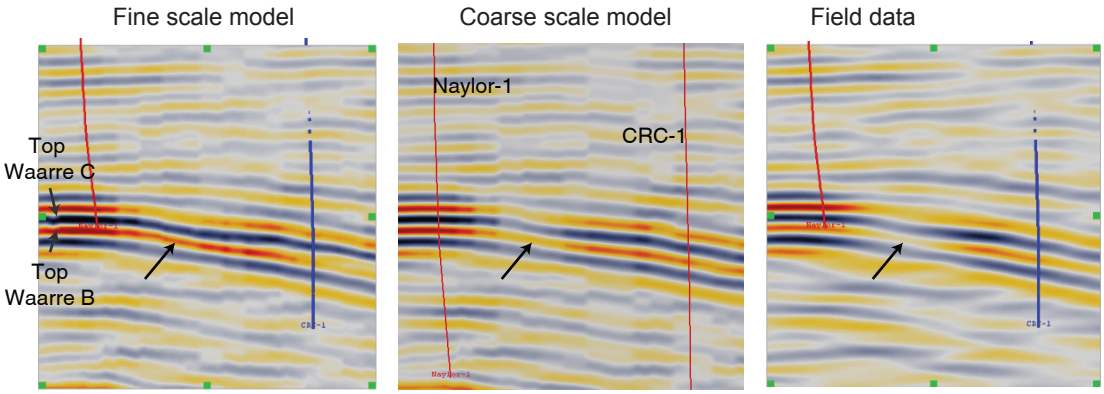

Figure 4.4: Comparison of synthetic data sets and field data with calibrated amplitudes on a line along the wells CRC-1 and Naylor-1. The black arrow indicates the largest differences in amplitudes.

On the other hand, the simple averaging of the porosity model is not a proper up-scaling to the resolution scale achieved in the AI inversion. First, it does not assure that the two data sets are consistent in each point of the reservoir grid. More precisely, a proper up-scaling would require that the model is more or less consistent with the porosity - AI relationships observed in the well data. Second, the porosity of the geological model determines the volume of the fluids in the flow simulation results so every proper up-scaling of porosity would have to pre-

serve the volume of fluids. Another option would have been to down-scale the AI inversion result to the grid scale of the porosity model: however, in this case, consistent porosity - AI relations have to be assured as well. A simple workaround might be to calculate the effect of CO_2/CH_4 on the fine scale model and then, to subtract the estimated time-lapse effect from the AI inversion baseline model (coarse scale model).

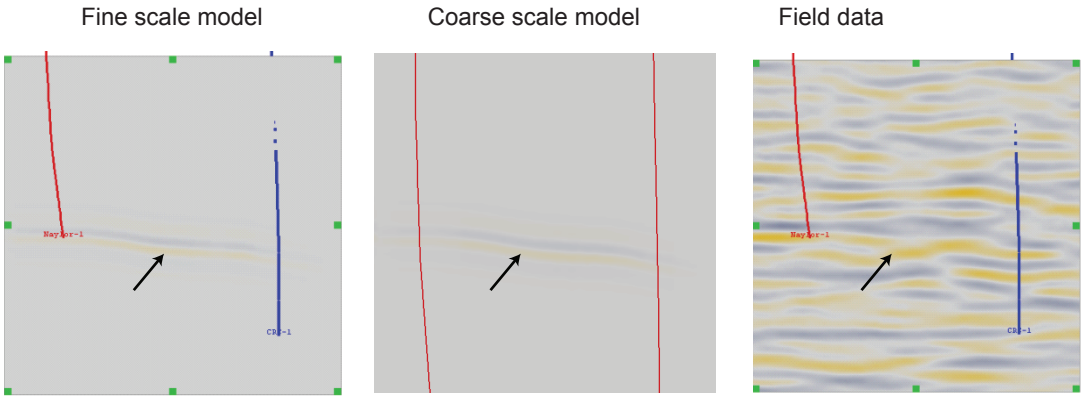

Figure 4.5: Comparison of time-lapse signal from the synthetic and field data on a line along the wells CRC-1 and Naylor-1. The black arrow indicates the largest differences in amplitudes.

Figure 4.5 displays the time-lapse signal compared to the noise level of the surface seismic field data. In both cases, the magnitude of the signal is smaller than the time-lapse noise. A comparison of the NRMS difference calculated over all differences related to changes in the reservoir level shows that the relative signal strength for the coarse scale model is slightly higher than for the fine scale model.

4.1.3 Discussion

The model obtained from the seismic inversion result reproduced the amplitude distribution of the seismic data better. However, the drawback of this model was that either the AI inversion result has to be downscaled or the porosity has to be up-scaled. Further, it is crucial that the model reflects the elastic property - porosity relation in the well data.

Therefore, to properly integrate seismic inversion results into a 4D feasibility study, a more unified approach should be attempted. One way is geostatistical inversion of the seismic data. Such an approach has not been tested in this study but the basic concepts are outlined in the following. The basic idea is to utilize geostatistical methods, such as collocated kriging, to create multiple local realisations of acoustic impedance traces on a 3D model from log data. These impedance traces are then convolved with a wavelet from the seismic data set and compared to the actual seismic trace. The process is repeated until a reasonable match is obtained. The results are multiple equi-probable realisations of acoustic impedance volumes on a vertical scale suitable for reservoir simulations constrained with seismic data. Since the vertical scale is below the seismic bandwidth (resolution), the solution remains non-unique and several models can explain the seismic data (*Dubrule*, 2003). The same parameters as in a standard geostatistical study, such as variograms etc. can be utilized to constrain the model. That allows to integrate geological principles, well log and core data, as well as seismic amplitude information. Petrophysical properties can then be obtained by joint simulation of e.g. lithology and AI or porosity and AI.

The relationships between the elastic properties and the petrophysical properties, e.g. AI - porosity relations are crucial for a joint approach. Such relationships can be obtained by analysing log data with rock physics modelling. The next section focuses on elastic property - porosity relationships and illustrates the importance of the dry rock and solid grain material compressibilities for fluid substitution modelling.

4.2 Elastic property - porosity relationships

Feasibility analysis of seismic monitoring of CO_2 sequestration involves modelling changes of elastic properties of rocks caused by saturation effects. To estimate the changes in elastic properties by CO_2 saturation effects from reservoir simulations, the simulation grid has to be populated with elastic properties. It is crucial to populate the reservoir simulation grid with a consistent set of parameters, includ-

ing velocities of the rock saturated with in-situ fluids and porosity as well as the bulk modulus of the dry rock and solid grain material. In order to achieve this, relations between the different rock properties have to be established. In this section, we test and compare two different workflows designed to establish such relationships on the data example of the Paaratte formation (CO2CRC Otway project). One relies on statistical correlations between parameters and the other, on deterministic rock physics modelling. The prediction of changes in elastic properties in both methods is based on the Biot-Gassmann theory (*Gassmann*, 1951) which describes the dependence of velocities on saturating fluid properties.

Elastic property - porosity trends of the reservoir can vary considerably, depending on lithology, mineralogy and diagenesis (*Avseth et al.*, 2005). The Paaratte formation comprises heterogeneous reservoir sections that vary from clean, high porosity sandstone to shaly sandstone; the former often hosting stiff intervals strongly cemented by diagenesis. These reservoir sections are interspersed with shale layers, which act as possible flow barriers for the injected CO_2/CH_4 (*Dance et al.*, 2012). The first perforation interval is a thin 7 m high porosity clean sandstone interval. The second perforation interval is much more heterogeneous with a thickness of approximately 15 - 20 m (Figures 4.7 and 4.8). In such a reservoir, the seismic sensitivity to changes in pore fluids can vary significantly.

Five key geological facies are identified in the lower Paaratte formation (*Dance et al.*, 2012):

- Distal mouthbar (DM) and delta front (DF): shales
- Proximal mouthbar (PM) and distributary channel (DC): clean sandstone to shaly sandstone
- Cements (CM): cemented by diagenesis

These three groups exhibit distinct elastic property - porosity trends, shown in Figure 4.6. The gentle P-wave modulus porosity trend of the sandstones (proximal mouthbar and distributary channel) is characteristic of variations in sorting

and clay content. Much steeper trends are representative of porosity variations controlled by diagenesis; such behaviour can be found for the cement facies.

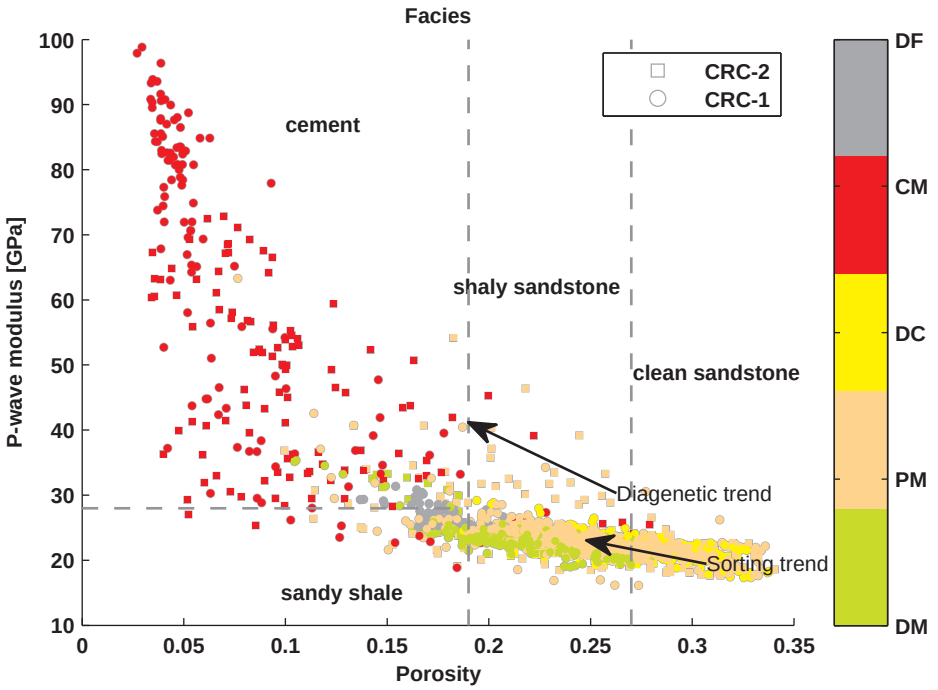

Figure 4.6: Crossplot of P-wave modulus against porosity for the log data shown in Figure 4.7 and 4.8. Colour-codes are the different geological facies.

To capture the observed trends in an elastic model, two different approaches to populate the static geological model with elastic properties are tested. The first approach is based on geostatistical interpolation (collocated cokriging). The second approach is based on deterministic rock physics modelling. The advantage of the geostatistical method is that the trends and the variability of the log data can be captured. In contrast, deterministic rock physics modelling relies on the data trends. The purpose of rock physics modelling in this study is to gain a better understanding of the physical properties of the reservoir, such as the compressibility of the dry rock frame and the solid grain material. These two parameters are crucial to estimate the effect of fluid saturation on elastic properties of rocks, and hence to predict the time lapse seismic response as accurately as possible. Figures 4.7 and 4.8 display the log data (P-wave velocity, S-wave velocity, density and porosity) from the wells CRC-1 and CRC-2 on which the elastic models are based. In the following, we analyse the second perforation zone.

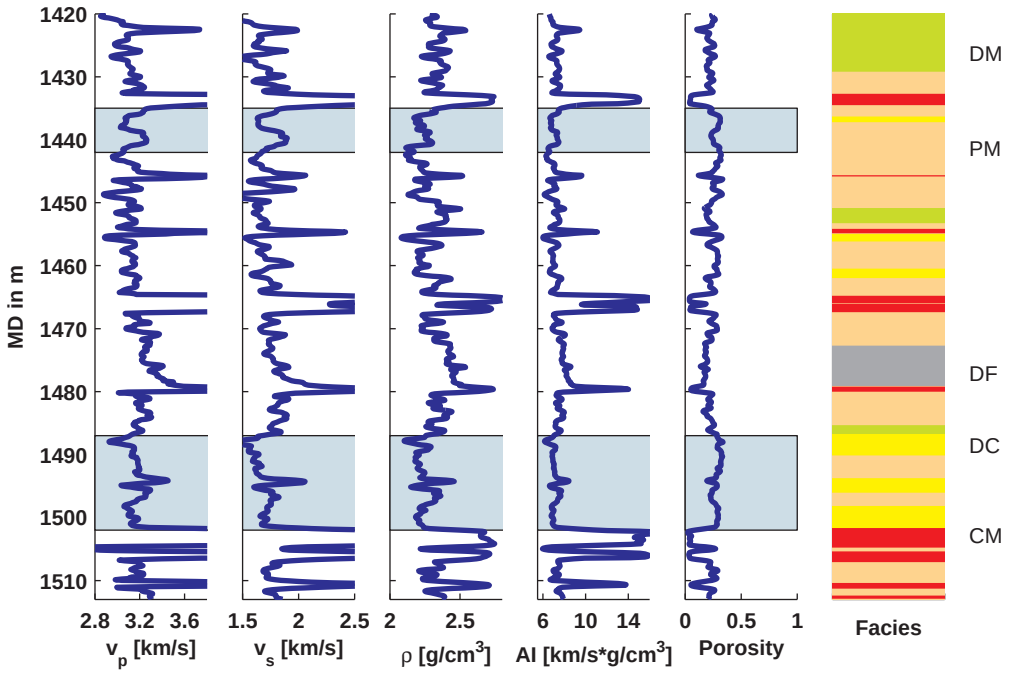

Figure 4.7: CRC-1 log data: P-wave velocity, S-wave velocity, AI, density, porosity and geological facies. Blue marked areas show the perforation intervals.

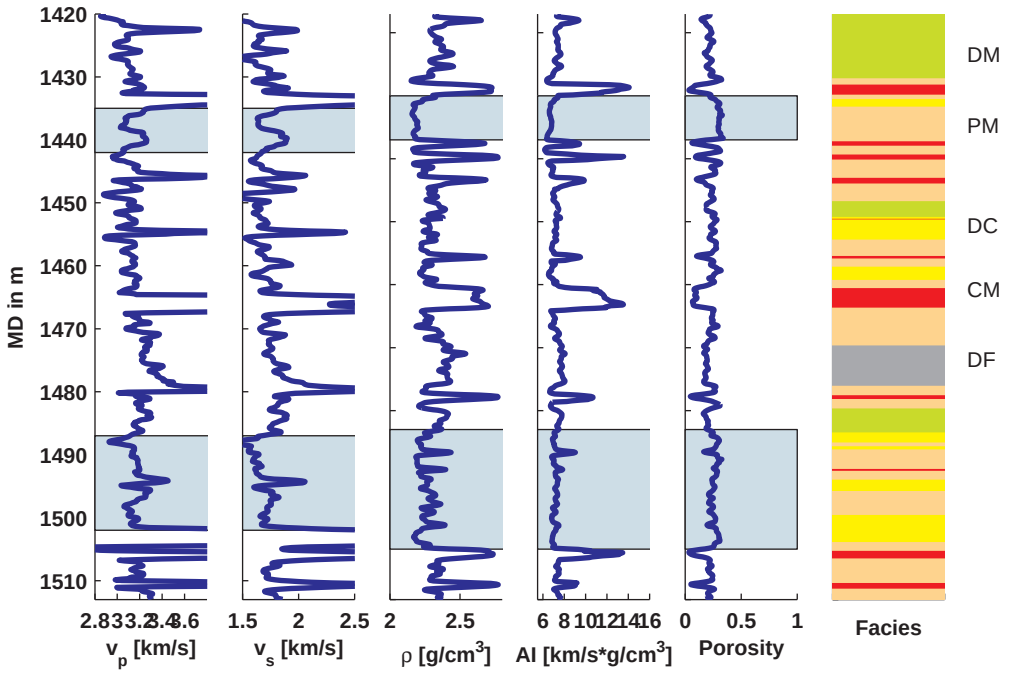

Figure 4.8: CRC-2 log data: P-wave velocity, S-wave velocity, AI density, porosity and geological facies. Blue marked areas show the perforation intervals.

4.2.1 Geostatistical modelling

In order to assign P-wave and S-wave velocities to each cell of the static geological model, we interpolate and extrapolate the well data of CRC-1 and CRC-2 by collocated cokriging using the Petrel© software package. Since the interest is a velocity model that is consistent with the porosity of the static geologic model, porosity is used as a guide for the interpolation. The underlying assumption is that porosity and velocity are correlated with each other (in a linear manner). Given that the different facies are characterised by distinct velocity - porosity trends, the correlation process is performed for each facies separately. More precisely, for each facies, a correlation coefficient between porosity and velocity is estimated from upscaled well logs. The spatial variation of velocities in the 3D model is defined by variograms of the static geological model. Then, away from the wells, velocities are estimated using velocity information at well locations incorporating porosity information at other locations (spatial distribution) and the correlation between both variables.

In Figure 4.9, the final porosity - acoustic impedance trend of the 3D model is compared to the log data. The 3D velocity model reproduces the log data quite well, except for the high porosities of the cement facies. A possible reason is, that not enough data points were available for the correlation process to capture the trend of the high porosities of the cement facies adequately after upscaling the log data. Therefore, we exclude the cement facies from fluid substitution modelling. This is a reasonable approximation since the expected changes in elastic properties of the cement facies due to CO_2/CH_4 injection, are small. This is because first, it is not likely that the gas will enter the pore-space (low permeability) and second, the porosity is low and the rock is very stiff (low sensitivity to fluid changes).

Calculation of post-injection velocities from the 3D velocity model using Gassmann's fluid substitution workflow requires additional elastic parameters. The dry compressibility of the rock frame is obtained from the 3D velocity model by solving the inverse Gassmann equation. This, in turn, involves knowledge of the solid grain material. Given that the considered perforation intervals vary from

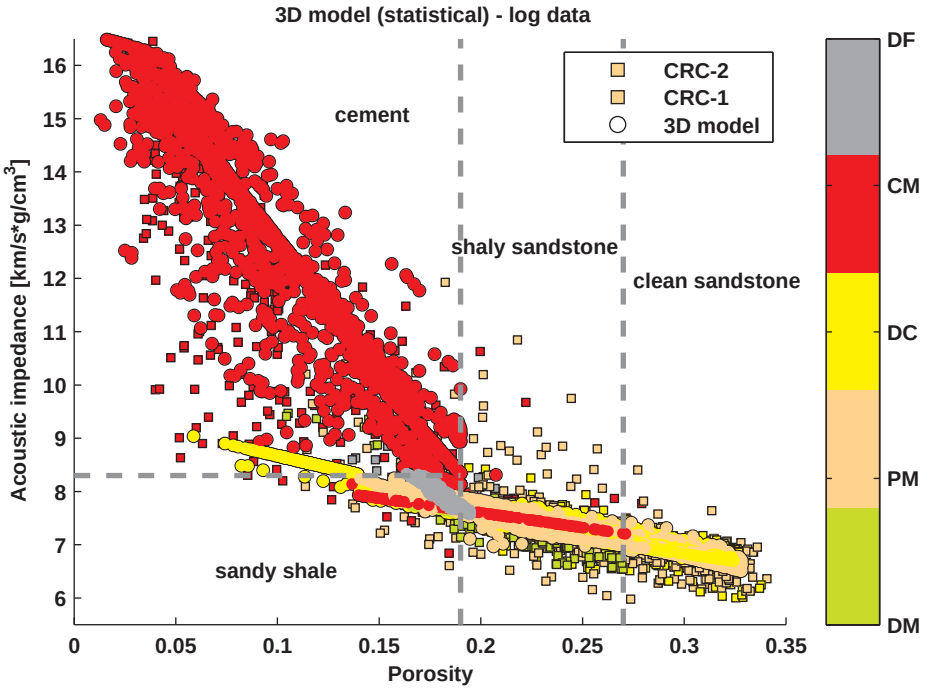

Figure 4.9: AI vs. porosity crossplot Comparison of log data (circle) and computed values for the static geological model (squares).

clean high porosity sandstone to shaly sandstone, the rock matrix is assumed to be a composite of clay and quartz. The effective properties of the composite material are calculated by an average of upper and lower Hashin-Shtrikman bounds. A principle problem is the estimation of elastic properties of clay, which can vary significantly. For the current workflow, literature values for wet porous clay are used (Table 4.1). The effect of clay and its properties are investigated in more detail in the next section. The clay content in each cell of the simulation grid is estimated by an empirical porosity - clay relation obtained from the log data (Figure 4.10):

$$V_{clay} = -2.36\phi + 0.84\,.$$

Alternatively, net to gross estimations from the geological model can be used if available. The density of the rock is directly calculated from the porosity values assuming a matrix density of $2.72\,\mathrm{g/cm^3}$ and a brine density of $0.9876\,\mathrm{g/cm^3}$ (before injection of CO_2/CH_4).

Table 4.1: Petrophysical input parameters

Geostatistical model			
Rock properties	K_g (GPa)	G_g (GPa)	ρ_g (g/cm^3)
Quartz*	37	44	2.72
Clay*	11.3	3	2.72

* literature value *Mavko et al.* (1998)

4.2.2 Deterministic rock physics modelling

Three different rock physics models are calibrated to the log data of the CRC-1 and CRC-2 wells for the key facies in the lower Paaratte formation. The rock physics models are chosen to reflect the main trends of the log data and to be consistent with the Biot-Gassmann theory of poroelasticity, while having a minimum number of input parameters.

The main focus of the rock physics modelling is to gain a better understanding of the compressibilities of the dry rock frame and grain material. In principle, the compressibility of the dry rock can be obtained from well-log velocity data using the inverse Gassmann equation. However, this involves information about the elastic properties of the solid grain material which are difficult to estimate and can vary significantly in sand-shale environments. Consequently, models that provide an explicit relationship between the elastic properties of the dry and saturated rock, the components of the solid grain material and pore fluid are desirable, so that unknown parameters can be calibrated with the log data in a consistent manner. The calibration process for the following rock physic models is based on simple least square fitting:

$$S = \frac{1}{N}\sum_{i=1}^{N}(m_i - d_i)^2\,,$$

where m_i are the calculated moduli and d_i the measured values from the log data. No weighting functions are used; however, the parameter ranges are constrained to make the fitting process more stable.

Another aspect that plays a role in clay rich rocks is the effect of clay in the rock matrix on fluid substitution modelling. A basic assumption of Gassmann's

equation is that pore pressure variations, induced by propagating seismic waves, are equilibrated throughout the rock. This might be violated in clay rich rocks since bound water in clays is immobile and thus, it might not be in equilibrium with the rest of the pore space (*Carcione et al.*, 2000). To overcome this problem, we utilize the fluid substitution scheme of *Dvorkin et al.* (2007). This workflow is based on the concept of effective rather than total porosity. Effective porosity considers only the pore volume which is accessible to injected fluids and thus makes Gassmann's equation applicable to shaley sediments.

A challenge for rock physics modelling are the cement layers, since they cover a wide range of velocities and porosities. These varying properties are analysed in more detail and a rock physics model reproducing a part of the steep diagenetic trend is proposed.

Clean sandstone to shaly sandstone

Comparing the log data for the proximal mouthbar and distributary channel facies to known effective medium models for unconsolidated sandstone (*Dvorkin and Nur*, 1996) and quartz contact cemented sandstones (*Dvorkin et al.*, 1994) shows that the data points fall between these two trends (Figure 4.11). One possible explanation is that some grain contacts are cemented in the sandstone and further porosity reduction occurred due to clay filling up the pore space. The later mechanism is in agreement with the porosity - clay trend of the log data (Figure 4.10) where total porosity linearly decreases with increasing clay content, while the P-wave velocity increases. *Marion et al.* (1992) report such a dependence of porosity, clay and P-wave velocity for the transition from clean sandstone to shaly sandstone and explain the data trend by clay progressively filling up the pore space of the clean sandstone.

To model these observations, we employ the contact cement model (CCT) with clay as contact cement. To take into account the clay content in fluid substitution modelling, the CCT model is combined with the fluid substitution scheme in shaly sediments (*Dvorkin et al.*, 2007). This fluid substitution method

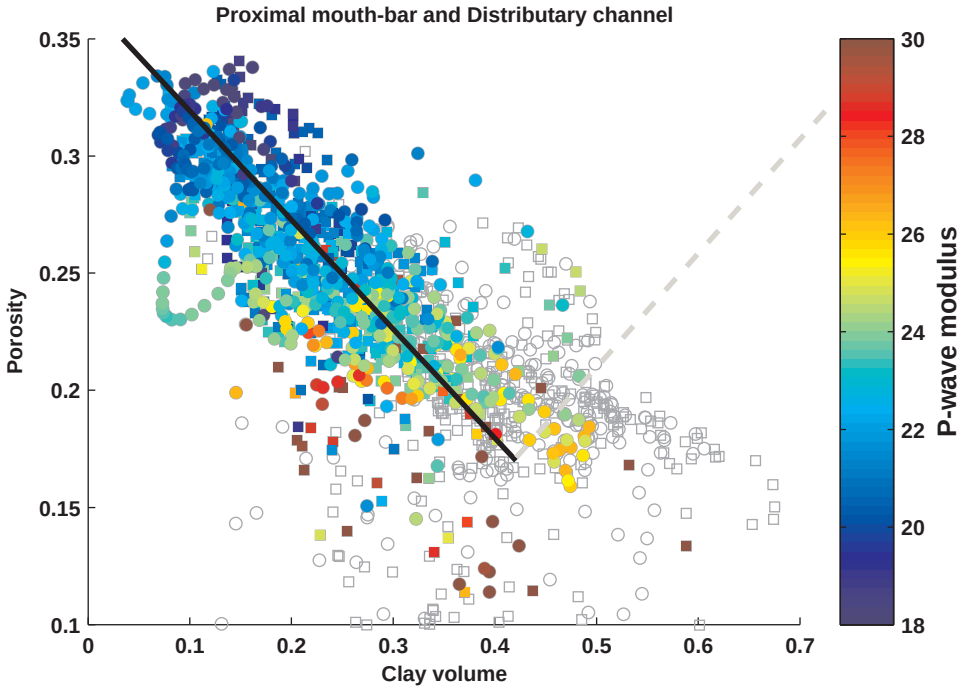

Figure 4.10: Clay volume vs. porosity crossplot: The black line provides the linear porosity - clay relation for the proximal mouthbar and distributary channel facies and the dashed grey line indicates the theoretical trend of sandy shales. Colour code is the P-wave modulus.

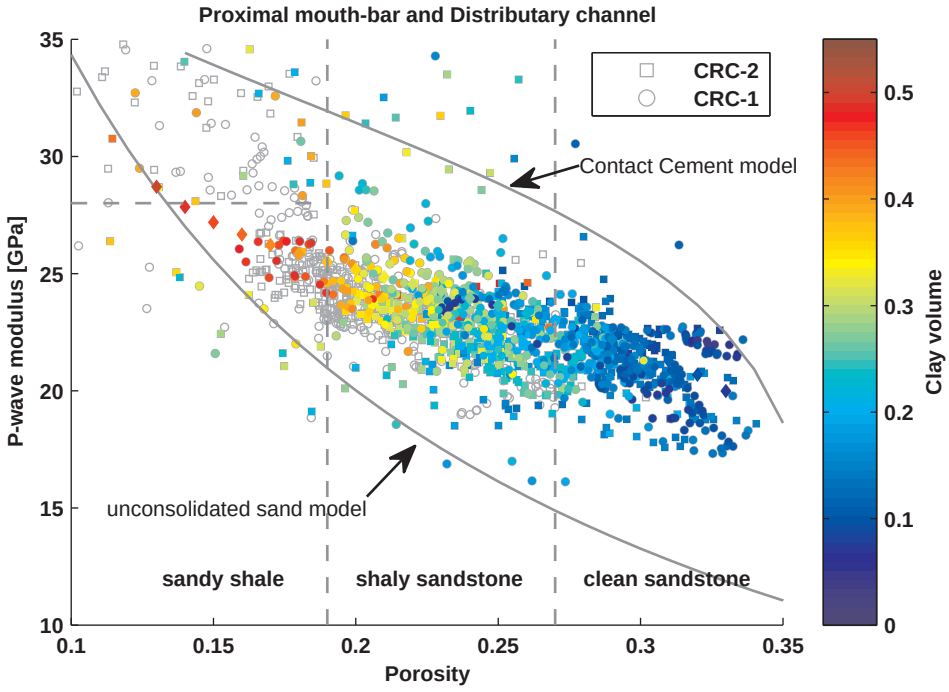

Figure 4.11: P-wave modulus vs porosity crossplot: Comparison of log data with the unconsolidated sand and contact cement model. Colour code is the clay volume.

assumes wet porous clay to be part of the solid grain material.

The conceptual idea of the combined rock physics model is illustrated in Figure 4.12. The starting framework, which defines the initial matrix of the dry rock, is a random pack of spherical quartz grains. The total porosity reduces from the initial porosity of the rock through deposition of clay cement at grain contacts, in which clay forms a layer around each quartz grain and the contact points of the layers are defined as contact cement (*Mavko et al.*, 1998). The contact cementation causes an increase of the effective elastic rock properties. To incorporate the fluid substitution method in the CCT model, we assume that the cement is wet porous clay and builds a part of the dry rock matrix. Hence, the porosity within the clay is excluded from the total porosity, so that the porosity accessible for the injected fluid is the effective porosity. This, in turn, means that the model is only applicable until the wet porous clay fills up the whole pore space of the initial clean sand.

The effective moduli of the CCT model (Eq. (2.22)) are given by

$$K^*_{CCT} = \frac{1}{6}C(1-\phi_c)H_{clay}\hat{\tau_n}$$
$$G^*_{CCT} = \frac{3}{5}K^*_{CCT} + \frac{3}{20}C(1-\phi_c)G_{clay}\hat{\tau_t}\,,$$

where H_c and G_c are now the P-wave and shear wave modulus of the wet porous clay and ϕ_c is the initial porosity of the dry sand pack without clay. The parameters $\hat{\tau_n}$ and $\hat{\tau_t}$ are proportional to stiffnesses of the cemented grain contact and given by the following expressions:

$$\hat{\tau_n} = a_n\alpha^2 + b_n\alpha + c_n\,,$$
$$\hat{\tau_t} = a_t\alpha^2 + b_t\alpha + c_t\,.$$

The coefficients a_n, b_n, c_n, a_t, b_t and c_t are given in Eqs. (2.23) and (2.24). The amount of clay α can be related to the reduction of porosity by assuming a certain deposition scheme. If the clay forms a layer around the grain mineral, α can be

written as

$$\alpha = \sqrt{\frac{2(\phi_c - \phi_e)}{3(1-\phi_c)}}\,,$$

where ϕ_e is the effective porosity of the pore-space. The effective porosity is the porosity accessible to the injected fluid and is given by

$$\phi_e = \phi - f_{clay}\phi_{clay}\frac{1-\phi}{1-\phi_{clay}}\,.$$

The parameter f_{clay} denotes the volume fraction of the clay mineral in the solid matrix and ϕ_{clay} is the porosity within the clay. The effective modulus K^*_{CCT} is the dry bulk modulus of the rock with wet porous clay as cement. This modulus can be inserted in Gassmann's equation for shaly sediments (Eq. 2.41).

$$K^*_{\phi_e} = K^*_{CCT}(K^*_s, \phi_e) + \alpha(K^*_s)^2 M \quad \text{with} \quad M = \left(\frac{\alpha(K^*_s) - \phi_e}{K^*_s} + \frac{\phi_e}{K^*_f}\right)^{-1}\,.$$

The effective modulus of the solid material K^*_s is obtained by the lower Hashin-Shtrikman bound

$$K^*_s = \left(\frac{f_{Pclay}}{K_{clay}+G_{clay}} + \frac{1-f_{Pclay}}{K_g+G_{clay}}\right)^{-1} - \frac{4}{3}G_{clay}\,,$$

where f_{Pclay} is the volume fraction of the wet porous clay in the solid matrix (Eq. (2.40)). The effective fluid modulus using Wood's mixing rule is

$$K^*_f = \left(\frac{S_{gas}}{K_{gas}} + \frac{1-S_{gas}}{K_{brine}}\right)^{-1} \quad \text{with} \quad S_{gas} = \frac{\phi(1-S_{brine})}{\phi_e}\,.$$

The cement or equivalently clay volume is estimated from the total porosity using an empirical relationship (black line in Figure 4.10), given by

$$f_{clay} = -2.14\phi + 0.78\,.$$

Other input parameters are the grain and wet clay properties (bulk and shear modulus), the intrinsic porosity of the clay and the coordination number of the

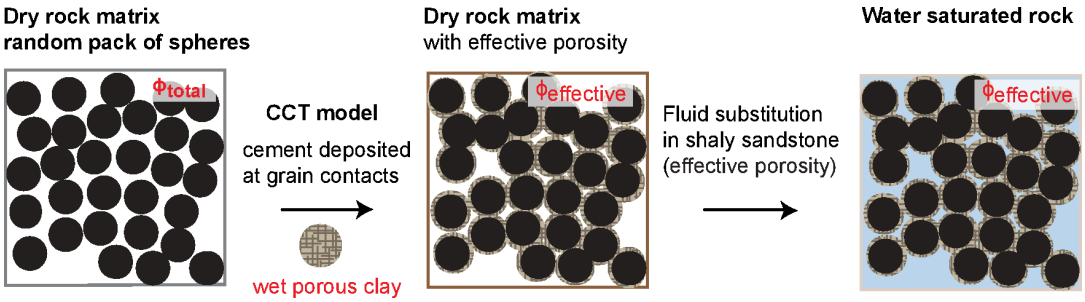

Figure 4.12: Conceptual illustration of the combined rock physics model: Contact cement model (CCT) and fluid substitution in shaly sediments.

initial dry rock. The grain material of the clean sand is assumed to be pure quartz and the intrinsic porosity of the clay is approximated from clay bound water estimations. Wet clay properties and the coordination number are fitting parameters. The coordination number gives the average number of contacts of a grain with its surrounding grains. The higher the coordination number, the stiffer the dry rock frame. Four different trends are fitted to the log data with varying coordination numbers.

Note that the fitted coordination numbers (C=5.2-7) have quite low values which might be unrealistic for cemented sandstone. It was not possible to fit the data with higher coordination numbers in the combined approach of the CCT model and fluid substitution in shaly sediments. However, *Makse et al.* (2004) report in experiments with glass beads and computer simulation that such low numbers are possible under certain conditions. Further, the data plots above the unconsolidated sand model for the whole range of reasonable coordination numbers (5 - 9) for unconsolidated sediments. All final values are listed in Table 4.2. For these parameters, clay fills up the effective pore space at a minimum total porosity of ∼13% and the predicted clay content reaches 50%. For smaller total porosities, the model breaks down and the water saturation becomes negative.

Figures 4.13, 4.14 and 4.15 compare the four fitted models for various properties with the log data (P-wave modulus, S-wave modulus as function of porosity and P-wave velocity as function of density). Colour code is the clay content of the log data and the predicted clay content of the rock physics model. The

Table 4.2: Petrophysical input parameters

Proximal mouthbar & distributary channel: CCT model + fluid sub. in shaly sediments			
Rock properties	K_g (GPa)	G_g (GPa)	intrinsic porosity
Quartz	37*	44*	
Clay	11.4	5.32	0.2
	Initial porosity	Coordination number	Shear reduction num.
CCT model	0.38	5.7, 6	0.7

* literature value *Mavko et al.* (1998)

rock physics model explains the elastic property - porosity trends and fit the clay content of the log data quite well. In Figure 4.15 the two black lines are Gardner's empirical velocity - density relations (*Gardner et al.*, 1974) for sandstone and shale. A single empirical relation cannot describe the density variations of the log data. This is because the data shows a transition from clean sandstone to shaly sandstone. However, for a fixed clay content the increase in density and velocity is broadly consistent with Gardner's relation.

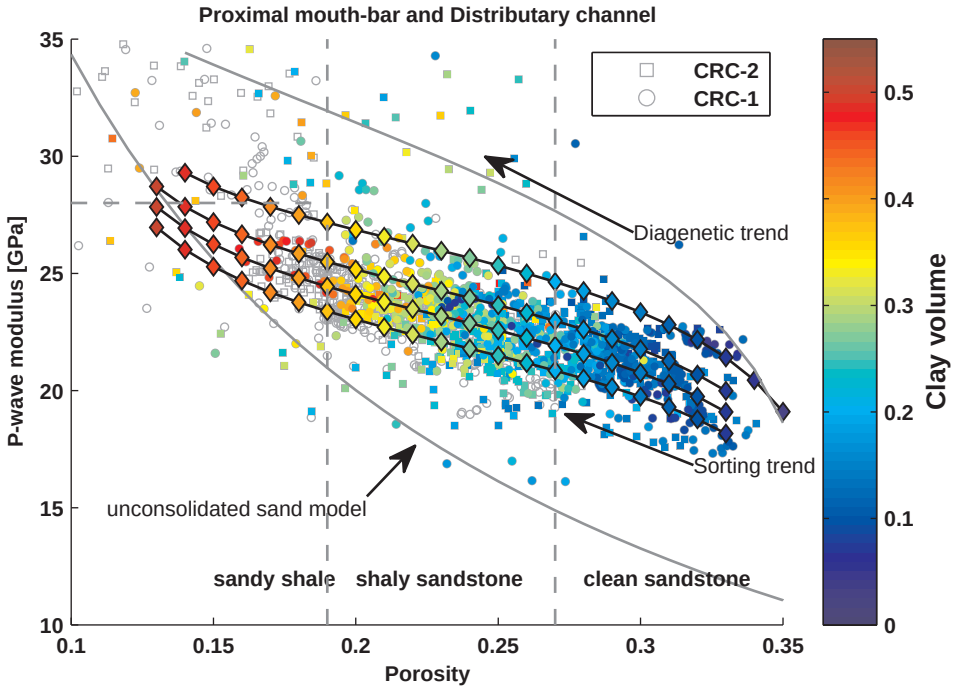

Figure 4.13: Comparison of P-wave modulus - porosity crossplot (log data) with rock physics model predictions. Black lines denote the fitted models with increasing coordination number from bottom to top and the coloured diamonds indicate the predicted clay volume. Coloured squares and circles show the clay volume for the log data of the wells CRC-1 and CRC-2, respectively.

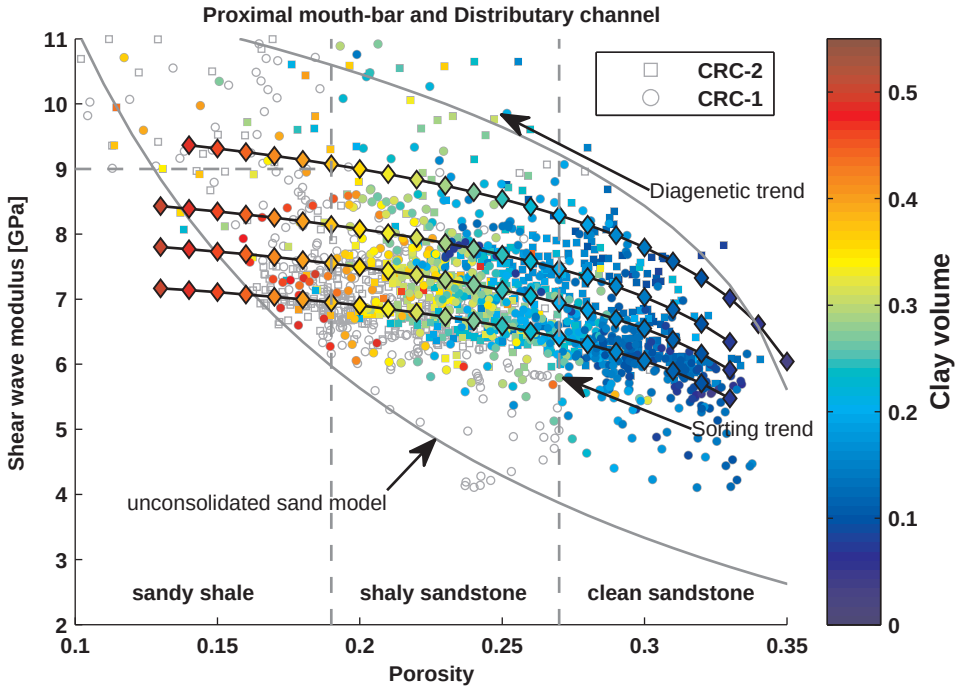

Figure 4.14: Comparison of S-wave modulus - porosity crossplot (log data) with rock physics model predictions.

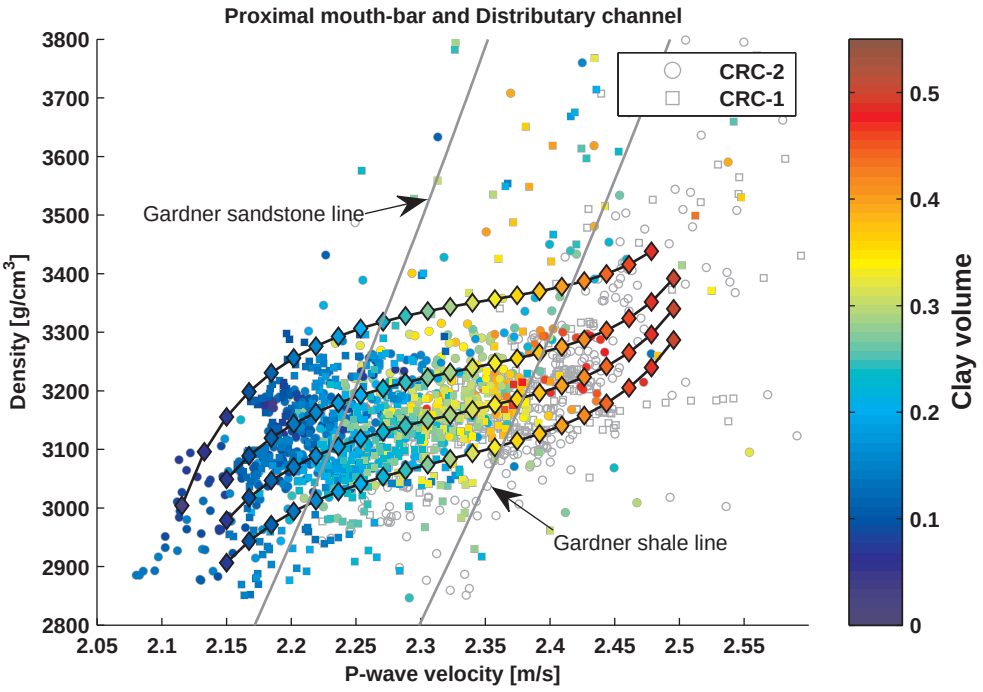

Figure 4.15: Comparison P-wave velocity - density crossplot (log data) with rock physics model predictions and standard empirical relations.

Validation of the rock physics model with laboratory measurements

A crucial parameter for time-lapse studies is the compressibility of the dry rock frame since this parameter determines the sensitivity of the rock to fluid changes

within the pore space, e.g. replacing brine with CO_2/CH_4. To validate the calculated dry compressibility of the rock physics model, we compare the modelled dry properties to dry properties obtained from ultrasonic dry core measurements. Four core samples from the CRC-2 well, which are located in the reservoir sections of interest, have been measured. Samples 1 to 3 are classified as proximal mouthbar and distributary channel sandstones, while sample 4 is a cemented sandstone. The samples can be described as follows (*Lebedev et al.*, 2013):

Sample 1 (1442.1 m) consists of a homogeneous sandstone with only a few laminations parallel to the bedding plane. This highly porous and permeable sandstone contains well sorted, fine to medium, rounded grains of predominately quartz, minor feldspar and mica matrix with kaolinite and chlorite clay as weak cement.

Sample 2 (1500.83 m) is a fine-grained and well-sorted quartz sandstone, but with the occasional mottled structure from bioturbation (sand filled burrows) and small quartz pebbles. It exhibits some gradational bedding and fine cross-bedded lamination.

Sample 3 (1509.6 m) contains a distinct wavy carbonaceous lamination within a medium- to very course-grained cross-stratified sandstone. Mica-rich clays and coaly flakes are common within the quartz, feldspar and sandstone matrix.

Sample 4 (1513.82 m) is of a cemented sandstone. The original fabric is a very fine to fine-grained clean quartz sandstone, but dolomite pervades throughout the pore space coating grains and reducing the porosity.

Ultrasonic compressional and shear wave velocities of the dry samples were measured at a temperature of 45°C and several confining pressures. For the comparison, we chose the measurements with effective pressures between 15 - 19 MPa as the effective pressure (difference between confining and pore pressure) of the Paaratte formation is approximately 17 MPa. Figure 4.16 compares the dry bulk modulus, dry P-wave modulus, S-wave modulus and v_p/v_s ratio from the measurement of the core samples with calculated values of the rock physics models for

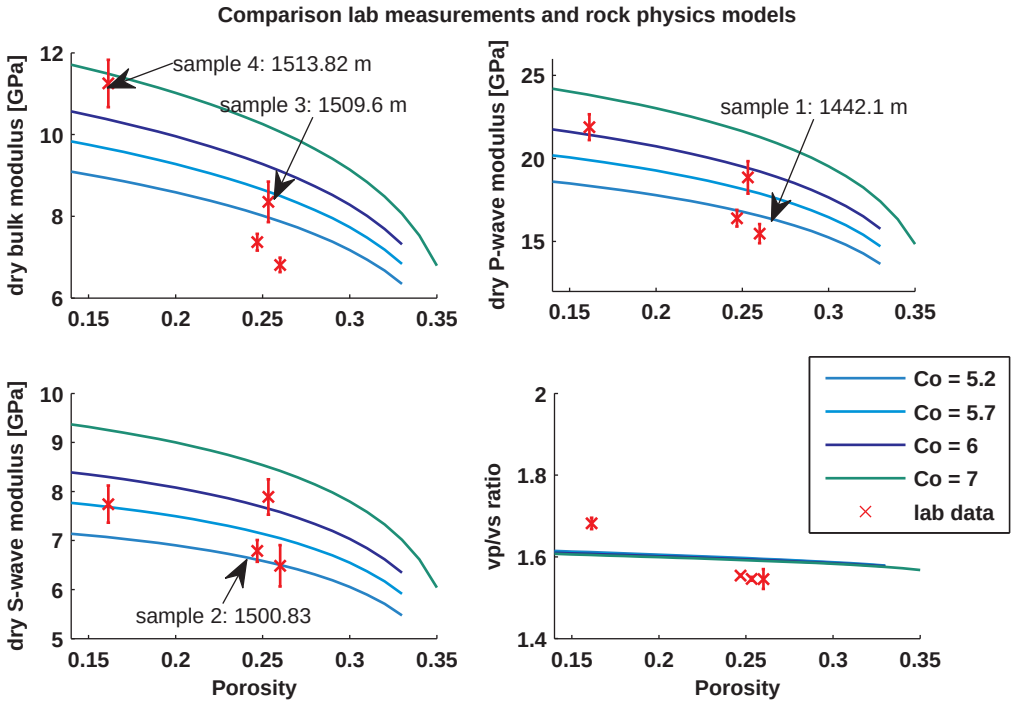

Figure 4.16: Comparison of dry properties obtained from ultrasonic core measurements (red crosses) and predicted dry property trends from rock physics modelling (lines) for different coordination numbers.

different coordination numbers. The computed dry bulk moduli are higher than the measured values for sample 1 and 2, while the bulk modulus of sample 3 is in the same range as the predicted values. The calculated dry P- and S-wave moduli of sample 1 and 2 fit the laboratory data better. There might be several reasons for this behaviour. One aspect is that the v_p/v_s ratio of the lab measurements for samples 1 - 3 is lower and for sample 4 higher than in the predicted data trends. This, in turn, can cause the mismatch between the different moduli.

For the final 3D elastic model, we use the rock physics models with coordination number 5.7 and 6. These models predict a stiffer rock than inferred from core measurements and thus predict a smaller response due to changes in fluid saturation. The dry measurements of the cemented sandstone can be fitted by models with different coordination lines for different elastic properties, but cannot be explained by one model. However, the dry bulk and P-wave moduli plot between the models with coordination number 6 and 7. Therefore, we choose to model grid cells that are classified as cement facies in the geological model and have porosities greater than 15%, with the trend corresponding to the coordination

number of 7.

Cement facies

The formation intervals classified as cement facies exhibit a wide range of elastic properties. Two clusters of data points can be identified in the elastic property-porosity crossplots (Figures 4.17 to 4.19). For the first cluster, the stiffness of the rock increases moderately with porosity reduction and follows roughly the trend of the shaly sandstones, while for the second cluster at porosities around 14% the stiffness of the rock increases considerably. Thin sections of this rock type reveal the pervasive nature of the carbonate (Calcite/Dolomite) cements (*Dance et al.*, 2012). An example is shown in Figure 4.20.

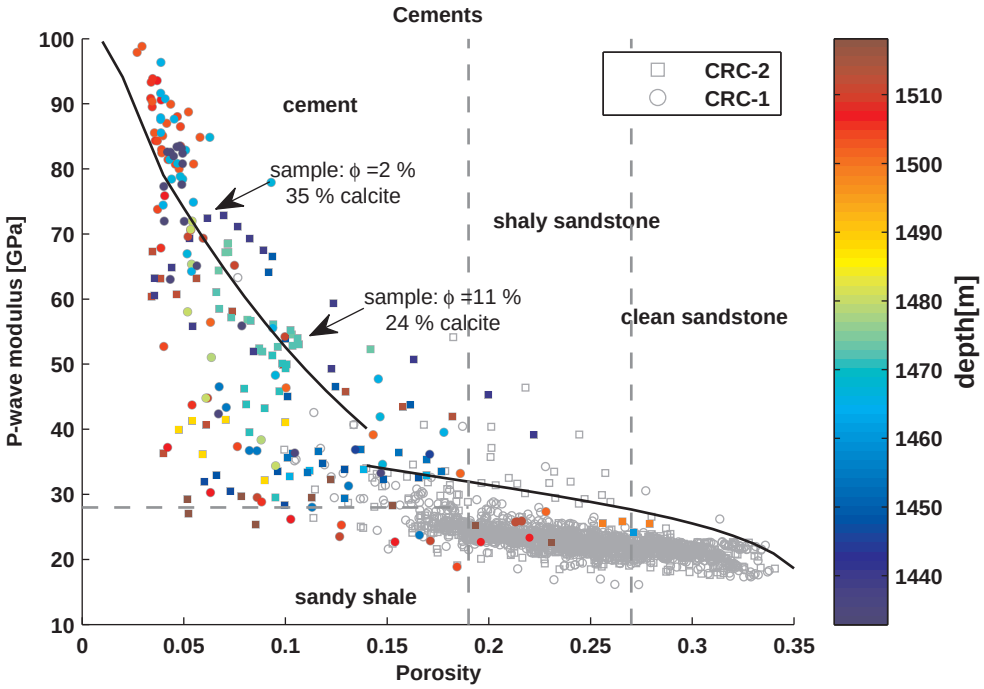

Figure 4.17: Comparison of P-wave modulus porosity crossplot (log data) with rock physics model predictions. Black lines denote the fitted models. In the porosity range from 14% - 35%, the black line correspond to the conceptual model shown in Figure 4.12 and the black line at lower porosities correspond to the cement model.

A single rock physics model cannot describe these two trends. Here, we choose a rock physics model that reflects the steep trend of the second data cluster. Such a steep trend is typical for porosity variations controlled by diagenesis (*Avseth et al.*, 2005), e.g. cementation. In order to model this trend, we utilize the

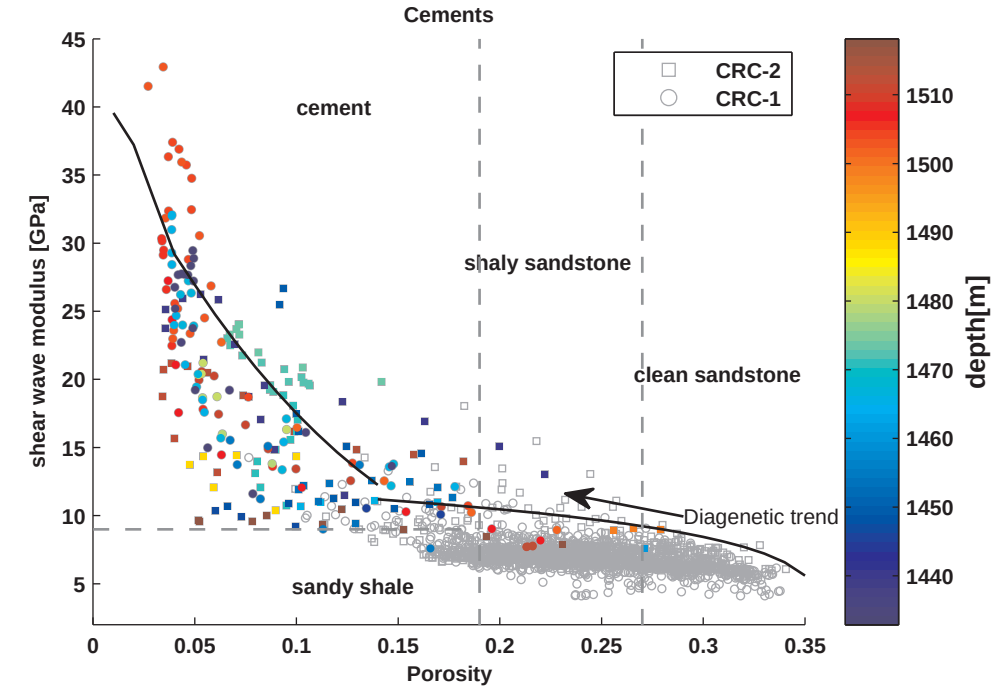

Figure 4.18: Comparison of S-wave modulus porosity crossplot (log data) with rock physics model predictions.

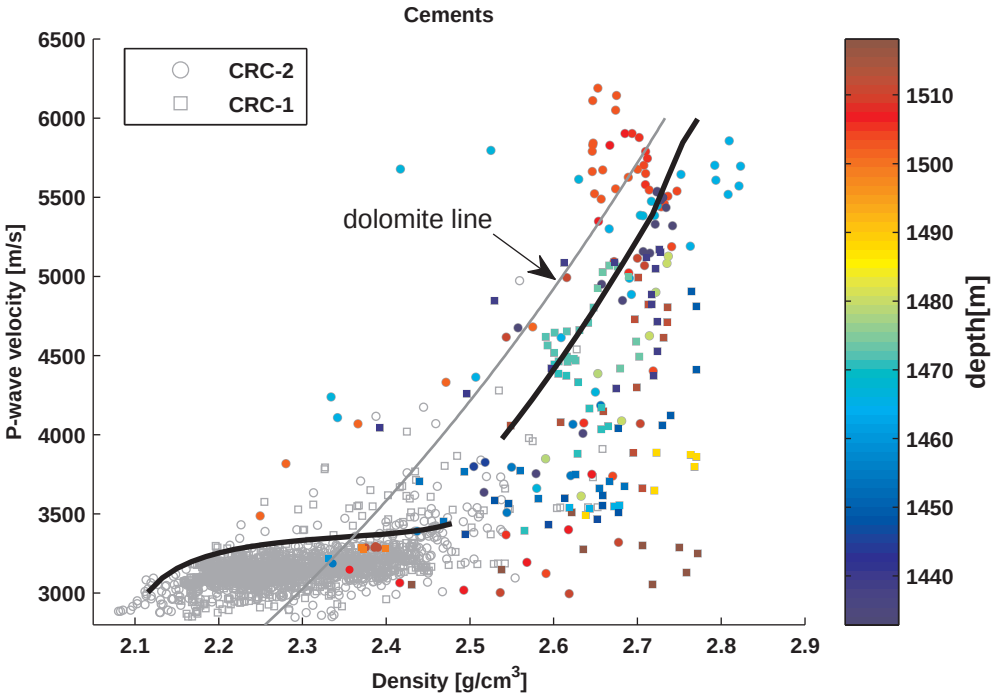

Figure 4.19: Comparison of P-wave velocity density crossplot (log data) with rock physics model predictions and standard empirical relations.

modified differential effective medium (DEM) theory with critical porosity constraints (*Mukerji et al.*, 1995). The DEM approach (Eq. (2.18)) can be thought of

as a physical analogue of incrementally embedding inclusions into a background medium (*Dræge et al.*, 2006). The process is as follows: we start with a background matrix (mineral point) consisting of 40% cement (calcite or dolomite) and 60% quartz and gradually embed inclusions of a second material until the desired material composition is reached. In each step, the effective properties of the composite medium are calculated and the background matrix for the next step is formed by the composite medium of the previous step. In this original DEM scheme, the initial background medium stays connected until 100% of the second material is reached. In contrast, in the modified approach, a critical porosity is introduced at which the medium consists completely of the second material. For material two or equivalently the inclusions, we choose a quartz contact cemented rock. To calculate the elastic properties of the inclusions we apply the CCT theory (Eq. (2.22)). The brine saturated rock properties are obtained by applying Gassmann's fluid substitution (Eq. (2.26)) in each step of the modelling. The conceptual model is illustrated in Figure 4.20. In principle, saturated inclusions could be embedded in the matrix in each step. However, the inclusions are isolated with respect to flow and do not account for pressure equilibration (*Mavko et al.*, 1998). This might be true at very low porosities or high frequencies, but does not explain the behaviour of the rock at moderate porosities and seismic frequencies. For porosities below 5% we embed inclusions which are water saturated as suggested in *Dræge et al.* (2006).

Input parameters are the properties of quartz and cement, the critical porosity of the DEM model and the coordination number of the CCT model. The critical porosity is set to 14%, where the transition from a moderate to a steep increase in elastic properties with a decrease in porosity can be observed. The cement properties and coordination number are fitting parameters and the final values are listed in Table 4.3. The fitted cement values are in the same range as literature values for calcite. To calculate the effective elastic properties of the initial background matrix (mineral point) we use the upper Hashin-Shtrikmann bound (Eq. (2.14)) which is the stiffest arrangement for an isotropic rock matrix.

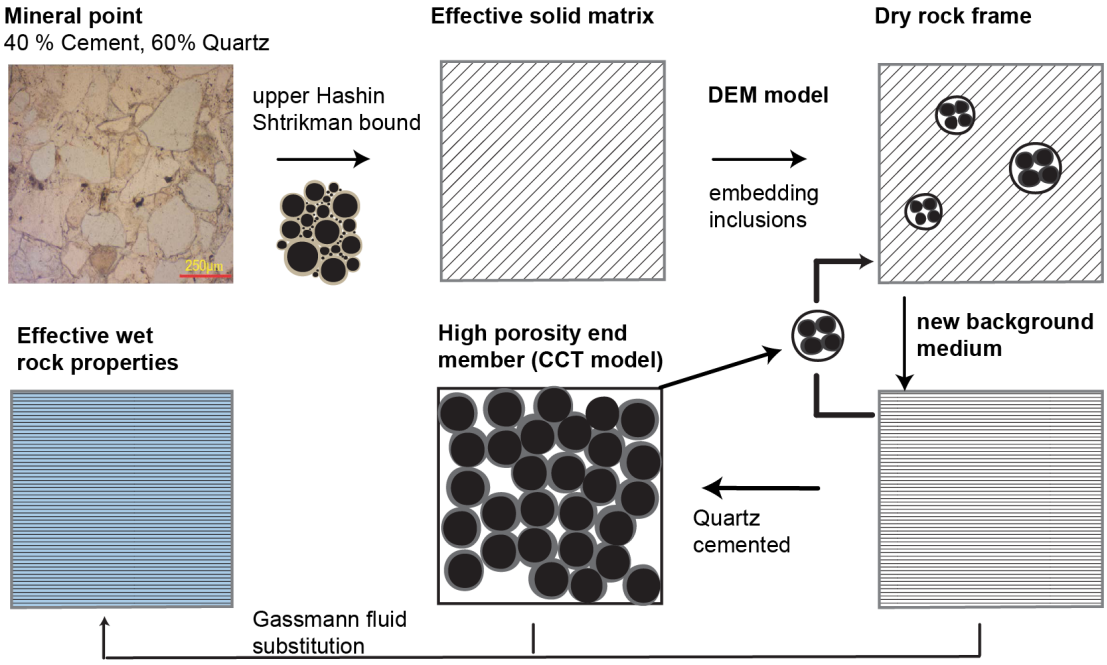

Figure 4.20: Conceptual illustration of the combined rock physics model: modified differential effective medium model and contact cement model.

Table 4.3: Petrophysical input parameters

Cement facies: Modified DEM + CCT model			
Rock properties	K_g (GPa)	G_g (GPa)	
Quartz	37*	44*	
Cement	75	35.32	
	Initial porosity	Coordination number	Shear reduction num.
CCT model	0.34	9.86	0.5

* literature value *Mavko et al.* (1998)

In Figures 4.17 - 4.19 the rock physics model is compared with the log data. For the P-wave modulus, the model captures the main trend of the data quite well. However, a problem is to fit a trend simultaneously to the same data points for the P-and S-wave modulus. This is due to the fact that shear and compressional data show a slightly different behaviour, with decreasing porosity. Nevertheless, since the crucial parameter is the acoustic impedance in our forward modelling, we did not investigate the problem further.

Shales

The shale layers are considered to act as possible flow barriers for the injected CO_2/CH_4. Therefore, we assume in our modelling that no changes in elastic properties due to gas injection will occur in these layers.

Table 4.4: Petrophysical input parameters

Distal mouthbar & delta front: VPC model			
Rock properties	K_g (GPa)	G_g (GPa)	Krief exponent
Quartz	37*	44*	3.2
Clay	18.5	7	

* literature value *Mavko et al.* (1998)

Given that these two facies possess only moderate clay contents (between 30% and 60%), we apply the semi-empirical velocity - porosity - clay model (*Goldberg and Gurevich*, 1998) which is suitable for sand-shale environments. In a first step, the effective properties of the solid grain material, consisting of clay and quartz, are calculated using the lower Hashin-Shtrikman bound (Eq. (2.15)). This corresponds to a composite medium in which clay is the load bearing material. The dry properties of the rock are obtained from the empirical relation of *Krief et al.* (1990), which is a function of the effective properties of the solid grain material (K_g) and porosity (ϕ), expressed as

$$K_d = K_g(1-\phi)^{m\phi}\,,$$

where m is an empirical constant. Finally, the saturated compressional and shear wave velocities are calculated using Gassmann's equation (Eq. (2.26)). The clay properties and the empirical coefficient in Krief's relation are fitting parameters (Table 4.4). Note that the clay properties differ from the previously obtained values for the proximal mouthbar and distributary channel facies. The reason is that in the latter approach, the properties are estimated for porous wet clay. Figure 4.21 to 4.23 demonstrate that the model fits the log data reasonably well.

Discussion

Before building the elastic model, we verify that the calibrated porosity - elastic property transforms are in agreement with the log data by plotting the predictions of all three rock physics models against the measured log data (Figures 4.24 and 4.25). Overall, the predicted P-wave velocities of the shale and sandstone facies show a reasonably good match with the observed velocities and confirm that the derived transforms do not systematically over- or underestimate the ob-

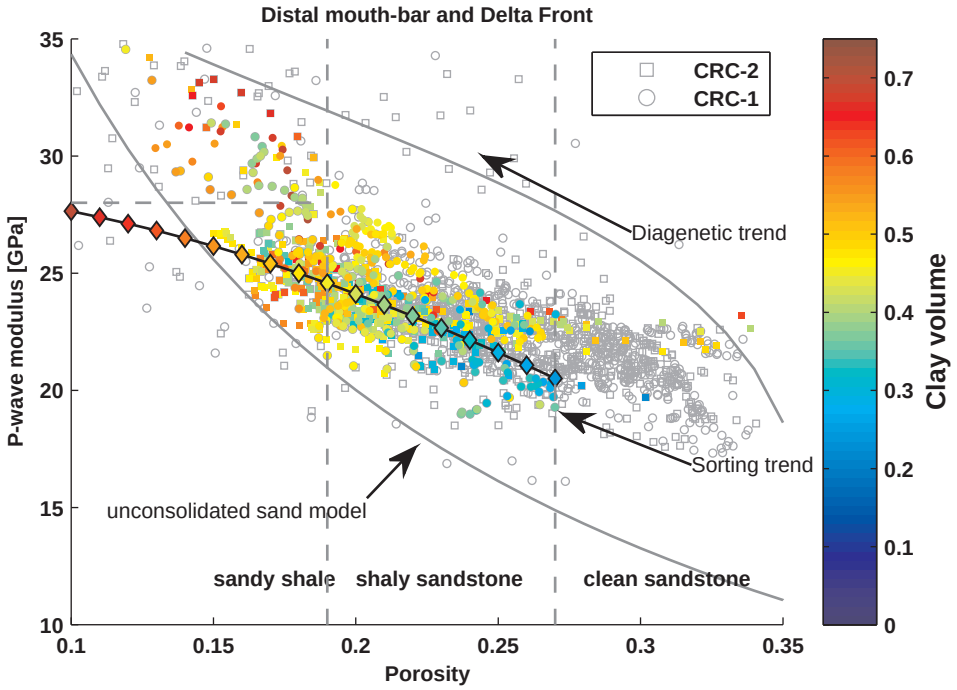

Figure 4.21: P-wave modulus - porosity crossplot (log data): The black line denotes the fitted rock physics model and the coloured diamonds indicate the predicted clay volume

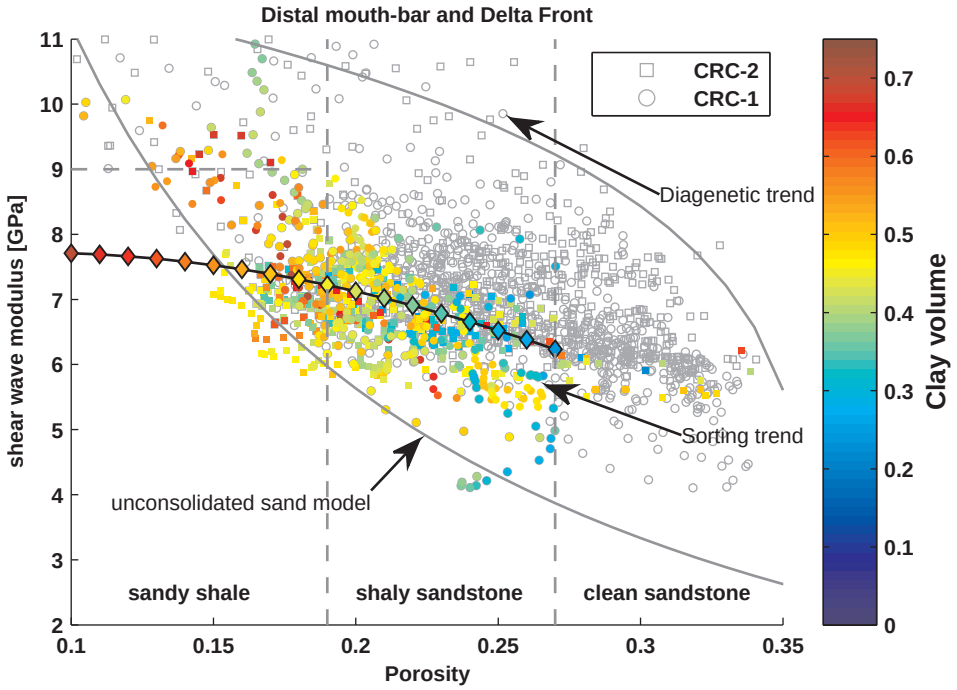

Figure 4.22: Comparison of S-wave modulus - porosity crossplot (log data) with rock physics model predictions.

served data. However, the variability of the clean and shaly sandstones is not captured by the corresponding rock physics model, since the elastic properties

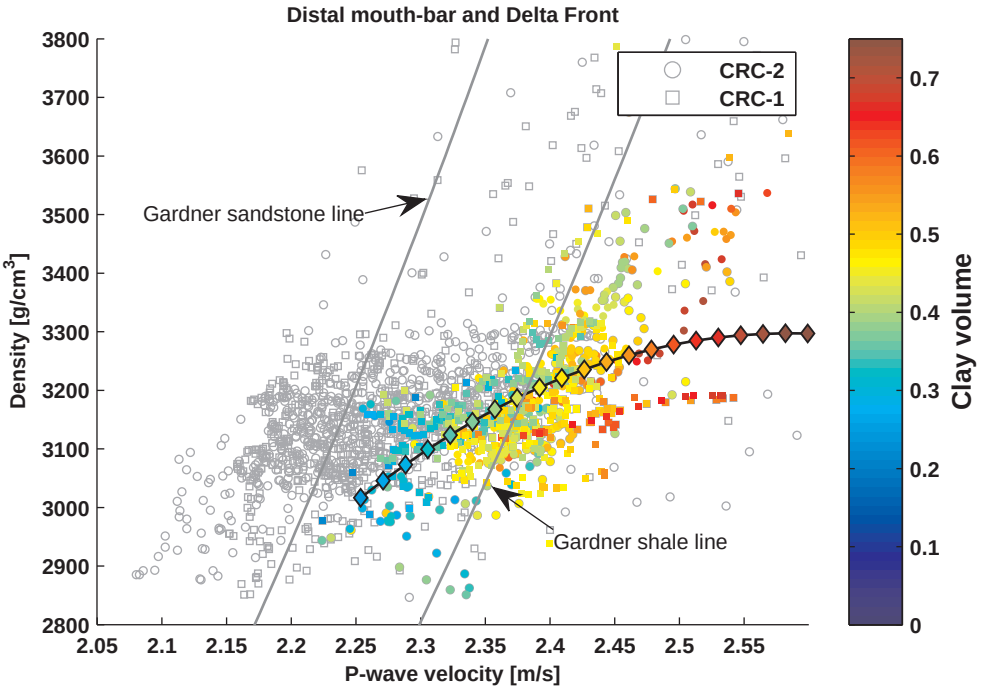

Figure 4.23: Comparison of P-wave velocity - density crossplot (log data) with rock physics model predictions and standard empirical relations.

are not only controlled by porosity reduction. Other factors that might play a role include different types of contact cement, different degrees of cementation or varying numbers of grain contacts. As shown in Figures 4.13, 4.14 and 4.15, the variability of the data could be modelled by varying the coordination numbers in the rock physics model. Nevertheless, given that the porosity is the only input parameter (from the static geological model) the variability of elastic properties at a certain porosity value, can only be taken into account in a statistical manner. As expected, the P-wave velocities of the cement facies are overestimated for several data points since we only tried to model the steep diagenetic trend of the data. The predicted density values are in good agreement with the measured values (Figure 4.25).

Finally, we apply the calibrated rock physics models to obtain the elastic properties for the static porosity model. All parameters are summarised in Table 4.5. A comparison of the computed acoustic impedance model for the base realisation of the geological model with the log data shows that the main data trends are captured in the 3D model, shown in Figure 4.26. This approach was employed

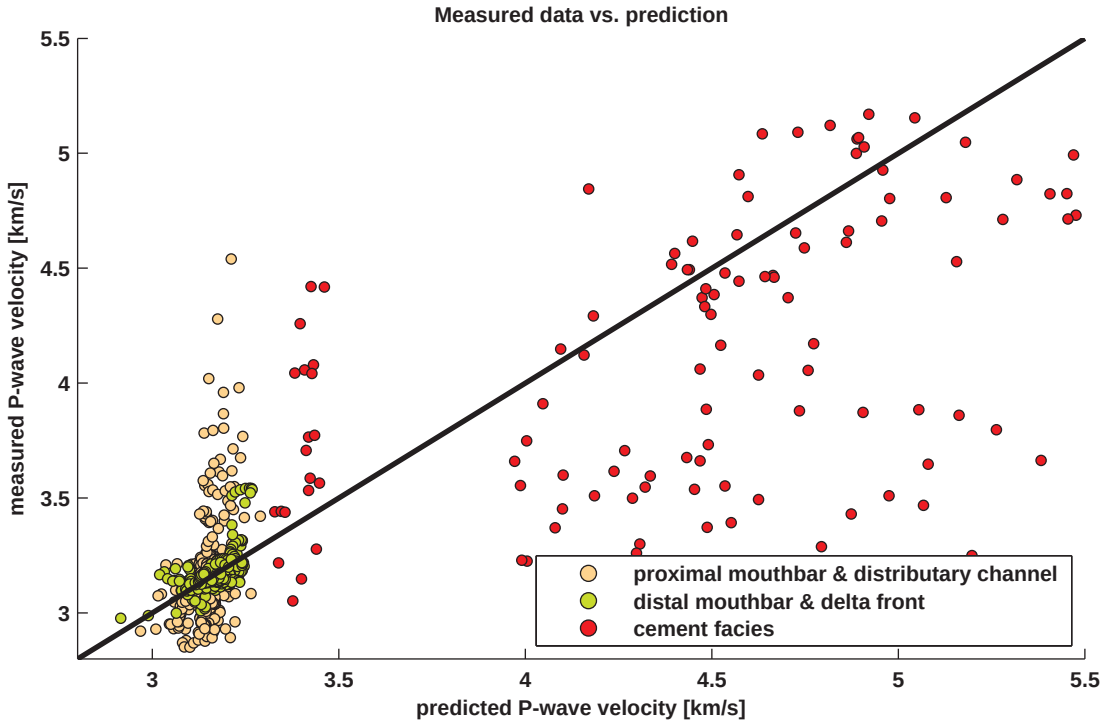

Figure 4.24: Predicted vs. measured P-wave velocity (log data).

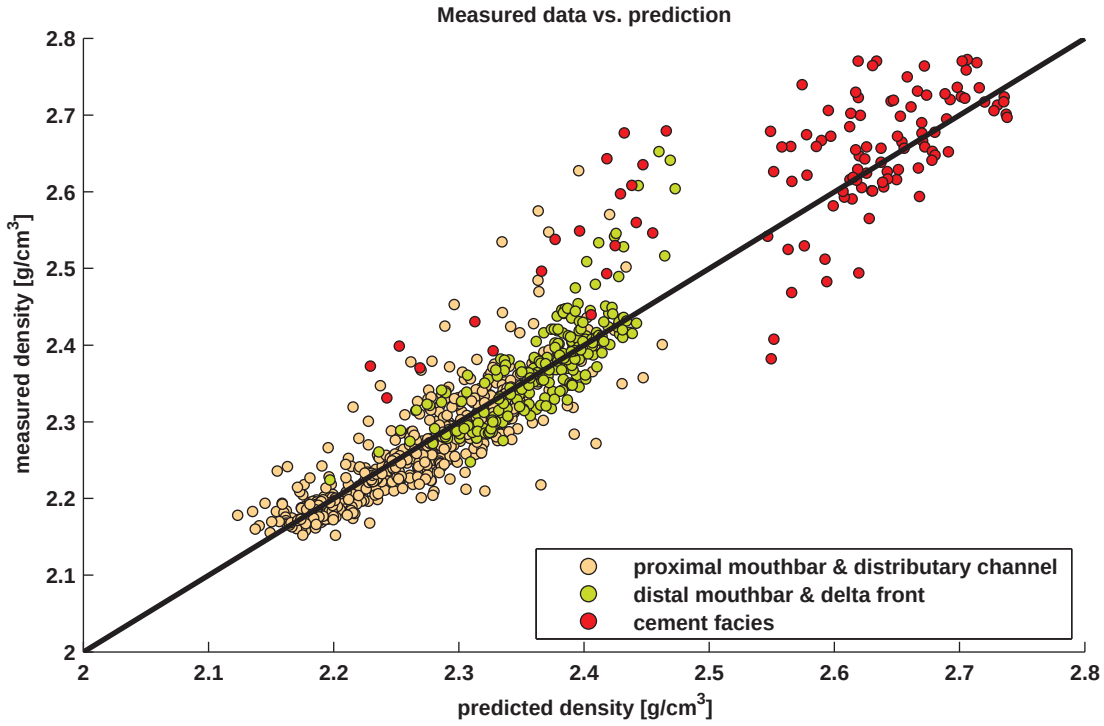

Figure 4.25: Predicted vs. measured density (log data).

in the previous chapter to compute the time-lapse acoustic impedance volumes, which were needed as input for the convolutional modelling.

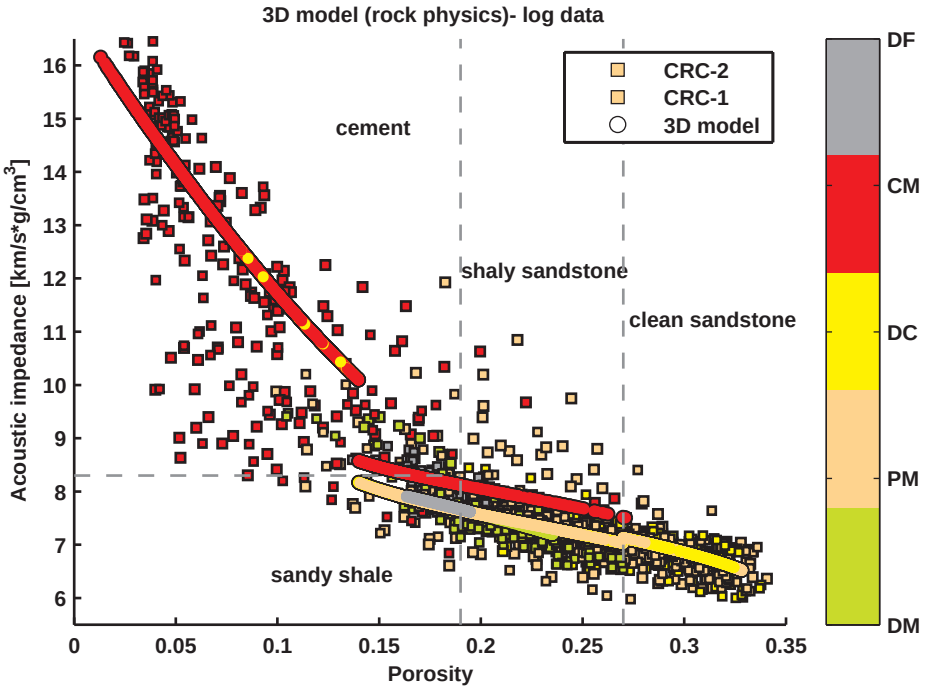

Figure 4.26: AI vs. porosity crossplot: Comparison of log data (circle/coloured thick lines) and computed values for the static geological model (squares).

4.2.3 Comparison of geostatistical and rock physics modelling

In the next step, the two 3D elastic models are compared regarding their predictions of changes in elastic properties caused by CO_2/CH_4 injection. For the geostatistical model and the cement facies of the rock physics model, we employ Gassmann's fluid substitution workflow. For the proximal mouthbar and distributary channel facies of the rock physics model, we apply the modified fluid substitution for shaly sediments. To assume realistic fluid saturations and properties, the flow simulation results for 30.000 t of injected CO_2/CH_4 at the end of injection are employed.

Figure 4.27 displays histograms of the computed relative changes in acoustic impedance for both models. It can be observed that relative changes in AI are larger for the rock physics approach than for the geostatistical approach. This can be explained by the fact that for the latter model the dry bulk modulus on average is larger than for the former model. For porosities from 20% to 33%, the mean dry bulk modulus for the geostatistical model is 10.1 GPa $\pm$ 0.5 GP,

Table 4.5: Summary of petrophysical input parameters

Geostatistical model			
Rock properties	K_g (GPa)	G_g (GPa)	ρ_g (g/cm^3)
Quartz*	37	44	2.72
Clay*	11.3	3	2.72

Proximal mouthbar & distributary channel: CCT model + fluid sub. in shaly sediments			
Rock properties	K_g (GPa)	G_g (GPa)	intrinsic porosity
Quartz	37*	44*	
Clay	11.4	5.32	0.2
	Initial porosity	Coordination number	Shear reduction num.
CCT model	0.38	5.7, 6	0.7

Cement facies: Modified DEM + CCT model			
Rock properties	K_g (GPa)	G_g (GPa)	
Quartz	37*	44*	
Cement	75	35.32	
	Initial porosity	Coordination number	Shear reduction num.
CCT model	0.34	9.86	0.5

Distal mouthbar & delta front: VPC model			
Rock properties	K_g (GPa)	G_g (GPa)	Krief exponent
Quartz	37*	44*	3.2
Clay	18.5	7	

* literature value *Mavko et al.* (1998)

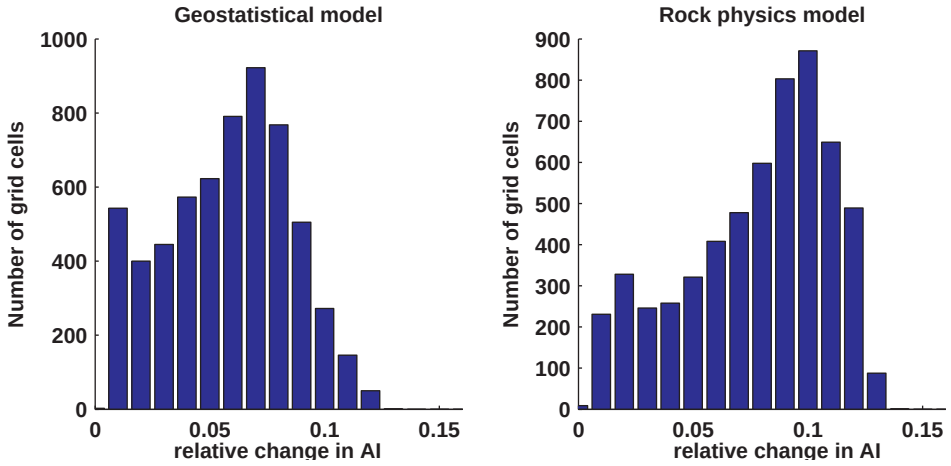

Figure 4.27: Histograms of relative changes in acoustic impedance for the geostatistical and rock physics model.

which is significantly larger than the dry bulk modulus derived from laboratory measurements and predicted by rock physics modelling (Figure 4.16). Figure 4.28 shows histograms for the dry bulk modulus and porosity for both models. Note, that the porosity is different since we have used an effective porosity for the rock physics model. Another aspect is that for small porosities and high clay content the fluid substitution methods for shaly sediments predict somewhat larger

changes in the P-wave impedance than standard Gassmann fluid substitution (*Dvorkin et al.*, 2007). However, this effect has only a minor contribution to our results.

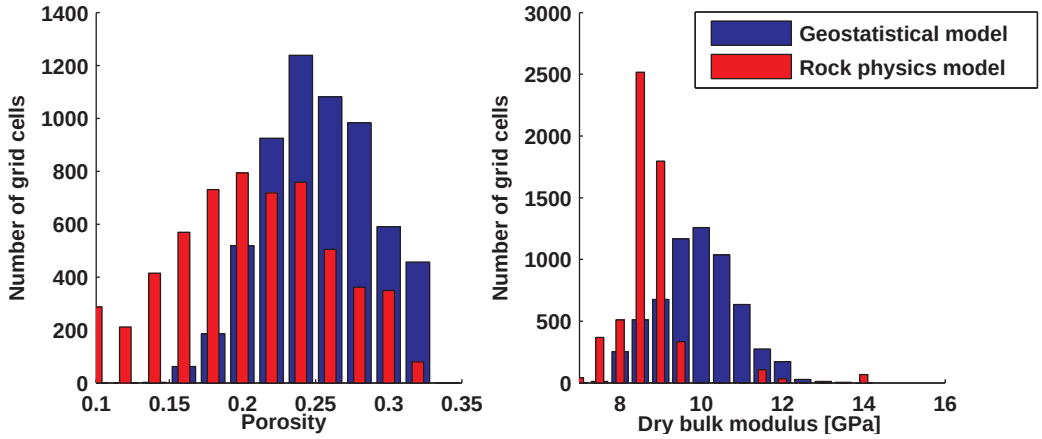

Figure 4.28: Histograms of porosity and dry bulk modulus for the geostatistical and rock physics model.

Finally, we compute the time-lapse seismic response using convolutional modelling. Figure 4.29 shows the RMS amplitude for both models. As expected, the TL signal for the geostatistical model is smaller. However, the signal strength has the same order of magnitude.

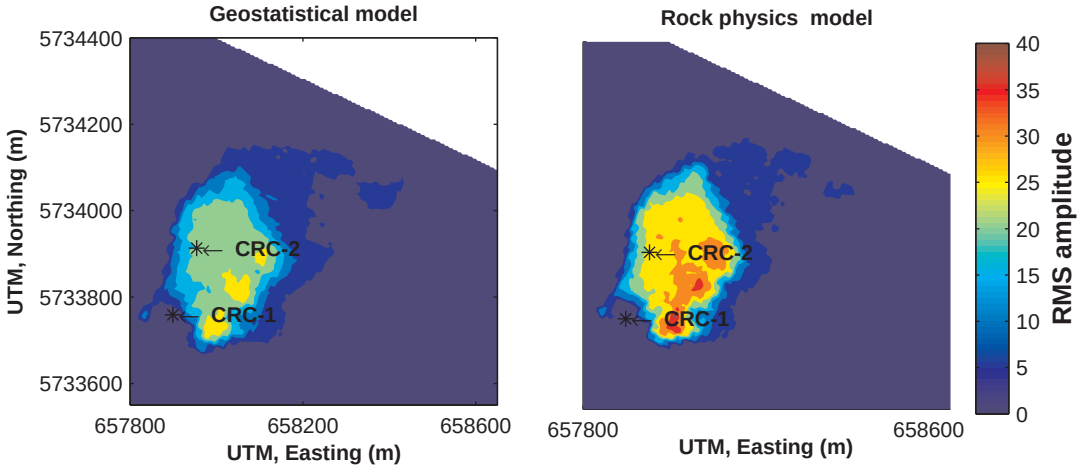

Figure 4.29: Histograms of porosity and dry bulk modulus for the geostatistical and rock physics model.

4.3 Discussion and conclusions

In order to predict the time-lapse seismic response based on reservoir simulations, various data sets have to be integrated on one modelling grid. To obtain meaningfull predictions of the time-lapse seismic response, the data sets have to be on the same scale and consistent with each other. Two elastic models with a different level of detail were build for the Waarre-C reservoir. The fine scale, model based on the static geological model, honoured the well data and reservoir simulation results. The coarse scale model, based on the acoustic impedance inversion, honoured the seismic data. The disadvantage of the latter model is that it cannot capture properly the elastic property - porosity trends observed at well locations. These relationships are crucial in time-lapse studies.

The second part of the chapter analysed two different workflows to obtain such relationships for the Paaratte formation. The first method was based on geostatistical interpolation and takes the variability of the log data into account. The second method, deterministic rock physics modelling, relied on the data trends. However, the latter approach allows to calibrate all necessary parameters based on explicit relations in a consistent manner. Though both approaches reproduced the data trends of the log data quite well, they differed regarding their predictions of the TL seismic signal. These differences are mainly caused by different estimations of the dry rock compressibility.

The dry compressibility of the rock, which itself depends on the porosity, the bulk modulus of the solid grain material and the microstructure of the rock, cannot be measured directly in-situ. One way to constrain this parameter are measurements on core samples. Another possibility to improve the predictions are calibrated rock physics models. These models make some assumptions about the microstructure of the rock. To justify these assumptions, geological information and information from thin sections of rock samples can be included in the modelling process. For instance, a detailed classification scheme of rock physics models to describe diagenetic trends of the rock is given in *Dræge et al.* (2006). In the presented rock physic modelling, an attempt was made to include some ad-

ditional information about the microstructure of the rock. The dry bulk moduli predicted by the rock physics model matched the measurements on core samples quite well. However, that might not be enough information to conclude that the rock physics model reproduces the reservoir properties better than the geostatistical model.

Nevertheless, the modelling study illustrates that the dry compressibility of the rock is a crucial parameter for TL seismic studies. In this sense, even the microstructure of the rock can have a significant influence on the TL seismic signal. A friable sandstone will always predict a very different 4D signal than a well cemented sandstone.

Chapter 5

Velocity - saturation relations

So far, only the influence of varying rock properties on the velocity-saturation relations has been considered. In the previous case studies, we assumed that the rock was uniformly saturated or, equivalently, that the fluid phases were in hydraulic equilibrium within the cell size of dynamic modelling. For instance, for a gas saturation of 5 %, Gassmann's equation with Wood's mixing rule was applied to each 0.1 m interval of the log data in the CRC-2 well (Section 3.3.1). Figure 5.1 a displays the obtained velocity-saturation relations (VSRs) for the second possible perforation interval in the Paaratte formation. This illustrates that VSRs strongly depend on the properties of the rock. However, if the pore space of a rock is saturated with two immiscible fluids, such as brine and CO_2, the VSR also depends on the distribution of the fluids in the pore space.

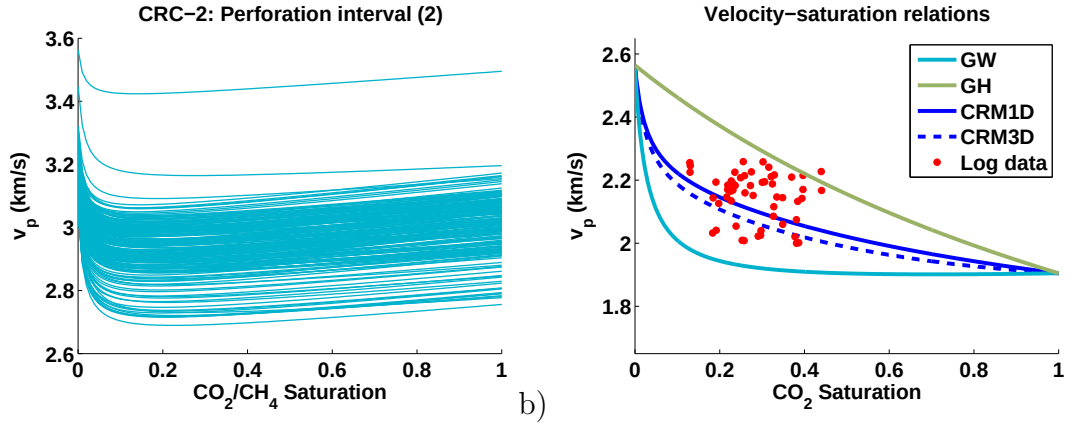

a) b)

Figure 5.1: Velocity-saturation-relations: a) Variation of the Gassmann-Wood relation with rock properties (log data CRC-2). b) Theoretical VSRs compared to time-lapse log data from the Nagaoka CO_2 project.s

This is due to the fact that passing seismic waves induce pressure gradients between regions of the reservoir with different gas saturation levels. The characteristic length scale of saturation heterogeneities compared to the measurement frequency determines if there is enough time for pressure gradients to relax during the time-scale of wave propagation. Depending on this length-scale, different VSRs are applicable. The two well-known VSRs, the uniform (GW) and patchy saturation (GH) relationships give the low and high-frequency limits of VSR, respectively. They represent lower and upper bounds such that, at a finite frequency, the velocity must lie in between these bounds. The variation of velocity with frequency (and corresponding attenuation) can be explained in terms of wave-induced fluid flow on mesoscopic saturation heterogeneities. Mesoscopic refers to a length scale that is large compared to a typical pore size but small compared to the wavelength. This dependence of velocity on saturation, frequency and geometrical distribution of fluids, in particular the characteristic length scale of fluid patches, can be modelled by the continuous random media (CRM) models (Section 2.4.2) suggested by *Müller and Gurevich* (2004) and *Toms et al.* (2007). Figure 5.1b) shows an example of the time-lapse log data from the Nagaoka CO_2 project compared to theoretical VSRs.

Knowledge of the characteristic length scale of fluid patches is necessary to predict the time-lapse seismic response. Conversely, knowledge of the acoustic response of a partially saturated medium provides a pathway to estimate the characteristic length scale of CO_2 distribution. CO_2 patch size estimates have been reported on the basis of laboratory ultrasound measurements on partially saturated rock samples (*Lei and Xue*, 2009; *Lebedev et al.*, 2009). However, in-situ estimates remain elusive.

In the first part of the Chapter VSRs of the Nagaoka time-lapse log data are analysed using the CRM models and in-situ CO_2 patch sizes are estimated from these VSRs. This provides an insight into characteristic length scales at sonic frequencies. However, it is still not clear which saturation scales play a role at seismic frequencies. In the second part of the chapter, a sensitivity study is per-

formed for the Paaratte formation. The aim is to analyse if poroelastic effects play a role at seismic frequencies for the Paaratte formation and therefore, have to be included in the modelling of the time-lapse seismic response. To analyse poroelastic effects, we perform 1.5 D poroelastic modelling at seismic frequencies (Biot's theory) based on realistic saturation scenarios from reservoir simulations.

The chapter includes the paper "Caspari, E., T. Müller, and B. Gurevich (2011), Time-lapse sonic logs reveal patchy CO_2 saturation in-situ, *Geophysical Research Letters*, *38*(13) " published by AGU (Copyright 2011 by the American Geophysical Union) and a sensitivity study published in the report"Watson, M., Y. Cinar, T. Dance, R. Pevzner, E. Tenthorey, E. Caspari, J. Ennis-King, V. Shulakova, M. Bunch, M. Urosevic, R. Singh, B. Gurevich, L. Paterson, C. Jenkins, and M. Raab (2012), Otway Stage 2C Science Report - Verification of CO_2 Storage in a Saline Formation (Paaratte) Using Time Lapse Seismic., (Publication Number RPT12-4109)." by CO2CR. These two references are not cited anymore in the following.

5.1 Velocity-saturation relation from time-lapse log data of the Nagaoka CO_2 project

Time-lapse sonic and neutron logs of the Nagaoka CO_2 sequestration experiment (*Konishi et al.*, 2009) provide an opportunity to study the VSR at in-situ conditions in the sonic log frequency band. These logs have been analysed in previous studies. However, conclusions about the saturation state and corresponding fluid distribution are still a matter of debate (*Xue et al.*, 2006; *Konishi et al.*, 2009). *Xue et al.* (2006) perform history matching with the sonic logs using the uniform saturation model. On the other hand, *Konishi et al.* (2009) show that the VSR follows a linear trend broadly consistent with the patchy saturation model. However, their VSR trends are rather broad due to strong vertical heterogeneity of the injection interval and random errors in log measurements.

The aim of this study is to analyse VSRs from the Nagaoka time-lapse logs and

to estimate in-situ CO_2 patch sizes from these VSRs. To eliminate the effect of heterogeneity, we analyse the time-lapse log data separately for two thin reservoir intervals. We then model the VSR with the 1D and 3D continuous random media (CRM) theories of patchy saturation (*Müller and Gurevich*, 2004; *Toms et al.*, 2007).

5.1.1 Time-lapse log data analysis

At the Nagaoka CO_2 test site, 10400 t of 99.9% pure CO_2 were injected in an onshore saline aquifer at a depth of around 1100 m. The target is a 12 m thin permeable zone of porous sandstone. The initial temperature and pore pressure of the formation were 48°C and 10.8 MPa, respectively, so that CO_2 was in supercritical state at reservoir conditions. An extensive monitoring program was performed including time-lapse log measurements in 3 observation boreholes. A summary of the results is given in *Xue et al.* (2006). In this study, we analyse the time-lapse data of the observation well OB2 located 40 m down dip from the injection well.

In the observation well OB2, time-lapse sonic and neutron porosity logs were recorded; 23 logs during a 18 months CO_2 injection period and 14 logs after the injection stopped (*Xue et al.*, 2006). The averages of the first 13 sonic and neutron porosity logs recorded before the CO_2 breakthrough are used as baseline data and the logs 17 to 26 as monitoring data (Figure 5.2). *Sato et al.* (2011) report that the log responses vary with depth in the reservoir zone (1112-1118 m) indicating that this zone is heterogeneous. Therefore, a VSR inferred from log responses of the whole reservoir zone is probably influenced by variations of rock properties with depth and will mask the true VSR. To eliminate the ambiguity caused by this effect, we analyse only two 0.5 m thick intervals with relatively small depth variations.

The CO_2 saturation is estimated from differences in the time-lapse neutron logs. Given that the neutron log is sensitive to the water content, changes in water saturation caused by CO_2 injection can be used to calculate the CO_2 saturation

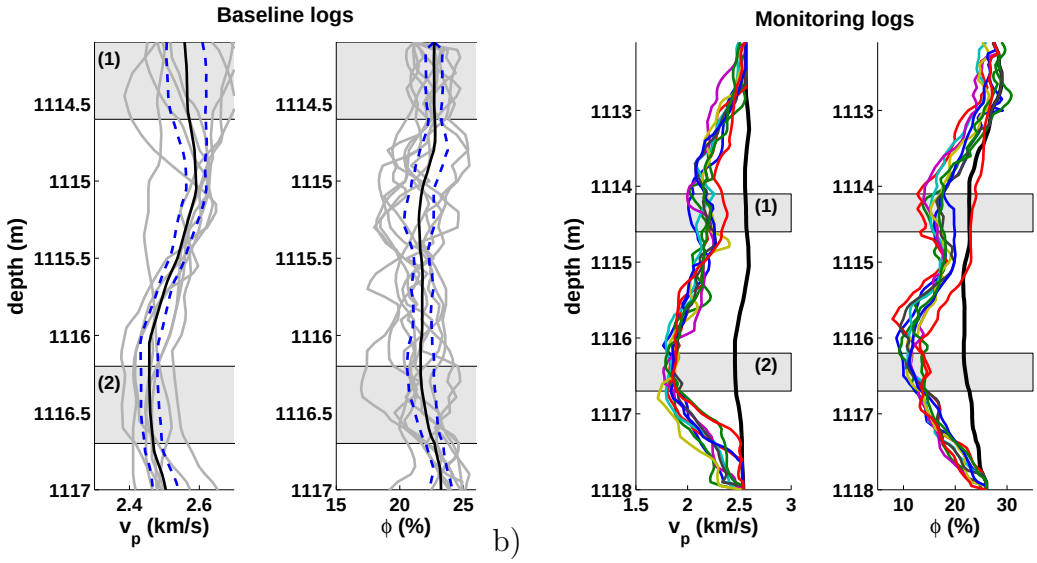

a) b)

Figure 5.2: a) Sonic and neutron porosity baseline logs 1 - 13 (gray lines), averaged baseline log (black line) and the corresponding standard variation (dashed blue line). b) Sonic and neutron porosity monitoring logs 17 - 26 (colored lines) and averaged baseline log (black line). Gray boxes indicate the chosen depth intervals (data from *Konishi et al.* (2009))

as follows:

$$S_{CO_2} = (\phi_b - \phi_m)/\phi_b \,, \tag{5.1}$$

where ϕ_b and ϕ_m denote the baseline and monitoring neutron porosity, respectively (*Konishi et al.*, 2009).

The baseline logs exhibit strong fluctuations between subsequent runs (Figure 5.2). Such non-repeatability produces random variations in P-wave velocity and CO_2 saturation with time (*Sato et al.*, 2011). To minimise the problem of random fluctuations in the monitoring logs, the TL data points are approximated by smooth functions of time t for each individual depth. More precisely, we use

$$S_{CO_2} = S_{max}(1 - e^{-\alpha t}) \,, \tag{5.2}$$

$$v_P = v_{Pmax} - \Delta v_P (1 - e^{-\beta t}) \,, \tag{5.3}$$

where S_{max} and v_{Pmax} are respectively the maximum saturation and P-wave velocity, and Δv_P denotes the difference between the maximum and minimum P-wave velocity. The coefficients α and β are fitting parameters. Figure 5.3 shows

the P-wave velocity and CO_2 saturations for each depth sample as function of time (subsequent log runs) and the corresponding smoothed functions.

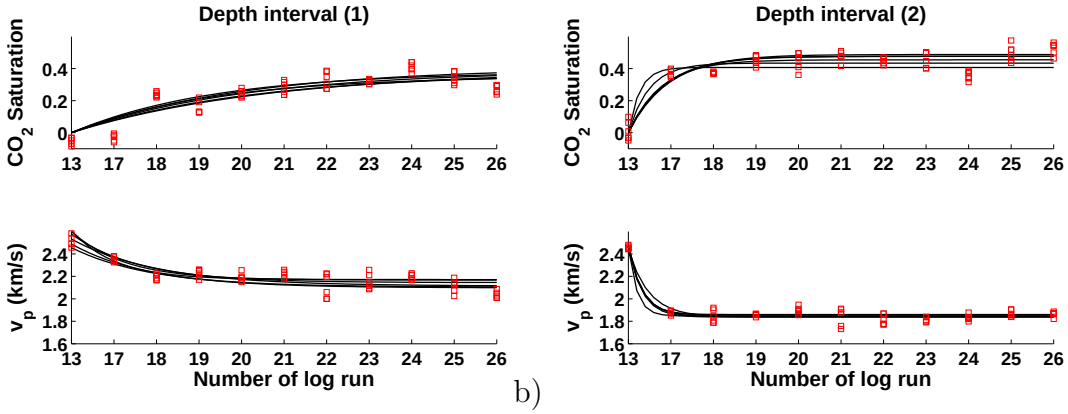

Figure 5.3: P-wave velocity and CO_2 saturation as a function of time (subsequent log runs) for the first (a) and second (b) depth interval. Red squares denote samples from the log data, while the black lines are the fitting functions.

We note that the use of fitting functions is a simplification as it implies a constant CO_2 supply into the reservoir. This is not necessarily guaranteed as the injection rate was not constant during the injection period (*Xue et al.*, 2006). However, from *Sato et al.* (2011) we infer that fluctuations in CO_2 saturation and velocity are uncorrelated. This indicates the presence of random fluctuations and justifies the smoothing approach.

5.1.2 Velocity-saturation relation in random media

The behaviour between the two frequency limits of uniform and patchy saturation can be explained in terms of the mechanism of wave induced fluid flow between mesoscopic fluid heterogeneities. At these intermediate frequencies, wave attenuation and velocity dispersion occurs and produces a specific VSR. The latter can be modelled by the 1D and 3D continuous random media models (*Müller and Gurevich*, 2004; *Toms et al.*, 2007) .

The 1D model represents a system of alternating CO_2 and brine layers of random thicknesses while the 3D model represents a system of randomly distributed fluid patches in space. These random variations are described by a normalised au-

tocorrelation function of the fluid bulk moduli. In particular, for an exponential correlation function, the dynamic-equivalent P-wave modulus for the 1D model is

$$H_{1D}(\omega) = H_{\mathrm{GW}} \left[1 + \frac{s}{1 + \frac{2i}{k_D d}} \right] , \tag{5.4}$$

with the slow P-wave number

$$k_D = \sqrt{\frac{i\omega}{\kappa}} \frac{\sqrt{\eta_w N_w} S_w + \sqrt{\eta_{CO_2} N_{CO_2}} S_{CO_2}}{N_w S_w + N_{CO_2} S_{CO_2}} .$$

The degree of inhomogeneity is given by the parameter $s = H_{GH}/H_{GW} - 1$, where H_{GW} and H_{GH} respectively denote the P-wave modulus defined by the Gassmann-Wood and Gassmann-Hill theory. The correlation length d describes a characteristic patch size of the medium. The P-wave modulus for the 3D model can be written as

$$H_{3D}(\omega) = H_{\mathrm{GW}} \left[1 + \frac{H_{\mathrm{GH}} - H_{\mathrm{GW}}}{H_h - H_l} \frac{H_{eff} - H_l}{H_{\mathrm{GW}}} \right] , \tag{5.5}$$

where H_{eff} is the effective complex P-wave modulus and H_l and H_h are the low and high frequency limits derived from H_{eff}. This effective P-wave modulus for an exponential correlation function is defined as

$$H_{eff} = H_0 \left(1 - \Delta_2 - \frac{\Delta_1 k_D^2 d^2}{(i k_D d - 1)^2} \right)^2$$

with

$$k_D = \sqrt{\frac{i\omega\eta}{\kappa N}}, \quad \Delta_1 = \frac{L\Delta_2}{H}, \quad \Delta_2 = \frac{\alpha^2 M \sigma_{MM}^2}{2H} . \tag{5.6}$$

The parameter σ_{MM}^2 is the normalised variance of the fluid storage modulus. The average background P-wave modulus H_0 is calculated from Gassmann's equation using an average fluid modulus. The low and high frequency limits of H_{eff} are given by

$$H_l = H_0(\Delta_2 - 1)^2, \quad H_h = H_0(1 - \Delta_2 + \Delta_1)^2 .$$

Table 5.1: Petrophysical properties of the rock and fluids

Rock	Kg (GPa)	K_d (GPa)	μ (GPa)	ρ_g (g/cm^3)	ϕ	κ (mD)
Nagaoka (OB2)	27.74	2.5 - 3.3*	2.4 - 3.3*	2.5	0.23	10
Tako sandstone	38	6	6	2.5	0.25	15
Fluids	K (GPa)		ρ (g/cm^3)		η (Pa s)	
Brine (Nagaoka)	2.5		1		1e-3	
Brine (Tako)	2.25		0.997		8e-4	
supercritical CO_2 (Nagaoka)	0.0465		0.623		4.4e-5	
supercritical CO_2 (Tako)	0.046		0.62		7e-5	

Rock and fluid properties are taken from *Konishi et al.* (2009), *Xue et al.* (2006) and *Lei and Xue* (2009)
* calculated properties
***Han et al.* (1986)

The real parts of the P-wave moduli (Eq. (5.4)) and (Eq. (5.6)) yield the VSRs. They are a function of the wave frequency, the fluid patch size, and the ratio of the permeability and the fluid shear viscosity. The 1D and 3D CRM models constitute two end-member scenarios with respect to the patch geometry. Fluid patches are not expected to be perfect layers nor fully isotropic in 3D space but more likely something in between.

5.1.3 Velocity-saturation relation at Nagaoka

VSR modelling requires the knowledge of the elastic properties of the dry rock frame. Since the reservoir shows vertical heterogeneity, we calculate the dry bulk modulus K_d from the sonic baseline data for each depth rather than using an average value for the whole reservoir. As no S-wave velocity is available, we choose a v_p/v_s ratio of 1.52 from literature data (*Han et al.*, 1986). This ratio is substituted into Gassmann's equation which is then solved for K_d. The computed dry bulk moduli (2.5 - 3.3 GPa) are comparable to the values derived by *Xue et al.* (2006) and *Konishi et al.* (2009) using the unconsolidated sand model. *Xue et al.* (2006) report that the dry properties could not be measured due to the friable nature of the rock. Such a soft rock is favorable for seismic monitoring purposes as then strong time-lapse signals can be expected (*Lumley*, 2010). The rock and fluid parameters are summarized in Table 5.1 .

The GW and GH bounds for the Nagaoka data are shown in Figure 5.4. It can be observed that most raw data points (red squares) fall between the uniform and

patchy saturation bounds. That is still true if we take into account the standard variation of the baseline logs ($\sigma_{std}(BL)$) indicated by gray lines. Compared to the raw data, the smoothed data points (black circles) exhibit less scatter and allow us to define a distinct velocity-saturation trend.

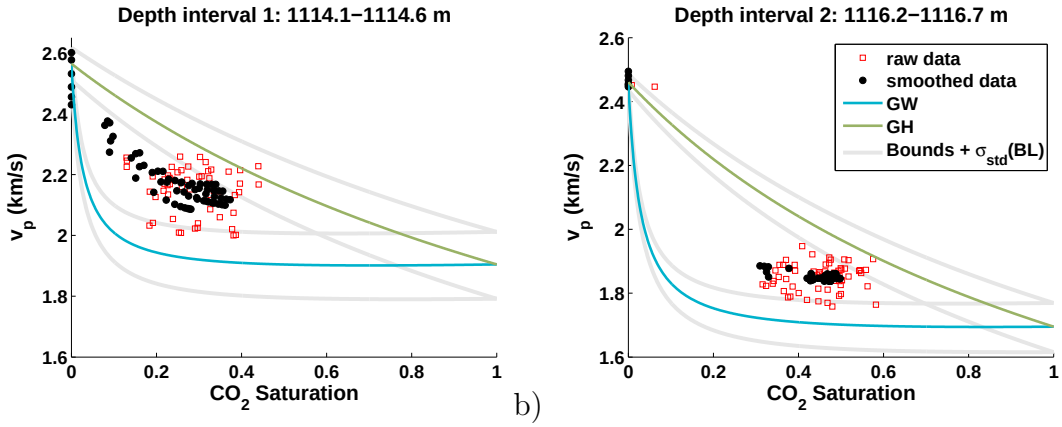

Figure 5.4: Comparison between theoretical bounds (GW and GH) and log data for the (a) first and (b) second depth interval. The gray lines show the deviations of the GW and GH bounds, obtained from the standard variation (non-repeatability) of the repeated baseline logs (dashed blue lines in Figure 5.2).

In the next step, we model the VSR employing the CRM models. Using a typical sonic log frequency and the known permeability and fluid viscosities (Table 3.2) yield velocity-saturation predictions based on Eqs. (5.4) and (5.6) which depend on the correlation length d. For $d = 0.1\,\text{mm}$, the predictions converge to the GW bound whereas for $d = 3\,\text{cm}$, the prediction is close to the GH bound. The velocity-saturation trend of the smoothed data follows the predictions of the CRM models for a range of correlation lengths (Figure 5.5). This in turn allow us to infer characteristic patch sizes of CO_2 by fitting a 1D and 3D CRM model to each point of the smoothed data. The resulting correlation lengths are between 1-5 mm. Figure 5.5 shows the corresponding VSRs for 1 mm and 5 mm.

One difficulty in modelling the VSRs for partially saturated rocks lies in the fact that the VSR, is controlled by the characteristic patch size, which itself can depend on saturation (*Toms-Stewart et al.*, 2009). However, the VSR trend in Figure 5.5 appears to be parallel to the CRM lines, indicating no distinct variation of the patch size with saturation. The fluid patch sizes inferred from the

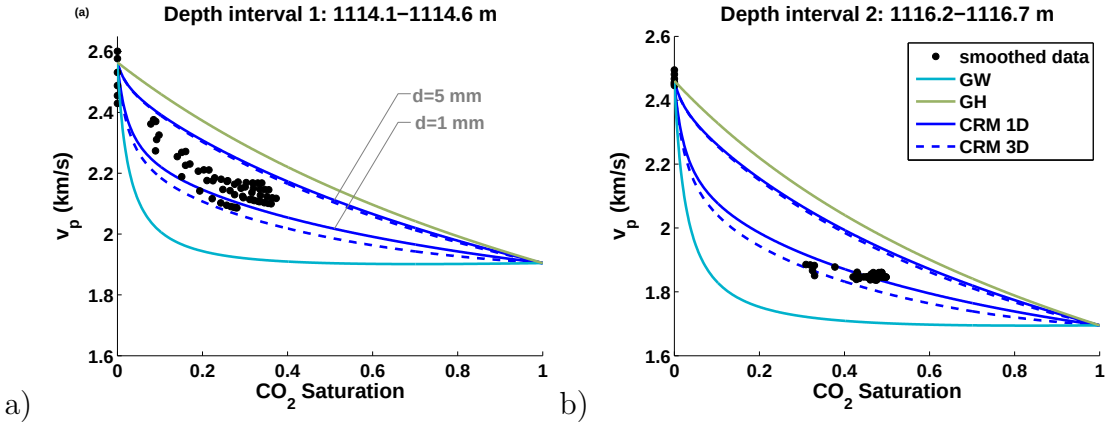

Figure 5.5: Comparison between CRM models and smoothed log data for the (a) first and (b) second depth intervals at sonic frequencies.

3D CRM model are consistently larger compared to the 1D CRM model. This is explained by the slightly larger velocity of the 1D CRM model at intermediate frequencies and accounts for the fact that wave-induced flow in 1D heterogeneous media occurs in a broader frequency range compared to the 3D situation (*Müller and Gurevich*, 2004). Furthermore, in the first depth interval, patches are slightly larger than in the second one, which demonstrates that the patch sizes are likely to vary from one layer to the other (Figure 5.6). These layer-dependent patch size variations can originate from variations of other poroelastic parameters (e.g. porosity) across the depth interval. Another possible explanation is that lower CO_2 saturations (first depth interval) are more prone to patchiness than higher CO_2 saturations. This highlights the importance of analysing the VSR independently for different depth intervals.

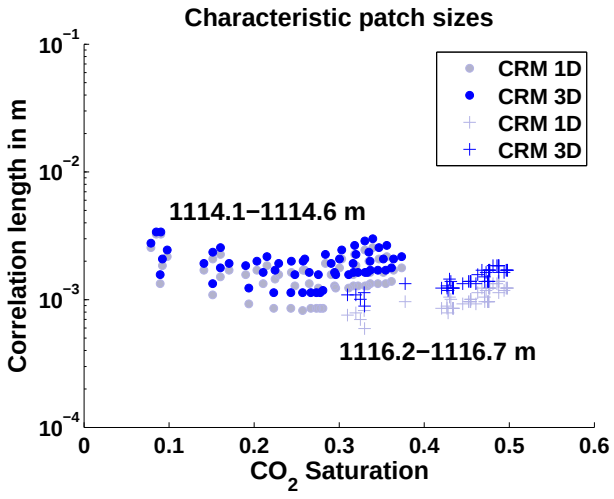

Figure 5.6: Calculated correlation length from smoothed log data. Circles denote the first depth interval and crosses the second.

5.1.4 Discussion

The estimated characteristic size of fluid patches is on the order of a few millimeters. Comparing these estimates with the pore-scale features of a reservoir thin section (*Xue et al.*, 2006) demonstrates that the patch sizes are indeed much larger than a typical pore size. This indicates that wave-induced fluid flow between mesoscopic inhomogeneities may occur at sonic frequencies and therefore strongly controls the velocity-saturation behaviour.

Our patch size estimates are consistent with those from *Lei and Xue* (2009) inferred from laboratory ultrasound measurements on Tako sandstone using the White-Dutta-Odé model (*Dutta and Odé*, 1979) for patchy saturation (1.3 - 1.5 mm). The petrophysical properties of Tako sandstone and the Nagaoka reservoir are quite comparable (Table 5.1). The main difference is that the Tako sandstone is well cemented in contrast to the friable reservoir samples from the well OB2. However, the fluid diffusion lengths $\lambda_d = 0.25\,\text{mm}$ (Tako - ultrasonic frequencies) and $\lambda_d = 0.65\,\text{mm}$ (Nagaoka - sonic frequencies) are of the same order of magnitude. This indicates that similar patch sizes can play a role in laboratory ultrasound and sonic log measurements. It shows an intriguing possibility that laboratory fluid injection experiments may be used to simulate in-situ conditions in the sonic frequency band.

5.1.5 Implications for seismic frequencies

In order to understand if heterogeneities of this length scale have any effect in the seismic frequency band, we model the VSR for a frequency of 50 Hz and a correlation length of 3 mm (Figure 5.7). The 3D CRM model coincides with the GW limit, whereas the VSR for the 1D CRM model converges slower to this bound as attenuation and dispersion occur in a broader frequency range. Thus, for patch sizes in the millimeter range, the GW limit can be used as a first order approximation.

We analysed two small depth intervals using wireline logging data. Hence, the VSR results are limited by the penetration depth of the log measurements and

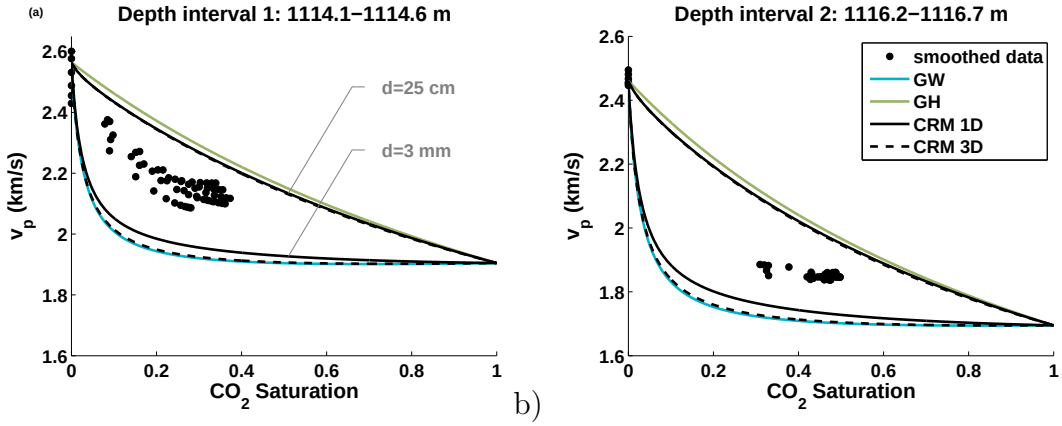

Figure 5.7: Comparison between CRM models and smoothed log data for the (a) first and (b) second depth interval at seismic frequencies.

do not permit any conclusion on fluid distribution on a larger scale. To analyse if attenuation and dispersion play a role at seismic frequencies, we estimate a characteristic length scale of the depth variations. First, the depth trend from the sonic monitoring data is removed. Then, the autocorrelation of the remaining fluctuations is calculated for each run and a characteristic correlation length of 25 cm is inferred. Figure 5.7 shows the VSR for a seismic frequency of 50 Hz and a patch size of 25 cm. It can be seen that heterogeneities of this size could cause dispersion and attenuation at seismic frequencies according to the CRM models. Nevertheless, it has to be further investigated whether the magnitudes of the fluctuations reflect random variations of layer properties rather than random noise associated with measurement errors.

In the next section, we investigate poroelastic effects on the example of the Paratte formation based on reservoir simulation results.

5.2 Numerical simulation of the effect of fine-scale saturation distribution on the seismic response

In a heterogeneous reservoir with different rock types, adjacent layers can have very different gas saturations. These saturation heterogeneities are mainly con-

trolled by the permeability of different rock types. The aim of the sensitivity study is to analyse if such permeability variations and corresponding saturation heterogeneities have an influence on the time-lapse seismic response of the Paaratte formation. In order to do that, we utilise reservoir simulation results.

In addition to the reservoir simulation results used in chapter 3 for the deeper perforation interval of the Paaratte formation, radial reservoir simulation with a refined grid (grid resolution of 0.34 m) have been performed (*Watson et al.*, 2012). The refined simulations are more suitable for the sensitivity study since they capture saturation variations on a finer scale. These simulations are based on a 1D vertical cross-sectional model at the CRC-2 location. Figure 5.8 shows a representative profile of the modelled gas saturation, vertical permeability, and rock type (facies). The gas is injected in a high permeability layer at the bottom of the reservoir and migrates upwards through clean and shaly sandstone sections to the reservoir top. The varying permeabilities of the different rock types result in a distinct gas saturation profile. These saturation heterogeneities are below the resolution of the seismic method (Figure 5.8). Nevertheless, the distribution of fluids, as well as the properties of the rock, will affect the velocity-saturation relationship and thus the response of the time lapse seismic signal.

5.2.1 Saturation scales which play a role at seismic frequencies

In the previous section, it has been shown that non-uniform (patchy) saturation can play a role at well logging frequencies but it is still not clear if it will affect the signal at seismic frequencies. To get a first idea which saturation scales could play a role at seismic frequencies in the Paaratte formation, we utilize the 1D random medium model of *Müller and Gurevich* (2004). This model represents a system of alternating CO_2 and brine saturated porous layers of random thickness and takes the mechanism of wave-induced fluid flow into account. As an input, we use the measured petrophysical properties of the rock sample 1444.2 V (see description in Section 4.2.2). The modelling is performed with a frequency of

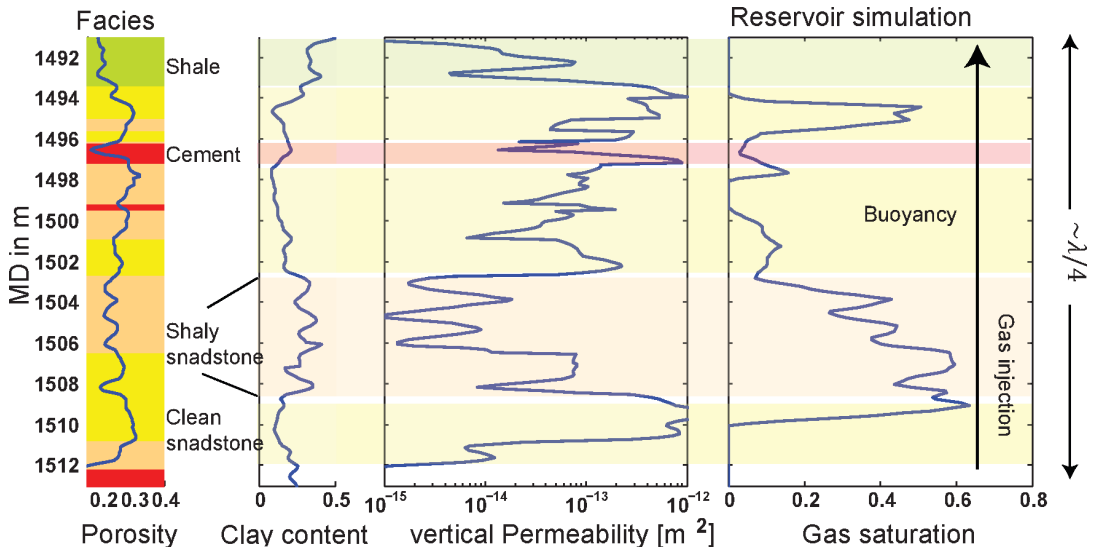

Figure 5.8: Petrophysical properties for the second perforation interval and a gas saturation profile from the refined reservoir simulations. The arrow on the right side indicates the resolution of the seismic method

45 Hz for different length scales and the results are shown in Figure 5.9b. Note, that these results do not consider heterogeneities in the rock properties; however they include layers with 100% gas and water saturation. This corresponds to the largest possible contrast between porous layers (with the same elastic parameters) due to fluid distribution and thus it has a significant effect on the VSRs for length scales greater than 0.2 m.

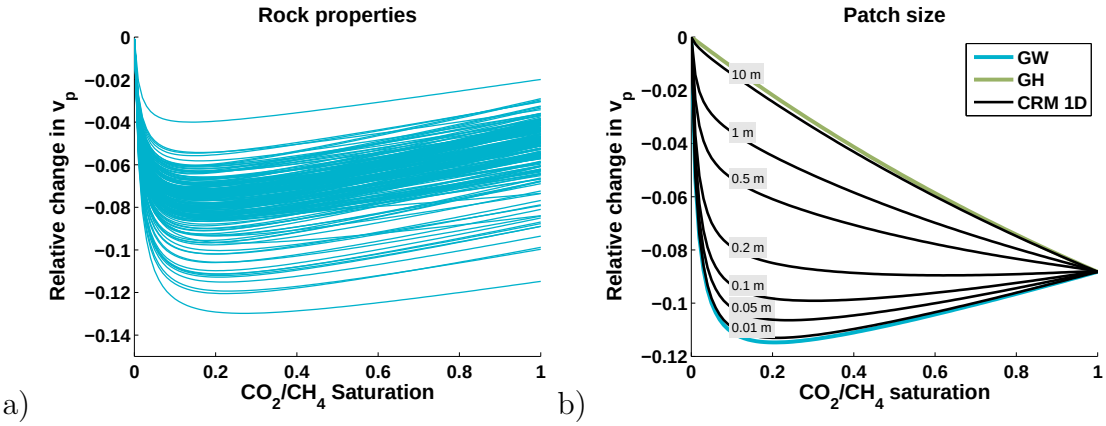

Figure 5.9: Velocity saturation relations for a) varying rock properties (second injection interval CRC-2) and b) for different fluid distributions with characteristic length scales of 0.01- 10 m at a frequency of 45 Hz (rock sample 1444.2 V)

In order to model a more realistic scenario, we perform 1.5D poroelastic modelling (Biot's theory) based on the log data from the CRC-2 well and the saturation profile obtained from reservoir simulations. In contrast to non-dispersive

elastic modelling, poroelastic modelling accounts for dispersion and attenuation of fast seismic P-waves as a result of mode conversion between slow and fast P-waves at interfaces and heterogeneities. The slow P-wave is a diffusive wave in the seismic frequency regime and describes the process of wave-induced fluid flow. These poroelastic effects will be large for interfaces with high contrast, such as 100% water and gas saturated porous layers.

5.2.2 Saturation scenarios and formation properties

Different scenarios are analysed: a constant gas saturation of 15.58% (S1), a saturation profile (S2) obtained from reservoir simulations (radial modelling) and a profile with an enhanced variability in saturation (S3) to exaggerate poroelastic effects. The constant saturation is chosen so that the gas column height of the original saturation profile from the reservoir simulator is preserved. Then, the constant saturation (S1) can be calculated by

$$S1 = \frac{\sum_{i=1}^{N} \phi_{sim}^{i} S2^{i} \Delta^{i} z_{sim}}{\sum_{j=1}^{N} \phi_{log}^{j} \Delta^{j} z_{log}} \tag{5.7}$$

where the sum in the numerator is the gas column hight of the profile S2, Δz_{sim} and Δz_{log} are the grid resolution of the simulator and the sampling rate of the log data, respectively. The indices i and j denote the i^{th} layer of the simualtor grid and j^{th} sample of the log data, respectively. An enhanced variability in gas saturation is introduced somewhat heuristically and is not based on multi-phase flow principals. The aim is to increase poroelastic effects. This is done in two steps. First a running average ($S2_{av}$) of the simulator saturation profile is calculated. Afterwards the variability of the gas saturation is enhanced by a factor n. The final profile S3 is calculated by the following formula

$$S3 = S2_{av} + (S2 - S2_{av})n. \tag{5.8}$$

The factor n is determined iteratively with the condition that the gas column height of the original profile is preserved. The resulting saturation profiles are shown in Figure 5.10.

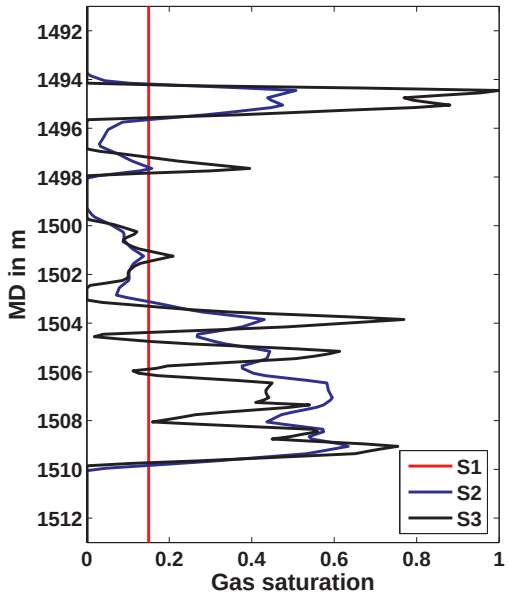

Figure 5.10: Saturation scenarios for seismic forward modelling:

S1: 15.8% gas saturation,

S2: Profile from reservoir simulator,

S3: Enhanced variability of saturation.

From these saturation profiles an effective fluid bulk modulus is calculated by Wood's mixing rule for each 0.1 m thin layer, assuming that the fluid phases within these intervals are equilibrated. The assumption is based on the results shown in Figure 5.9b which illustrates that significant effects can be expected for saturation inhomogeneities larger than 0.2 m. The dry bulk modulus and grain properties of the rock are obtained as described for the 1D elastic modelling in Section 3.3.1. All parameters required for poroelastic modelling are listed in Table 5.2. The pore-size parameter is calculated by $a = \phi d/(3 - 3\phi)$ (*Hovem and Ingram*, 1979), where d is the diameter of a spherical grain. However, the pore-size parameter and tortuosity of the rock will only effect the signal above Biot's critical frequency. Since the seismic frequency regime is far below Biot's critical frequency, inertial effects acting on the fluid are negligible.

5.2.3 1.5D poroelastic and elastic modelling

For these layered porous medium models, we perform 1.5D modelling using the Biot module (poroelastic) of the OASES software (*Schmidt and Tango*, 1986), which accounts for all poroelastic effects at the interfaces between layers. We also perform elastic modelling for these profiles, which are based on equivalent elastic models obtained by the Gassmann-Wood relation. The effective elastic

Table 5.2: Petrophysical properties of the rock and fluids (Paaratte formation)

Rock properties	K_g (GPa)	G_g (GPa)
Quartz	36.6	45
Clay	11.4	3

In-situ conditions	T (°C)	P (MPa)
	57	14.6

Fluid properties	K (GPa)	ρ (g/cm^3)	η (Pa , s)	Salinity (ppm)
Brine*	2.465	0.9876	0.5 1e-3	750
CO_2(80%)/CH_4(20%)**	0.0289	0.359	4.6 1e-05	

* *Batzle and Wang* (1992) (gas free)
** *Kunz et al.* (2006)

properties are calculated for each 0.1 m thin layer. For the forward modelling, the same seismic parameters and basic processing steps as in Section 3.3.1 are employed.

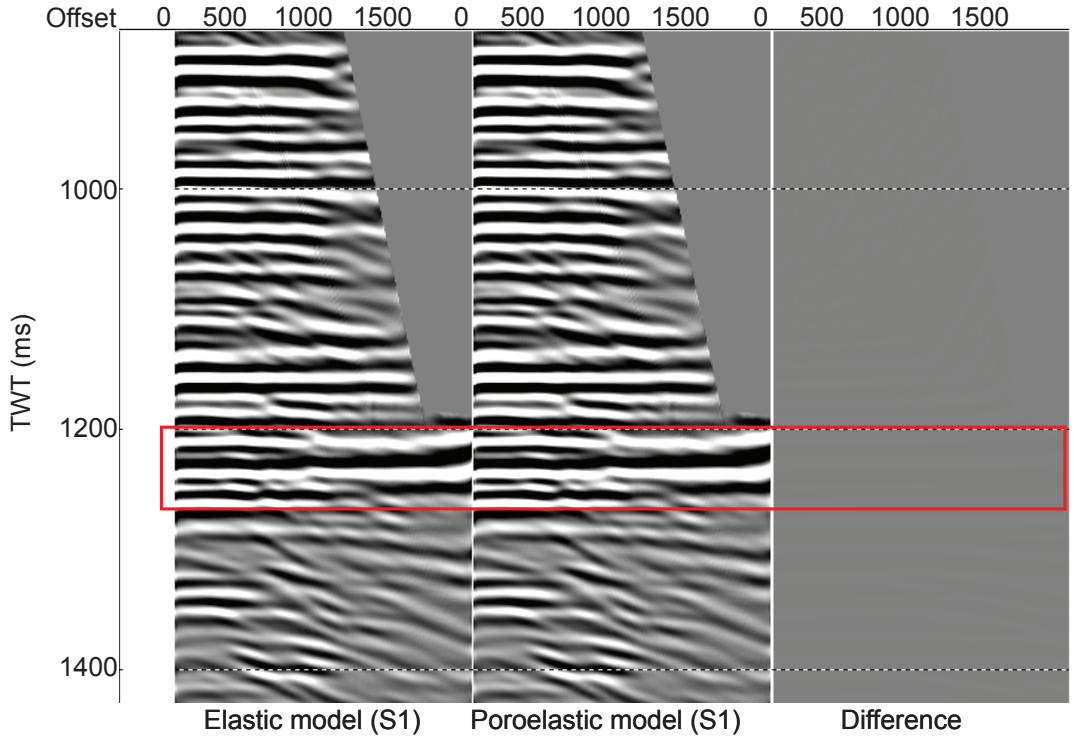

Figure 5.11: Elastic and poroelastic modelling results for the saturation profile S2 and the corresponding difference. The red box indicates the alternative perforation interval.

Figure 5.11 and 5.12 compare the poroelastic and elastic modelling results. The difference between poroelastic and elastic modelling for the saturation profile from the reservoir simulator (S2) is approximately 1000 times smaller than

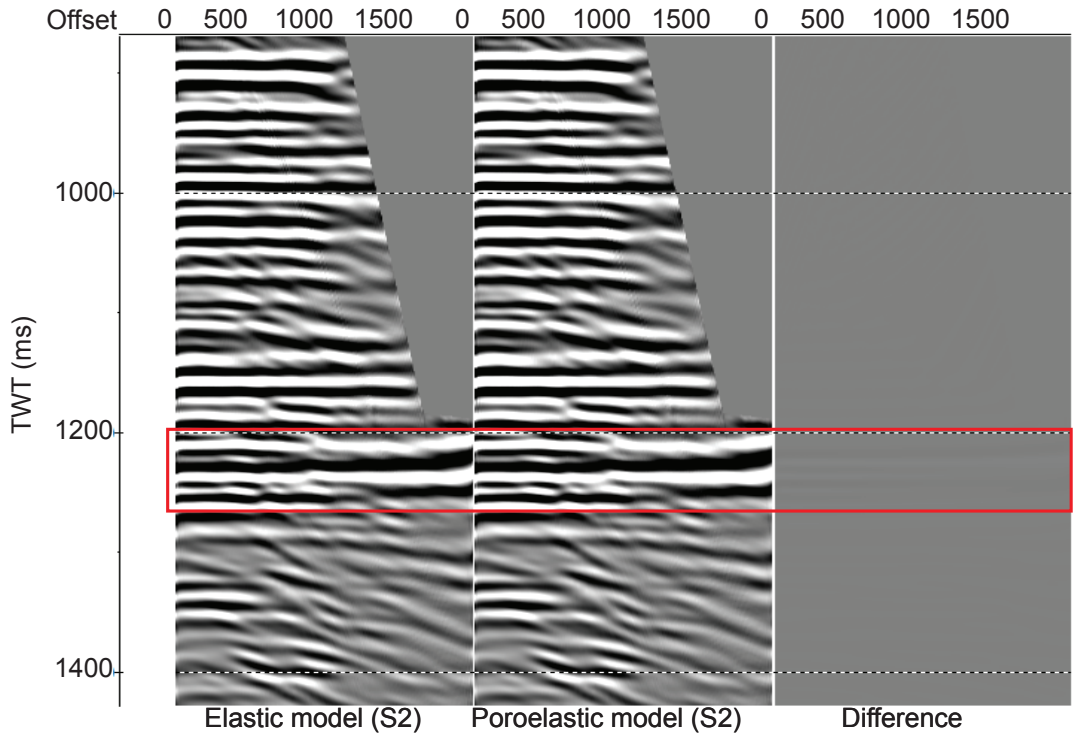

Figure 5.12: Elastic and poroelastic modelling results for the saturation profile S3 and the corresponding difference. The red box indicates the alternative perforation interval.

the seismic signal and as expected even smaller for the constant saturation profile (not shown here). For profile S3, with an enhanced variability of gas saturation, there are some visible differences between the two modelling approaches. However, these differences are still significantly lower than the computed seismic signal (approximately 100 times).

Next, we compare the magnitude of the time-lapse seismic response of the elastic modelling for scenarios S1, S2 and S3 with the time-lapse response of poroelastic modelling for scenarios S2 and S3 Figure 5.13. All three saturation cases contain approximately the same amount of gas. The seismic response for all scenarios looks quite similar. To quantify the differences, we compute the RMS amplitude of the time lapse signal in a 30 ms window around the reflection event indicated in Figure 5.13. Interestingly, the time-lapse signal at near offsets has the largest magnitude for the saturation profile (S2) directly obtained from the flow simulator (Figure 5.14), whereas at far offsets the largest magnitude is obtained for the saturation scenario S1 (constant gas saturation of 15.8%).

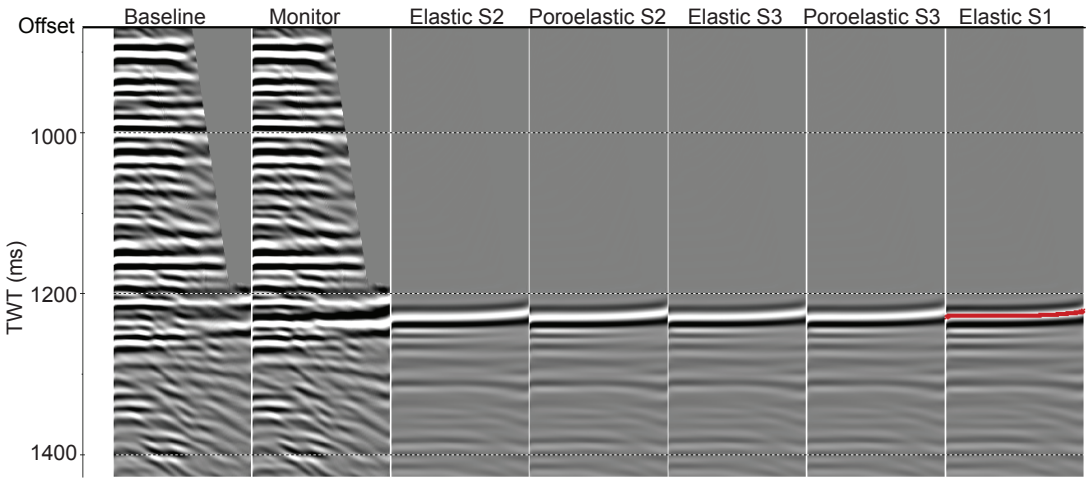

Figure 5.13: Time lapse seismic signal for elastic and poroelastic modelling with different saturation profiles. Red curve indicates the reflection for the calculation of the RMS amplitudes.

The differences between scenarios S1 - S3 are most likely due to constructive and destructive interference (stratigraphic filtering). Further, there are minor differences between the elastic and poroelastic cases for the enhanced variability of saturations. Overall, we can conclude that for the modelled scenarios, the distribution of the fluids and the resulting impedance contrasts between the layers affect the TL seismic response more than the obtained poroelastic effects. Saturation heterogeneities below the grid size of the reservoir simulator might have some additional effects on the seismic response and will be analysed in the future.

Finally, we compare these results to the elastic modelling with a constant gas saturation of 5% (Section 3.3.1). Note that the gas saturation (5%) is 3 times smaller than for the constant saturation case S1 and thus, we expect the signal to be smaller. Figure 5.14 demonstrates that this leads to the smallest time-lapse signal with an RMS amplitude which is approximately 20% smaller than for scenario S2.

5.3 Discussion and conclusions

Based on time-lapse logs, a velocity-saturation relation at reservoir depth is retrieved. It does not coincide with either of the end-member models of uniform and patchy saturation but falls in between even if realistic error estimates for

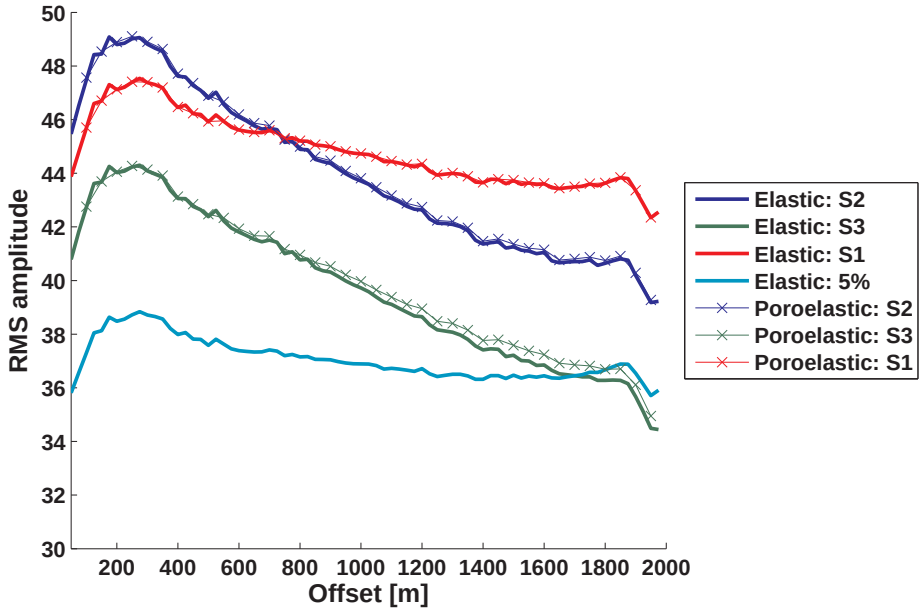

Figure 5.14: RMS amplitudes of elastic and poroelastic forward modelling for the different saturation scenarios.

the host rock properties are considered. Assuming a random distribution of CO_2 patches, it is shown that the mechanism of wave-induced flow can explain this velocity-saturation relation. Characteristic CO_2 patch size estimates range from 1 to 5 mm. Such mesoscopic heterogeneity can be responsible for attenuation and dispersion in the well logging frequency band. However, at seismic frequencies for these patch sizes the GW limit can be used as a first order approximation. Due to the limited penetration depth of the log measurements, fluid distributions on a larger scale could not be investigated. Using the characteristic length scale of depth variations as a measure for fluid heterogeneities indicated that patch sizes of 25 cm could cause attenuation and dispersion at seismic frequencies.

In the second case study (Paaratte formation), larger fluid heterogeneities were investigated based on reservoir simulation results. A rough estimation of length scales that could cause attenuation and dispersion showed that, in this case, for patch sizes of 0.25 m, the GW limit might be still applicable. This is due to the fact that in the former case, the diffusion length at seismic frequencies is around 0.15 m, while for the Paaratte formation the diffusion length varies between $0.05 - 0.8$ m. Especially, the clean sandstone sections have very high per-

meabilities, which in turn result in a large diffusion length. Hence, within these layers, pressure gradients can quickly equilibrate. In this respect, it is not surprising that the differences between poroelastic and elastic modelling were negligible. Larger poroelastic effects can be expected for low permeable rocks and a series of layers with a strong contrast.

However, different distributions of the fluids (saturation profiles) resulted in different contrasts between layers and thus lead to different magnitudes of the TL seismic signal. These differences can be explained by multiple scattering (stratigraphic filtering) and are not due to intrinsic attenuation (local fluid effects). Though the variations in layer properties are below the resolution of the seismic method, they affect the TL signal and have to be taken into consideration. *Sengupta et al.* (2003) already noted that subresolution saturation scales might affect TL seismic data. They reported that by downscaling very coarse reservoir simulator results to more realistic fluid distributions, a better match with measured TL seismic data could be obtained.

Further, the two case studies illustrate that the frequency range, in which dispersion and attenuation of the fast P-wave occurs is not only determined by the length-scale of saturation heterogeneities and the contrast of the fluid, but also by the diffusion length scale of the medium. The major factor controlling pressure diffusion is the permeability of the medium. It has been shown in previous studies that the effective flow permeability depends on the observation scale. *Shapiro and Müller* (1999) noted that the exact flow permeability might be not the permeability controlling seismic attenuation and dispersion related to wave-induced fluid flow in a layered medium. Further, *Müller et al.* (2007) demonstrated that random fluctuations of permeabilities influence the frequency regime in which attenuation and dispersion occurs. In the next chapter, a model which takes into account the effect of strong fluctuations of hydraulic conductivity (mesoscopic heterogeneities) on the diffusivity of the medium is derived.

Chapter 6

Dynamic equivalent hydraulic conductivity

Effective properties of heterogeneous porous rocks represent the average physical behaviour of the medium at a certain scale. If the effective properties are not only controlled by the spatial distribution of the medium components but also by the time-dependence of the physical mechanism, spatial and temporal upscaling is required. Therefore, proper upscaling is frequency-dependent. For instance, for the fast P-wave of a partially saturated rock the GW relation provides the low-frequency limit, while the GH relation provides the high-frequency limit. For poroelastic parameters most of the existing statistical effective medium methods are limited to low contrast. However, in many instances the contrast in properties is high, e.g. inhomogeneities in hydraulic conductivity, CO_2 injection in an aquifer or fractured rocks. In this chapter we investigate the applicability of a strong contrast approximation, suggested in the context of the dynamic dielectric constant (*Rechtsman and Torquato*, 2008), to poroelastic parameters. For simplicity we focus on a porous medium with strong fluctuations in hydraulic conductivity at mesocopic scales.

Determining transport properties of heterogeneous porous rocks, such as an effective hydraulic conductivity, arises in a range of geoscience problems, from groundwater flow analysis to hydrocarbon reservoir modelling. In the presence of formation-scale heterogeneities, non-stationary flows, as induced by pumping

tests or propagating elastic waves, entail localized pressure diffusion processes with a characteristic frequency depending on the pressure diffusivity and size of the heterogeneity. Then, on a macroscale, a homogeneous equivalent medium exists, which has a frequency-dependent effective conductivity.

The frequency-dependence of the conductivity can be analysed with Biot's equations of poroelasticity. In the quasi-static frequency regime of this framework the slow compressional wave is a proxy for pressure diffusion processes. This slow compressional wave is associated with the out-of-phase motion of the fluid and solid phase, thereby creating a relative fluid-solid displacement vector field. Decoupling of the poroelasticity equations gives a diffusion equation for the fluid-solid displacement field valid in a poroelastic medium with spatial fluctuations in hydraulic conductivity. The presence of spatial heterogeneities in hydraulic conductivity can be understood as a perturbation of the micro-structure of the medium, which affects the dissipation behaviour in Biot's equations. This, in turn, influences seismic attenuation and dispersion related to wave-induced fluid flow in a partially saturated rocks.

The chapter combines the journal paper " Caspari, E., B. Gurevich, and T. Müller (2013), Frequency-dependent effective hydraulic conductivity of strongly heterogeneous media, *Physical Review E*, *88*(4), 042119, " published by APS (Copyright 2013 by the American Physical Society) and a conference paper "Caspari, E., T. Müller, J. Rubino, and B. Gurevich (2013), Biot's slow wave and effective hydraulic conductivity in random media, in *Poromechanics V: Proceedings of the Fifth Biot Conference on Poromechanics*, pp. 217–226, ASCE" published by ASCE (Copyright 2013 by the American Society of Civil Engineers). In the first part of the chapter a theoretical model for a frequency-dependent effective conductivity is derived. In the last section, the influence of a frequency-dependent effective conductivity on the VSR of Sec. 5.2.1 is estimated.

6.1 Frequency-dependent effective hydraulic conductivity of strongly heterogeneous media

Computing an effective hydraulic conductivity is an integral part for the characterization of flow in heterogeneous porous media. If, in addition to the spatial heterogeneity, the temporal variation of the flow field is of importance, then the effective conductivity becomes time-dependent (*Dagan*, 1982), or equivalently, its Fourier transform will be a frequency-dependent quantity (*Indelman*, 1996). Oscillating flow, or generally, transient flows arise in hydrogeology and reservoir engineering in a number of contexts. Examples include diurnal variations (tides in surface water bodies affecting contiguous groundwater), seasonal variations (winter-summer variations in rainfall recharge) and pumping tests (*Sanchez-Vila et al.*, 2006). On a much shorter time-scale oscillating flows can be induced by seismic waves and may affect seismic signals (*Müller et al.*, 2007).

Though natural porous media are heterogeneous on many length scales, it is common in hydrogeology to classify spatial variability at three different scales: pore, formation, and regional (*Dagan*, 1986; *Gelhar*, 1986). In this paper we focus on the local or formation scale. As this local scale, heterogeneity is intermediate between pore-scale heterogeneities and regional scale heterogeneities; it is sometimes referred to as mesoscopic heterogeneity. Variability of the hydraulic conductivity at this mesoscopic scale in sedimentary aquifers occurs over lengths on the order of meters in the horizontal direction and on the centimeter scale in the vertical direction (*Murphy et al.*, 1984; *Gelhar*, 1986). It means that the characteristic length scale ℓ_{meso} of these heterogeneities obeys the relation

$$\ell_{\text{pore}} \ll \ell_{\text{meso}} \ll \ell_{\text{regional}} \,, \tag{6.1}$$

where ℓ_{pore} represents pore scale heterogeneity such as grain size or pore throat diameter and ℓ_{regional} is a proxy for the volume of investigation (support volume) such as the sample size or the seismic wavelength.

The definition of effective conductivity in the context of transient flow in ran-

dom media is problematic in general. This is because, in a strict sense, a true effective conductivity only exists if the support volume is infinite (*Nötinger* (1994); *Indelman* (1996); see also discussion in *Sanchez-Vila et al.* (2006)). Conversely, for a finite inhomogeneous medium, a pseudo-effective conductivity can be defined that depends on the spatial coordinates. Indeed, as shown by *Tartakovsky and Neuman* (1998), expressions for the pseudo-effective flow conductivity depend on the boundary conditions given at the surfaces of the support volume and hence on the relative proximity to these boundary surfaces. Only in the limit of an infinite support volume, their results converge to the results for an effective conductivity earlier presented by *Dagan* (1982). Then, the transient effective conductivity is expressed in terms of a frequency-dependent function. Recently, *Rabinovich et al.* (2013) analysed at which frequencies and conductivities dynamic effects become significant for a simple geometry and periodic time-variations.

There is at least one physical system in which low- and high-frequency regimes for dynamic-equivalent effective conductivity are meaningful. This is the case for oscillatory flows induced by propagating elastic waves (*Müller et al.*, 2007; *Müller et al.*, 2010). Such a system can be modelled using the theory of dynamic poroelasticity (*Biot*, 1962). In the low-frequency regime of this theory, propagating elastic waves couple with a diffusion wave, the so-called Biot slow compressional wave. This diffusion wave is a proxy for the fluid pressure diffusion process initiated at the interfaces of the mesoscopic heterogeneity. The wavelength λ of the propagating wave takes on the role of the support scale and, with Eq. (6.1), it is understood that $\lambda \gg \ell_{\mathrm{meso}}$. In order to have a physically meaningful effective conductivity, the diffusion length has to be significantly smaller than the support scale, i.e.

$$\lambda_{\mathrm{D}} \ll \lambda \,. \tag{6.2}$$

This is always fulfilled in Biot's low-frequency regime. Given that the diffusion and elastic wavelengths can be represented as $\lambda_{\mathrm{D}} \propto \sqrt{D/\omega}$ and $\lambda \propto c/\omega$ with the pressure diffusivity D, propagation velocity c and circular frequency ω, Eq. (6.2) implies that

$$\omega \ll c^2/D \,. \tag{6.3}$$

The latter relation yields a restriction on the largest frequency compatible with Eq. (6.2). Note, however, that c^2/D for fluid-saturated consolidated rocks is on the order of 10^5 Hz and is therefore not considered to be a severe limitation, even in the sonic frequency band, say 20 kHz. It is important to note that pore-scale heterogeneities are also responsible for a frequency-dependent conductivity. This phenomenon, however, is related to the cross-over from the viscosity- (Biot' low-frequency regime) to inertia-dominated regime (*Johnson et al.*, 1987; *Müller and Sahay*, 2011) and is outside the scope of our analysis.

A low-frequency regime for the effective hydraulic conductivity can then be defined in the sense that the wavelength of the diffusion wave λ_{D} is much larger than the characteristic heterogeneity size: $\lambda_{\mathrm{D}} \gg \ell_{\mathrm{meso}}$. A high-frequency regime exists if $\lambda_{\mathrm{D}} \ll \ell_{\mathrm{meso}}$. Then, the question about the meaning of spatial averaging arises given that the random media approach developed below makes use of the ergodicity assumption when replacing ensemble averages by spatial averages. However, as the wave propagates through the medium, local oscillatory flows are induced in different spatial domains such that the averages over these domains are representative of the ensemble average even in this high-frequency regime.

Previous works on effective conductivity in transient flow include *Indelman* (1996); *Dagan* (1982); *Müller and Gurevich* (2006). These results are based on weak-contrast perturbation theories and therefore limit their application to materials with weak permeability fluctuations. *Indelman* (2002) introduced a general mathematical model of average flow in media of random conductivity and storativity and analysed for which flow conditions an average flow model exists. The results of this study are not limited to weak heterogeneities. However no explicit solutions are given for the effective conductivity and storativity. *Tartakovsky and Neuman* (1998) used the residual flux theory to derive a second order approximation for the effective hydraulic conductivity which is valid for mildly heterogeneous media with a log conductivity variance of $\sigma^2 < 1$. Improved perturbation theories for steady state flow have been reported by *Hristopulos and Christakos* (1997) based on variational methods and by *Teodorovich* (1997) based on Feynman path integrals.

In this paper, we derive analytical expressions for a two-component medium with strong-contrast mesoscopic heterogeneities using the strong-contrast expansion method suggested in the context of the dynamic-equivalent dielectric constant (*Rechtsman and Torquato*, 2008). In the case of hydraulic conductivity, such a medium can be used to describe low-conductivity inclusions such as silt-clay deposits in a sandy aquifer or the opposite sand lenses embedded in a clayey-silty deposit (*Sanchez-Vila et al.*, 2006; *Revil and Cathles*, 1999). We further restrict our analysis to transient flow in a statistically isotropic, unbounded and stationary composite medium. The outline of the paper is as follows. First, we derive a diffusion equation for the relative fluid-solid displacement from Biot's equation of poroelasticity. To gain a better understanding of this diffusion mechanism, we perform numerical simulations for a 2D rock sample with strong fluctuations in hydraulic conductivity. Then, we formulate an integral equation for the case where the hydraulic conductivity exhibits a randomly fluctuating component. We then analyse this integral equation using the formalism suggested by *Rechtsman and Torquato* (2008) and derive strong-contrast expansions for the effective hydraulic conductivity in 1D and 3D. Finally, we give closed form expressions for some special cases and compare the results to the weak contrast expansion derived by *Müller and Gurevich* (2006).

6.1.1 Diffusion equation from Biot's theory of poroelasticity

Time-dependent flow in fluid-saturated porous media caused by transient effects of the head gradient can be analysed by a diffusion equation for the pore fluid pressure or head gradient. Various methods exist to estimate an effective hydraulic conductivity for unsteady flow based on an averaged Darcy's law in conjunction with the time-dependent continuity equation. *Chandler and Johnson* (1981) have shown that an equivalent diffusion equation is contained in the quasistatic limit of Biot's equations of poroelasticity.

Derivation

We start our analysis from Biot's equations (*Biot*, 1962) and derive a diffusion equation in terms of the relative fluid-solid displacement $\mathbf{w} = \phi(\mathbf{U} - \mathbf{u})$, where ϕ is the porosity, $\mathbf{U}$ and $\mathbf{u}$ are the macroscopic fluid and solid displacements, respectively. In the low-frequency regime, inertial coupling between the solid and fluid motion can be neglected and dissipation of energy can be attributed to viscous coupling only. In this case, Biot's slow P-wave is a pressure diffusion wave and the pressure diffusivity D depends on the fluid shear viscosity η, the permeability k and the poroelastic parameter N. The diffusivity is given by $D = \kappa N$, where the hydraulic conductivity κ is the ratio of permeability and fluid shear viscosity. Ignoring inertial effects and sources, Biot's equation of motion (2.8) in the quasistatic limit can be written in the frequency domain (the time-harmonic dependence $e^{-i\omega t}$ is omitted) as

$$\nabla \cdot \boldsymbol{\sigma} = 0, \tag{6.4}$$

$$\nabla p = \frac{i\omega}{\kappa_0}\mathbf{w}\,. \tag{6.5}$$

The constitutive relations are given by

$$\boldsymbol{\sigma} = [(H - 2G)\nabla \cdot \mathbf{u} + \alpha M \nabla \cdot \mathbf{w}]\mathbf{I} + G[\nabla \mathbf{u} + (\nabla \mathbf{u})^T] \tag{6.6}$$

$$-p = \alpha M \nabla \cdot \mathbf{u} + M \nabla \cdot \mathbf{w}\,, \tag{6.7}$$

where $\boldsymbol{\sigma}$ is the total stress tensor, p is the pore fluid pressure and $\mathbf{I}$ denotes the unit tensor. G and H are the shear wave modulus of the porous material and the undrained low-frequency P-wave modulus. The undrained P-wave modulus is defined as $H = L + \alpha^2 M$ with the dry P-wave modulus L, the Biot-Willis coefficient $\alpha = 1 - K_d/K_s$ and the fluid storage coefficient $M = [(\alpha - \phi)/K_s + \phi/K_f]^{-1}$. The parameters K_d, K_s, K_f denote the drained frame, the solid phase and the fluid phase bulk moduli, respectively.

Substituting the constitutive relations into the equilibrium condition for the total stress field (6.4) and Darcy's law (6.5) leads to a closed system of equations

for the displacement fields

$$\nabla \cdot \boldsymbol{\sigma} = \nabla \cdot [(H - 2G)(\nabla \cdot \mathbf{u})\mathbf{I} + \alpha M \nabla(\cdot \mathbf{w})\mathbf{I}] + \nabla \cdot G[\nabla \mathbf{u} + (\nabla \mathbf{u})^T] = 0 \quad (6.8)$$

$$\nabla[\alpha M \nabla \cdot \mathbf{u} + M \nabla \cdot \mathbf{w}] = -\frac{i\omega}{\kappa_0}\mathbf{w} - \mathbf{f}\,. \quad (6.9)$$

We further assume an irrotational displacement field ($\nabla \times \mathbf{u} = 0$) in an infinite domain and only pressure gradient sources $\mathbf{f}$ in the fluid phase, so that the system of Eqs. (6.8)-(6.9) reduces to

$$\nabla \cdot \sigma = \nabla \cdot [(H(\nabla \cdot \mathbf{u})\mathbf{I} + \alpha M(\nabla \cdot \mathbf{w})\mathbf{I}] = 0 \quad (6.10)$$

$$\nabla[\alpha M \nabla \cdot \mathbf{u} + M \nabla \cdot \mathbf{w}] = -\frac{i\omega}{\kappa_0}\mathbf{w} - \mathbf{f}\,. \quad (6.11)$$

Using the vector identity $\nabla \cdot (\nabla \cdot \mathbf{u})\mathbf{I} = \nabla\nabla\cdot$ and eliminating the solid displacement field $\mathbf{u}$ yields an inhomogeneous diffusion equation for the relative fluid-solid displacement field

$$N \nabla\nabla \cdot \mathbf{w} + \frac{i\omega}{\kappa_0}\mathbf{w} = -\,\mathbf{f} \quad (6.12)$$

with $N = \frac{ML}{H}$. This longitudinal vector Helmholtz equation can be interpreted as a diffusion equation for the slow P-wave. The slow P-wave is then a diffusion wave with the wave number $k_0 = \sqrt{i\omega/\kappa_0 N}$ in a homogeneous medium.

Green's function solution

The formal solution of Eq. (6.12) for the relative fluid-solid displacement can be written as an integral equation

$$\mathbf{w}(\mathbf{r}) = \mathbf{w}_0(\mathbf{r}) + \int_V dV' \mathbf{G}_0(\mathbf{r}, \mathbf{r}'; \omega) \cdot (-\mathbf{f})\,, \quad (6.13)$$

where $\mathbf{w}_0$ is the solution of the homogeneous equation (Eq. (6.12) with $\mathbf{f}$=0) and the volume integral is the particular solution with $-\mathbf{f}$ being a pressure gradient source. The Green's function $\mathbf{G}_0(\mathbf{r}, \mathbf{r}'; \omega)$ has to fulfill the tensor differential

equation

$$N\nabla\nabla\cdot\mathbf{G}_0(\mathbf{r},\mathbf{r}';\omega)+\frac{i\omega}{\kappa_0}\mathbf{G}_0(\mathbf{r},\mathbf{r}';\omega)=\delta_l(\mathbf{r}-\mathbf{r}')\mathbf{I}\,. \tag{6.14}$$

where $\delta_l(\mathbf{r}-\mathbf{r}')\mathbf{I}$ is the longitudinal part of the dyadic Dirac delta function (*Morse and Feshbach*, 1953) with $\mathbf{r}'$ and $\mathbf{r}$ being the position vectors of the source and the observation points, respectively. The corresponding infinite space Green's function $\mathbf{G}_0(\mathbf{r},\mathbf{r}';\omega)$ for a homogeneous isotropic medium outside of the source region ($\mathbf{r}\neq\mathbf{r}'$) is given by (*Müller and Gurevich*, 2006; *Karpfinger et al.*, 2009)

$$\begin{aligned}\mathbf{G}_0(\mathbf{r},\mathbf{r}';\omega)&=-\frac{\kappa_0}{i\omega}\nabla\nabla\frac{e^{ik_0r}}{4\pi r}\\&=-\frac{\kappa_0}{i\omega}\left[k_0^2r^2\frac{e^{ik_0r}}{4\pi r^3}\hat{\mathbf{r}}\hat{\mathbf{r}}+(1-ik_0r)\frac{e^{ik_0r}}{4\pi r^3}(\mathbf{I}-\mathbf{3}\hat{\mathbf{r}}\hat{\mathbf{r}})\right].\end{aligned} \tag{6.15}$$

In the second line, the Green's function is represented as the sum of the longitudinal far field (polarisation: $\hat{\mathbf{r}}\hat{\mathbf{r}}$)and near field (polarisation $\mathbf{I}-\mathbf{3}\hat{\mathbf{r}}\hat{\mathbf{r}}$). In the source region $\mathbf{r}=\mathbf{r}'$, care has to be taken when interchanging the differential operator and integration to obtain the integral equation (6.13). The singularity of the Green's function at $\mathbf{r}=\mathbf{r}'$ has to be properly taken into account by excluding an infinitesimal volume around the singularity (*Torquato*, 2002). This leads to a Dirac delta contribution in the dyadic Green's function of the form (*Belinfante*, 1946)

$$\mathbf{G}_\delta(\mathbf{r},\mathbf{r}';\omega)=-\frac{2}{3}\frac{\kappa_0}{i\omega}\delta(\mathbf{r}-\mathbf{r}')\mathbf{I}\,. \tag{6.16}$$

This source dyadic accounts for the depolarisation of the excluded volume and, in general, depends on the shape of the specified exclusion volume. Eq. (6.16) corresponds to a spherical exclusion volume. The resulting dyadic Green's function is valid for all $\mathbf{r}$ including the source region and can be expressed as

$$\mathbf{G}(\mathbf{r},\mathbf{r}';\omega)=\mathbf{G}_\delta(\mathbf{r},\mathbf{r}';\omega)+\mathbf{G}_H(\mathbf{r},\mathbf{r}';\omega)\,, \tag{6.17}$$

where the regular part $\mathbf{G}_H(\mathbf{r},\mathbf{r}';\omega)$ is given by Eq. (6.15).

In the 1D case, the Green's function does not possess a singularity, and has a simple form

$$G_0 = \frac{e^{ik_0|x|}}{2k_0 i}. \tag{6.18}$$

In the following sections, we analyse the diffusion process for the slow P-wave in the presence of strong fluctuations in hydraulic conductivity. As a first step, we perform numerical simulations to elucidate the characteristics of the diffusion wave (Biot's slow wave) in an inhomogeneous medium.

6.1.2 Numerical simulations of the diffusion process in a medium with conductivity heterogeneities

Rubino et al. (2012) have shown that the influence of hydraulic conductivity fluctuations on the fast P-wave signatures can be analysed using oscillatory compressibility simulations based on Biot's quasi-static poroelastic equations. In this work, we follow a similar approach to study the influence of these kinds of heterogeneities on slow P-waves. We consider a 2D water-saturated rock sample containing mesoscopic hydraulic conductivity fluctuations. The spatial distribution of the logarithm of the hydraulic conductivity is obtained by using a von-Karman spectral density function with a correlation length a of 10 cm and a Hausdorff fractal dimension $D = 2.5$ (Figure 6.1a). The fractal dimension $D = E + 1 - H$ depends on the Euclidean dimension E and the roughness and complexity of the random process described by the parameters H (*Tronicke and Holliger*, 2005). The spectral density function is given by

$$S_d(k_x, k_y) = S_0(1 + k_x^2 a_x^2 + k_y^2 a_y^2)^{-(H+E)/2}, \tag{6.19}$$

where k_x,k_y and a_x,a_y are the horizontal and vertical wavenumbers and correlation length, respectively and the parameter S_0 is a normalization constant (*Rubino and Holliger*, 2012). All other physical properties of the rock are spatially constant and summarized in Table 6.1.

Table 6.1: Rock and fluid properties for the numerical example

K_s (GPa)	ρ_s (g/cm^3)	K_m (GPa)	G (GPa)	ϕ	K_f (GPa)	η (Pa s)
37	2.65	12.1	14.4	0.2	2.25	0.003

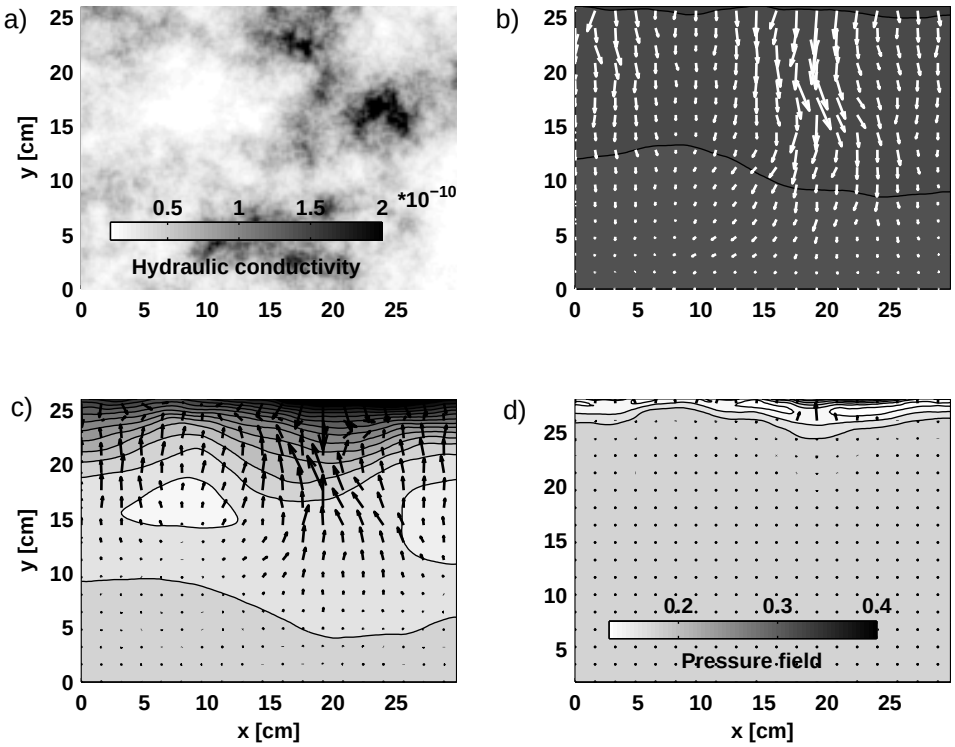

Figure 6.1: a) Hydraulic conductivity and fluid pressure fields for a frequency of b) 1Hz, c) 31.6 Hz and d) 1kHz. The arrows indicate the relative solid-fluid displacement field.

At the top of the sample a plane diffusion wave is generated, and the quasi-static poroelastic equations are solved to obtain the behaviour of the slow P-wave. In order to study the characteristics of such fluid pressure perturbation, the simulations are repeated for three different frequencies (1 Hz, 31.6 Hz and 1 kHz). Figures 6.1 b), c) and d) show the fluid pressure and relative fluid-solid displacement fields obtained in each case.

For the lowest frequency (Figure 6.1 b), the pressure differences are rather small. This is expected, as the diffusion wavelength is comparable to the size of the sample and, therefore, much larger than the typical size of the heterogeneities. Consequently, there is enough time during each half-cycle for the pore fluid pressure to equilibrate and thus the relative solid-fluid displacement field points in the main flow direction.

At a frequency of 31.6 Hz (Figure 6.1c), elevated pressure regions occur in the high conductivity channel ($x = 20$ cm, $y = 15$ cm) and at the same time pressure sinks are created in the low conductivity regions ($x = 7.5$ cm, $y = 25$ cm). This results in local pressure gradients with orientations different from the main flow direction. The relative solid-fluid displacement adjusts accordingly with upward pointing components. This local, upward pointing field can be understood as a poroelastic polarisation field since the local relative displacement fields have components opposite to the plane diffusion wave.

For 1kHz (Figure 6.1 d) the diffusion wave senses only the immediate vicinity of the top of the sample. In this case the diffusion wavelength is smaller than the typical heterogeneity size and local flows (i.e. polarisation fields) occur at spatial scales smaller than the characteristic correlation length.

These snapshots illustrate that the induced polarisation field depends on the frequency. Therefore, a corresponding effective hydraulic conductivity for a heterogeneous conductivity field should be frequency-dependent. The presence of heterogeneities in hydraulic conductivity can be understood as a perturbation of the microstructure of the medium, which affects the dissipation behaviour (diffusivity of the medium). In the next section, we analyse the diffusion equation in a medium with strong fluctuations in hydraulic conductivity and apply a perturbation theory to derive closed form expressions for an effective hydraulic conductivity.

6.1.3 Diffusion equation for a heterogeneous medium

In a heterogeneous medium, the diffusion wave (slow P-wave) will be attenuated and dispersed due to multiple scattering at inhomogeneities. In such a random medium, the poroelastic coefficients vary spatially and, therefore, they can be seen as random parameters describing the inhomogeneities of the medium. We consider the random parameter $q(\mathbf{r}) = i\omega/\kappa(\mathbf{r})$, in which only the hydraulic conductivity varies spatially while all other poroelastic parameters are constant.

Since we assume in the following analysis a random two-component medium, the perturbed microstructure can be thought of as a 'double conductivity structure' with constant porosity. Locally, the 'double conductivity structure' is defined by $q(\mathbf{r}) = q_1 I^{(1)}(\mathbf{r}) + q_2 I^{(2)}(\mathbf{r})$, where $I^{(1)}(\mathbf{r})$ and $I^{(2)}(\mathbf{r})$ are indicator functions for component one and two, respectively. The indicator function $I^{(j)}(\mathbf{r})$ for a component j can be written as

$$I^{(j)}(\mathbf{r}) = \begin{cases} 1 & \mathbf{r} \text{ in } \Omega_j \\ 0 & \text{otherwise,} \end{cases}$$

where the domain Ω_j is occupied by the component $j = 1, 2$. Ensemble averaging of the indicator functions leads to n-point probability functions

$$S_n^{(j)} = \langle I^{(j)}(r_1) I^{(j)}(r_2) .... I^{(j)}(r_n) \rangle \tag{6.20}$$

which contain micro-structural information of the random heterogeneous medium (*Torquato*, 2002). The angular brackets denote ensemble averaging and ergodicity (ensemble averaging and spatial averaging are equivalent) is assumed. The complete statistical information about a random medium is needed to evaluate its properties (*Brown Jr*, 1955). However, approximations based on lower- order truncated statistical moments can provide good estimates of the effective hydraulic conductivity. In the following, we take into account only the one-point $S_1^{(j)}$ and two-point $S_2^{(j)}$ probability functions. $S_1^{(j)}$ gives the probability that a randomly chosen point belongs to component j, which is equivalent to the volume concentration of this component, whereas $S_2^{(j)}$ reflects the extent to which properties at two points are correlated in the system.

Following the formalism suggested by *Rechtsman and Torquato* (2008), we assume that the random medium is embedded in an infinite homogeneous reference medium. Hence, the random medium can be regarded to cause perturbations with respect to the reference medium. This is expressed by a perturbing operator $\tilde{l}$. This operator contains fluctuations of the reciprocal hydraulic conductivity

and is given by

$$\tilde{l} = q(\mathbf{r}) - q_0 = i\omega \left(\frac{1}{\kappa_j} - \frac{1}{\kappa_0} \right) I^{(j)}(\mathbf{r}) = \frac{i\omega}{\kappa_0} \left(\frac{\kappa_0 - \kappa_j}{\kappa_j} \right) I^{(j)}(\mathbf{r}), \tag{6.21}$$

where the conductivity κ_j is either associated with component one or two and κ_0 is the conductivity of the reference medium. In general, the reference medium can be freely chosen and defines about which microstructure the expansion perturbs. For example, if the reference medium is chosen to be one of the components of the composite medium, then the effective conductivity can be interpreted to perturb about the optimal microstructure of the two-phase Hashin-Shtrikman bounds (*Pham and Torquato*, 2003).

The homogeneous diffusion equation in the presence of the random parameter field q($\mathbf{r}$) is

$$N\nabla\nabla \cdot \mathbf{w}(\mathbf{r}) + q(\mathbf{r})\mathbf{w}(\mathbf{r}) = 0\,. \tag{6.22}$$

Substituting Eq. (6.21) into Eq. (6.22) leads to

$$N\nabla\nabla \cdot \mathbf{w}(\mathbf{r}) + \frac{i\omega}{\kappa_0}\mathbf{w}(\mathbf{r}) = -\,\tilde{l}\mathbf{w}(\mathbf{r})\,. \tag{6.23}$$

The left hand side of Eq. (6.23) is a partial differential equation with constant coefficients and the right hand side can be interpreted as a source term due to the presence of random fluctuations. Then, the formal solution to Eq. (6.23) can be written as

$$\mathbf{w}(\mathbf{r}) = \mathbf{w}_0(\mathbf{r}) + \int_V dV' \mathbf{G}(\mathbf{r}, \mathbf{r}'; \omega)\mathbf{P}(\mathbf{r}) \tag{6.24}$$

$$\text{with} \quad \mathbf{P}(\mathbf{r}) = \tilde{l}\mathbf{w}(\mathbf{r})\,, \tag{6.25}$$

where $\mathbf{P}$ can be interpreted as a poroelastic polarisation field caused by induced local pressure gradients relative to the reference medium, which in turn, induce local oscillatory flows. These local sources occur only in the embedded random medium and hence the polarisation field is zero in the reference medium. The

displacement field $\mathbf{w}_0$ is an external field acting as an external source term on the total displacement field (*Ramshaw*, 1984) equivalent to the plane diffusion wave generated in the numerical experiment. Note that the integral is taken over the volume of the embedded random medium and therefore the solution depends on the boundary condition at the surface of the random medium volume.

6.1.4 Statistical approach

To derive a perturbation expansion for the effective hydraulic conductivity, we apply the formalism described by *Rechtsman and Torquato* (2008) to the integral equation (6.24). Instead of obtaining an expansion for the total field $\mathbf{w}$, an auxiliary field is introduced in this formalism. It consists of the field outside of the source regions ($\mathbf{r} \neq \mathbf{r}'$). We call this field the cavity displacement field in analogy to the cavity intensity field in the dielectric context (*Rechtsman and Torquato*, 2008). The perturbation expansion leads to expressions for the effective conductivity in 1D and 3D that only depend on the choice of the reference medium and the statistical properties of the medium.

Strong contrast expansion in 3D

Cavity displacement field The integral in Eq. (6.24) for the total field can be further divided into

$$\mathbf{w}(\mathbf{r}) = \mathbf{w}_0(\mathbf{r}) + \int_{V_\delta} dV' \mathbf{G}_\delta(\mathbf{r}, \mathbf{r}'; \omega)\mathbf{P}(\mathbf{r}) + \int_{V - V_\delta} dV' \mathbf{G}_H(\mathbf{r}, \mathbf{r}'; \omega)\mathbf{P}(\mathbf{r}) \,, \quad (6.26)$$

where V_δ is the exclusion volume. The first integral is the contribution of the field inside the source region in the limit $r \to r'$ (self-depolarisation), whereas the second integral denotes the scattered field outside of the source regions. From Eq. (6.26), we define the cavity displacement field, i.e. the total field without the field inside of the source regions as

$$\mathbf{w}_c(\mathbf{r}) \equiv \mathbf{w}(\mathbf{r}) - \int_{V_\delta} dV' \mathbf{G}_\delta(\mathbf{r}, \mathbf{r}'; \omega)\mathbf{P}(\mathbf{r}). \quad (6.27)$$

Then, from Eq. (6.26) it follows that this cavity displacement field is given by

$$\mathbf{w}_c(\mathbf{r}) = \mathbf{w}_0(\mathbf{r}) + \int_{V-V_\delta} dV' \mathbf{G}_H(\mathbf{r}, \mathbf{r}'; \omega)\mathbf{P}(\mathbf{r}) \,. \tag{6.28}$$

Here the integral is the principal value of the integral in Eq. (6.24) in the limit that the exclusion volume shrinks to zero (*Torquato*, 2002). Comparing the expressions (6.27) and (6.28) and using Eqs. (6.16) and (6.21) yields the relationship between the total field and cavity displacement field

$$\mathbf{w}(\mathbf{r}) = \left(\frac{3\kappa_j}{2\kappa_0 + \kappa_j} \right) I^{(j)}(\mathbf{r}) \mathbf{w}_c(\mathbf{r}) \,. \tag{6.29}$$

From Eq. (6.25) and Eq. (6.29), it follows that the cavity displacement field is directly related to the polarisation field by

$$\mathbf{P}(\mathbf{r}) = \underbrace{\frac{3i\omega}{2\kappa_0}}_{c} \underbrace{\frac{\kappa_0 - \kappa_j}{\kappa_0 + (1/2)\kappa_j} I^{(j)}(\mathbf{r})}_{\tilde{L}} \mathbf{w}_c(\mathbf{r}) \equiv c\tilde{L}\mathbf{w}_c(\mathbf{r}) \,, \tag{6.30}$$

where the constant parameter c contains the reciprocal of the depolarisation factor (2/3) and the wave number. $\tilde{L}$ can be understood as a generalized polarisability of the medium. Both the cavity displacement field and the polarisability depend on the geometry of the exclusion volume (*Torquato*, 2002).

Effective operator We aim to replace the random medium by a homogeneous medium with an effective operator L^*. In order to achieve this, we take an ensemble average of Eq. (6.30). If such an effective homogeneous medium exists then the average polarisation field is related to the averaged cavity displacement field by

$$\langle \mathbf{P}(\mathbf{r}) \rangle = cL^* \langle \mathbf{w}_c(\mathbf{r}) \rangle \,. \tag{6.31}$$

We further assume that L^* is of the same functional form as the polarisabilities $\tilde{L}$:

$$L^* = \frac{\kappa_0 - \kappa^*}{\kappa_0 + (1/2)\kappa^*} \,, \tag{6.32}$$

where κ^* denotes the searched-for effective hydraulic conductivity.

Expression for L^* In order to find an expression for the effective perturbing operator L^*, or equivalently, the effective hydraulic conductivity, we seek a second relation between the averaged polarisation field $\langle \mathbf{P} \rangle$ and the averaged cavity displacement field $\langle \mathbf{w}_c \rangle$.
Eq. (6.28) with Eq. (6.30) leads to an implicit integral equation for the cavity displacement field

$$\mathbf{w}_c(\mathbf{r}) = \mathbf{w}_0(\mathbf{r}) + \int_{V-V_\delta} dV' \mathbf{G}_H(\mathbf{r}, \mathbf{r}'; \omega) \underbrace{c\tilde{L}\mathbf{w}_c(\mathbf{r})}_{\mathbf{P}(\mathbf{r})}, \tag{6.33}$$

Multiplying this equation by the perturbing operator $c\tilde{L}$ and iteratively substituting it in itself leads to a solution for the polarisation field in form of a scattering series $\mathbf{S}$. Ensemble averaging of this scattering series yields in operator form (integral signs are omitted)

$$\langle \mathbf{P} \rangle = c\langle \tilde{L} \rangle \mathbf{w}_0 + c^2 \langle \tilde{L} \mathbf{G}_H \tilde{L} \rangle \mathbf{w}_0 + c^3 \langle \tilde{L} \mathbf{G}_H \tilde{L} \mathbf{G}_H \tilde{L} \rangle \mathbf{w}_0 ... \equiv \langle \mathbf{S} \rangle \mathbf{w}_0 \,. \tag{6.34}$$

Since we are interested in a solution for an infinite random medium, the Sommerfeld radiation condition applies. This condition requires that the field $\mathbf{P}$ has no sources at infinity. A problem arises when the external field $\mathbf{w}_0$ does not vanish as $r \to \infty$. Consequently, the infinite random medium will depend on the chosen geometry of the embedded medium (*Ramshaw*, 1984). To avoid this problem, we replace the external field with fields that are only non-zero in the embedded random medium. Such an expression is obtained by solving the scattering series for $\mathbf{w}_0$ by successive substitution in itself (*Brown Jr*, 1955). Considering only terms to second order we obtain

$$\mathbf{w}_0 = \frac{\langle \mathbf{P} \rangle}{c\langle \tilde{L}(\mathbf{r}) \rangle} - \frac{\langle \tilde{L}(\mathbf{r}) \mathbf{G}_H \tilde{L}(\mathbf{r}') \rangle}{\langle \tilde{L}(\mathbf{r}) \rangle \langle \tilde{L}(\mathbf{r}') \rangle} \langle \mathbf{P} \rangle .... = \langle \mathbf{S} \rangle^{-1} \langle \mathbf{P} \rangle \,. \tag{6.35}$$

Substituting the scattering series for $\mathbf{w}_0$ back into Eq. (6.28) and ensemble averaging provides the final relation between the averaged cavity displacement and

polarisation field

$$\begin{aligned}\langle \mathbf{w}_c \rangle =& [\langle \mathbf{S} \rangle^{-1} + \mathbf{G}_H] \langle \mathbf{P} \rangle \\ =& \frac{\langle \mathbf{P}(\mathbf{r}) \rangle}{c \langle \tilde{L}(\mathbf{r}) \rangle} - \int_V dV \frac{\langle \tilde{L}(\mathbf{r}) \tilde{L}(\mathbf{r}') \rangle - \langle \tilde{L}(\mathbf{r}) \rangle \langle \tilde{L}(\mathbf{r}') \rangle}{\langle \tilde{L}(\mathbf{r}) \rangle \langle \tilde{L}(\mathbf{r}') \rangle} \langle \mathbf{P}(\mathbf{r}, \mathbf{r}') \rangle \mathbf{G_H}(\mathbf{r}, \mathbf{r}'; \omega) \,.\end{aligned} \tag{6.36}$$

In expression (6.36), we can take the integral over the infinite volume and hence it becomes independent of the geometry of the embedded random medium. $\langle \tilde{L}(\mathbf{r}) \rangle$ and $\langle \tilde{L}(\mathbf{r}) \tilde{L}(\mathbf{r}') \rangle - \langle \tilde{L}(\mathbf{r}) \rangle \langle \tilde{L}(\mathbf{r}') \rangle$ are the one-point and two-point correlation functions. Assuming an isotropic two-component medium, we obtain the following relations

$$\langle \tilde{L}(\mathbf{r}) \rangle = L_1 \phi_1 + L_2 \phi_2 \equiv \bar{L} \quad \text{with } L_1 = \frac{(\kappa_0 - \kappa_1)}{\kappa_0 + (1/2)\kappa_1} \,,\; L_2 = \frac{(\kappa_0 - \kappa_2)}{\kappa_0 + (1/2)\kappa_2} \tag{6.37}$$

$$\frac{\langle \tilde{L}(\mathbf{r}) \tilde{L}(\mathbf{r}') \rangle - \langle \tilde{L}(\mathbf{r}) \rangle \langle \tilde{L}(\mathbf{r}') \rangle}{\langle \tilde{L}(\mathbf{r}) \rangle \langle \tilde{L}(\mathbf{r}') \rangle} = \frac{(L_1 - L_2)^2 \phi_1 \phi_2}{(L_1 \phi_1 + L_2 \phi_2)^2} \, S_2(\mathbf{r}) = \sigma_{LL}^2 \, S_2(\mathbf{r}) \,, \tag{6.38}$$

where $S_2(\mathbf{r})$ denotes the two-point probability function and κ_1, κ_2 are the hydraulic conductivities of the medium components. Expression (6.37) is the mean value ($\bar{L}$) and σ_{LL}^2 (in Eq. (6.38)) is the normalized variance of the polarisability L. The parameters L_1 and L_2 denote the polarisabilities of one component, κ_1 or κ_2, with respect to the reference medium.

A comparison between the term $\langle \mathbf{S} \rangle^{-1} + \mathbf{G}_H$ in Eq. (6.36) and L^{*-1} in Eq. (6.31) results in the searched-for expression for the effective operator L^*:

$$\frac{1}{L^*} = \frac{1}{\bar{L}} - \sigma_{LL}^2 c \int_V dV' S_2(\mathbf{r}) \, \mathbf{G}_H(\mathbf{r}, \mathbf{r}'; \omega) \,. \tag{6.39}$$

The normalized variance σ_{LL}^2 determines the magnitude of the perturbation, while the integral describes the spatial correlation of the heterogeneities. Eq. (6.39) can be solved for the effective hydraulic conductivity. Since we assume a statistically isotropic medium, the integral in Eq. (6.39) simplifies to

$$\int_{-\infty}^{\infty} dV' S_2(\mathbf{r}) \, \frac{Tr(\mathbf{G}_H(\mathbf{r}, \mathbf{r}'; \omega))}{3} = -\frac{1}{3N} \int_0^{\infty} dr \, S_2(\mathbf{r}) \, r e^{ik_0 r} \,, \tag{6.40}$$

where we have taken the trace of the dyadic Green's function and integrated over angular coordinates. The simplified integral Eq. (6.39) for the effective operator L^* given by

$$\frac{1}{L^*} = \frac{1}{\bar{L}} + \frac{1}{2} k_0^2 \sigma_{LL}^2 \int_0^\infty dr\, S_2(\mathbf{r})\, r e^{ik_0 r} \tag{6.41}$$

is the central result of the paper. It shows how L^* in a three- dimensional random two-component medium can be obtained from the statistical properties of the medium. In the next section, we derive a similar expression for the effective operator in 1D.

Strong contrast expansion in 1D

The derivation in 1D is simpler since the Green's function does not contain a singularity. Instead of finding an expression for the average cavity displacement field $\mathbf{w}_c(\mathbf{r})$, we seek a solution of the average fluid-solid displacement field w in 1D from the integral equation

$$w(x) = w_0(x) + \int d(x - x') G_0(x - x'; \omega) P \quad \text{with} \quad P = k_0^2 \tilde{l} w(x) \tag{6.42}$$

where $\tilde{l}$ is given by

$$\tilde{l} = \left(\frac{\kappa_0 - \kappa_j}{\kappa_j} \right) I^{(j)}(x) \tag{6.43}$$

and the effective operator l^* is defined as

$$l^* = \left(\frac{\kappa_0 - \kappa^*}{\kappa^*} \right) . \tag{6.44}$$

Following the steps in Section 6.1.4 to eliminate the external filed $w_0(x)$ yields a similar integral equation for the effective operator l^* in 1D

$$\frac{1}{l^*} = \frac{1}{\bar{l}} - \sigma_{\tilde{l}\tilde{l}}^2 k_0^2 \int_{-\infty}^\infty S_2(x - x')\, G_0(x - x'; \omega) d(x - x') \,. \tag{6.45}$$

In the remaining sections of the paper, we give closed-form expressions for the effective conductivity in 3D and 1D for a specific correlation function and analyse

the frequency dependence of the effective conductivity in detail. Further, we compare the new results with the results obtained by *Müller and Gurevich* (2006).

6.1.5 Analysis of frequency dependence

We considered Biot's equation of poroelasticity in the quasi-static limit by neglecting the inertial terms and derived a strong contrast expansion for the effective hydraulic conductivity. Another requirement for the validity of our results is that the characteristic length of the heterogeneities is small compared to the wavelength of the propagating wave (support scale). However, even under these conditions, the effective hydraulic conductivity κ^* is frequency-dependent. This can physically be attributed to the fact that local oscillatory flow occurs due to accumulation and depletion processes at randomly spaced inhomogeneities (Sec.6.1.2). The relaxation time of this process depends on the characteristic size of the medium heterogeneities compared to the diffusion wavelength $\lambda_D = 2\pi\sqrt{D/\omega}$.

Exact results of the frequency limits are known for the effective hydraulic conductivity κ^* in 1D which is bounded by the arithmetic and harmonic average in the high and low-frequency limits (*Matheron*, 1967), respectively. In general, the low-frequency limit in a 3D heterogeneous medium depends on all details of the microstructure of the medium (*Indelman*, 1996). The exact low-frequency limit of effective conductivity in a 3D heterogeneous medium is known only for certain optimal micro structures.

Low- and high frequency limits - strong contrast expansion

In order to analyse the frequency limits of the strong contrast expansion in 1D and 3D, we choose an exponential correlation function $e^{(-|(r-r')/d|)}$ for S_2 in Eq. (6.45) and (6.39). Here d is the correlation length describing the characteristic size of heterogeneities. A free parameter in the above theory is the reference medium conductivity.

A natural choice in 1D for a two-component random medium is either component one or two. This leads to a closed form expression for the effective hydraulic

conductivity

$$\kappa^* = \frac{\kappa_2\kappa_h + \kappa_a\kappa_h k_0 d}{\kappa_2 + \kappa_h k_0 d}\,, \tag{6.46}$$

where k_0, κ_a, κ_h are the wave number of the reference medium with $\kappa_0 = \kappa_1$, the arithmetic average and the harmonic average, respectively. The low - and high frequency limits of Eq. (6.46) are

$$\kappa^*(\omega \to 0) = \kappa_h, \quad \kappa^*(\omega \to \infty) = \kappa_a$$

which agree with the exact bounds in 1D. In fact, the strong contrast expansion converges to the low-frequency limit for arbitrary contrasts and regardless of the choice of the reference medium. This is because in a 1D medium there is only one realisable two-phase microstructure, since in the low-frequency limit, the effective conductivity does not depend on the sequence of the layers and their thicknesses.

The 3D effective hydraulic conductivity for an exponential correlation function $S_2(\mathbf{r}) = e^{(-|(r-r')/d|)}$ can be obtained from Eq (6.41) as follows

$$\frac{1}{L^*} = \frac{\kappa_0 + (1/2)\kappa*}{\kappa_0 - \kappa*} = \frac{1}{L_1\phi_1 + L_2\phi_2} - \frac{(L_1 - L_2)^2}{(L_1\phi_1 + L_2\phi_2)^2} A\,, \tag{6.47}$$

where the frequency dependence is contained in

$$A = -\frac{1}{2}\phi_2\phi_1 \frac{k_0^2 d^2}{k_0^2 d^2 + 2ik_0 d - 1}\,.$$

The conductivity of the reference medium κ_0 is kept as a free parameter and $k_0 = \sqrt{i\omega/\kappa_0 N}$ is the wave number for the respective reference medium.

In the low-frequency limit, the term A vanishes and in the high frequency limit, A reduces to $-1/2\phi_1\phi_2$. Using Eqs. (6.37), (6.38) and (6.47) the limits of

the effective hydraulic conductivity can be expressed as

$$\kappa^*(\omega \to 0) = \kappa_0 \left(1 - \frac{3}{2} \frac{\langle L \rangle}{1 + \frac{1}{2}\langle L \rangle}\right) \tag{6.48}$$

$$\kappa^*(\omega \to \infty) = \kappa_0 \left(1 - \frac{3}{2} \frac{\langle L \rangle}{1 + \frac{1}{2}\frac{\langle L^2 \rangle}{\langle L \rangle}}\right) . \tag{6.49}$$

In both cases, κ^* is a real number. Further, from Eqs. (6.49) and (6.48), it directly follows that $\kappa^*(\omega \to \infty) \geq \kappa^*(\omega \to 0)$, independently of the choice of the reference medium, since the variance $\langle L^2 \rangle - \langle L \rangle^2$ is always positive.

If we choose the reference medium to be component one or two, it can be shown, after some algebra, that the high-frequency limit of the effective hydraulic conductivity yields

$$\kappa^*(\omega \to \infty) = \phi_1 \kappa_1 + \phi_2 \kappa_2 = \kappa_a \, . \tag{6.50}$$

In the low-frequency limit, the effective hydraulic conductivity can be written as

$$\frac{\kappa_0 - \kappa^*}{\kappa^* + 2\kappa_0} = \frac{\kappa_0 - \kappa_1}{\kappa_1 + 2\kappa_0}\phi_1 + \frac{\kappa_0 - \kappa_2}{\kappa_2 + 2\kappa_0}\phi_2 \, . \tag{6.51}$$

This coincides with the generalized Maxwell approximation (*Benveniste*, 1987a). The low-frequency limit depends on the choice of the reference medium, since the expansion is constructed in the sense that it perturbs around a certain micro structure. For a reference medium choice with $\kappa_0 > max(\kappa_1, \kappa_2)$, the low frequency limit coincides with the upper multiphase Hashin Shtrikman bound and for $\kappa_0 < min(\kappa_1, \kappa_2)$ with the lower multiphase Hashin Shtrikman bound (*Torquato*, 2002). In case that the reference medium is chosen to be component one, the result leads to the lower (HS^-) or upper (HS^+) Hashin-Shtrikman bound

$$\kappa^*(\omega \to 0) = \kappa_a + \frac{\phi_1 \phi_2 (\kappa_2 - \kappa_1)^2}{3\kappa_1 - \phi_1(\kappa_2 - \kappa_1)} \tag{6.52}$$

$$HS^- : \quad \kappa_1 < \kappa_2 \quad HS^+ : \quad \kappa_1 > \kappa_2$$

These are the narrowest bounds for a macroscopically isotropic two-component

medium if only the volume fractions are specified (*Markov and Preziosi*, 2000). For optimal microstructures such as the coated sphere model or coated laminates, the bounds provide the exact effective conductivity values. These optimal composites have the property that for the lower (upper) bound, the medium with the smaller (larger) conductivity is the connected percolating component. Such a choice of the reference medium means in turn that the strong-contrast expansion at the two-point level is a good approximation, only if the reference medium is the connected component. The reason is that the two-point correlation function does not incorporate information about the connectivity of the medium components and thus does not account for their percolation behaviour. In this sense, the strong-contrast expansion yields reliable predictions only for a small number of inclusions (low volume fraction) below the percolation threshold, which do not build large clusters (*Torquato*, 2002). *Rechtsman and Torquato* (2008) suggest a practical way to circumvent this problem by interpolating between the expressions, that attain the lower and upper bound, around the percolation threshold. However, to account for the percolation behaviour higher-order microstructural information is necessary, which will lead to narrower bounds on the low-frequency limit (*Markov and Preziosi*, 2000). For real materials, such detailed information is rarely available.

6.1.6 Comparison between weak- and strong-contrast methods

Several approximations exist for the effective hydraulic conductivity for transient flow in an unbounded isotropic and stationary domain. *Indelman* (1996) has derived a local expression for the effective hydraulic conductivity in the Fourier-Laplace domain. The results are in agreement with the weak contrast expansion derived by *Müller and Gurevich* (2006) based on Biot's equation of poroelasticity. We compare the results obtained from the strong contrast expansion to the results obtained by *Müller and Gurevich* (2006). The weak contrast expansions in 1D

and 3D for an exponential correlation function are given by

$$\kappa_e = \kappa_a \left(1 - \sigma^2_{\kappa\kappa} + \sigma^2_{\kappa\kappa} \frac{k_0 d}{k_0 d + i}\right) \quad \text{(1D)}\,, \tag{6.53}$$

$$\kappa_e = \kappa_a \left(1 - \frac{\sigma^2_{\kappa\kappa}}{3} - \frac{\sigma^2_{\kappa\kappa}}{3} \frac{(k_0 d)^2}{1 - (k_0 d)^2 - 2ik_0 d}\right) \quad \text{(3D)}\,. \tag{6.54}$$

Here k_0 denotes the wave number of a homogeneous background medium with $\kappa_0 = \kappa_a$ and $\sigma^2_{\kappa\kappa}$ is the normalized variance of κ.

A principal difference between the strong contrast expansion and the method of statistical smoothing applied by *Müller and Gurevich* (2006) is the underlying medium parameterisation. While the former approach is based on a discrete two-component random medium, the latter is based on a continuous random medium (Figure 6.2). However, the two methods can be compared if equivalent values for the medium parameters are chosen. Note that the weak-contrast expansion is an approximation for small variances ($\sigma^2_{\kappa\kappa} \ll 1$). The normalized variance calculated from a two-component medium is given by

$$\sigma^2_{\kappa\kappa} = \frac{\phi_1 + (\frac{\kappa_2}{\kappa_1})^2 \phi_2}{\left(\phi_1 + \frac{\kappa_2}{\kappa_1}\phi_2\right)^2} - 1$$

and thus depends on the conductivity contrast as well as on the volume fractions of the components.

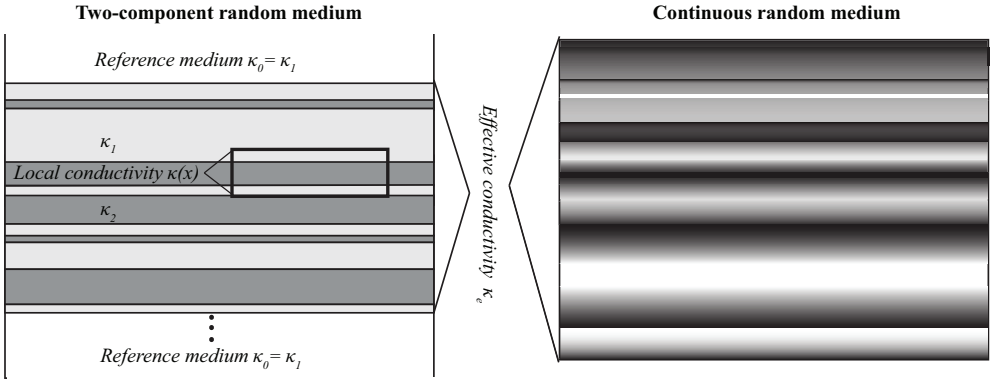

Figure 6.2: Comparison between a discrete two-component and a continuous random medium

A comparison of the two expansion methods for a 1D random medium is

shown in Figure 6.3. It can be observed that the weak contrast expansion violates the low-frequency limit for the chosen contrast, while the strong contrast expansion coincides with the exact bound. In Figure 6.4, the low-frequency limit of the effective hydraulic conductivity is plotted as a function of the conductivity contrast. For low contrasts ($\kappa_2/\kappa_1 \leq 2$), the two approximations are in good agreement, as expected, and coincide with the exact low-frequency limit (κ_h), but for larger conductivity contrast, they increasingly diverge. Interestingly, if $\phi_1 = \phi_2 = 0.5$ the weak-contrast expansion coincides with the harmonic average even for high contrasts. Indeed, for a two-component medium at this particular volume fraction the low-frequency limit for the weak-contrast expansion, given by

$$\begin{aligned}\kappa^*(\omega \to 0) &= \kappa_0(1 - \sigma^2_{\kappa\kappa}) \\ &= 2\phi^2(\kappa_1 + \kappa_2) - \frac{\phi(\kappa_1^2 + \kappa_2^2)}{(\kappa_1 + \kappa_2)} = \frac{\kappa_1\kappa_2}{\kappa_1 + \kappa_2} = \kappa_h, \end{aligned} \tag{6.55}$$

attains the harmonic average.

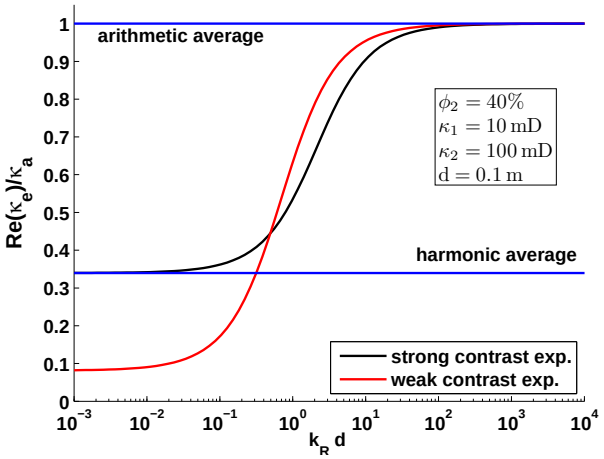

Figure 6.3: Normalized effective conductivity of a randomly layered medium (1D) vs. dimensionless frequency $k_R d$, where k_R is the real part of k_0. The blue The blue lines indicate the 1D frequency limits.

Figure 6.5 shows a comparison of the weak- and strong-contrast expansions in 3D for two examples. In the first example, the reference medium (κ_1) is chosen to be the less conducting component ($\kappa_1 < \kappa_2$) and in the second, it is the more conducting component ($\kappa_1 > \kappa_2$) with a volume fraction of 0.8 in each case. For the former, the strong-contrast expansion coincides with the lower HS-bound and for the later with the upper HS-bound, whereas the weak-contrast expansion

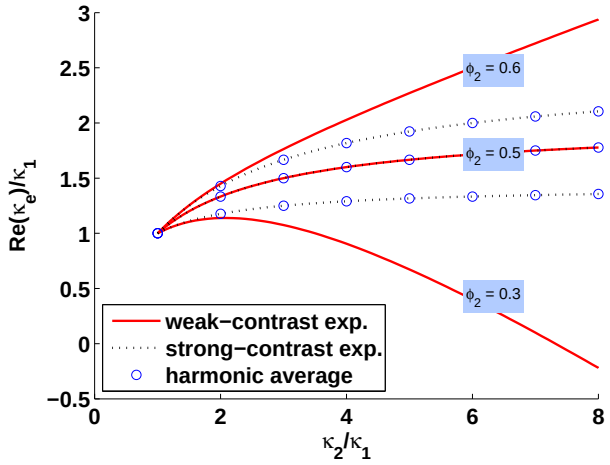

Figure 6.4: a) Normalized effective conductivity (1D) in the low frequency limit ($f = 0.01Hz$) as a function of conductivity contrast for volume fractions of 0.3, 0.5 & 0.6. The circles denote the exact low frequency limit.

violates these bounds. In Figure 6.6, the low-frequency limit of the effective conductivity is plotted as a function of conductivity contrast for several volume fractions. For small contrast the two approximations are in good agreement, but afterwards for most volume fractions they increasingly diverge. Interestingly, the weak-contrast expansion attains the HS-bounds for volume fractions of 0.25 and 0.75 and falls between the bounds for volume fractions between 0.25 and 0.75 even for high contrasts. This is because the variance does not exceed a value of 3 if

$$\sigma^2_{\kappa\kappa}(\kappa_2/\kappa_1 \to \infty) = \frac{\phi_1}{\phi_2} < 3 \quad \Rightarrow \quad \phi_1 < 0.75$$
$$\sigma^2_{\kappa\kappa}(\kappa_1/\kappa_2 \to \infty) = \frac{\phi_2}{\phi_1} < 3 \quad \Rightarrow \quad \phi_1 > 0.25$$

and thus the low-frequency limit given by $\kappa^*(\omega \to 0) = \kappa_0\,(1 - (1/3)\sigma^2_{\kappa\kappa})$ remains physical. However, this is merely a characteristic of calculating the variance from a two-component medium. As expected, the low-frequency limit of the strong-contrast expansion remains physical for high contrast and all volume fractions and coincides either with the upper or lower HS-bound since the expansion is constructed in this way. However, note that for the whole frequency range the strong-contrast expansion is only meaningful for small volume fractions of κ_2, since the chosen Debye random medium (exponential correlation function) exhibits a percolation threshold. As discussed in the previous section, percolation behaviour is not captured by the two-point approximation. To account for this effect, higher correlation functions are necessary.

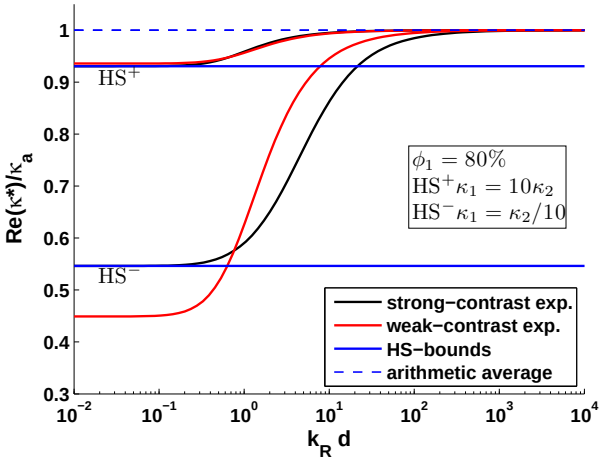

Figure 6.5: Normalised effective conductivity (3D) vs. dimensionless frequency $k_R d$, where k_R is the real part of k_0.

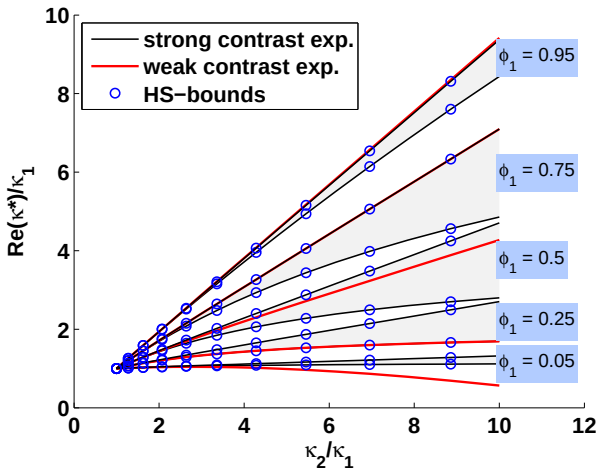

Figure 6.6: Normalised effective conductivity as a function of contrast. The gray areas indicate the domains, in which the low-frequency limit lies between the Hashin-Shtrikmann bounds for different volume fractions. The circles correspond to the upper and lower HS-bounds.

6.1.7 Discussion and Conclusions

The application of the strong-contrast expansion method of *Rechtsman and Torquato* (2008) leads to closed-form expressions for the effective hydraulic conductivity in a 1D and 3D two-component media, depending on the choice of the reference medium and on the second order statistics. We find that this method coincides with the exact bounds for arbitrarily high contrasts in 1D, i.e. the harmonic and arithmetic averages. Furthermore, the strong-contrast expansion method attains the low-frequency limit for all volume fractions and any choice of the reference medium in 1D. It is therefore superior to the weak-contrast approximation that diverges at high contrasts.

The strong-contrast expansion method applied to 3D media yields in the low-frequency limit the generalized Maxwell approximation and depends on the choice

of the reference medium. A comparison with the weak-contrast expansion (*Müller and Gurevich*, 2006) has shown that the low-frequency limit for both expansions converge for small contrasts. Further, the derived expansion attains the HS-bounds, which incorporate two-point information and does not diverge for high contrast. However, the truncated expansion at the two-point level does not capture percolation behaviour and therefore is only a good approximation for small volume fractions of inclusions below the percolation threshold. To obtain narrower bounds on the steady-state effective conductivity, the expansion has to be extended to higher-order correlation functions, which we plan to do in the future.

As can be seen from Eq. (6.51), the steady-state value of the effective hydraulic conductivity does not depend on the size of the heterogeneities (the correlation length), since the term A (Eq. (6.47)) incorporating the correlation structure vanishes at low frequencies. However, the size of the heterogeneities plays a role for the frequency-dependence of the effective hydraulic conductivity since this measure determines at which frequencies the low-frequency ($\lambda_d \gg a$) or high-frequency limits ($\lambda_d \ll a$) are obtained. Larger heterogeneities will shift the dispersion curve to lower frequencies, which means that it will take longer for pressure gradients to equilibrate. This pressure diffusion process controls the dissipation behaviour of Biot's equation in the low frequency regime and thus it depends on a dynamic-equivalent effective conductivity.

It is understood that higher-order corrections will improve the estimation of the low-frequency limit, however it is not clear how they will affect the dispersion curve itself. We plan to apply the same approach to the coupled problem of poroelasticity. The aim is to derive a model for effective seismic properties, which is valid for high contrast in fluid properties. This is related to the problem of estimating effective seismic properties of porous formations saturated with a mixture of fluids such as CO_2 and brine. In this special case, the high- and low-frequency limits are known and it would be interesting to understand if higher-order terms play a significant role on the frequency-dependence.

6.2 Influence on velocity-saturation relations

The numerical example illustrated that the presence of heterogeneities in hydraulic conductivity affect the dissipation behaviour (diffusivity) of the medium. The derived frequency-dependent effective conductivity for a medium with a "double conductivity structure" takes this effect into account. To understand the influence of a heterogeneous conductivity field on the VSR in a partially saturated rock, we introduce the effective conductivity into the slow P-wave number of the 1D CRM model (Eq. (2.33)) as follows:

$$k = \sqrt{\frac{i\omega}{\kappa^*(\omega)}} \frac{\sqrt{\eta_w N_w} S_w + \sqrt{\eta_{CO_2} N_{CO_2}} S_{CO_2}}{N_w S_w + N_{CO_2} S_{CO_2}} .$$

The approach is somehow heuristically, since both theories are based on different medium parameterisations and coupling effects of saturation and permeability heterogeneities are neglected. However, to first order the results should reflect the influence of conductivity fluctuations on the dissipation behaviour.

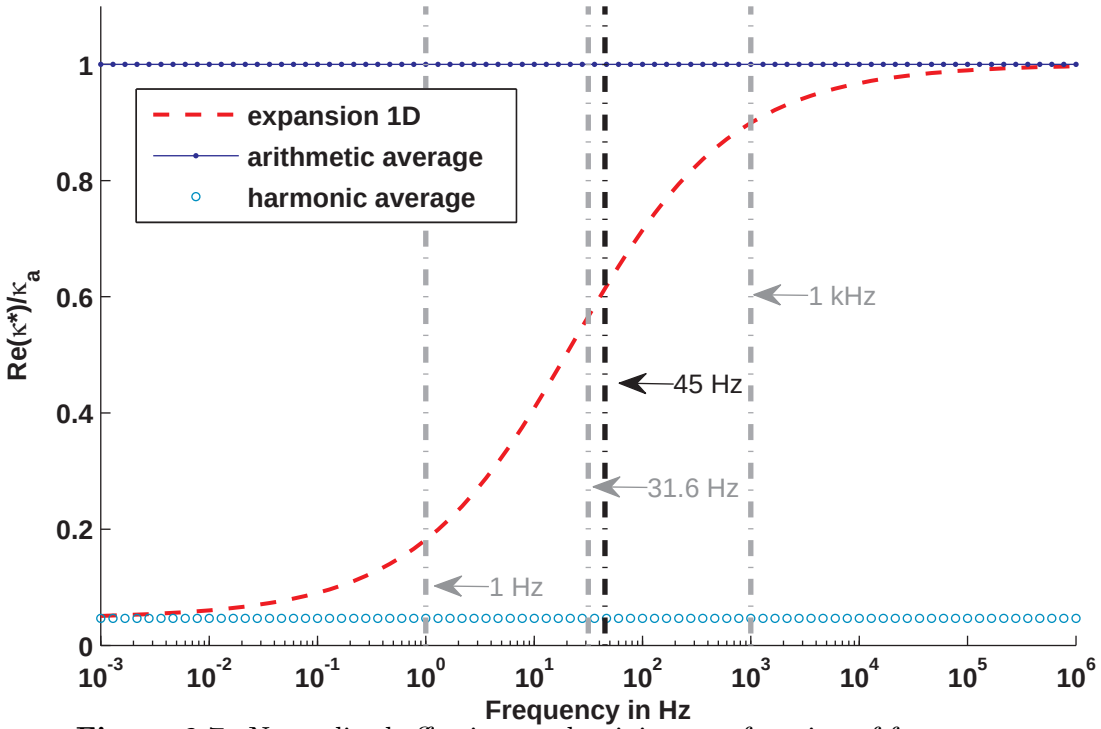

Figure 6.7: Normalized effective conductivity as a function of frequency.

We construct a simple example using the petrophysical properties of the rock sample 1444.2 V (see description in section 4.2.2). We assume that the medium

is characterized by two permeabilities, $\kappa_1 = 10^{-13}$ m^2 and $\kappa_2 = 10^{-15}$ m^2. The frequency-dependence of the effective hydraulic conductivity is shown in Figure 6.7. The correlation length for saturation and permeability heterogeneities is chosen to be $d = 0.25$ m and the gas saturation S_g and volume fraction of κ_1 is 30%. Three cases are considered the harmonic average and the arithmetic average of the conductivities and the effective conductivity. The harmonic and arithmetic average correspond to the low- and high-frequency limits for the effective conductivity, respectively.

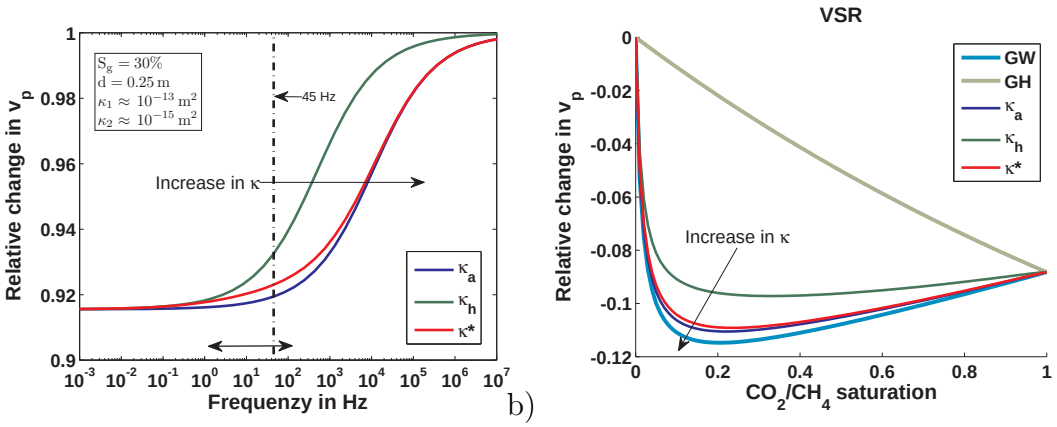

Figure 6.8: a)Frequency dependence of P-wave velocity and b)velocity saturation relations with varying permeabilities. The double arrow in a) indicates the seismic frequency range.

Figure 6.8a) shows the resulting dispersion curves for the fast P-wave. It can be observed that the dispersion curve with a frequency-dependent effective conductivity, interpolates between the two limiting cases and hence the slope of the dispersion curve is smaller. This, in turn, results in less attenuation, however, attenuation occurs over a broader frequency range. The same behaviour was observed by *Rubino and Holliger* (2012). They performed numerical simulations in a medium with random fluctuations in elastic parameters and hydraulic conductivity. Finally, we calculate the VSRs for a frequency of 45 Hz (Figure 6.8b)). In this case the VSR for the effective conductivity is close to the VSR for the arithmetic average. The examples illustrates that the presence of conductivity fluctuations has an influence on the VSRs.

Chapter 7

Conclusions

The objective of the thesis was to analyse which scales, properties and physical processes have to be considered in a time-lapse seismic study to predict the seismic response caused by CO_2 saturations effects. Crucial factors for the prediction of the signal strength are the distribution of fluids and the in-situ properties of the reservoir. To investigate these factors case studies using data examples of Stage 1 and Stage 2 of the Otway project and the Nagaoka CO_2 project were performed.

In the Paaratte case (Otway Stage 2) study the influence of different fluid distributions on the seismic response was investigated. Two different zones in this formation were analysed, a very permeable clean sandstone interval and a thicker and more heterogeneous interval. Though the predicted changes in elastic properties were larger for the former interval, the determining factor for the strength of the TL seismic signal was the thickness of the gas plume. In the high permeable zone, strong buoyancy effects lead to a thin gas plume at the top of the formation. This makes the detection of the gas plume with surface seismic imaging more challenging. For the second zone a more compact and thicker plume was predicted leading to a more robust TL seismic signal. For this zone different injection volumes and distributions of the reservoir properties (geological realisations), which in turn resulted in different geometrical sizes of the plume, were investigated. A larger injection volume did not necessarily lead to a significant improvement of the seismic detectability. This is due to the fact that most of the additional gas volume was predicted to spread out below the reservoir seal

in a thin layer, close to the detection limit of the seismic method. The different geological realisations resulted in spatial variations of the TL signals. However, all cases produced a substantial signal, which exceeded the TL seismic noise of the field data.

The changes in elastic properties due to saturation effects are controlled by the compressibility of the dry rock, the porosity and compressibility contrast of the saturating fluids. Rocks with a large compressibility and a large compressibility contrast between saturating fluids, cause a strong TL seismic signal (Lumley, 2010). The Waarre C modelling study (Otway Stage 1) showed that the challenge for seismic monitoring in the depleted gas reservoir was the small change in elastic properties due to a low contrast in fluid properties. The case study confirmed that the TL signal is too small or the TL noise too high to detect a signal robustly with the acquired surface seismic data.

In a 4D seismic feasibility study it is crucial to build a model of the subsurface with a consistent set of porosity and elastic properties. Therefore, calibrated elastic property - porosity relations are needed. For the Paaratte model two workflows were tested to obtain such relations calibrated with available well log data. Though, both approaches reproduced the data trends of the log data quite well, they differed regarding their predictions of the TL seismic signal. These differences were mainly caused by different estimations of the dry rock compressibility. The dry rock compressibility is difficult to estimate in a TL seismic study since it cannot be measured directly in-situ. Laboratory measurements on rock samples are the only way to measure the dry rock compressibility directly, thus available information on that property is typically limited to a few samples. Another pathway to improve the estimation of this parameter might be rock physics modelling constrained by geological information. This involves certain assumptions about the microstructure of the rock. For instance, a friable sandstone will always predict a very different TL signal than a well cemented sandstone. In this sense even the microstructure can have a significant influence on the TL seismic signal.

The Paaratte and Waarre C case studies illustrated that the magnitude of changes in elastic properties is strongly controlled by the properties of the reservoir, resulting in very different velocity-saturation relations. However, if the pore space of a rock is saturated with two immiscible fluids, such as brine and CO_2, the VSR also depends on the distribution of the fluids in the pore space. Depending on the length scale of saturation heterogeneities and the measurement frequency, intrinsic attenuation due to the mechanism of wave-induced fluid flow may take place and lead to smaller TL signals. A VSR at reservoir depth was retrieved from time-lapse sonic and neutron porosity logs from the Nagaoka CO_2 sequestration experiment. It was shown that the mechanism of wave-induced flow can explain this velocity-saturation relation. Characteristic CO_2 patch sizes were estimated to be in the range from 1 to 5 mm and hence, mesoscopic heterogeneities can be responsible for attenuation and dispersion in the well logging frequency band. For the Paaratte formation fluid heterogeneities were investigated at seismic frequencies based on reservoir simulation results. In this case wave-induced fluid flow between layers with different saturations had only a minor effect on the TL seismic response. The main reason is the high permeability of the clean sandstone sections. However, larger poroelastic effects can be expected for low permeable rocks and a series of layers with a strong contrast in fluid properties. Nevertheless, different distributions of the fluids (saturation profiles) resulted in different impedance contrasts between layers and thus lead to different magnitudes of the TL seismic signal. These differences can be explained by multiple scattering (stratigraphic filtering) and are not due to intrinsic attenuation (local fluid effects). Though, the variations in layer properties are below the resolution of the seismic method, they affect the TL signal and have to be taken into consideration.

The frequency regime in which mesoscopic flow (wave-induced fluid flow) occurs depends not only on the length scale of saturation heterogeneities but also on the diffusivity of the medium (hydraulic conductivity). The effective hydraulic conductivity of a medium is a function of frequency itself and can vary quite significantly at seismic to ultrasonic frequencies from the flow permeability used in reservoir simulations. The dissipation behaviour of Biot's equation in the low fre-

quency regime depends on this dynamic-equivalent effective conductivity. In the last chapter a model was proposed for such a dynamic-equivalent effective conductivity for a "double conductivity medium". This theory leads to closed-form expressions for the frequency-dependent, effective conductivity as a function of the one- and two-point probability functions of the conductivity fluctuations. In 1D, these expressions are consistent with exact solutions in both low- and high-frequency limits for arbitrary conductivity contrast. In 3D, the low-frequency limit depends on the details of the microstructure. However, the derived approximation for the effective conductivity is consistent with the Hashin-Shtrikman bounds. This effective conductivity was utilized to estimate the influence of fluctuations in hydraulic conductivity on VSRs. However, the model does not account for the coupling between saturation and hydraulic conductivity heterogeneities. Therefor, the coupled problem of poroelasticity has to solved.

For the Waarre C case study a workflow was tested to integrate the inversion result of the surface seismic data and results from the reservoir simulator on one modelling grid. The main problem was that these two data sets were on different scales and not consistent with each other, since the static geological model could not reproduce the amplitude distribution of the surface seismic data. Therefore, to take all information of available data sets into account an integrated approach such as geostatistical inversion is necessary. This method relies on calibrated relations of rock properties. The thesis focused on such effective elastic properties for the prediction of the TL seismic signal. Further, we considered the frequency dependence of the effective properties due to heterogeneities in saturation and hydraulic conductivity. However in principle, proper upscaling of all properties depends not only on the spatial distribution but also on the frequency of the process.

Outlook

In this work different scales and mechanisms that can influence the TL seismic response were analysed. The main focus of this study was on the effect of sat-

uration and fluid distribution and the influence of elastic properties on the TL seismic signal. VSRs were investigated at sonic and seismic frequencies for two data examples. However, to obtain conclusive results about adequate VSRs at in-situ conditions a more comprehensive study on several data examples is necessary. Furthermore, the VSRs might be influenced by additional mechanisms which were not considered in this thesis. In the following, a way to retrieve VSRs at in-situ conditions by comparing measurements of different data sets is briefly outlined and additional mechanisms that influence VSRs are summarized.

Comparing data with data

A main aspect of this study was the analysis of VSRs. The TL neutron and sonic logs of the Nagaoka CO_2 project provided the opportunity to study VSRs at in-situ conditions in the sonic log frequency band. However, at seismic frequencies we relied on saturation predictions from reservoir simulations. On one hand this approach neglects inhomogeneities on smaller scales than the reservoir simulation grid and on the other hand this does not provide effective properties of the reservoir at the resolution of surface seismic data. To achieve this the reservoir model has to be upscaled to the resolution of the seismic data. At this scale a representative VSR for a reservoir with e.g. interbedded very low permeable layers might be rather the patchy saturation model than the uniform saturation model. This is due to the fact that for very low permeabilities there is no pressure communication between the different layers during the time-scale of seismic wave propagation.

However, probably the biggest drawback is that reservoir simulations are based on the static geological model and hence, we obtain only conclusive results from 4D seismic data about an appropriate VSR at in-situ conditions if the geological model is well calibrated with seismic amplitude data. Another pathway to evaluate VSRs at in-situ conditions might be a comparison of seismic data with a second independently measured property; e.g. electric resistivity. Electric resistivity can be measured at various scales and is sensitive to the saturation of the rock. For instance, within the Cranfield and Nagaoka CO_2 projects TL re-

sistivity and seismic tomography data is acquired. Furthermore, TL resistivity and sonic logs are available for the Nagaoka CO_2 project and at the Ketzin CO_2 test site electric resistivity is measured in the laboratory and at the field scale. By comparing these TL data sets to theoretical VSRs, one might get a better understanding which VSRs are appropriate at a certain scale and frequency.

Other aspects which influence VSRs

In chapter 6 of this thesis it was shown that heterogeneities of hydraulic conductivity affect the VSR. However, the approach was somehow heuristically and did not consider coupling effects of saturation and hydraulic conductivity heterogeneities. To take these effects properly into account the strong contrast expansion has to be applied to the coupled problem of poroelasticity. In principle, the frequency dependence of all poroelastic parameters has to be considered. Furthermore, laboratory measurements of *Lebedev et al.* (2009) indicated that the patch size itself can depend on the saturation. This might be related to percolation behaviour of two fluids occupying the same pore space.

But there are even more saturation mechanisms, which might affect the seismic response and are not taken into account by Biot's theory of poroelasticity; e.g multi phase flow and capillary forces. Multi-phase flow results in a reduction of the effective permeability due to the presence of a second fluid. Recently, (*Azuma and Chisato Konishi*, 2013) suggested considering this effect by including the irreducible water saturation into VSRs. The modified VSR has as an end-member a mixture of irreducible water saturation and injected gas instead of 100% gas saturation. Further, (*Qi et al.*, 2013) noted that a rock stiffening effect can be caused due to membrane tension between saturation heterogeneities, which is a macroscopic expression for capillary forces.

Aside from saturation effects, there are many other mechanisms which affect the TL seismic signal of CO_2 sequestration; e.g. pressure changes in the reservoir and geochemical reactions of CO_2 with the reservoir rock.

Bibliography

Ajo-Franklin, J. B., J. Peterson, J. Doetsch, and T. M. Daley (2013), High-resolution characterization of a CO_2 plume using crosswell seismic tomography: Cranfield, ms, USA, *International Journal of Greenhouse Gas Control*, doi:doi.org/10.1016/j.ijggc.2012.12.018, online publication date 1-Jan-2013, in press. (Cited on page 2.)

Aki, K., and P. Richards (1980), *Quantitative seismology*, Freeman San Francisco. (Cited on pages 11, 13 and 17.)

Amini, H., E. Alvarez, C. MacBeth, and A. Shams (2012), Finding a Petro-elastic Model Suitable for Sim2seis Calculation, in *74th EAGE Conference & Exhibition*. (Cited on page 3.)

Arts, R., O. Eiken, A. Chadwick, P. Zweigel, L. van der Meer, and B. Zinszner (2004), Monitoring of CO_2 injected at Sleipner using time-lapse seismic data, *Energy*, *29*, 1383–1392. (Cited on page 1.)

Asgharzadeh, M., E. Caspari, M. Urosevic, and R. Pevzner (2010), Acoustic inversion of time-lapse seismic data: CO2CRC Otway Project case study, in *CO2CRC Research Symposium, Melbourne, Australia, 1-3 December.*, poster. (Cited on pages 46 and 79.)

Avseth, P., and T. A. Johansen (2012), Explorational rock physics and seismic reservoir prediction, in *EAGE short course*. (Cited on page 22.)

Avseth, P., T. Mukerji, and G. Mavko (2005), *Quantitative seismic interpretation*, vol. 1, Cambridge University Press (ISBN 0521816017). (Cited on pages 24, 86 and 101.)

Azuma, H., and Z. X. Chisato Konishi (2013), Introduction and application of the modified patchy saturation for evaluating CO_2 saturation by seismic velocity, *Energy Procedia*, gHGT-11, in press. (Cited on page 170.)

Backus, G. E. (1962), Long-wave elastic anisotropy produced by horizontal layering, *Journal of Geophysical Research*, *67*(11), 4427–4440. (Cited on page 18.)

Batzle, M., and Z. Wang (1992), Seismic properties of pore fluids, *Geophysics*, *57*(11), 1396–1408. (Cited on pages 36, 42, 46, 57 and 130.)

Bear, J. (2013), *Dynamics of fluids in porous media*, Dover Publications. (Cited on page 36.)

Belinfante, F. J. (1946), On the longitudinal and the transversal delta-function, with some applications, *Physica*, *12*(1), 1–16. (Cited on page 143.)

Benveniste, Y. (1987a), A new approach to the application of Mori-Tanaka's theory in composite materials, *Mechanics of materials*, *6*(2), 147–157. (Cited on page 156.)

Benveniste, Y. (1987b), A new approach to the application of Mori-Tanaka's theory in composite materials, *Mechanics of materials*, *6*(2), 147–157. (Not cited.)

Berryman, J. G. (1980), Long-wavelength propagation in composite elastic media II. Ellipsoidal inclusions, *Journal of the Acoustical Society of America*, *68*(6), 1809–1819. (Cited on page 22.)

Berryman, J. G. (1992), Single-scattering approximations for coefficients in biot's equations of poroelasticity, *The Journal of the Acoustical Society of America*, *91*(2). (Cited on page 23.)

Berryman, J. G. (1995), *Mixture theories for rock properties*, pp. 205–228, Washington, USA: American Geo-physical Union. (Cited on pages 20 and 21.)

Biot, M. A. (1956a), Theory of propagation of elastic waves in a fluid-saturated porous solid. I. Low-frequency range, *Journal of the Acoustical Society of America*, *28*, 168–178. (Cited on pages 14 and 16.)

Biot, M. A. (1956b), Theory of propagation of elastic waves in a fluid-saturated porous solid. II. Higher frequency range, *Journal of the Acoustical Society of America*, *28*, 179–191. (Cited on pages 14 and 15.)

Biot, M. A. (1962), Mechanics of deformation and acoustic propagation in porous media, *Journal of applied physics*, *33*(4), 1482–1498. (Cited on pages 14, 17, 138 and 141.)

Brown Jr, W. F. (1955), Solid mixture permittivities, *Journal of Chemical Physics*, *23*, 1514. (Cited on pages 147 and 151.)

Carcione, J. M., B. Gurevich, and F. Cavallini (2000), A generalized Biot–Gassmann model for the acoustic properties of shaley sandstones, *Geophysical Prospecting*, *48*(3), 539–557. (Cited on pages 34 and 92.)

Caspari, E., T. Müller, and B. Gurevich (2011), Time-lapse sonic logs reveal patchy CO_2 saturation in-situ, *Geophysical Research Letters*, *38*, L13,301, doi: 10. (Not cited.)

Caspari, E., J. Ennis-King, R. Pevzner, and B. Gurevich (2012), Prediction of the seismic time-lapse signal of CO_2/CH_4 injection into a depleted gas reservoir-Otway project, in *Proceedings of the ASEG 22nd Geophysical Conference*, CSIRO. (Cited on page 41.)

Caspari, E., T. M. Müller, J. G. Rubino, and B. Gurevich (2013a), Biot's slow wave and effective hydraulic conductivity in random media, in *Poromechanics V: Proceedings of the Fifth Biot Conference on Poromechanics*, pp. 217–226, ASCE, doi:10.1061/9780784412992.025. (Not cited.)

Caspari, E., B. Gurevich, and T. Müller (2013b), Frequency-dependent effective hydraulic conductivity of strongly heterogeneous media, *Physical Review E*, *88*(4), 042,119–10, doi:10.1103/PhysRevE.88.042119. (Not cited.)

Chadwick, A., G. Williams, N. Delepine, V. Clochard, K. Labat, S. Sturton, M.-L. Buddensiek, M. Dillen, M. Nickel, A. L. Lima, R. Arts, F. Neele, and G. Rossi (2010), Quantitative analysis of time-lapse seismic monitoring data at the Sleipner CO_2 storage operation, *The Leading Edge*, *29*(2), 170–177. (Cited on pages 1 and 2.)

Chadwick, R., R. Arts, and O. Eiken (2005), 4D seismic quantification of a growing CO_2 plume at Sleipner, North Sea, in *Geological Society, London, Petroleum Geology Conference series*, vol. 6, pp. 1385–1399, Geological Society of London. (Cited on page 58.)

Chandler, R. N., and D. L. Johnson (1981), The equivalence of quasistatic flow in fluid-saturated porous media and Biots slow wave in the limit of zero frequency, *Journal of Applied Physics*, *52*(5), 3391–3395. (Cited on pages 29 and 140.)

Dagan, G. (1982), Analysis of flow through heterogeneous random aquifers: 2. Unsteady flow in confined formations, *Water Resources Research*, *18*(5), 1571–1585. (Cited on pages 137, 138 and 139.)

Dagan, G. (1986), Statistical theory of groundwater flow and transport: pore to laboratory, laboratory to formation, and formation to regional scale, *Water Resources Research*, *22*(9S), 120S–134S. (Cited on pages 5 and 137.)

Dance, T., L. Spencer, and J.-Q. Xu (2009), Geological characterisation of the Otway project pilot site: What a difference a well makes, *Energy Procedia*, *1*(1), 2871–2878. (Cited on pages 39, 40 and 79.)

Dance, T., M. Arnot, M. Bunch, R. Daniel, A. Hortle, M. Lawrence, and J. Ennis-King (2012), Geocharacterisation and static modelling of the lower Paaratte formation. CO2CRC Otway project - phase ii., *Co2crc publication number rpt12-3481*, Cooperative Research Centre for Greenhouse Gas Technologies, Canberra, Australia. (Cited on pages 39, 40, 86 and 101.)

Digby, P. J. (1981), The effective elastic moduli of porous granular rocks, *Journal of Applied Mechanics*, *48*, 803–808. (Cited on page 23.)

Donaldson, E. C., and W. Alam (2008), *Wettability*, Gulf Publishing Company. (Cited on page 36.)

Dræge, A., T. A. Johansen, I. Brevik, and C. T. Dræge (2006), A strategy for modelling the diagenetic evolution of seismic properties in sandstones, *Petroleum Geoscience*, *12*(4), 309–323. (Cited on pages 103 and 112.)

Dubrule, O. (2003), *Geostatistics for Seismic Data Integration in Earth Models: 2003 Distinguished Instructor Short Course*, 6, SEG Books. (Cited on pages 3 and 85.)

Dutta, N., and H. Odé (1979), Attenuation and dispersion of compressional waves in fluid-filled porous rocks with partial gas saturation (White model)-Part I: Biot theory, *Geophysics*, *44*(11), 1777–1788. (Cited on pages 30 and 124.)

Dvorkin, J., and A. Nur (1996), Elasticity of high-porosity sandstones: Theory for two North Sea data sets, *Geophysics*, *61*(5), 1363–1370. (Cited on pages 24, 25, 26 and 92.)

Dvorkin, J., A. Nur, and H. Yin (1994), Effective properties of cemented granular materials, *Mechanics of Materials*, *18*(4), 351–366. (Cited on pages 24, 25, 26 and 92.)

Dvorkin, J., G. Mavko, and B. Gurevich (2007), Fluid substitution in shaley sediment using effective porosity, *Geophysics*, *72*(3), 1–8. (Cited on pages 34, 35, 92 and 111.)

Ennis-King, J., T. Dance, J. Xu, C. Boreham, B. Freifeld, C. Jenkins, L. Paterson, S. Sharma, L. Stalker, and J. Underschultz (2011), The role of heterogeneity in CO_2 storage in a depleted gas field: History matching of simulation models to field data for the CO2CRC Otway Project, Australia, *Energy Procedia*, *4*, 3494–3501. (Cited on pages 40 and 79.)

Gardner, G. H. F., L. W. Gardner, and A. R. Gregory (1974), Formation velocity and density - the diagnostic basics for stratigraphic traps, *Geophysics*, *39*(6), 770–780. (Cited on page 97.)

Gassmann, F. (1951), Über die Elastizität poröser Medien:, *Vier. der Natur. Gesellschaft in Zürich*, *96*, 1–23. (Cited on pages 27 and 86.)

Gelhar, L. W. (1986), Stochastic subsurface hydrology from theory to applications, *Water Resources Research*, *22*(9S), 135S–145S. (Cited on pages 5 and 137.)

Gelhar, L. W., and C. L. Axness (1983), Three-dimensional stochastic analysis of macrodispersion in aquifers, *Water Resour. Res*, *19*(1), 161–180. (Not cited.)

Goldberg, I., and B. Gurevich (1998), A semi-empirical velocity-porosity-clay model for petrophysical interpretation of P-and S-velocities, *Geophysical Prospecting*, *46*(3), 271–285. (Cited on page 105.)

Guéguen, Y., and V. Palciauskas (1994), *Introduction to the Physics of Rocks*, Princeton University Press. (Cited on page 6.)

Gurevich, B., and S. Lopatnikov (1985), Attenuation of longitudinal waves in a saturated porous medium with random inhomogeneities, in *Doklady Earth Science Sections*, vol. 281, pp. 47–50. (Cited on page 30.)

Gurevich, B., and S. L. Lopatnikov (1995), Velocity and attenuation of elastic waves in finely layered porous rocks, *Geophysical Journal International*, *121*(3), 933–947. (Cited on pages 18 and 31.)

Han, D., A. Nur, and D. Morgan (1986), Effects of porosity and clay content on wave velocities in sandstones, *Geophysics*, *51*(11), 2093–2107. (Cited on page 121.)

Hashin, Z., and S. Shtrikman (1963), A variational approach to the theory of the elastic behaviour of multiphase materials, *Journal of the Mechanics and Physics of Solids*, *11*(2), 127–140. (Cited on page 20.)

Hill, R. (1963), Elastic properties of reinforced solids: some theoretical principles, *Journal of the Mechanics and Physics of Solids*, *11*(5), 357–372. (Cited on page 21.)

Hovem, J. M., and G. D. Ingram (1979), Viscous attenuation of sound in saturated sand, *Journal of the Acoustical Society of America*, *66*(6), 1807–1812. (Cited on page 129.)

Hristopulos, D. T., and G. Christakos (1997), Variational calculation of the effective fluid permeability of heterogeneous media, *Physical Review E*, *55*(6), 7288–7298. (Cited on page 139.)

Indelman, P. (1996), Averaging of unsteady flows in heterogeneous media of stationary conductivity, *Journal of Fluid Mechanics*, *310*, 39–60. (Cited on pages 137, 138, 139, 154 and 157.)

Indelman, P. (2002), On mathematical models of average flow in heterogeneous formations, *Transport in porous media*, *48*(2), 209–224. (Cited on page 139.)

Jenkins, C. R., P. J. Cook, J. Ennis-King, J. Undershultz, C. Boreham, T. Dance, P. de Caritat, D. M. Etheridge, B. M. Freifeld, A. Hortle, D. Kirste, L. Paterson, R. Pevzner, U. Schacht, S. Sharma, L. Stalker, and M. Urosevic (2011), Safe storage and effective monitoring of CO_2 in depleted gas fields, pp. E35–E41. (Cited on page 1.)

Johnson, D. L. (2001), Theory of frequency dependent acoustics in patchy-saturated porous media, *Journal of the Acoustical Society of America*, *110*(2), 682–694. (Cited on pages 26, 29 and 30.)

Johnson, D. L., J. Koplik, and R. Dashen (1987), Theory of dynamic permeability and tortuosity in fluid-saturated porous media, *Journal of Fluid Mechanics*, *176*(1), 379–402. (Cited on page 139.)

Karal Jr, F. C., and J. B. Keller (1964), Elastic, electromagnetic, and other waves in a random medium, *Journal of Mathematical Physics*, *5*, 537–548. (Cited on page 31.)

Karpfinger, F., T. M. Müller, and B. Gurevich (2009), Green's functions and radiation patterns in poroelastic solids revisited, *Geophysical Journal International*, *178*(1), 327–337. (Cited on page 143.)

Konishi, C., H. Azuma, D. Nobuoka, Z. Xue, and J. Watanabe (2009), Quantitative CO_2 saturation estimation from P-wave velocity changes by considering patchy saturation, in *SEG Summer Research Workshop*. (Cited on pages 116, 118, 121 and 188.)

Kragh, E., and P. Christie (2002), Seismic repeatability, normalized rms, and predictability, *The Leading Edge*, *21*(7), 640–647. (Cited on page 49.)

Krief, M., J. Garat, J. Stellingwerff, and J. Ventre (1990), A petrophysical interpretation using the velocities of P and S waves (full waveform sonic), *Log Analyst*, *31*, 355–369. (Cited on page 105.)

Kunz, O., R. Klimeck, W. Wagner, and M. Jaeschke (2006), *The GERG-2004 Wide-Range Reference Equation of State for Natural Gases and Other Mixtures.*, Ber. VDI-Verlag, Düsseldorf. (Cited on pages 35, 36, 42, 57 and 130.)

Kuster, G. T., and M. N. Toksöz (1974), Velocity and attenuation of seismic waves in two-phase media: Part I. Theoretical formulations, *Geophysics*, *39*(5), 587–606. (Cited on page 22.)

Lebedev, M., J. Toms-Stewart, B. Clennell, M. Pervukhina, V. Shulakova, L. Paterson, T. M. Müller, B. Gurevich, and F. Wenzlau (2009), Direct laboratory observation of patchy saturation and its effects on ultrasonic velocities, *The Leading Edge*, *28*(1), 24–27. (Cited on pages 115 and 170.)

Lebedev, M., V. Mikhaltsevitch, O. Bilenko, T. Dance, M. Pervukhina, and B. Gurevich (2013), An experimental study of acoustic responses on the injection of supercritical CO_2 into sandstones from the Otway basin, *Geophysics*, *78*(4), doi:10.1190/GEO2012-0528.1. (Cited on pages 4, 56 and 99.)

Lei, X., and Z. Xue (2009), Ultrasonic velocity and attenuation during CO_2 injection into water-saturated porous sandstone: Measurements using difference seismic tomography, *Physics of the Earth and Planetary Interiors*, *176*(3-4), 224–234. (Cited on pages 4, 115, 121 and 124.)

Liu, Y. (1998), Acoustic properties of reservoir fluids, Ph.D. thesis, Stanford University. (Cited on pages 36 and 42.)

Lumley, D. (2010), 4D seismic monitoring of CO_2 sequestration, *The Leading Edge*, *29*(2), 150–150. (Cited on page 121.)

Makse, H. A., N. Gland, D. L. Johnson, and L. Schwartz (2004), Granular packings: Nonlinear elasticity, sound propagation, and collective relaxation dynamics, *Physical Review E*, *70*(6), 061,302. (Cited on pages 24 and 96.)

Mandelis, A. (2001), *Diffusion-Wave Fields: Mathematical Methods and Green Functions*, Springer Verlag. (Not cited.)

Marion, D., A. Nur, H. Yin, and D.-H. Han (1992), Compressional velocity and porosity in sand-clay mixtures, *Geophysics*, *57*(4), 554–563. (Cited on page 92.)

Markov, K. Z., and L. Preziosi (2000), *Heterogeneous Media: Micormechanics Modeling Methods and Simulations*, Springer. (Cited on page 157.)

Matheron, G. (1967), *Eléments pour une théorie des milieux poreux*, Mason, Paris. (Cited on page 154.)

Mavko, G., and D. Jizba (1991), Estimating grain-scale fluid effects on velocity dispersion in rocks, *Geophysics*, *56*(12), 1940–1949. (Cited on page 26.)

Mavko, G., and T. Mukerji (1998), Bounds on low frequency seismic velocities in partially saturated rocks, *Geophysics*, *63*(3), 918–924. (Cited on pages 27, 29 and 42.)

Mavko, G., C. Chan, and T. Mukerji (1995), Fluid substitution: Estimating changes in V_p without knowing V_s, *Geophysics*, *60*(6), 1750–1755. (Cited on pages 9, 46 and 82.)

Mavko, G., T. Mukerji, and J. Dvorkin (1998), *The rock physics handbook: tools for seismic analysis of porous media*, Cambridge University Press. (Cited on pages 15, 17, 20, 24, 28, 53, 91, 94, 97, 103, 104, 105, 110 and 184.)

Morse, P. M., and H. Feshbach (1953), *Methods of theoretical physics (Part 2)*, Springer New York. (Cited on page 143.)

Mukerji, T., J. Berryman, G. Mavko, and P. Berge (1995), Differential effective medium modeling of rock elastic moduli with critical porosity constraints, *Geophysical Research Letters*, *22*(5), 555–558. (Cited on page 102.)

Müller, T. M., and B. Gurevich (2004), One-dimensional random patchy saturation model for velocity and attenuation in porous rocks, *Geophysics*, *69*(5), 1166–1172. (Cited on pages 30, 32, 115, 117, 119, 123 and 126.)

Müller, T. M., and B. Gurevich (2005), A first-order statistical smoothing approximation for the coherent wave field in random porous media, *Journal of the Acoustical Society of America*, *117*(4), 1796–1805. (Cited on page 31.)

Müller, T. M., and B. Gurevich (2006), Effective hydraulic conductivity and diffusivity of randomly heterogeneous porous solids with compressible constituents, *Applied Physics Letters*, *88*(12), 121,924–1 –3. (Cited on pages 139, 140, 143, 154, 157, 158 and 162.)

Müller, T. M., and P. N. Sahay (2011), Stochastic theory of dynamic permeability in poroelastic media, *Phys. Rev. E*, *84*, 026,329, doi:10.1103/PhysRevE.84.026329. (Cited on page 139.)

Müller, T. M., G. Lambert, and B. Gurevich (2007), Dynamic permeability of porous rocks and its seismic signatures, *Geophysics*, *72*(5), E149–158. (Cited on pages 33, 134, 137 and 138.)

Müller, T. M., B. Gurevich, and M. Lebedev (2010), Seismic wave attenuation and dispersion resulting from wave-induced flow in porous rocks − A review, *Geophysics*, *75*, 75–147. (Cited on pages 17, 19, 26 and 138.)

Murphy, W. F., J. N. Roberts, D. Yale, and K. W. Winkler (1984), Centimeter scale heterogeneities and microstratifaction in sedimentary rocks, *Geophysical Research Letters*, *11*(8), 697–700. (Cited on page 137.)

Norris, A. N. (1985), A differential scheme for the effective moduli of composites, *Mechanics of materials*, *4*(1), 1–16. (Cited on page 22.)

Nötinger, B. (1994), The effective permeability of a heterogeneous porous medium, *Transport in Porous Media*, *15*(2), 99–127. (Cited on page 138.)

Peng, D.-Y., and D. B. Robinson (1976), A new two-constant equation of state, *Industrial & Engineering Chemistry Fundamentals*, *15*(1), 59–64. (Cited on pages 36 and 57.)

Pevzner, R., E. Caspari, A. Bona, R. Galvin, M. Madadi, M. Urosevic, T. Dance, V. Shulakova, B. Gurevich, and Y. Cinar (2011a), Feasibility of time-lapse seismic monitoring of CO_2 injection into Paaratte formation, CO2CRC Otway project., *RPT:11-3161*, Cooperative Research Centre for Greenhouse Gas Technologies, Canberra, Australia. (Cited on pages 41 and 59.)

Pevzner, R., V. Shulakova, A. Kepic, and M. Urosevic (2011b), Repeatability analysis of land time-lapse seismic data: CO2CRC Otway pilot project case study, *Geophysical prospecting*, *59*(1), 66–77. (Cited on page 50.)

Pevzner, R., R. J. Galvin, M. Madadi, M. Urosevic, E. Caspari, B. Gurevich, D. Lumley, V. Shulakova, Y. Cinar, and V. Tcheverda (2012), Monitoring CO_2 injection into a saline aquifer: Otway Project feasibility study, in *SEG Technical Program Expanded Abstracts 2012*. (Cited on page 41.)

Pevzner, R., M. Urosevic, E. Caspari, R. J. Galvin, M. Madadi, T. Dance, V. Shulakova, B. Gurevich, V. Tcheverda, and Y. Cinar (2013), Feasibility of Time-lapse Seismic Methodology for Monitoring the Injection of Small Quantities of CO_2 into a Saline Formation, CO2CRC Otway Project, *Energy Procedia*, *37*, 4336–4343. (Cited on pages 41, 59, 64, 65, 185 and 186.)

Pham, D. C., and S. Torquato (2003), Strong-contrast expansions and approximations for the effective conductivity of isotropic multiphase composites, *Journal of applied physics*, *94*(10), 6591–6602. (Cited on page 148.)

Pride, S. R., and M. W. Haartsen (1996), Electroseismic wave properties, *Journal of the Acoustical Society of America*, *100*. (Not cited.)

Pride, S. R., J. G. Berryman, and J. M. Harris (2004), Seismic attenuation due to wave-induced flow, *Journal of Geophysical Research*, *109*(B01201), doi:10.1029/2003JB002639. (Cited on page 19.)

Qi, Q., T. Müller, B. Gurevich, S. Lopes, and B. Gurevich (2013), Effects of mesoscopic flow on utrasonic velocities, in *2nd IWRP*. (Cited on page 170.)

Rabinovich, A., G. Dagan, and T. Miloh (2013), Dynamic effective properties of heterogeneous geological formations with spherical inclusions under periodic time variations, *Geophys. Res. Lett.*, *40*, 1345–1350, doi:10.1002/grl.50319. (Cited on page 138.)

Ramshaw, J. D. (1984), Dielectric polarization in random media, *Journal of statistical physics*, *35*(1), 49–75. (Cited on pages 149 and 151.)

Rechtsman, M. C., and S. Torquato (2008), Effective dielectric tensor for electromagnetic wave propagation in random media, *Journal of Applied Physics*,

103(8), 084,901–1 –15, doi:10.1063/1.2906135. (Cited on pages 135, 140, 147, 149, 157 and 161.)

Reuss, A. (1929), Berechnung der Fließgrenze von Mischkristallen auf Grund der Plastizitätsbedingung für Einkristalle, *ZAMM-Journal of Applied Mathematics and Mechanics/Zeitschrift für Angewandte Mathematik und Mechanik*, *9*(1), 49–58. (Cited on page 20.)

Revil, A., and L. M. Cathles (1999), Permeability of shaly sands, *Water Resources Research*, *35*(3), 651–662. (Cited on page 140.)

Rubino, J., and K. Holliger (2012), Seismic attenuation and velocity dispersion in heterogeneous partially saturated porous rocks, *Geophysical Journal International*, *188*(3), 1088–1102. (Cited on pages 144 and 164.)

Rubino, J. G., L. B. Monachesi, L. Guarracino, T. M. Müller, and K. Holliger (2012), Dynamic permeability of heterogeneous porous rocks having strong permeability fluctuations and its effects on seismic attenuation and velocity dispersion, in *SEG Technical Program Expanded Abstracts 2012*, SEG. (Cited on page 144.)

Russell, B., and M. N. Toksöz (1991), Comparison of poststack seismic inversion methods, in *1991 SEG Annual Meeting*. (Cited on page 81.)

Sams, M., I. Millar, W. Satriawan, D. Saussus, and S. Bhattacharyya (2011), Integration of geology and geophysics through geostatistical inversion: a case study, *First Break*, *29*(8), 47–56. (Cited on page 3.)

Sanchez-Vila, X., A. Guadagnini, and J. Carrera (2006), Representative hydraulic conductivities in saturated groundwater flow, *Reviews of Geophysics*, *44*, RG3002, doi:10.1029/2005RG000169. (Cited on pages 137, 138 and 140.)

Sato, K., S. Mito, T. Horie, H. Ohkuma, H. Saito, J. Watanabe, and T. Yoshimura (2011), Monitoring and simulation studies for assessing macro-and meso-scale migration of CO_2 sequestered in an onshore aquifer: Experiences from the Nagaoka pilot site, Japan, *International Journal of Greenhouse Gas Control*, *5*(1), 125–137. (Cited on pages 117, 118 and 119.)

Schmidt, H., and G. Tango (1986), Efficient global matrix approach to the computation of synthetic seismograms, *Geophys. J. Roy. Astr. Soc.*, *84*, 331–359. (Cited on pages 13, 61 and 129.)

Sengupta, M., G. Mavko, and T. Mukerji (2003), Quantifying subresolution saturation scales from time-lapse seismic data: A reservoir monitoring case study, *Geophysics*, *68*(3), 803–814. (Cited on page 134.)

Shapiro, S. A., and T. M. Müller (1999), Seismic signatures of permeability in heterogeneous porous media, *Geophysics*, *64*(1), 99–103. (Cited on page 134.)

Siggins, A., M. Lwin, and P. Wisman (2010), Laboratory calibration of the seismo-acoustic response of CO_2 saturated sandstones, *International Journal of Greenhouse Gas Control*, *4*(6), 920–927. (Cited on page 44.)

Smith, T. M., C. H. Sondergeld, and C. S. Rai (2003), Gassmann fluid substitutions: A tutorial, *Geophysics*, *68*(2), 430–440. (Cited on pages 28 and 42.)

Span, R., and W. Wagner (1996), A new equation of state for carbon dioxide covering the fluid region from the triple-point temperature to 1100 K at pressures up to 800 MPa, *Journal of physical and chemical reference data*, *25*(6), 1509–1596. (Cited on page 35.)

Tartakovsky, D. M., and S. P. Neuman (1998), Transient effective hydraulic conductivities under slowly and rapidly varying mean gradients in bounded three-dimensional random media, *Water resources research*, *34*(1), 21–32. (Cited on pages 138 and 139.)

Teodorovich, E. V. (1997), Calculation of the effective permeability of a randomly inhomogeneous porous medium, *Journal of Experimental and Theoretical Physics*, *85*(1), 173–178. (Cited on page 139.)

Toms, J., T. M. Müller, and B. Gurevich (2007), Seismic attenuation in porous rocks with random patchy saturation, *Geophysical Prospecting*, *55*(5), 671–678. (Cited on pages 30, 32, 33, 115, 117 and 119.)

Toms-Stewart, J., T. M. Müller, B. Gurevich, and L. Paterson (2009), Statistical characterization of gas-patch distributions in partially saturated rocks, *Geophysics*, *74*(2), WA51–WA64. (Cited on pages 31 and 122.)

Torquato, S. (2002), *Random Heterogeneous Materials: Microstructure and Macroscopic Properties*, Springer New York. (Cited on pages 143, 147, 150, 156 and 157.)

Tronicke, J., and K. Holliger (2005), Quantitative integration of hydrogeophysical data: Conditional geostatistical simulation for characterizing heterogeneous alluvial aquifers, *Geophysics*, *70*(3), H1–H10. (Cited on page 144.)

Tsang, L., and J. A. Kong (1981), Scattering of electromagnetic waves from random media with strong permittivity fluctuations, *Radio Science*, *16*(3), 303–320. (Not cited.)

Tserkovnyak, Y., and D. Johnson (2002), Can one hear the shape of a saturation patch?, *Geophysical Research Letters*, *29*(7), 1108, doi:10.1029/2001GL014709. (Cited on page 26.)

Underschultz, J., C. Boreham, T. Dance, L. Stalker, B. Freifeld, D. Kirste, and J. Ennis-King (2011), CO_2 storage in a depleted gas field: An overview of the CO2CRC Otway project and initial results, *International Journal of Greenhouse Gas Control*, *5*(4), 922 – 932, doi:10.1016/j.ijggc.2011.02.009. (Cited on page 1.)

Vanorio, T., G. Mavko, S. Vialle, and K. Spratt (2010), The rock physics basis for 4D seismic monitoring of CO_2 fate: Are we there yet?, *The Leading Edge*, *29*(2), 156–162, doi:10.1190/1.3304818. (Cited on page 3.)

Wang, H. F. (2000), *Theory of Linear Poroelasticity: With Applications to Geomechanics and Hydrogeologoy*, Princeton University Press. (Cited on pages 28 and 184.)

Wang, Z., M. E. Cates, and R. T. Langan (1998), Seismic monitoring of a CO_2 flood in a carbonate reservoir: A rock physics study, *Geophysics*, *63*(5), 1604–1617. (Cited on page 4.)

Watson, M., Y. Cinar, T. Dance, R. Pevzner, E. Tenthorey, E. Caspari, J. Ennis-King, V. Shulakova, M. Bunch, M. Urosevic, R. Singh, B. Gurevich, L. Paterson, C. Jenkins, and M. Raab (2012), Otway Stage 2C Science Report - Verification of CO_2 Storage in a Saline Formation (Paaratte) Using Time Lapse Seismic., *RPT:12-4109*, Cooperative Research Centre for Greenhouse Gas Technologies, Canberra, Australia. (Cited on pages 40, 41, 61, 126 and 185.)

White, D. J., G. Burrowes, T. David, Z. Hajnal, K. Hirsche, I. Hutcheon, E. Majer, B. Rostron, and S. Whittaker (2004), Greenhouse gas sequestration in abandoned oil reservoirs: The International Energy Agency Weyburn pilot project, *GSA Today*, *14*(7), 4–10. (Cited on page 1.)

White, J. E. (1975), Computed seismic speeds and attenuation in rocks with partial gas saturation, *Geophysics*, *40*(2), 224–232. (Cited on page 30.)

Widess, M. B. (1973), How thin is a thin bed?, *Geophysics*, *38*(6), 1176–1180. (Cited on page 38.)

Winkler, K. W. (1983), Contact stiffness in granular porous materials: Comparison between theory and experiment, *Geophysical Research Letters*, *10*(11), 1073–1076, doi:10.1029/GL010i011p01073. (Cited on page 23.)

Wood, A. B. (1955), *A textbook of sound*, The MacMillan Co., New York, 3rd revised edition. (Cited on page 29.)

Xue, Z., and T. Ohsumi (2004), Seismic wave monitoring of CO_2 migration in water-saturated porous sandstone, *Exploration Geophysics*, *35*(1), 25–32. (Cited on page 1.)

Xue, Z., D. Tanase, and J. Watanabe (2006), Estimation of CO_2 saturation from time-lapse CO_2 well logging in an onshore aquifer, Nagaoka, Japan, *Exploration Geophysics*, *37*(1), 19–29. (Cited on pages 1, 2, 116, 117, 119, 121 and 124.)

Yilmaz, Ö. (2001), *Seismic data analysis: processing, inversion, and interpretation of seismic data*, 10, SEG Books. (Cited on page 37.)

Zöppritz, K. (1919), Erdbebenwellen VIIIB, Über Reflexion and Durchgang seismischer Wellen duch Unstetigkeitsflächen, *Göttinger Nachr.*, *I*, 66–84. (Cited on page 13.)

Every reasonable effort has been made to acknowledge the owners of copyright material. I would be pleased to hear from any copyright owner who has been omitted or incorrectly acknowledged.

List of Tables

List of Figures

Appendix A

Copyright consent

Re: Copyright permission

Associate Publisher <assocpub@aps.org>

Tue 1/04/2014 12:03 AM

To:Eva Caspari <eva.caspari@postgrad.curtin.edu.au>;

Dear Dr. Caspari,

Thank you for your email. As the author, you have the right to use the article or a portion of the article in a thesis or dissertation without requesting permission from APS, provided the bibliographic citation and the APS copyright credit line are given on the appropriate pages.

Best wishes,

Jamie Casey

Circulation and Fulfillment Assistant

American Physical Society

http://librarians.aps.org/

On Fri, Mar 21, 2014 at 2:56 AM, Eva Caspari <eva.caspari@postgrad.curtin.edu.au> wrote:

> Dear Associate Publisher,
>
> It is my understanding that APS holds copyrights in the following material:
>
> E. Caspari, B. Gurevich, and T. M. Müller, Frequency-dependent effective hydraulic conductivity of strongly heterogeneous media, 2013, Phys. Rev. E 88, 042119
> DOI: 10.1103/PhysRevE.88.042119
>
> I would like to reproduce this work (figures/caption and text) in a doctoral thesis which I am currently undertaking at Curtin University in Perth, Western Australia. I intend to integrate the article into a thesis chapter, so the formatting will be the one of my thesis. The title of the thesis is "Effect of scale and saturation on effective properties of porous rocks for seismic monitoring of CO2 sequestration".
>
> Once completed, the thesis will be made available in hard-copy form in the Curtin Library and in digital form on the Internet via the Australasian Digital Thesis Program. The material will be provided strictly for educational purposes and on a non-commercial basis. Further information on the ADT program can be found at http://adt.caul.edu.au.
>
> I would be most grateful for your consent to the copying and communication of the work as proposed. Full acknowledgement of the ownership of the copyright and the source of the material will be provided with the material. I would be willing to use a specific form of acknowledgement that you may require and to communicate any conditions
> relating to its use.
>
> If you are not the copyright owner of the material in question, I would be grateful for any information you can provide as to who is likely to hold the copyright. I look forward to hearing from you and thank you in advance for your consideration of my request.
>
> Yours sincerely
> Eva Caspari

JOHN WILEY AND SONS LICENSE
TERMS AND CONDITIONS

Mar 21, 2014

This is a License Agreement between Eva Caspari ("You") and John Wiley and Sons ("John Wiley and Sons") provided by Copyright Clearance Center ("CCC"). The license consists of your order details, the terms and conditions provided by John Wiley and Sons, and the payment terms and conditions.

All payments must be made in full to CCC. For payment instructions, please see information listed at the bottom of this form.

License Number	3353480105044
License date	Mar 21, 2014
Licensed content publisher	John Wiley and Sons
Licensed content publication	Geophysical Research Letters
Licensed content title	Time-lapse sonic logs reveal patchy CO2 saturation in-situ
Licensed copyright line	Copyright 2011 by the American Geophysical Union.
Licensed content author	E. Caspari,T. M. Müller,B. Gurevich
Licensed content date	Jul 1, 2011
Start page	n/a
End page	n/a
Type of use	Dissertation/Thesis
Requestor type	Author of this Wiley article
Format	Print and electronic
Portion	Full article
Will you be translating?	No
Title of your thesis / dissertation	Effect of scale and saturation on effective properties of porous rocks for seismic monitoring of CO2 sequestration
Expected completion date	Mar 2014
Expected size (number of pages)	195
Total	0.00 USD
Terms and Conditions	

TERMS AND CONDITIONS

This copyrighted material is owned by or exclusively licensed to John Wiley & Sons, Inc. or one of its group companies (each a "Wiley Company") or a society for whom a Wiley Company has exclusive publishing rights in relation to a particular journal (collectively "WILEY"). By clicking "accept" in connection with completing this licensing transaction, you agree that the following terms and conditions apply to this transaction (along with the billing and payment terms and conditions established by the Copyright Clearance Center Inc., ("CCC's Billing and Payment terms and conditions"), at the time that you opened your RightsLink account (these are available at any time at http://myaccount.copyright.com).

Terms and Conditions

1. The materials you have requested permission to reproduce (the "Materials") are protected by copyright.

2.You are hereby granted a personal, non-exclusive, non-sublicensable, non-transferable, worldwide, limited license to reproduce the Materials for the purpose specified in the licensing process. This license is for a one-time use only with a maximum distribution equal to the number that you identified in the licensing process. Any form of republication granted by this license must be completed within two years of the date of the grant of this license (although copies prepared before may be distributed thereafter). The Materials shall not be used in any other manner or for any other purpose. Permission is granted subject to an appropriate acknowledgement given to the author, title of the material/book/journal and the publisher. You shall also duplicate the copyright notice that appears in the Wiley publication in your use of the Material. Permission is also granted on the understanding that nowhere in the text is a previously published source acknowledged for all or part of this Material. Any third party material is expressly excluded from this permission.

3. With respect to the Materials, all rights are reserved. Except as expressly granted by the terms of the license, no part of the Materials may be copied, modified, adapted (except for minor reformatting required by the new Publication), translated, reproduced, transferred or distributed, in any form or by any means, and no derivative works may be made based on the Materials without the prior permission of the respective copyright owner. You may not alter, remove or suppress in any manner any copyright, trademark or other notices displayed by the Materials. You may not license, rent, sell, loan, lease, pledge, offer as security, transfer or assign the Materials, or any of the rights granted to you hereunder to any other person.

4. The Materials and all of the intellectual property rights therein shall at all times remain the exclusive property of John Wiley & Sons Inc or one of its related companies (WILEY) or their respective licensors, and your interest therein is only that of having possession of and the right to reproduce the Materials pursuant to Section 2 herein during the continuance of this Agreement. You agree that you own no right, title or interest in or to the Materials or any of the intellectual property rights therein. You shall have no rights hereunder other than the license as provided for above in Section 2. No right, license or interest to any trademark, trade name, service mark or other branding ("Marks") of WILEY or its licensors is granted hereunder, and you agree that you shall not assert any such right, license or interest with respect thereto.

5. NEITHER WILEY NOR ITS LICENSORS MAKES ANY WARRANTY OR REPRESENTATION OF ANY KIND TO YOU OR ANY THIRD PARTY, EXPRESS, IMPLIED OR STATUTORY, WITH RESPECT TO THE MATERIALS OR THE ACCURACY OF ANY INFORMATION CONTAINED IN THE MATERIALS, INCLUDING, WITHOUT LIMITATION, ANY IMPLIED WARRANTY OF MERCHANTABILITY, ACCURACY, SATISFACTORY QUALITY, FITNESS FOR A PARTICULAR PURPOSE, USABILITY, INTEGRATION OR NON-INFRINGEMENT AND ALL SUCH WARRANTIES ARE HEREBY EXCLUDED BY WILEY AND ITS LICENSORS AND WAIVED BY YOU.

6. WILEY shall have the right to terminate this Agreement immediately upon breach of this Agreement by you.

7. You shall indemnify, defend and hold harmless WILEY, its Licensors and their respective directors, officers, agents and employees, from and against any actual or threatened claims, demands, causes of action or proceedings arising from any breach of this Agreement by you.

8. IN NO EVENT SHALL WILEY OR ITS LICENSORS BE LIABLE TO YOU OR ANY OTHER PARTY OR ANY OTHER PERSON OR ENTITY FOR ANY SPECIAL, CONSEQUENTIAL, INCIDENTAL, INDIRECT, EXEMPLARY OR PUNITIVE DAMAGES, HOWEVER CAUSED, ARISING OUT OF OR IN CONNECTION WITH THE DOWNLOADING, PROVISIONING, VIEWING OR USE OF THE MATERIALS REGARDLESS OF THE FORM OF ACTION, WHETHER FOR BREACH OF CONTRACT, BREACH OF WARRANTY, TORT, NEGLIGENCE, INFRINGEMENT OR OTHERWISE (INCLUDING, WITHOUT LIMITATION, DAMAGES BASED ON LOSS OF PROFITS, DATA, FILES, USE, BUSINESS OPPORTUNITY OR CLAIMS OF THIRD PARTIES), AND WHETHER OR NOT THE PARTY HAS BEEN ADVISED OF THE POSSIBILITY OF SUCH DAMAGES. THIS LIMITATION SHALL APPLY NOTWITHSTANDING ANY FAILURE OF ESSENTIAL PURPOSE OF ANY LIMITED REMEDY PROVIDED HEREIN.

9. Should any provision of this Agreement be held by a court of competent jurisdiction to be illegal, invalid, or unenforceable, that provision shall be deemed amended to achieve as nearly as possible the same economic effect as the original provision, and the legality, validity and enforceability of the remaining provisions of this Agreement shall not be affected or impaired thereby.

10. The failure of either party to enforce any term or condition of this Agreement shall not constitute a waiver of either party's right to enforce each and every term and condition of this Agreement. No breach under this agreement shall be deemed waived or excused by either party unless such waiver or consent is in writing signed by the party granting such waiver or consent. The waiver by or consent of a party to a breach of any provision of this Agreement shall not operate or be construed as a waiver of or consent to any other or subsequent breach by such other party.

11. This Agreement may not be assigned (including by operation of law or otherwise) by you without WILEY's prior written consent.

12. Any fee required for this permission shall be non-refundable after thirty (30) days from receipt

13. These terms and conditions together with CCC's Billing and Payment terms and conditions (which are incorporated herein) form the entire agreement between you and WILEY concerning this licensing transaction and (in the absence of fraud) supersedes all prior agreements and representations of the parties, oral or written. This Agreement may not be amended except in writing signed by both parties. This Agreement shall be binding upon and inure to the benefit of the parties' successors, legal representatives, and authorized assigns.

14. In the event of any conflict between your obligations established by these terms and conditions and those established by CCC's Billing and Payment terms and conditions, these terms and conditions shall prevail.

15. WILEY expressly reserves all rights not specifically granted in the combination of (i) the license details provided by you and accepted in the course of this licensing transaction, (ii) these terms and conditions and (iii) CCC's Billing and Payment terms and conditions.

16. This Agreement will be void if the Type of Use, Format, Circulation, or Requestor Type was misrepresented during the licensing process.

17. This Agreement shall be governed by and construed in accordance with the laws of the State of New York, USA, without regards to such state's conflict of law rules. Any legal action, suit or proceeding arising out of or relating to these Terms and Conditions or the breach thereof shall be instituted in a court of competent jurisdiction in New York County in the State of New York in the United States of America and each party hereby consents and submits to the personal jurisdiction of such court, waives any objection to venue in such court and consents to service of process by

registered or certified mail, return receipt requested, at the last known address of such party.

Wiley Open Access Terms and Conditions

Wiley publishes Open Access articles in both its Wiley Open Access Journals program [http://www.wileyopenaccess.com/view/index.html] and as Online Open articles in its subscription journals. The majority of Wiley Open Access Journals have adopted the Creative Commons Attribution License (CC BY) which permits the unrestricted use, distribution, reproduction, adaptation and commercial exploitation of the article in any medium. No permission is required to use the article in this way provided that the article is properly cited and other license terms are observed. A small number of Wiley Open Access journals have retained the Creative Commons Attribution Non Commercial License (CC BY-NC), which permits use, distribution and reproduction in any medium, provided the original work is properly cited and is not used for commercial purposes.

Online Open articles - Authors selecting Online Open are, unless particular exceptions apply, offered a choice of Creative Commons licenses. They may therefore select from the CC BY, the CC BY-NC and the Attribution-NoDerivatives (CC BY-NC-ND). The CC BY-NC-ND is more restrictive than the CC BY-NC as it does not permit adaptations or modifications without rights holder consent.

Wiley Open Access articles are protected by copyright and are posted to repositories and websites in accordance with the terms of the applicable Creative Commons license referenced on the article. At the time of deposit, Wiley Open Access articles include all changes made during peer review, copyediting, and publishing. Repositories and websites that host the article are responsible for incorporating any publisher-supplied amendments or retractions issued subsequently.
Wiley Open Access articles are also available without charge on Wiley's publishing platform, **Wiley Online Library** or any successor sites.

Conditions applicable to all Wiley Open Access articles:

- The authors' moral rights must not be compromised. These rights include the right of "paternity" (also known as "attribution" - the right for the author to be identified as such) and "integrity" (the right for the author not to have the work altered in such a way that the author's reputation or integrity may be damaged).

- Where content in the article is identified as belonging to a third party, it is the obligation of the user to ensure that any reuse complies with the copyright policies of the owner of that content.

- If article content is copied, downloaded or otherwise reused for research and other purposes as permitted, a link to the appropriate bibliographic citation (authors, journal, article title, volume, issue, page numbers, DOI and the link to the definitive published version on Wiley Online Library) should be maintained. Copyright notices and disclaimers must not be deleted.
    - Creative Commons licenses are copyright licenses and do not confer any other rights, including but not limited to trademark or patent rights.

- Any translations, for which a prior translation agreement with Wiley has not been agreed, must prominently display the statement: "This is an unofficial translation of an article that appeared in a Wiley publication. The publisher has not endorsed this translation."

If you would like to pay for this license now, please remit this license along with your payment made payable to "COPYRIGHT CLEARANCE CENTER" otherwise you will be invoiced within 48 hours of the license date. Payment should be in the form of a check or money order referencing your account number and this invoice number RLNK501256989. Once you receive your invoice for this order, you may pay your invoice by credit card. Please follow instructions provided at that time.

Make Payment To:
Copyright Clearance Center
Dept 001
P.O. Box 843006
Boston, MA 02284-3006

For suggestions or comments regarding this order, contact RightsLink Customer Support: customercare@copyright.com or +1-877-622-5543 (toll free in the US) or +1-978-646-2777.

Gratis licenses (referencing $0 in the Total field) are free. Please retain this printable license for your reference. No payment is required.